

EXTENSIONAL DEFORMATION AND VOLCANISM WITHIN THE NORTHERN  
PUERTECITOS VOLCANIC PROVINCE, SIERRA SANTA ISABEL, BAJA CALIFORNIA,  
MEXICO

Thesis by

Elizabeth Ann Nagy

In Partial Fulfillment of the Requirements

for the Degree of

Doctor of Philosophy

California Institute of Technology

Pasadena, California

1997

(Submitted April 18, 1997)

© 1997

Elizabeth Ann Nagy

All rights Reserved

“Myself when young did eagerly frequent  
Doctor and Saint, and heard great Argument  
    About it and about: but evermore  
Came out by the same Door as in I went.”

Quatrain XXVII from the *Rubáiyát of Omar Khayyám*

### Acknowledgments

First and foremost I thank my field assistants Tom Tyndall (the Great Ponderer), Karen Holt (the Trailblazer), Katrina Rostedt (the Discoverer), and Karah Wertz (La Chanteuse) who hiked many miles with me over some pretty rough terrain, often carrying plenty of weight. Without their assistance this project would not have been possible, and I thank each of them for their patience with me and their input on interpreting the geologic story preserved in the Santa Isabel Wash.

I thank my thesis advisor Joann Stock who gave me many opportunities to interact with others working in Baja California and mainland Mexico, and who never discouraged me from trying a new technique or approach to solving a problem. I thank Claudia Lewis for discussions and reviews of my early results and thesis chapters, preprints of submitted manuscripts, and most importantly for her Ph.D. thesis work which provided important guidelines for the project I designed here. She has been an invaluable resource throughout my thesis work and I greatly appreciate her assistance.

A 3-day visit to my field area with Peter Kokelaar and Malcolm Howells was invaluable for my understanding of certain types of volcanic deposits, and their enthusiasm for the geology helped greatly to keep me motivated. I also thank Robert L. Smith for his visit to the field region. It is a true learning experience to be with Bob in the field, and I hope some day to be as observant a field geologist as he is.

Several people at Caltech have provided important assistance to various aspects of this project. I thank Mahmood Chaudhry for help with mineral separation techniques, Paul Carpenter for guidance on the electron microprobe, Anne Lilje for computer graphics assistance, Jan Mayne for drafting assistance and advice, and Jim O'Donnell for making all aspects of library-related inquiries smooth and efficient. I thank work-study students Tessa Miller, Vicky Tanusheva, and Sara Russell for helping me with tedious mineral separation procedures, cutting thin section, and running paleomagnetic samples. Martha House, Adam Kent, and Joe Kirschvink are thanked for carefully reviewing early versions of various chapters. I modified a computer program from Dave Evans (who modified it from P. McFadden and M. McElhinny), and I thank him for helping me wade through the tricky parts. I thank John Holt for helping me wrestle with MSWD values.

I thank Marty Grove at the UCLA geochronology laboratory for his assistance in the lab as well as his review of an early draft of the geochronology chapter. I thank T. Mark Harrison for permitting use of his lab, and Keith Mahon for discussions on statistical treatment of the data.

I also thank many others who have helped with various aspects of this project through discussions or technical assistance including Mark Abolins, Gary Axen, Wendy Bohrson,



Cheryl Contopulos, Evelina Cui, Becky Dorsey, Brian Hausback, Rowena Lohman, Arturo Martín-Barajas, Tim Melbourne, Mike Oskin, Mark Peters, George Rossman, Craig Scrivner, Lee Silver, Paul Umhoefer, Laura Wasylenki, Brad Woods, Blair Zajac, and Lupei Zhu. I thank my officemates Jean Hsieh and Judy Zachariasen for, among other things, allowing me to have two desks.

I would also like to take this opportunity to thank two professors from my undergraduate education. Bruce Wilkinson at the University of Michigan and Hartmut Spetzler at the University of Colorado played important roles in encouraging me to pursue geology and to appreciate it as a challenging science. I thank both of them for being approachable, honest, and helpful.

I thank my parents, Robert and Julie Nagy, for their constant love and encouragement.

I thank Xavier Quidelleur most sincerely for the many ways in which he helped me with this project, including assistance collecting paleomagnetic samples, guidance in running and analyzing samples at the UCLA geochronology lab, his time spent reanalyzing some of the geochronology data in order to improve the measurement precision, discussions and reviews of several of my thesis chapters, assistance compiling data tables, and moral support. I thank him for teaching me to continue asking questions about something until it is understood on the most fundamental level possible.

It is simply not possible to thank the many friends I have known since I have been in Pasadena at Caltech. You know who you are. To all my friends!

Abstract

Geologic features at the western edge of the Gulf Extensional Province (GEP) in northeastern Baja California, Mexico, record details of Pacific-North American (PAC-NAM) plate boundary history prior to and during its establishment within the Gulf of California. Methods of study in Santa Isabel Wash (SIW) (informally named) in the northern Sierra Santa Isabel include geologic mapping of ~140 km<sup>2</sup> (1:20000 scale) along the northern margin of the Miocene-Pliocene Puertecitos Volcanic Province (PVP), <sup>40</sup>Ar/<sup>39</sup>Ar geochronology, electron microprobe analysis, paleomagnetic study, and petrography. Local Neogene stratigraphy (spanning ~17-6 Ma) includes volcanoclastic breccias, basaltic to dacitic lava flows, and rhyolitic pyroclastic flow deposits. The completeness of the lithologic package improves stratigraphic correlations between the PVP and nearby regions.

High-angle extension-related faults cut all rocks in SIW. The southeastward projection of the pre-6 Ma Matomí accommodation zone, which separates a northern region of greater and more prolonged extension from a less extended southern zone, may pass on the north side of SIW. Paleomagnetic analysis indicates no vertical axis rotations in SIW since 6 Ma. This contrasts with regions north of the Matomí accommodation zone where clockwise rotation has accompanied extensional deformation since 3-6 Ma. About 500 meters of post-6 Ma, E-side-down displacement occurs across two major, NNW-striking normal faults on the west side of SIW. These, and smaller synthetic and antithetic faults in the hanging walls, accommodate up to 4% E- to ENE-directed extension. Quaternary deformation is also documented.

A new model developed to explain ENE-directed extension in northeastern Baja California partitions present-day PAC-NAM plate motion between NNW-striking, sinistral dip-slip faults and N- to NNW-striking, dextral (oblique?) strike-slip fault(s) in the northernmost Gulf of California. The model offers explanations for the geometry of plate motion accommodation between the latitudes of the Agua Blanca fault and the PVP, bathymetric features near Wagner and Consag basins, the position and jumps of nearby spreading centers since 6 Ma, the greater width and bend in coastline of the northernmost Gulf of California, the incorporation of the PVP into the GEP 2-3 Ma, and suggests a transitional tectonic scenario between oceanic spreading centers and continental transforms (“Wagner Transition Zone”).

Table of Contents

Acknowledgments.....	iv
Abstract.....	vi
List of Plates.....	xi
Chapter I. Introduction.....	1
1.1. <i>Overview</i> .....	2
1.2. <i>Pacific-North America plate boundary</i> .....	3
A. <i>30 Ma to 12.5 Ma</i> .....	3
B. <i>12.5 Ma to 5.5 Ma</i> .....	5
C. <i>5.5 Ma to present</i> .....	8
1.3. <i>Gulf Extensional Province (GEP)</i> .....	11
1.4. <i>Geologic setting of northeastern Baja California, Mexico</i> .....	11
1.5. <i>Santa Isabel Wash</i> .....	14
Figures for Chapter I.....	16
Chapter II. Geologic setting and lithology of units in Santa Isabel Wash.....	30
2.1. <i>Introduction</i> .....	31
2.2. <i>Preserved geologic record</i> .....	32
2.3. <i>Techniques and terminology</i> .....	34
2.4. <i>Lithologic units</i> .....	36
2.5. <i>Regional lithologic correlations</i> .....	72
2.6. <i>Summary</i> .....	87
Figures for Chapter II.....	89
Chapter III. $^{40}\text{Ar}/^{39}\text{Ar}$ geochronology of lithologic units in Santa Isabel Wash.....	99
3.1. <i>Introduction</i> .....	100
3.2. <i>Basic theory of <math>^{40}\text{Ar}/^{39}\text{Ar}</math> geochronology</i> .....	102
3.3. <i>Laboratory techniques</i> .....	104
A. <i>Basic mineral separation procedures</i> .....	104
B. <i>Non-conventional mineral separation procedures - exposure to <math>^{137}\text{Cs}</math></i> .....	106

C. <i>Packaging and irradiation</i> .....	107
D. <i>Analytical methods - overview</i> .....	107
E. <i>Heating methods and analysis details</i> .....	108
F. <i>Data analysis</i> .....	110
3.4. <i>Results and Interpretations</i> .....	113
A. <i>Measurement precision</i> .....	113
B. <i>Flux monitors and J-factors</i> .....	114
C. <i>Internal standard</i> .....	115
D. <i>Samples exposed to <sup>137</sup>Cs</i> .....	116
E. <i>All other samples</i> .....	117
3.5. <i>Discussion</i> .....	121
A. <i>Volcanism and structural implications</i> .....	121
B. <i>Other geochronologic studies of same units</i> .....	122
3.6. <i>Conclusions</i> .....	124
Tables for Chapter III.....	126
Figures for Chapter III.....	137
Chapter IV. <i>Map and structural analysis of Santa Isabel Wash in the northern Sierra Santa Isabel region</i> .....	156
4.1. <i>Introduction</i> .....	157
4.2. <i>Previous work</i> .....	158
4.3. <i>1:20000 geologic map and cross section</i> .....	160
A. <i>Overview</i> .....	160
B. <i>Thickness changes in 6 Ma pyroclastic flow deposits</i> .....	161
C. <i>Tilts</i> .....	165
D. <i>Faults</i> .....	166
i. <i>Pre-6-7 Ma deformation</i> .....	167
ii. <i>Post-6 Ma (excluding Quaternary) deformation</i> .....	168
iii. <i>Quaternary deformation</i> .....	174
4.4. <i>Structural model</i> .....	175

4.5. <i>Conclusions</i> .....	176
Figures for Chapter IV.....	178
Chapter V. Paleomagnetic study of 6 Ma volcanic tuffs in Santa Isabel Wash.....	194
5.1. <i>Introduction</i> .....	195
5.2. <i>Field and laboratory methods</i> .....	197
A. <i>Sample collection and preparation for measurement</i> .....	197
B. <i>Demagnetization strategies</i> .....	199
C. <i>Rock magnetic and magnetic susceptibility tests</i> .....	203
5.3. <i>Results</i> .....	205
A. <i>Statistical methods and stability of RM within sites</i> .....	205
B. <i>Site to site synthesis</i> .....	208
C. <i>Test for common mean direction</i> .....	209
5.4. <i>Interpretation</i> .....	212
A. <i>Group means relative to each other</i> .....	213
B. <i>Group means relative to geomagnetic north</i> .....	214
5.5. <i>Comparison of results to Sierra San Fermín and Sierra San Felipe regions</i> .....	216
A. <i>Lithologic correlations</i> .....	216
B. <i>Relative rotations</i> .....	221
5.6. <i>Conclusions</i> .....	224
Tables for Chapter V.....	227
Figures for Chapter V.....	239
Chapter VI. Regional synthesis and Summary.....	280
6.1. <i>Summary of geologic history of Santa Isabel Wash in the northern Sierra Santa Isabel</i> .....	281
6.2. <i>Comparison with adjacent areas (Southern Valle Chico, Sierra San Fermín, PVP) and relationship to Matomí accommodation zone</i> .....	287
6.3. <i>Relationship to Gulf Extensional Province and Gulf of California spreading system</i> ....	292
6.4. <i>Relationship to PAC-NAM plate boundary</i> .....	294

<i>6.5. Model to explain present-day ENE-directed extension in northeastern Baja California, Mexico</i> .....	298
<i>6.6. Implications for the propagation of oceanic rifts into continents</i> .....	303
<i>6.7. Conclusions</i> .....	304
Figures for Chapter VI.....	307
References.....	330
Appendices:	
Appendix A. Results from electron microprobe analyses (atomic proportions).....	341
Appendix B. Results from electron microprobe analyses (mineral compositions)...	345
Appendix C. Mineral separation techniques.....	350
Appendix D. <sup>40</sup> Ar/ <sup>39</sup> Ar laser fusion analytical data.....	353
Appendix E. Collection techniques for paleomagnetic samples.....	363

List of Plates

Plate I. Geologic map of the northern Sierra Santa Isabel (informally referred to as the Santa Isabel Wash region). Note that Santa Isabel Wash and Arroyo Oculito are informal names assigned here for the first time.

Plate II. Cross sections to accompany the geologic map of the northern Sierra Santa Isabel. No vertical exaggeration. The map units are listed from youngest (top) to oldest (bottom) in the legend. The ages of *Tma<sub>hem</sub>* and *Tma<sub>ugl</sub>* relative to *Tmr<sub>can</sub>* and *Tma<sub>gem</sub>* are not clear on the basis of field relationships, although they are interpreted to have been deposited at the same time as *Tma<sub>gem</sub>*. Additional information for each lithologic unit is given in the Legend of Plate I.

Chapter I

Introduction

1.1. *Overview*

1.2. *Pacific-North America plate boundary*

A. *30 Ma to 12.5 Ma*

B. *12.5 Ma to 5.5 Ma*

C. *5.5 Ma to present*

1.3. *Gulf Extensional Province (GEP)*

1.4. *Geologic setting of northeastern Baja California, Mexico*

1.5. *Santa Isabel Wash*



### 1.1. *Overview*

The present-day Pacific-North America (PAC-NAM) plate boundary, which accommodates the northwestward motion of PAC relative to NAM, consists in different localities of the three major types of plate tectonic boundaries. For example, subduction of PAC below NAM occurs along the Aleutian arc, transform faults such as the San Andreas (California) and Queen Charlotte (Canada) faults allow the two plates to slide past each other, and spreading centers within the Gulf of California have formed where the plates are pulling apart from each other. The nature of these various types of plate boundaries is a function of the geometric relationship between the forces driving relative plate motions, the orientation of the deforming plate boundary, and any partitioning of plate boundary displacement onto more than one structure.

The study area described here is located in northeastern Baja California, Mexico, (referred to hereafter simply as Baja California) near the coast of the Gulf of California (also called the Sea of Cortez) (Figure 1.1). The PAC-NAM plate boundary is presently located within the Gulf of California, and some of the history of its development is recorded in the study area. The motivation behind this study was to examine and document that geologic history in much greater detail than had previously been attempted, and to place the results into a regional context. This study provides further understanding of the volcanic and deformational history associated with the developing rift system. Regional correlations established in this study help clarify and simplify the volcanic stratigraphy of a larger area mapped by previous workers.

This introductory chapter gives a brief history of the plate boundary, describes major geologic features in northeastern Baja California, and briefly introduces the study area. Chapter II details the lithologic history of the mapped area as determined from field study, including classification and description of map units, outcrop, hand sample, and thin section descriptions, and electron microprobe results. Local lithologic correlations are discussed. Age constraints are summarized for each unit based upon field relationships and  $^{40}\text{Ar}/^{39}\text{Ar}$  geochronology. Chapter III describes mineral separation and measurement procedures for

the geochronologic analyses performed at the UCLA  $^{40}\text{Ar}/^{39}\text{Ar}$  facility. Crystallization ages for 21 samples are calculated and discussed. Chapter IV presents a 1:20000 geologic map based upon eight months of field study. Emphasis is placed on the structures accommodating extensional deformation and cross sections are presented. Chapter V discusses a paleomagnetic study of 218 rock cores collected in the study area from a series of 6 Ma pyroclastic flow deposits. Sampling and demagnetization techniques, statistical treatment of the data, and interpretation of the results are presented. Comparisons are made between this study and a similar study in a nearby region to the north where rotational deformation was detected via paleomagnetic analysis of some of the same lithologic units. Chapter VI integrates and summarizes the results from each of the previous chapters, and discusses the relationship between geologic features found in the study area, a structural accommodation zone to the northwest, the nearby system of transform faults and spreading centers within the Gulf of California to the southeast, and parameters such as timing and direction of extension determined in other areas along the margins of the Gulf of California. Finally, a new model of the PAC-NAM plate boundary in the northernmost Gulf of California is presented and discussed.

## 1.2. *Pacific-North America plate boundary*

### A. *30 Ma to 12.5 Ma*

Reconstructions characterizing the Cenozoic evolution of the PAC-NAM plate boundary were performed in a classic study by Atwater (1970) on the basis of magnetic anomaly patterns preserved on the Pacific plate. In short, the East Pacific Rise came into contact with the subduction zone where the Farallon Plate was subducting beneath western North America at Chron 10 time (~ 30 Ma). The triple junction which formed where these three plates met was dynamically unstable and two migrating triple junctions resulted. Ignoring some geometric complexities, the Mendocino triple junction migrated northwestward (isolating the Juan de Fuca Plate) and the Rivera triple junction migrated

southeastward (isolating the Guadalupe Plate from fragments of the Farallon plate which were farther south, e.g., Nazca and Cocos plates). As each of these triple junctions migrated, subduction ceased in their wake and the plate boundary was replaced by the formation of the San Andreas transform between them. Subduction west of Baja California was gradually replaced by a similar transcurrent fault zone. This change occurred ~ 20 Ma west of northernmost Baja California and migrated southwards. By ~ 13 Ma subduction was only occurring west of the southern half of the peninsula (Stock and Lee, 1994).

Tertiary extension in western North America coincided with the change from a subduction to transform boundary (Zoback et al., 1981). This extension has been documented and studied in detail by many workers (e.g., see overview by Metcalf and Smith, 1995) and probably resulted from a number of plate boundary-related processes (see Stock and Hodges (1989) for a summary of possible causes, as well as explanations for extension not related to plate boundary development). To the east of the present-day Baja California peninsula, ENE-WSW-directed extensional faulting in Sinaloa, Mexico, generally began 17 Ma (but as early as 32 Ma) and is believed to have been within the southwestern extent of the early phase (30-10 Ma) of Basin and Range extension (also ENE-WSW-directed) in the western United States (Zoback et al., 1981; Henry, 1989; Henry and Aranda-Gomez, 1992). It has also been postulated that some of this early extension in Sinaloa might represent back-arc extension related to subduction west of Baja California (e.g., Karig and Jensky, 1972), or gravitational collapse of thick crust along inferred, pre-existing, tensional fault planes (e.g., Moore, 1973). Additionally, evidence of middle Miocene extensional deformation exists on Isla Tiburón (an island within the Gulf of California; see Figure 1.2), constrained between 13 and 15 Ma (Gastil et al., 1974), and in the southern Sierra Juárez of northeastern Baja California, sometime between 11 and 16 Ma (Lee et al., 1996). On the basis of tilted volcanic rocks, northern Sinaloa has experienced a total of 20-50% extension whereas southern Sinaloa has experienced < 10% (Henry, 1989). The magnitude of pre-11 Ma, E-W-directed extension in the southern Sierra Juárez is 14-16% (Lee et al., 1996).

### B. 12.5 Ma to 5.5 Ma

Ongoing subduction west of the southern half of Baja California appears to have ceased simultaneously along this portion of the peninsula at the end of Chron 5A (12.5 Ma) (Atwater, 1970; Mammerickx and Klitgord, 1982; Spencer and Normark, 1989; Atwater, 1989; Stock and Lee, 1994). The size and distribution of the Miocene, subduction-related, volcanic arc in the vicinity of Baja California is poorly constrained, and the present record of the arc consists primarily of volcanoclastic deposits which formed on the flanks of the volcanoes. Subduction-related andesitic volcanism ended 17-22 Ma in northern Baja California and 10-12 Ma in southern Baja California (Gastil and Krummenacher, 1977; Gastil et al., 1979; Hausback, 1984; Neuhaus et al., 1988; Stock, 1989; Sawlan, 1991; Martín-Barajas et al., 1995; Lewis, 1996; Chapter II and III of this study). Ages are poorly constrained along the east margin of the Gulf of California in Sinaloa, but span 14-21 Ma in northwestern Sonora (Gastil and Krummenacher, 1977). The ages and distributions of these subduction-related arc rocks are discussed in greater detail in Chapter II.

When subduction ended, the Tosco-Abrejos and San Benito transform faults along the Pacific margin of Baja California (see Figure 1.2 for location) became the primary structures accommodating PAC-NAM plate boundary motion at this latitude (Kraus, 1965; Spencer and Normark, 1979). The strike of these faults ( $325^{\circ} \pm 3^{\circ}$ ) (Spencer and Normark, 1989) was sub-parallel to relative plate motion at that time (Spencer and Normark, 1979; Hausback, 1984; Stock and Hodges, 1989). However, a  $30^{\circ}$  CCW rotation of PAC-NAM plate motion is present if one compares the intervals 20-10 Ma and 10-5 Ma. The relative plate motion direction from 10.6 Ma to 5.5 Ma varied between  $294^{\circ} \pm 11^{\circ}$  and  $298^{\circ} \pm 12^{\circ}$  (Stock and Hodges, 1989).

Because the orientation of the Tosco-Abrejos transform fault was oblique to the new relative plate motion direction at that time, a newly imparted extensional component of the PAC-NAM plate motion needed to be accommodated somewhere along the plate boundary. This ENE-WSW-directed extensional component to PAC-NAM plate motion was accommodated via "proto-Gulf" extension in the vicinity of the present-day Gulf of

California (Atwater, 1970; Hausback, 1984; Stock and Hodges, 1989). This partitioning of the plate boundary motion is best illustrated by examining Pacific plate velocity vectors calculated from revised constraints on PAC-NAM plate motion. These vectors are illustrated in Figure 1.3 (reproduced from Stock and Hodges, 1989) for three time intervals (20.0-10.6 Ma, 10.6-5.5 Ma, and 5.5-0 Ma) and show the CCW change in relative plate motion between 10.6 and 5.5 Ma which was accommodated by NE-SW-directed extension (see vectors at bottom of Figure 1.3).

The position and orientation of the “proto-Gulf” extensional province was quite likely dictated by the geometry of the early Miocene, subduction-related volcanic arc which undoubtedly produced a zone of thermally weakened crust parallel to the former trench (Hausback, 1984; Lonsdale, 1989; Stock and Hodges, 1989). Lithospheric yield stress calculations (Bohannon and Parsons, 1995) predict zones of crustal weakness following the cessation of subduction on both sides (east and west) of the Peninsular Ranges batholith (PRB). These calculations, which do not specifically include the thermal effects of the volcanic arc, suggest that extensional deformation would nucleate to the east of the PRB immediately following the end of spreading along the Magdalena ridge 12.5 Ma (“stall-and-deform” model of Bohannon and Parsons, 1995). It is also plausible that this Neogene extension localized along Cretaceous extensional structures (e.g., back-arc basin related to Mesozoic subduction) in which the PRB formed a rigid western boundary and the Sierra Madre Occidental resisted extension to the east.

Given the scenario that “proto-Gulf” extension accommodated a component of PAC-NAM relative plate motion since about 10-12 Ma (Stock and Hodges, 1989), and the fact that the Tosco-Abrejos transform fault was probably active until 5.5 Ma (Spencer and Normark, 1979; Curray and Moore, 1984), the Baja California peninsula appears to have been gradually transferred from the North America plate to the Pacific plate between about 10-12 Ma and 5.5 Ma (Stock and Hodges, 1989).

There is abundant geologic evidence for extensional deformation between 12.5 and 5.5 Ma along the margins of the present Gulf of California. Evidence primarily comes from detailed mapping and geochronology along subaerial exposures of the faulted rift margins

(e.g., Gastil et al., 1975, 1979; Dokka and Merriam, 1982; Hausback, 1984; Stock and Hodges, 1990; Lewis, 1994; Zanchi, 1994; Lewis and Stock, in review, *J. Struct. Geol.*; this study), and identification of deposits indicative of middle to late Miocene marine incursions and deep marine environments (e.g., McCloy et al., 1988; Smith, 1991; Stock et al., 1996a). To date, the position of a seaway linking the Gulf of California to the Pacific Ocean during this time period has not been identified; the timing and spatial distribution of marine incursions need to be further examined in order to reconstruct the geography of the “proto-Gulf.” These and other studies permit further refinement of the history of this early phase of extension in the Gulf of California by addressing such questions as direction, timing, and amount of extension, episodic versus continuous extension, and differences in history of deformation between the northern and southern portions of the Gulf of California. Although much detailed study is still needed, Lee and others (1996) give a very complete summary of this evidence in Table 3 of their study.

Basin and Range extension in the United States changed to NW-SE- or WNW-ESE-directed about 10 Ma (Zoback et al., 1981; Henry, 1989); however, as described above (and depicted in Figure 1.3), the extension direction in Baja California during this time period was predominantly NE-SW- to ENE-WSW-directed (Hausback, 1984; Stock and Hodges, 1989; Lewis, 1994; Lewis and Stock, in review in *J. Struct. Geol.*; this study). A major episode of ENE-WSW-directed extensional faulting also began about 12-13 Ma in the Mexican Basin and Range province (Henry and Aranda-Gomez, 1992). This pre-5.5 Ma extension may have displaced Baja California as much as 100-150 km to the west-southwest relative to North America (Stock and Hodges, 1989). Estimated amounts of local extension in northeastern Baja California for this time period are between 5% and 15% (Stock and Hodges, 1990; Lewis, 1994; Lewis and Stock, in review in *J. Geophys. Res.*). From 17 to 4.5 Ma the early San Andreas fault system became increasingly active and experienced 100-150 km of dextral offset (Humphreys and Weldon, 1991; Weldon et al., 1993). Transpeninsular faults such as the Agua Blanca and Elsinore faults (Figure 1.2) are also interpreted to have begun accommodating significant amounts of plate motion near the end of this time interval (Humphreys and Weldon, 1991).

### *C. 5.5 Ma to present*

Opening of the modern Gulf of California began about 5.5 Ma with brittle and ductile stretching of the upper and lower continental crust, respectively (Curry and Moore, 1984). By 4.5 Ma the tip of the northward propagating East Pacific Rise reached continental crust off the southern end of Baja California (Lonsdale, 1989). Pull-apart basins were formed in the Gulf of California by about 4 Ma at step-overs between dextral strike-slip fault zones (Lonsdale, 1989). The oldest oceanic crust produced from seafloor spreading in the mouth of the Gulf of California is about 3.5 Ma (Anomaly 2A) (Larson et al., 1968; Curry and Moore, 1984; Lonsdale, 1989). Note that this refers to ocean crust formed by PAC-NAM spreading north of the Tamayo fracture zone (Figure 1.1), and not PAC-Rivera spreading which occurs south of this fracture zone. Although continental rifting and the development of sea floor spreading are unequivocally recorded at the mouth of the Gulf of California (both north and south of the Tamayo fracture zone), magnetic anomalies have not been identified in the central or northern Gulf of California (Larson et al., 1972; Lyle and Ness, 1991). Many of the basins (i.e., inferred spreading centers) in the northern gulf are filled with sediment originating from the Colorado River at the north end of the Gulf of California. The orientation and location of several of these northernmost ridges are very approximately drawn (dashed) in Figure 1.1 on the basis of basin bathymetry (Dauphin and Ness, 1991). An alternative interpretation of the bathymetry in the northernmost Gulf of California will be presented in Chapter VI of this study. The locations of the other portions of the Gulf of California spreading system in Figure 1.1 are taken from Fenby and Gastil (1991).

The relative rate of modern-day PAC-NAM plate motion determined using Global Positioning System (GPS) estimates across southern California and northern Baja California is  $49 \pm 3$  mm/yr ( $1\sigma$ ) (Bennett et al., 1996), which agrees fairly well with values estimated by global plate motion models such as NUVEL-1A ( $46 \pm 1$  mm/yr over the past 3 Ma) (DeMets et al., 1990, 1994). A slight discrepancy between NUVEL-1A and seafloor spreading lineations in the mouth of the gulf suggests that the spreading rate may have increased

slightly in the past ~ 1 Ma to ~ 50 mm/yr (DeMets, 1995). This observation has interesting implications, as it means that either Baja California has not been rigidly coupled to the Pacific plate since 3.5 Ma (i.e., plate boundary motion was partially accommodated on other structures until ~ 1 Ma), or that PAC-NAM relative plate motion has increased in the past 1 Ma (DeMets, 1995). Lonsdale (1989) has noted that Baja California does not move at exactly the same plate velocity as the Pacific plate, which agrees with the former interpretation. Minster and Jordan (1978) calculated a slightly higher PAC-NAM relative plate motion rate of  $56 \pm 3$  mm/yr over the past 5 Ma from their global plate motion model, and Lonsdale (1989) estimates the spreading rate recorded by the magnetic anomalies in the Gulf of California to be 54 mm/yr. Summing deformation (primarily right-lateral shear on NW-striking faults) across southern California gives a rate of  $53 \pm 3$  mm/yr (Humphreys and Weldon, 1991).

Assuming a constant spreading rate of 56 mm/yr, Curray and Moore (1984) calculated about 300 km of relative PAC-NAM displacement since 5.5 Ma. This is in good agreement with post-5 Ma displacement on the various fault segments associated with the modern plate boundary in southern California which are estimated between 295 km and 337 km (Powell, 1993; Dickinson, 1996). Cumulative offset of basement rocks along the San Andreas fault system in central California using scattered-wave imaging also suggests ~ 315 km right-lateral slip (Revenaugh and Reasoner, 1997). These values also agree with approximately 300 km northwestward dextral offset across the Gulf of California of a Miocene (or early Tertiary) conglomerate containing distinct carbonate clasts with Permian fusulinids (Gastil et al., 1973).

There is some variation regarding the direction of PAC-NAM relative plate motion as determined from several different types of studies. Plate motion models predict a return to NW-SE-directed (~ 315°) extension from between 5 and 7 Ma until the present (Stock and Hodges, 1989) corresponding to a CW rotation of PAC-NAM relative plate motion (see Figure 1.3). On the other hand, CCW rotation of the relative plate motion from 3.5 Ma until the present is inferred to have caused several changes within the Gulf of California including (1) reorientation of transform fault azimuths and basin (“spreading center”) axes, (2) break-



up of spreading centers into offset pairs, and (3) the abandonment of old spreading centers and the creation of new ones (Lonsdale, 1989). Global plate motion models calculate the relative PAC-NAM plate motion direction to be  $325^\circ \pm 2^\circ$  over the past 5 Ma (Minster and Jordan, 1978) or  $324^\circ \pm 2^\circ$  over the past 3 Ma (DeMets et al., 1990, 1994). Earthquake slip vector azimuths from large ( $m_b$ , (body wave magnitude)  $> 5.3$ ) events within the Gulf of California recorded between 1963 to 1984 range from  $303^\circ$  to  $312^\circ$  (Goff et al., 1987), in good agreement with major bathymetric trends of transform faults. Clockwise rotation of PAC-NAM relative plate motion has been documented in central eastern Baja California where structures which developed during earlier NE-SW- to ENE-WSW-directed extension were reactivated during Plio-Quaternary time to accommodate E-W- to ESE-WNW-directed extension (Angelier et al., 1981). Other studies on the Baja California peninsula have identified E- to SE-directed, Pliocene extension as well (Bryant, 1986; Zanchi, 1994; Umhoefer and Stone, 1996). Contrary to these findings several studies find evidence for continued, post-5 Ma NE-SW- to ENE-WSW-directed extension in the Gulf of California region (Gastil et al., 1975; Dokka and Merriam, 1982; Hausback, 1984; Stock and Hodges, 1989; Martín-Barajas and Stock, 1993; Lewis, 1994; Umhoefer et al., 1994; Lewis and Stock, in review in *J. Struct. Geol.*; this study).

Historic seismicity in the California borderland north of Ensenada suggests present-day transfer of some PAC-NAM plate motion from within the Gulf of California to the northwest along the Agua Blanca fault system (Legg et al., 1991; see also Figure 1.2). Present-day activity along the Agua Blanca fault is also supported by features such as Holocene stream offsets and offsets within Quaternary (?) fan gravels (Allen et al., 1960). Rockwell and others (1993) estimate a slip rate of about 6 mm/yr on the Agua Blanca fault. Figure 1.2 shows the locations of this and other Quaternary faults in northern Baja California and southernmost California which accommodate the present-day PAC-NAM motion at this latitude. In northern Baja California, seismic activity has been recorded along the San Miguel fault zone, the Agua Blanca fault, the Sierra Juárez fault, and the San Pedro Mártir fault (e.g., Vidal and Mungúía, 1991).

### 1.3. *Gulf Extensional Province (GEP)*

The limits of extensional deformation bordering the Gulf of California spreading system (hereafter referred to as the Gulf Extensional Province (GEP) after Gastil and others (1975)) are asymmetrical (see Figure 1.1 and description in caption). The subaerial portion of the western GEP, located on the eastern side of the Baja California peninsula, is narrow and generally bounded by well-defined escarpment faults which are collectively referred to as the Main Gulf Escarpment. The broader eastern portion of the GEP extends farther from the spreading system within mainland Mexico. In the north the GEP merges with the southern Basin and Range (Henry, 1989; Henry and Aranda-Gomez, 1992). The Pacific Ocean and the Gulf of California presently cover many of the structures which could help address the question of plate boundary evolution. By studying the sub-aerial exposures along the margins of the GEP we can learn when, where, and in which direction continental extension began within the Gulf of California.

### 1.4. *Geologic setting of northeastern Baja California, Mexico*

The study area discussed here is from a portion of the western GEP margin in northeastern Baja California where the well-defined Main Gulf Escarpment terminates southwards (Hamilton, 1971; Dokka and Merriam, 1982; Stock and Hodges, 1990) against the Miocene-Pliocene (Gastil et al., 1975) Puertecitos Volcanic Province (PVP). The PVP is the largest of several late Miocene/early Pliocene syn-rift volcanic provinces along the western GEP margin (Gastil et al., 1975) and will be discussed further below. The Main Gulf Escarpment in northeastern Baja California basically consists of four parts (Axen, 1995). From north to south these include the steep E-dipping Sierra Juárez fault, which is a faulted rollover structure antithetic to an underlying W-dipping detachment, the ramp-like Sierra Las Tinajas accommodation zone, the well-defined, NNW-striking, E-dipping San Pedro Mártir fault, and the Puertecitos accommodation zone. The Sierra Juárez and San Pedro Mártir faults

are shown in Figure 1.2 and are also readily identifiable on the basis of an abrupt change in topography across the E-facing scarps in Figure 1.4.

A simplified geologic map shown in Figure 1.5 differentiates the Mesozoic and Paleozoic (batholithic and prebatholithic metasedimentary rocks) from Cenozoic (volcanic and sedimentary rocks) lithologic units in the vicinity of the study area (location of Figure 1.5 is indicated in inset as well as in Figure 1.2). Additional geographic names and the location of the study area within the PVP are given in Figure 1.6. The 100-km-long, E-dipping, San Pedro Mártir fault, which shows up to 5 km of normal separation (Gastil et al., 1975), seems to disappear, or at least become much less pronounced, at the latitude of the northern PVP (Figure 1.5). Measured displacement across the San Pedro Mártir fault decreases southwards to a maximum of 800 meters in southernmost Valle Chico (Stock, 1993). The western edge of the GEP is thus poorly defined at the latitude of the study area (Figures 1.5 and 1.6). Several workers (Dokka and Merriam, 1982; Stock and Hodges, 1990; Stock, 1993; Axen, 1995; Stock, in press) interpret the southern termination of the Main Gulf Escarpment at the PVP to mark the location of a W- to NW-striking accommodation zone (referred to throughout this study as the “Matomí accommodation zone” after Dokka and Merriam (1982)). A-A' marks the limits of the Matomí accommodation zone in Figure 1.6 as interpreted by Stock (in press). As will be developed in Chapter VI of this study, it is possible that the SE projection of the Matomí accommodation zone passes through the study area.

Several other north-to-south changes are apparent at the latitude where the San Pedro Mártir fault appears to terminate southwards against the PVP. The hanging wall of the San Pedro Mártir fault includes relatively more extended, Basin and Range-type topography (including (W to E in Figure 1.6) southern Valle Chico, Sierra San Felipe, Llanos de San Fermín, and the Sierra San Fermín) characterized predominantly by E-dipping normal faults (Figure 1.5), in contrast to the less extended PVP which consists of much more closely spaced, E- and W-dipping normal faults exhibiting smaller amounts of offset (Dokka and Merriam, 1982; Nagy et al., 1995). Additionally, post-6 Ma, vertical-axis rotational deformation in the Sierra San Fermín relative to the Sierra San Felipe (Lewis, 1994; Lewis and

Stock, in review in *J. Geophys. Res.*) has not been found in the northern PVP (Nagy et al., 1995; see also Chapter V).

The first detailed geologic analysis of the PVP and surrounding areas was presented by Dokka and Merriam (1982) on the basis of earlier work by several different authors (principally Hamilton, 1971; Sommer and Garcia, 1970; and Gastil et al., 1975) as well as ground studies, air photo interpretations, and observations from low-flying aircraft. Since this early study, detailed volcanic stratigraphy and deformation history within the PVP and nearby areas has gradually been compiled by workers who have mapped, collected, and examined the lithologic units in great detail. In particular, these areas (shown in Figure 1.6) include the Santa Rosa Basin (Bryant, 1986), southern Valle Chico (Stock, 1989, 1993) and the region south of it within the PVP (Stock, Lewis, Salton, and Holt, unpub. mapping), the region bordering Arroyo Matomí (Stock et al., 1991; Stock, unpub. mapping), the Sierra San Fermín and southern Sierra San Felipe (Lewis, 1994, 1996; Lewis and Stock, in review in *J. Struct. Geol.*), the eastern PVP adjacent to the Gulf of California between Arroyo Los Heme and Arroyo Matomí (Martín-Barajas et al., 1995), and scattered localities west and south of the PVP (Dorsey and Burns, 1994).

A general summary of the findings from these detailed studies is as follows: (1) pre-Miocene batholithic and prebatholithic rocks form the basement in the Sierra San Pedro Mártir, the Sierra San Felipe, the Sierra San Fermín, the Sierra Santa Rosa, and in regions to the south of the PVP, but are not exposed in the vicinity of Arroyo Matomí or anywhere within the PVP, (2) 15-17 Ma volcanoclastic breccias and other non-marine sediments derived from the mid-Miocene, subduction-related arc are found in all areas with the exception of Arroyo Matomí, (3) an important ~ 12 Ma pyroclastic flow deposit (Tuff of San Felipe after Stock and others (1996b, 1997)) is found in southern Valle Chico, Santa Rosa basin, Sierra San Felipe, and Sierra San Fermín, (4) a series of 6 Ma pyroclastic flow deposits (including the Tuffs of Matomí and Tuffs of El Canelo after Stock (1989) and Stock and others (1991)) occurs throughout the entire region, including the PVP, and is interpreted to cap a significant portion of the plateau-like, upper surface of the western PVP, (5) undated rhyolite lava flows overlie these pyroclastic flow deposits in the Sierra San Fermín and south of Arroyo Matomí,

(6) a series of 3 Ma pyroclastic flow deposits (including Tuffs of Mesa El Tábano, Tuffs of Valle Curbina, and Tuffs of Los Heme after Stock and others (1991) and Martín-Barajas and others (1995)) are restricted to southernmost Sierra San Fermín and the eastern PVP (south of Arroyo Matomí) and are interpreted to cap a significant portion of the plateau-like, upper surface of the eastern PVP, (7) late-Miocene to early Pliocene marine (and non-marine) sediments overlie the above lithologic units in the eastern regions (Santa Rosa basin, Sierra San Fermín, Arroyo Matomí, and the eastern PVP), and (8) a young pulse of andesitic volcanism includes the  $2.6 \pm 0.1$  Ma vent known as Volcan Prieto in the eastern PVP (Figure 1.5), and a  $0.91 \pm 0.67$  Ma lava flow in the northeastern PVP.

The commencement of normal faulting along the San Pedro Mártir and Sierra San Felipe faults (Figure 1.5) is constrained between 12 and 6 Ma due to angular unconformities between dated pyroclastic flow deposits ((3) and (4) in the above paragraph). In some localities (such as south of Arroyo Matomí at a location known as Mesa El Tábano) faulted 6 Ma units are overlain by undeformed 3 Ma units (Dokka and Merriam, 1982; Martín-Barajas et al., 1995), while in other places (such as the southern Sierra San Fermín and the eastern PVP) normal faulting disrupts the 3 Ma pyroclastic flow deposits as well as the younger marine sediments. In general the region is dominated by N- to NNW-striking normal faults and NE-striking sinistral strike-slip faults.

### 1.5. *Santa Isabel Wash*

The portion of the GEP studied here is located near the western margin of the extensional province at approximately  $30^{\circ}30'N$  latitude (Figure 1.1). The mapped area covers  $\sim 140$  km<sup>2</sup> in the northern Sierra Santa Isabel (Figure 1.6) along the north-central portion of the PVP (Figures 1.5). A large arroyo is informally named (here) Santa Isabel Wash, and the entire study area is referred to as “Santa Isabel Wash” throughout the text. Another unnamed arroyo along the eastern margin of the mapped area is also informally named here (Arroyo Oculito). A simplified geologic map of the study area is shown in Figure 1.7.

Santa Isabel Wash has been chosen for detailed geologic study for several reasons. The region has received attention for its extensional structures, volcanic history, and relationship to the history of the GEP (e.g., Gastil et al., 1975; Dokka and Merriam, 1982; Stock and Hodges, 1990; Axen, 1995); however, it has not been examined in detail with the exception of field checks for a geologic map (1:50000 scale) compiled from air surveillance (CETENAL, 1977). No prior lithologic descriptions or geochronology exists for the units studied here. For example, it has not been previously known if one of the highest peaks in the region, Los Heme (Figure 1.7), was a remnant andesitic volcano from mid-Miocene subduction, or a younger feature. Additionally, the study area provides excellent exposure of the profile of the northern margin of the PVP. In most other areas the character of the PVP is restricted to a flat, plateau-like, volcanic tableland of limited, principally fault-related, topography. Topographic relief on the PVP tableland is typically on the order of 50-100 meters. In Santa Isabel Wash, and the Arroyo Oculito region to the east, up to 700 meters of topographic relief exposes the units which underlie the plateau-forming tuffs, thus providing a window into the pre-late Miocene geologic history. Finally, Santa Isabel Wash is one of the few logistically accessible regions adjacent to the larger area described above generally mapped in similar detail (1:20000).

Lithologic correlations with adjacent areas, the establishment of a dated stratigraphy, assessment of potential vertical-axis rotational deformation, and constraints on the timing and direction of extension are important for understanding the regional geologic history for this portion of the GEP. As mentioned above, one of the most interesting structural features to investigate in the vicinity of Santa Isabel Wash includes the southeastward projection of the Matomí accommodation zone (Dokka and Merriam, 1982; Stock and Hodges, 1990; Stock, in press) from the southern Valle Chico region (A-A' in Figure 1.6) (also referred to as the Ultima Esperanza fault zone in southern Valle Chico), and the possible relationship with fracture zones of the Gulf spreading system, which intersect the PVP when projected northwestwards along their strike (Figure 1.1).

Figure 1.1. Digital topography of the region surrounding the Gulf of California. The present-day PAC-NAM plate boundary consists primarily of transform faults (solid black lines) and spreading ridges (double black lines) within the Gulf of California (after Fenby and Gastil, 1991). Spreading centers are dashed where inferred on the basis of basin bathymetry (after Dauphin and Ness, 1991). (Note that an alternative interpretation of the bathymetry in the northernmost Gulf of California is presented in Chapter VI of this study). The Gulf Extensional Province (GEP) spans the width of the Gulf of California. Its NW-SE-trending limits approximately correspond to the topographic changes from lower elevations (green) to higher ones (yellow and orange) east of the Peninsular Ranges batholith (PRB) in Baja California, Mexico, and west of the Sierra Madre Occidental on mainland Mexico. To the north the GEP merges with the southern Basin and Range. The study area is located on the western margin of the GEP. The Tamayo fracture zone is labeled "Tamayo FZ."



# Pacific-North America plate boundary in the Gulf of California

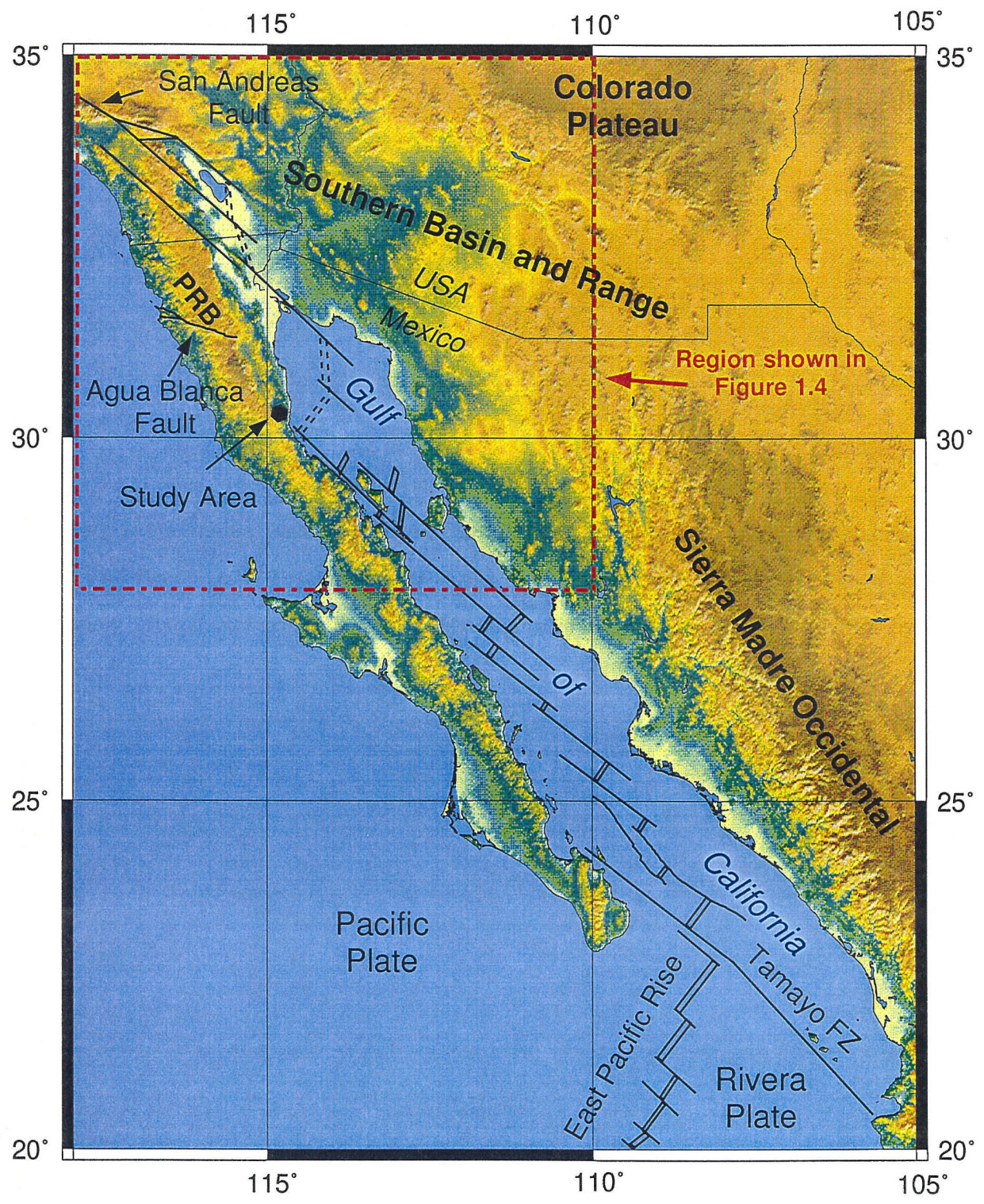




Figure 1.2. Present-day fault map for northern Baja California and southernmost California. The San Benito and Tosco-Abrejos faults partially accommodated PAC-NAM plate boundary motion between 12.5 and 5.5 Ma (figure modified from original provided by C. Lewis).

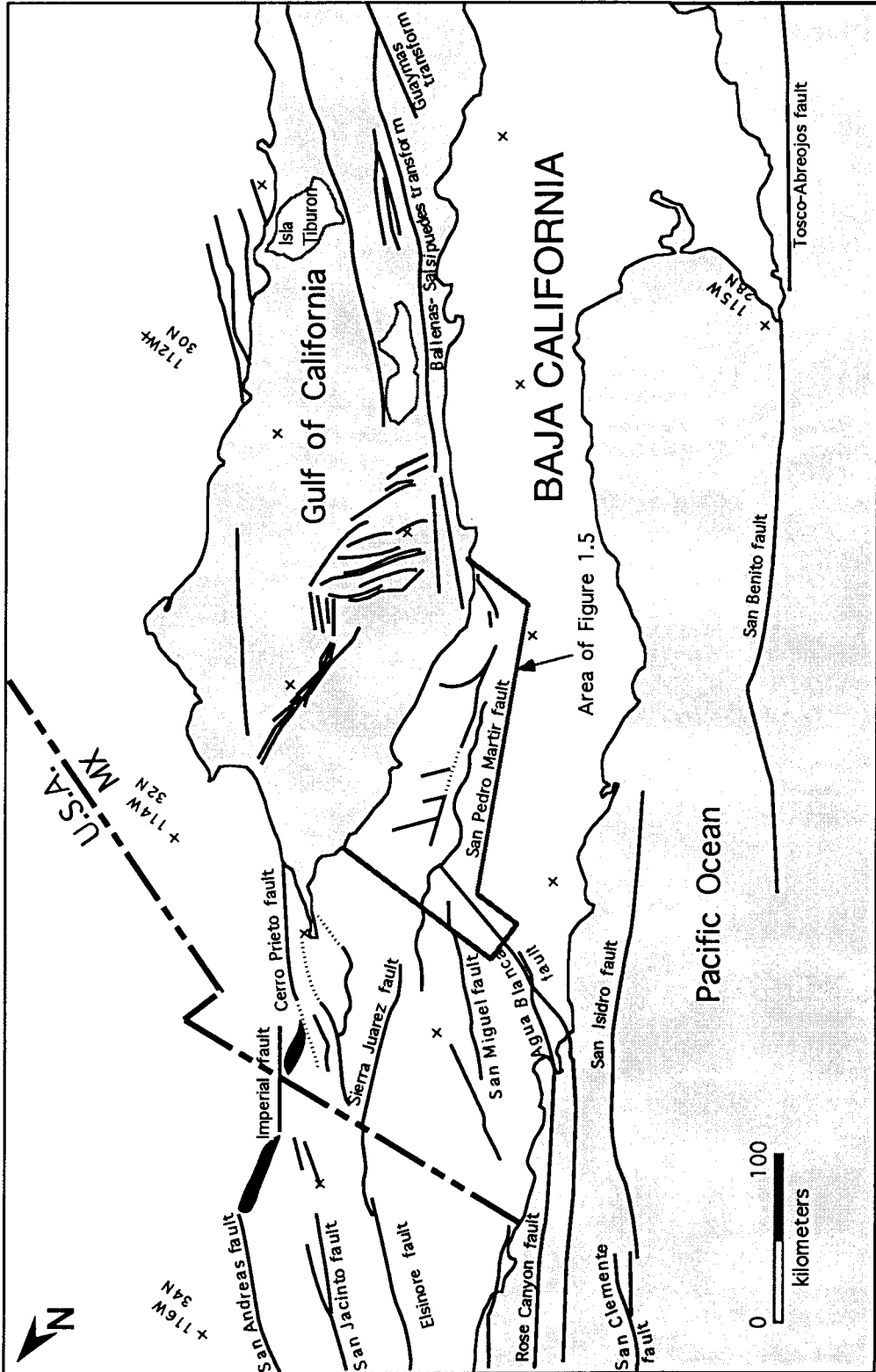


Figure 1.3. Velocities and uncertainties for Pacific plate points west of Baja California for the intervals 20.0 to 10.6 Ma (large ellipses), 10.6 to 5.5 Ma (medium ellipses, shaded), and 5.5 to 0 Ma (small ellipses). Oblique Mercator projection. Reproduced from Figure 6 of Stock and Hodges (1989). Note the CCW change in PAC-NAM relative plate motion between 10.6 and 5.5 Ma. Because of uncertainties related to chosen time intervals, the timing of this change could have been between 15 and 7 Ma or 9 and 5 Ma (Stock and Hodges, 1989).

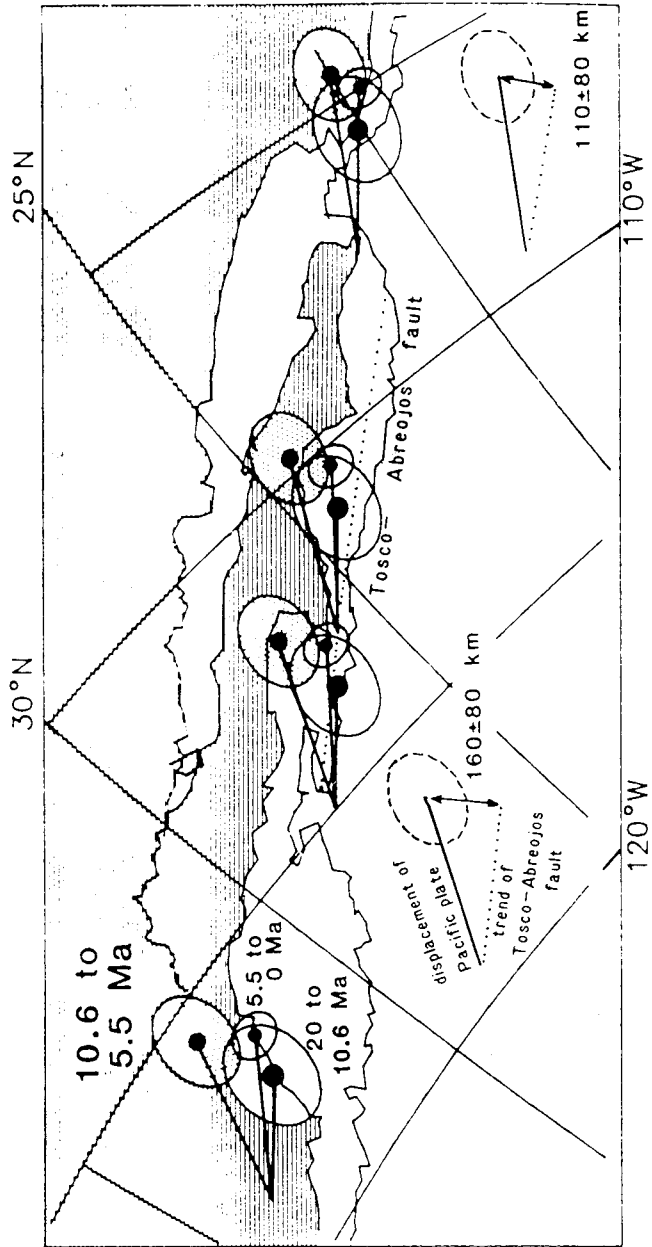


Figure 1.4. Digital topography of the northern GEP. Note the sharp western boundary in northeastern Baja California, formed by the Sierra Juárez and San Pedro Mártir faults, which becomes less well-defined at the study locality. Limits of the PVP are drawn schematically. Figure 1.1 shows where this Figure is located relative to several other features surrounding the Gulf of California.

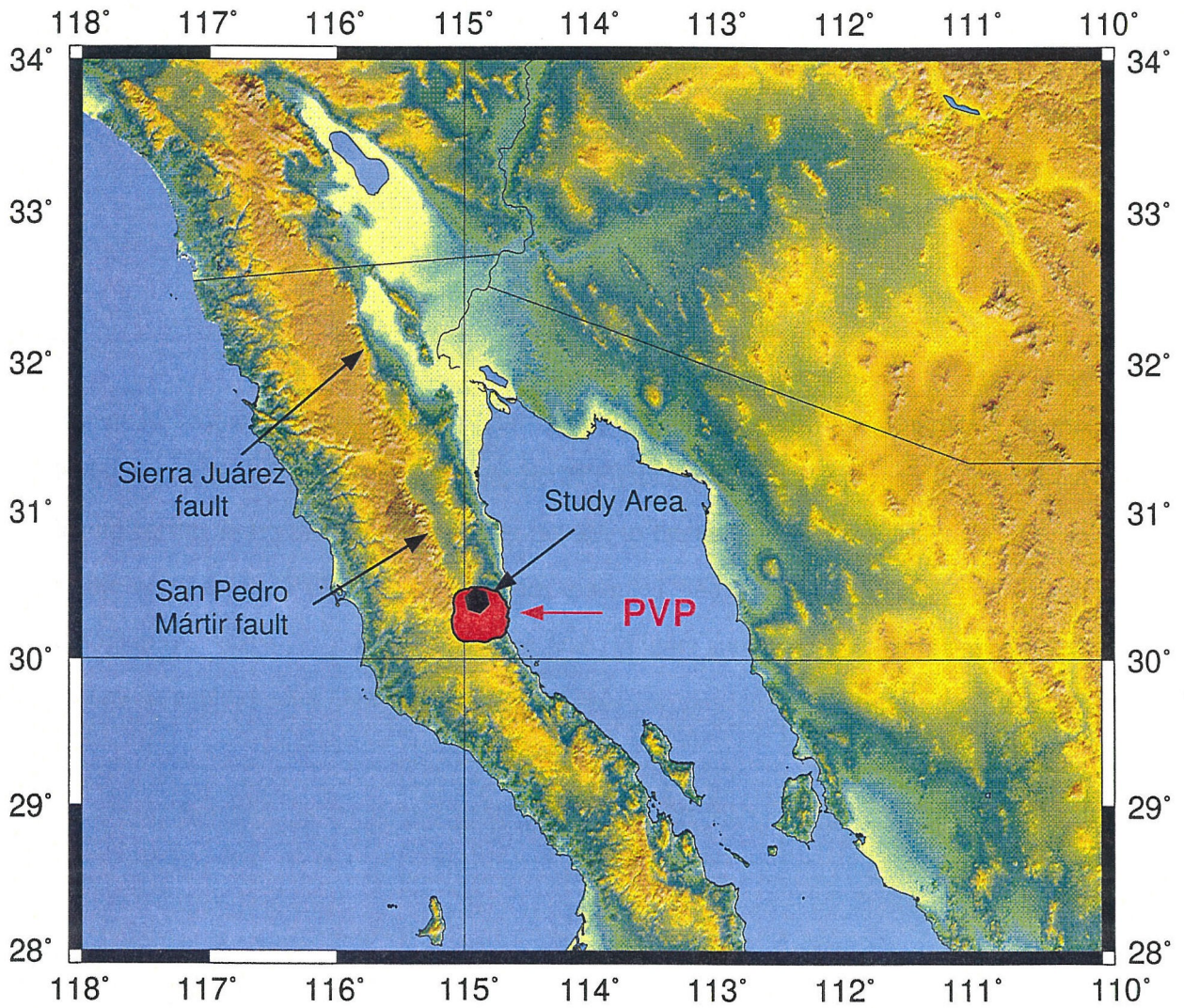


Figure 1.5. Simplified geologic map illustrating the abrupt southward termination of the San Pedro Mártir fault at the Miocene-Pliocene PVP (southern region patterned solid grey but not including the Sierra San Fermín or other regions to the north with similar pattern). The region to the north of the PVP is relatively more extended and consists of Basin and Range-type topography. “SSFF” is Sierra San Felipe fault. (Figure modified from original provided by C. Lewis; geology after Gastil et al., 1975.)

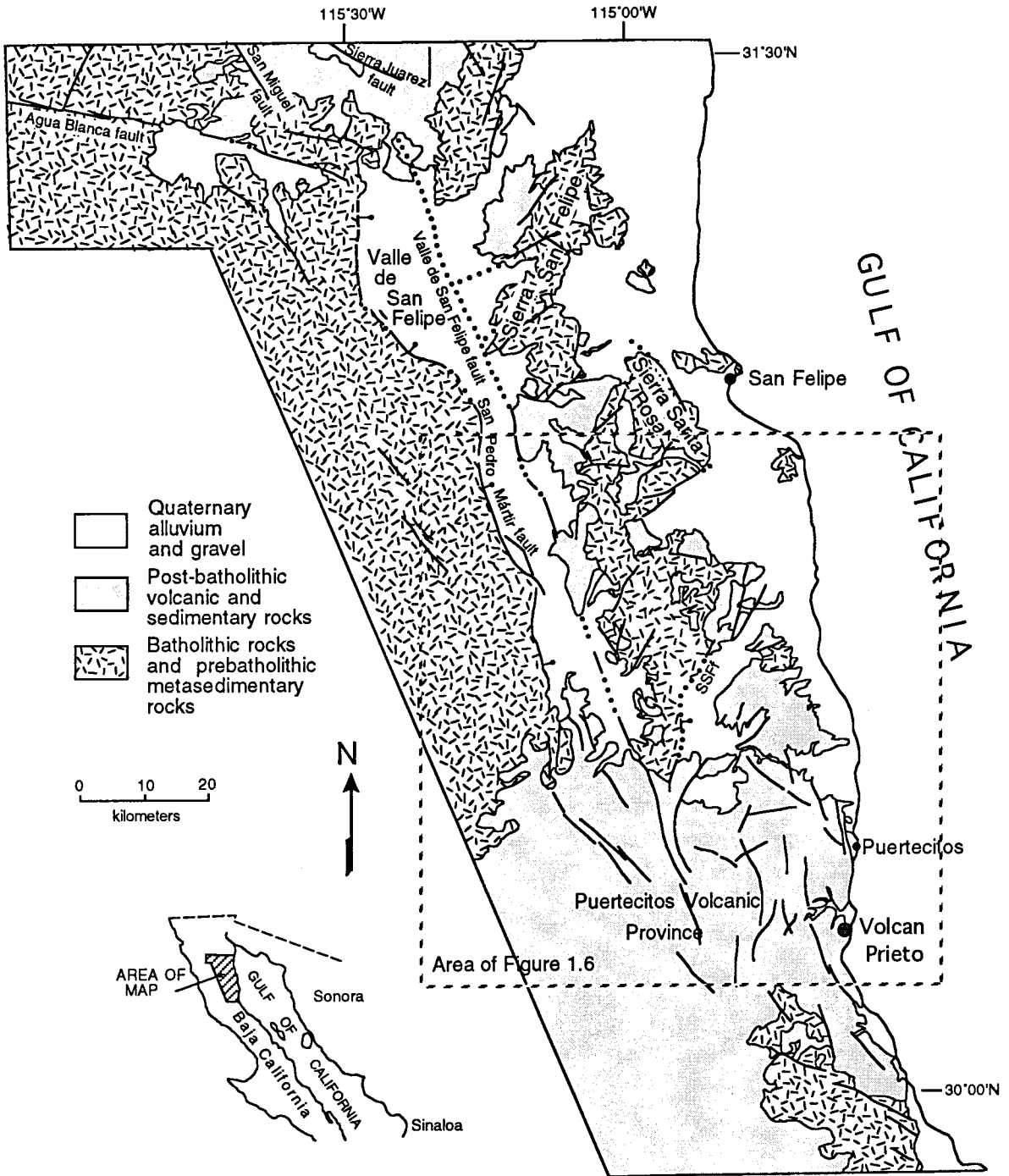




Figure 1.6. Geographic features and names in the vicinity of the study area. Quaternary alluvial deposits, and the Gulf of California, are not patterned. See Figure 1.5 for the limits of the PVP and the locations of major faults determined from previous studies. A-A' marks the limits of the Matomí accommodation zone as interpreted by Stock (in press). In addition, Stock (in press) believes that the accommodation zone may have been offset along a NE-striking, sinistral strike-slip fault near position A' and thus might project eastwards in the vicinity of Arroyo Matomí. An alternative possibility is offered in Chapter VI.

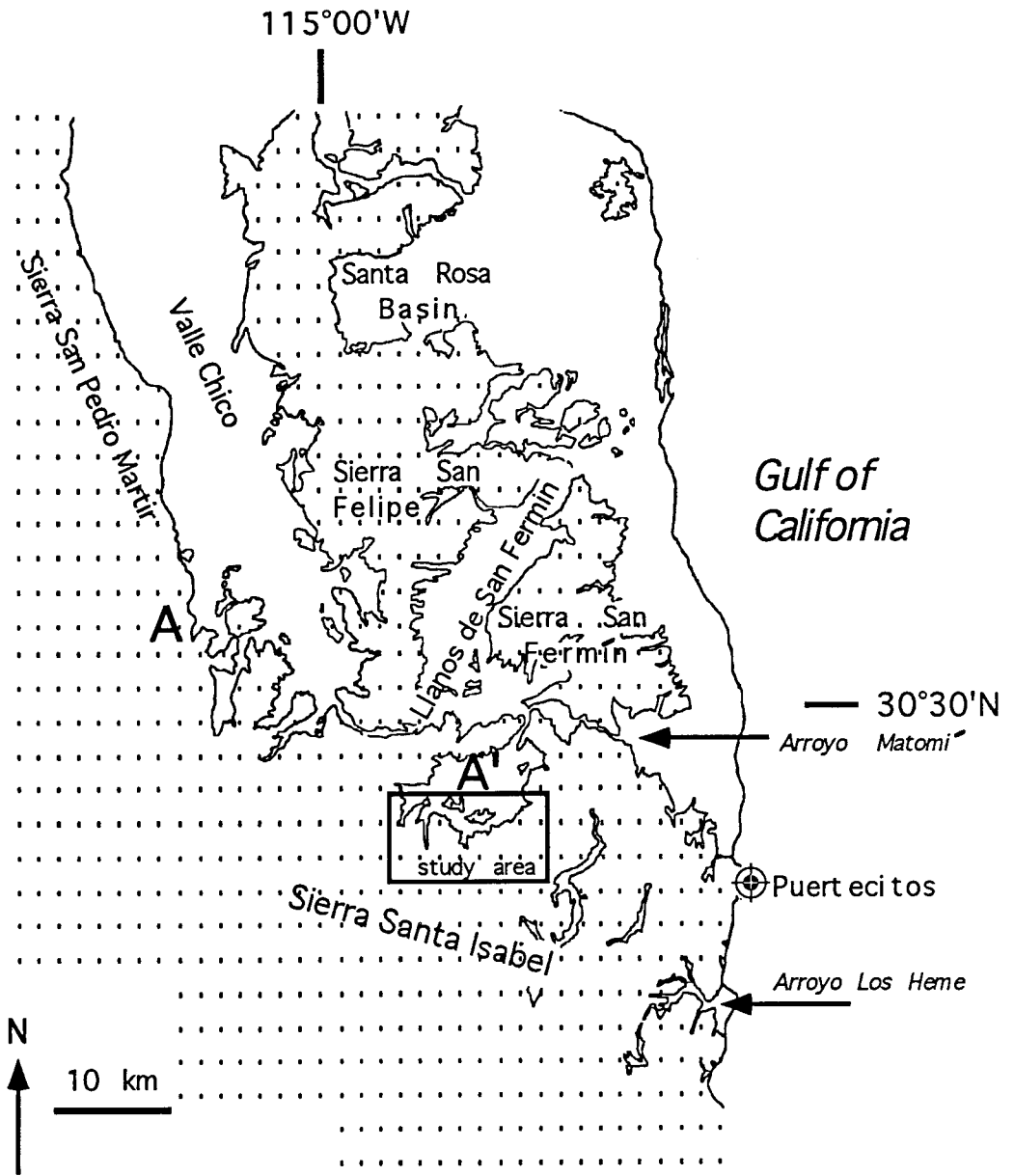
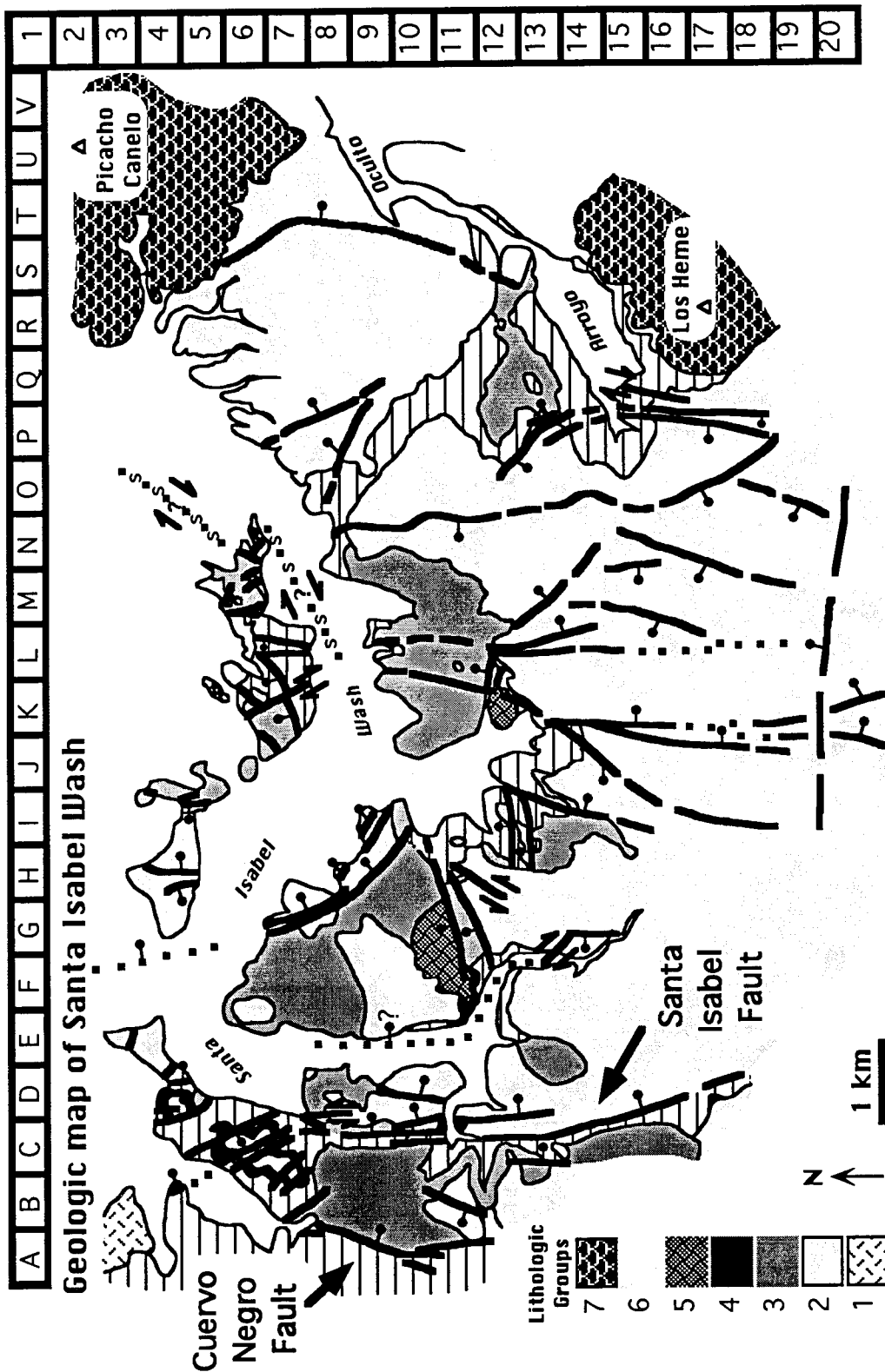


Figure 1.7. Simplified geologic map of study area. Santa Isabel Wash and Arroyo Oculito are informally named here, and the entire study area is informally referred to as Santa Isabel Wash.



Chapter II

Geologic setting and lithology of units in Santa Isabel Wash

2.1. *Introduction*

2.2. *Preserved geologic record*

2.3. *Techniques and terminology*

2.4. *Lithologic units*

2.5. *Regional lithologic correlations*

2.6. *Summary*

## 2.1. Introduction

The geology of a 140 km<sup>2</sup> area in the northern Sierra Santa Isabel, Baja California, Mexico, has been mapped at 1:20000 over the course of eight months of field study. The study location, informally named here Santa Isabel Wash, is within the northern portion of the late Miocene/early Pliocene Puertecitos Volcanic Province (PVP) which is located on the western margin of the Gulf Extensional Province (GEP) (see Figure 1.1 in Chapter I). An area on the eastern margin of the mapped area which borders a large, unnamed arroyo is also informally named here as Arroyo Oculito. As part of this study, 21 lithologic units were defined and mapped in the Santa Isabel Wash and Arroyo Oculito regions (not including Quaternary alluvium and playa deposits). The 21 units are consolidated into 7 Groups, the oldest of which (Group 1) comprises pre-Miocene batholithic and pre-batholithic basement rocks. The remaining 6 Groups are mid- to late-Miocene and consist primarily of stratified, poorly-sorted breccia lithofacies, dacitic, andesitic, and basaltic lava domes and associated breccias, and distal outflow sheets of rhyolitic pyroclastic flow deposits.

Understanding the stratigraphic sequence and depositional patterns of the geologic units in the northern PVP is mandatory to unraveling the history of deformation in the area. The nature of the lithologies exposed in this region makes this a challenging process. Different lava flows and breccias can contain similar phenocrysts and mineral assemblages, and can resemble each other in outcrop appearances. Contacts between brecciated flows can be difficult to identify. A pyroclastic flow deposit can change from thick, non-welded, and pumiceous in some localities to an order of magnitude thinner and densely welded in other places where it perhaps banked against steep topography. On the other hand, thicker deposits commonly exhibit a relatively higher degree of welding than thinner deposits due to lithostatic load (Smith, 1960), and this relationship, too, is observed in the field area.

Five of the lithologic units mapped in this study, *Tmvs*, *Tmr<sub>sf</sub>*, *Tmr3*, *Tmr4*, and *Tmr<sub>ec</sub>*, are correlated to units defined previously by workers studying nearby localities (Stock, 1989; Martín-Barajas et al., 1995; Lewis, 1996; Stock et al., 1991; 1996; 1997b). These and other more tentative lithologic correlations between deposits found in Santa Isabel Wash and nearby

areas will be discussed at the end of this chapter. Other units described in this study are given names and labels presented here for the first time. Discerning and categorizing the various lithologies is facilitated by  $^{40}\text{Ar}/^{39}\text{Ar}$  geochronology which provides crystallization ages for feldspar phenocrysts. Twenty-one rock samples spanning the deposition of all of the Tertiary units were dated; details of the geochronology are presented in the Chapter III. This chapter summarizes the following information for each lithologic unit: field observations such as location, size, and thickness of deposit, nature of contacts, outcrop and hand sample appearance, mineralogical and petrographic information from thin section analysis, electron microprobe results (if any), and a summary statement of the  $^{40}\text{Ar}/^{39}\text{Ar}$  geochronology (if any) with  $1\sigma$  uncertainties. Additional age constraints for some of the units based upon regional correlations are presented in the discussion section at the end of this chapter. A detailed geologic map with cross sections and a discussion of the structures are given in Chapter IV. A simplified geologic map showing the 7 lithologic Groups is shown in Figure 2.1 with an alphanumeric grid for identification of locations discussed in the text. A stratigraphic column is shown in Figure 2.2 with unit labels and names assigned here, as well as some taken from previous studies.

## *2.2. Preserved geologic record*

The rocks exposed in the vicinity of Santa Isabel Wash primarily span Miocene and Pliocene time. However, a few basement outcrops exist of undated granites and metasedimentary rocks. The metasedimentary rocks are probably correlative with the latest Precambrian through Paleozoic miogeoclinal to deep water facies found along the eastern side of peninsular Baja California (Gastil, 1993). The igneous rocks and associated dikes which cut the metasedimentary rocks are most likely related to the Mesozoic Peninsular Ranges Batholith (PRB) which makes up the central, N-S oriented spine of Baja California. The uplifted PRB is interpreted to represent the deeper portions of the Jurassic to Cretaceous subduction related arc formed as a result of the convergent Farallon-North American plate boundary (e.g., Silver et al., 1963, 1969) (see Chapter I for details of plate boundary history).

Where exposed at the surface in Santa Isabel Wash, the batholithic and pre-batholithic rocks are unconformably overlain by the younger units.

Up to 500 meters of volcanoclastic breccias and sedimentary debris flows unconformably overlie the basement rocks. These stratified, poorly sorted deposits are attributed to catastrophic sedimentation from the high-standing, unstable slopes of the early or mid-Miocene subduction-related volcanic arc. Andesitic clasts are most common although the deposits can consist of other clast types such as aphyric volcanic rocks. Laterally discontinuous lava flows and pyroclastic flow deposits also occur within the breccias and have generally been mapped with them in this study.

Voluminous dacitic lavas and their associated collapse breccias overlie the volcanoclastic breccias. Smaller volumes of basaltic lavas were also extruded at this time. The ~ 15.5-17 Ma crystallization ages of these units (see Chapter III) suggest that they, too, are related to mid-Miocene arc activity.

The late Miocene rocks in the area are generally between 13 and 6 Ma in age. They are principally the distal outflow sheets of pyroclastic flow deposits and are most likely associated with the continental extension which opened the Gulf of California. These ash-flow tuffs have filled irregular topography to produce the plateau-like, upper surface of the PVP. The source for some of these units has been identified between 20 and 30 kilometers to the north in the Sierra San Fermín and southern Sierra San Felipe (Lewis, 1996). The sources of other pyroclastic flow deposits may lie near or east of the modern shoreline in the Gulf of California which at the present time is ~ 25 km east of the study area. A few local andesitic to basaltic lava flows are present within the series of pyroclastic flow deposits. Based upon  $^{40}\text{Ar}/^{39}\text{Ar}$  geochronology, the majority of the pyroclastic flows in Santa Isabel Wash were deposited around 6-7 Ma.

Overlying the pyroclastic flow deposits are several andesite and rhyolite flows on the east side of the study area (in the Arroyo Oculito region; Figure 2.1).  $^{40}\text{Ar}/^{39}\text{Ar}$  geochronology was not successful at measuring a crystallization age for some of the andesitic lavas due to low radiogenic yields; however, the rhyolite flows yielded ages around 6 Ma.



Quaternary alluvial deposits surround isolated hills of the Miocene volcanic deposits and are related to modern arroyo sedimentation. Fine-grained, modern, playa deposits lie within closed basins up to 2 km in diameter. In some places older alluvial surfaces which are no longer active remain along the margins (at slightly higher elevations) of active drainages.

### 2.3. *Techniques and terminology*

Mineral identification was primarily performed by thin section analyses with an optical microscope. Over 260 rock samples were collected during eight months of field mapping, and most were cut into thin sections and examined. In addition, 22 rock samples were analyzed with an electron probe microanalyzer to determine chemical compositions of various mineral phases. Mounted in epoxy in cylindrical brass holders and polished to 0.25  $\mu\text{m}$  were 11 mineral separates (feldspars from 10 rock samples and amphibole from one of the samples), and 12 other hand samples were cut into thin sections and also polished to 0.25  $\mu\text{m}$ . All samples were carbon-coated prior to analysis to increase electrical conductivity and thereby prevent development of significant charge on the samples during analysis. Atomic proportions of 11 elements analyzed are given in Appendix A for 148 analyses. Four natural mineral standards (anorthite, Lake County plagioclase, Natural Bridge diopside, and Kakanui hornblende) used to calibrate the instrument are also listed in Appendix A. Calculated mineralogical formulas (or names from a mineral series) are given in brackets [] in this chapter with the petrographic descriptions of each unit, and are also given in Appendix B. Note that measurement transects across crystals were not performed and thus results do not characterize mineralogical variations in zoned crystals.

Since bulk chemical analyses were not performed in this study, rock classification for both lavas and tuffs has been based upon phenocryst assemblages and textures instead of chemical composition. Of the total feldspar content in a given rock, *rhyolites* generally contain > 35% potassium feldspar, *rhyodacites* 10-35% potassium feldspar, and *dacites* < 10% potassium feldspar. These felsic rocks contain any combination of phenocrysts of amphibole, pyroxene, and biotite, and may or may not contain equilibrium quartz. *Andesites*

contain no quartz in equilibrium and essentially no potassium feldspar but consist primarily of plagioclase feldspar and mafic phenocrysts such as clinopyroxene, orthopyroxene, and amphibole. Andesitic lavas are commonly porphyritic in texture with phenocrysts of plagioclase and mafics in a pilotaxitic groundmass. *Basalt* lava flows principally consist of olivine, pyroxene, and calcic plagioclase and commonly have intergranular, intersertal, or ophitic textures. Since olivine-bearing *basaltic andesites* are typically distinguished from basalts based upon higher SiO<sub>2</sub> content determined from chemical analysis (< 52% SiO<sub>2</sub> for basalts and 52-55% SiO<sub>2</sub> for basaltic andesites (e.g., Williams et al., 1982)), all olivine-bearing rocks in this study are called *basalts*.

Phenocrysts are listed as hyphenated prefixes before the rock name in order of increasing abundance (for example: olivine-pyroxene-plagioclase basalt has plagioclase > pyroxene > olivine). The prefixes are limited to a maximum of three mineral names for the sake of simplicity, but if additional phenocrysts exist they are mentioned in the text. Using the general prefix “pyroxene” in the name means that more than one kind has been identified with the electron microprobe, and, again, these are mentioned in the text.

The pyroclastic flow deposits are described as crystal-rich (> 5% phenocrysts) or crystal-poor (< 5% phenocrysts), and are named pumice-lapilli and/or lithic-lapilli pyroclastic flow deposits if pumice and/or lithic fragments fall into the lapilli size-range (2-64 mm). The term ash-flow tuff is taken here to be synonymous with the term pyroclastic flow deposit when the rock consists of > 50% ash-sized particles. Pyroclastic flow deposits are commonly massive and poorly sorted, thus mention of these characteristics will not be repeated for each unit description. Sizes given for clasts and pumice refer to their diameters or greatest length if they are elongate (e.g., “lithic clasts average 2-4 cm”). Similarly, phenocryst sizes from thin section analyses are typical diameters (e.g., “feldspar phenocrysts are 2-3 mm”).

Labels were assigned to volcanic units defined in this study such that the geologic period and epoch are indicated with a capital and small case letter, respectively, followed by a small case letter indicating composition (rhyolite - (r), dacite - (d), andesite - (a), and basalt -

(b)), in turn followed by an abbreviation in subscripts given to the unit usually designated by locality. For example, *Tmb<sub>new</sub>* indicates “Tertiary-Miocene-basalt-New Year's Mountain.”

A few sentences summarizing the general geologic nature of each of the 7 Groups is given in the Summary section at the end of this chapter. The following are detailed descriptions intended to aid in lithologic identification and attempts at local correlations.

#### 2.4. Lithologic units

### Group 1

#### Pre-Tertiary basement geology

Basement rocks of Group 1 crop out in the northwest portion of the mapped area and cover about 0.25 km<sup>2</sup> in map view (Figure 2.1). They consist of granite (*Mzg*) and metasedimentary rocks (*Pz*) pervasively intruded by 1-mm- to 4-cm-wide aplite dikes which have undergone extensive ductile deformation. Schists and slates are also present but not as abundant as chert and marble. The maximum, vertical, topographic relief present in these exposures is about 140 meters. The contact between *Mzg* and *Pz* is irregular and poorly defined; its location in the map area is approximate. Group 1 rocks are unconformably overlain by Group 2 rocks (*Tmvs*).

#### *Pz*

The metasedimentary rocks which make up *Pz* are foliated garnet-epidote paragneisses interspersed with thin layers of diopside marble. These rocks are calc-silicates and preserve original depositional features such as thin laminations, cm-scale bedding, and some fanning of layers which perhaps indicates penecontemporaneous tilting during deposition. The axes of folds, boudinage, and pencil structures plunge down to the southeast, and isoclinal folds and tension gashes suggest a southwest-down sense of motion. Weathered

surfaces are stained brown or orange. Fresh surfaces are steel grey with bands showing ductile flow features in a lighter grey shade and darker steel blue-grey shade. Alternating bands of different compositions can be < 1 mm thick to several cm thick. Individual crystals are not visible. Typical mineralogy is 30-50% quartz and 50-70% remaining minerals (commonly plagioclase > epidote > garnet > calcite and dolomite).

### Mzg

Outcrops of stained, weathered *Mzg* as well as fresh white *Mzg* exist in the field area. Sub-horizontal layering of feldspar phenocrysts is evident in some places. Tourmaline crystals were noted in a pegmatitic portion of the intrusion, and mafic pods 1-3 meters in diameter also exist. Fresh hand samples are predominantly grey (quartz) and white (feldspar) with well-developed, light-reflecting crystals of white mica. Hand lens examination reveals smaller crystal of biotite. In thin section the medium-grained, granular-textured granite is principally composed of potassium feldspar, plagioclase, quartz, muscovite, biotite and minor garnet.

### **Groups 2 to 7**

#### Miocene geologic units

The Miocene volcanic units exposed in Santa Isabel Wash and Arroyo Oculito are divided into 6 Groups. From oldest to youngest the Groups are as follows (listed with approximate ages): Group 2) pre-17 Ma volcanoclastic breccias, sedimentary rocks, and a local pyroclastic flow deposit (*Tmvs*, *Tmr<sub>bio</sub>*), Group 3) ~ 15.5-17 Ma dacitic and basaltic lava flows and associated epiclastic breccias (*Tmb<sub>kc</sub>*, *Tmb<sub>lol</sub>*, *Tmd<sub>tomb</sub>*), Group 4) ~ 12.5 Ma pyroclastic flow deposit (*Tmr<sub>sf</sub>*), Group 5) ~ 9 Ma andesite flows (*Tma<sub>toro</sub>*), Group 6) a series of ~ 6-7 Ma pyroclastic flow deposits (oldest to youngest: *Tmr<sub>siw</sub>*, *Tmr<sub>3</sub>*, *Tmr<sub>3-4</sub>* (mapped

with *Tmr4* but described separately here), *Tmr4*, *Tmr<sub>ao</sub>*, *Tmr<sub>ec</sub>*, *Tmr<sub>bs</sub>*, *Tmr<sub>fp</sub>*) and a local basalt flow (*Tmb<sub>new</sub>*) deposited between *Tmr<sub>siw</sub>* and *Tmr3*, and Group 7) 6 Ma (and younger?) andesitic and rhyolitic lava flows (*Tmagem*, *Tmr<sub>can</sub>*, *Tma<sub>ugl</sub>*, *Tmahem*).

The majority of the Santa Isabel Wash area consists of *Tmvs* from Group 2, *Tmd<sub>tomb</sub>* from Group 3, and the ash-flow tuffs from Group 6 (Figure 2.1). The next volumetrically significant rocks are the andesite and rhyolite lava flows from Group 7 which are restricted to the Arroyo Oculito region on the easternmost side of the mapped area.

## Group 2 - *Tmvs*, *Tmr<sub>bio</sub>*

### *Tmvs*

A thick, variable package of stratified, poorly-sorted breccia to conglomerate lithofacies, *Tmvs*, occurs throughout Santa Isabel Wash. The label is taken from Stock (1989; Miocene Volcaniclastic Sediments). Where the base is exposed *Tmvs* is deposited unconformably upon the rocks from Group 1; however, in general *Tmvs* is the “basement rock” upon which all other units were subsequently and unconformably deposited. Significant relief is evident on the upper surface of *Tmvs* prior to the deposition of subsequent units. For example, a steep-sided “paleocanyon” or “paleochannel” within *Tmvs* was later filled by a pyroclastic flow deposit (*Tmr<sub>bio</sub>*, see next lithologic unit description) which is discontinuously exposed over a distance of at least 4 km.

Deposits of *Tmvs* are extensive and occur throughout much of the field area. Total thickness varies from a few meters to at least 500 meters. Outcrops generally form steep, resistant cliffs, and subhorizontal bedding planes are discernible from several kilometers away. The thickest and most extensive exposures of *Tmvs* are in the footwall of the westernmost E-dipping fault in the study area (location A3-A11 in Figure 2.1) and in the vicinity of locations J13, L7, Q11, and P14 (Figure 2.1).

Outcrops commonly weather to pale blue or pink, although they can also be pale yellow, grey, tan, red, green, white, orange, brown, or black as well as a mixture of colors. Individual beds are generally 1-3 meters thick and are laterally discontinuous over distances of a few meters to hundreds of meters. Where bedding is discernible, beds dip from 10-40° generally to the north or west. The matrix is cryptocrystalline and ashy. Well-rounded pumice and lithic clasts within the matrix-supported, conglomeratic sections of *Tmvs* support the interpretation that some parts of the deposit are secondarily reworked.

Both monolithologic and heterolithologic deposits occur, and rare, interbedded, fluvial sandstone deposits help to constrain paleohorizontal. Fine-grained volcanic rocks are the most common clast type within *Tmvs*. Clasts tend to concentrate in discrete stratigraphic horizons and are usually 3-10 cm, poorly sorted, and comprise 10-25% of the rock. In some deposits lithic clasts are several meters in diameter. Common clast lithologies include hornblende-phyric andesite, red and orange porphyritic rhyolite, and brown and black, fine-grained volcanic rocks. Neither granitic nor metasedimentary clasts from Group 1 basement rocks were found within *Tmvs*.

Some exposures of *Tmvs* contain up to 70 meters of regularly alternating layers of poorly sorted, 1-m-thick, fine- and coarse-grained beds with inverse coarse-tail grading above each of the fine-grained layers. The lack of sharp contacts between the fine- and coarse-grained layers suggests that these portions of *Tmvs* were deposited quickly, such as in catastrophic debris flows. The angularity of clasts in these outcrops implies that transport distance was small. A likely depositional environment is from eruption-related (or not) mobilization of the sedimentary aprons surrounding the high-standing Miocene volcanic arc.

Thin (2-4 meters), laterally discontinuous, siliceous lava flows occur within *Tmvs* and have been mapped with it. Thin section descriptions are included below of an epidote-bearing, andesitic dike and a basaltic dike which cut *Tmvs* and have been mapped with it.

The following is a description of a typical hand sample. This particular sample is from the lowest portion of the *Tmvs* outcrop where it overlies the pre-Miocene Group 1 basement rocks. The matrix is a bluish-grey color on both weathered and fresh surfaces. Shiny phenocrysts of biotite (1-2%) can be seen in the matrix, as can quartz (~1%) and

feldspar (2-5%) phenocrysts with the aid of a hand lens. White, devitrified, amphibole-bearing pumice and a variety of lithic fragments make up 25-35% of the rock. Their average size is 0.5 cm (maximum: (pumice) - 2 cm; (lithic fragments) - 5 cm). The array of colors of the lithic clasts is characteristic of many *Tmvs* exposures. Although the lithic fragments are mineralogically similar, most commonly fine-grained volcanic rocks, varying degrees of alteration have changed the surface colors. In this sample lithic fragments are pale yellow, orange, brown, pistachio green, turquoise, brick red, and steel grey. Differences between this and other *Tmvs* samples include the absence of pumice, larger lithic fragments (and some monolithologic deposits), less biotite and larger feldspar phenocrysts.

One unusual version of *Tmvs* in a few localities is black on fresh surfaces; weathered surfaces are most commonly pale tan. Hand samples have distinct white equant feldspars (5-7%) and mafic phenocrysts (probably pyroxene) altered to bright red (1%). Lithic fragments are minor.

*Petrographic description:*

The ashy matrix of *Tmvs* can contain crystals of quartz, feldspar, biotite, amphibole, pyroxene, and olivine. In thin section the cryptocrystalline groundmass contains up to 10% pumice and 20-35% phenocrysts which are predominantly 1-2 mm. Euhedral, elongate plagioclase feldspar laths comprise the majority of the phenocrysts, followed in relative abundance by amphibole, clinopyroxene and orthopyroxene, and trace amounts of olivine, quartz, biotite, and Fe oxides. Alteration of the phenocrysts is rare. The most common clast lithology observed in thin section is porphyritic andesite with typical phenocryst assemblages of 7-15% plagioclase feldspar, 3-6% amphibole, and minor amounts of clinopyroxene  $\pm$  olivine  $\pm$  biotite in a microcrystalline groundmass.

A 1-2-m-wide, light to dark grey, andesitic dike cuts *Tmvs* near location I11 (Figure 2.1) and has been mapped with it. The dike is roughly vertical and strikes approximately E-W. Weathered surfaces are stained orange. Phenocrysts make up 7-10% and include epidote  $\approx$  clinopyroxene > orthopyroxene  $\approx$  disequilibrium quartz in a trachytic groundmass of plagioclase microphenocrysts. The epidote, distinctly green in hand samples, has probably

replaced original plagioclase, pyroxene, and/or glass as a result of hydrothermal alteration. A basaltic dike which cuts *Tmvs* and is mapped with it contains 7-12% phenocrysts of olivine > altered mafic minerals (?) > minor amounts of feldspar and disequilibrium quartz in a pilotaxitic groundmass. The olivine is altered to a distinct red color (in plane light).

<sup>40</sup>Ar/<sup>39</sup>Ar geochronology:

*Tmvs* was not dated in this study. Geochronology of overlying units (*Tmr<sub>bio</sub>*, *Tmd<sub>tomb</sub>*, *Tmb<sub>kc</sub>*) constrain deposition of *Tmvs* in Santa Isabel Wash to be pre-17 Ma.

*Tmr<sub>bio</sub>*

A non-welded, weakly indurated, crystal-rich, pumice- and lithic-lapilli pyroclastic flow deposit is named the Biotite Tuff (*Tmr<sub>bio</sub>*) for biotite phenocrysts distinctly visible in the pumice lapilli in hand samples. It is a small, local pyroclastic flow deposit which apparently filled a “paleocanyon” or “paleochannel” within *Tmvs* trending roughly east-west over a distance of ~ 4 km (locations E12-L12 in Figure 2.1). The largest exposure of this ash-flow tuff is about 80 meters thick at the head of Santa Isabel Wash (location E12 in Figure 2.1) where it is unconformably overlain by rocks from Groups 3, 4, and 6. Another outcrop of *Tmr<sub>bio</sub>* which is not in line with the axis of the “paleocanyon” is exposed a few kilometers northwest (location D4 in Figure 2.1) of the other outcrops. These are similarly deposited unconformably upon *Tmvs* and overlain by either Group 3 or 4 rocks.

Both weathered and fresh surfaces have a light brown matrix with well-rounded, lighter tan to white pumice. Weathered pumice can also be orange. The pumice pieces make up 10-15% of the rock and contain distinct black phenocrysts of amphibole and biotite. On average the pumice are 1-2 cm (maximum: 5 cm). A variety of lithic fragments make up 5-15% of the rock and range in size from < 1-12 cm. Most lithic fragments are fine-grained porphyritic volcanic rocks and average 3-5 cm. Phenocrysts in the matrix (feldspar, quartz, biotite) are readily visible with a hand lens. The unit is very friable.



*Petrographic description:*

*Tmr<sub>bio</sub>* contains 15-25% phenocrysts of plagioclase and potassium feldspar > amphibole > quartz ≈ biotite with trace amounts of pyroxene and Fe oxides. There are 10-15% volcanic lithic fragments and 10-15% pumice in a cryptocrystalline matrix. Pleochroic amphibole phenocrysts are a distinct forest-green color (in plane light). This differs from the characteristically brown, pleochroic amphiboles (“basaltic hornblende”?) within the lithic fragments. Lithic clasts are commonly hornblende-phyric andesite but coarse-grained igneous rocks of granitic composition are also found.

*<sup>40</sup>Ar/<sup>39</sup>Ar geochronology:*

Plagioclase separates from *Tmr<sub>bio</sub>* yielded an isochron age of  $17.1 \pm 1.2$  Ma.

**Group 3 - *Tmb<sub>kc</sub>*, *Tmb<sub>lob</sub>*, *Tmd<sub>tomb</sub>****Tmb<sub>kc</sub>*

A clinopyroxene-olivine-plagioclase basalt containing up to 4% disequilibrium quartz is named the Klondike Canyon Basalt (*Tmb<sub>kc</sub>*). It is exposed at the head of Santa Isabel Wash (location E13 in Figure 2.1), is 140 meters thick, and covers ~ 0.5 km<sup>2</sup> in map view. It is interpreted to have intruded Group 2 rocks and *Tmd<sub>tomb</sub>* (also in Group 3), and is unconformably overlain by the ash-flow tuffs from Group 6. A basal breccia is exposed in some localities, but in general outcrops consist of highly weathered and fractured boulder piles.

Weathered surfaces are altered bright orange to brown. Fresh surfaces are grey, red, or black, and sugary textured. Visible phenocrysts include glassy quartz aggregates up to 1 cm, white, altered (i.e., powdery) feldspars up to 0.5 cm, black amphiboles which are a few mm long and can be altered to red, and euhedral olivine up to 5 mm which commonly have black

rims and red altered interiors. The feldspar phenocrysts commonly have grey mottled outer rims and some of the quartz phenocrysts are surrounded by thick, dark brown reaction rims. The plagioclase, quartz, and olivine phenocrysts are commonly 2-3 mm and are thus readily identifiable in hand samples.

*Petrographic description:*

*Tmb<sub>kc</sub>* contains 6-17% phenocrysts of plagioclase (andesine [Ab<sub>61-64</sub>An<sub>30-37</sub>Or<sub>2-6</sub>] and labradorite [Ab<sub>31-36</sub>An<sub>63-68</sub>Or<sub>1</sub>]) ≥ quartz ≈ olivine [(Fe<sup>2+</sup><sub>0.72-0.88</sub>Mg<sub>0.12-0.28</sub>)<sub>2</sub>SiO<sub>4</sub>] > clinopyroxene (augite [(Na<sub>0.03</sub>Ca<sub>0.76</sub>Fe<sup>2+</sup><sub>0.19-0.24</sub>Mg<sub>0.84-0.92</sub>Fe<sup>3+</sup><sub>0.00-0.07</sub>Ti<sub>0.01-0.02</sub>)(Al<sub>0.16-0.17</sub>Si<sub>1.87-1.92</sub>)O<sub>6</sub>] and subcalcic augite [(Na<sub>0.06</sub>Ca<sub>0.49</sub>Fe<sup>2+</sup><sub>0.35</sub>Mg<sub>0.84</sub>Fe<sup>3+</sup><sub>0.19</sub>Ti<sub>0.05</sub>)(Al<sub>0.27</sub>Si<sub>1.75</sub>)O<sub>6</sub>]) ≈ amphibole ([hornblende] and cummingtonite [(Mg<sub>0.60</sub>Fe<sup>2+</sup><sub>0.40</sub>)<sub>7</sub>Si<sub>8</sub>O<sub>22</sub>(OH)<sub>2</sub>]) in a seriate-textured, in some cases trachytic, groundmass. The hornblende is very altered and the microphenocrysts of clinopyroxene are altered orange in plane light. Quartz xenocrysts (usually 3-4%) are rimmed with aggregates of needle-like minerals (possibly hypersthene?). The presence of disequilibrium quartz suggests that perhaps these xenocrysts came from the melting of country rock as the intrusion moved towards the surface, and could represent evidence of a batholithic basement below this part of the PVP. Vugs up to 1 cm in diameter contain aggregates of quartz.

*<sup>40</sup>Ar/<sup>39</sup>Ar geochronology:*

The isochron age determined for *Tmb<sub>kc</sub>* on plagioclase separates is 17.1 ± 1.1 Ma.

*Tmb<sub>lol</sub>*

An olivine-pyroxene-plagioclase basalt with minor hornblende phenocrysts is named the Land of the Lost Basalt (*Tmb<sub>lol</sub>*). It is a small, local basalt flow up to 60 meters thick and covering a map area of < 0.1 km<sup>2</sup> at location J13 (Figure 2.1). It intrudes Group 2 rocks and is unconformably overlain by rocks from Group 6. Its relationship to the other lithologic units in Group 3 is not evident in the field area; however, similarities in stratigraphic position

and  $^{40}\text{Ar}/^{39}\text{Ar}$  crystallization ages suggest it is essentially contemporaneous. The unit is steel-grey on fresh surfaces. Plagioclase phenocrysts are recognizable in hand samples as are bright yellow altered mafic phenocrysts (probably olivine). The base is brecciated but poorly exposed and is overlain by stony lava. Lithic fragments make up < 1% of the units and are trachytic, porphyritic andesites.

*Petrographic description:*

*Tmb<sub>lOl</sub>* has a devitrified, hyalopilitic groundmass with microphenocrysts of equant plagioclase crystals. *Tmb<sub>lOl</sub>* consists of 16-29% phenocrysts of plagioclase feldspar (andesine [ $\text{Ab}_{51-60}\text{An}_{38-47}\text{Or}_2$ ]) >> orthopyroxene (hypersthene [ $(\text{Fe}^{2+}_{0.42}\text{Mg}_{0.58})\text{SiO}_3$ ] and bronzite [ $(\text{Fe}^{2+}_{0.17}\text{Mg}_{0.83})\text{SiO}_3$ ]) and clinopyroxene (diopside [ $(\text{Na}_{0.02}\text{Ca}_{0.85}\text{Fe}^{2+}_{0.16}\text{Mg}_{0.87}\text{Fe}^{3+}_{0.03}\text{Ti}_{0.01})(\text{Al}_{0.15}\text{Si}_{1.91})\text{O}_6$ ]) ≥ olivine [ $(\text{Fe}^{2+}_{0.18}\text{Mg}_{0.82})_2\text{SiO}_4$ ]) > amphibole ([hornblende]) and trace amounts of Fe oxides (ilmenite [ $(\text{Mn}_{0.01}\text{Fe}^{2+}_{0.77}\text{Mg}_{0.10}\text{Fe}^{3+}_{0.25}\text{Ti}_{0.88})\text{O}_3$ ]). On average the plagioclase phenocrysts are smaller (1-2 mm) than those found in *Tmb<sub>kC</sub>*. Another difference between these two basalts is the general absence of quartz phenocrysts in *Tmb<sub>lOl</sub>*.

*$^{40}\text{Ar}/^{39}\text{Ar}$  geochronology:*

The isochron age determined for *Tmb<sub>lOl</sub>* on plagioclase separates is  $16.3 \pm 0.5$  Ma.

*Tmd<sub>tomb</sub>*

One of the most voluminous and mineralogically variable rock types in the mapped area is a bronzite-hornblende-plagioclase-phyric dacite (with minor amounts of quartz phenocrysts) named the Tombstone Dacite (*Tmd<sub>tomb</sub>*). Stony, sheer-faced lava plugs and surrounding brecciated flows occur throughout Santa Isabel Wash. Given typical height to radius ratios for lava domes of about 0.5 to 1.0 (Blake, 1990), it is likely that *Tmd<sub>tomb</sub>* flows, which average 100-200 m in height, are from several local vents. Although vent features have

not been identified/preserved, likely vent localities are shown in Figure 2.3 based upon the presence of the breccias and the locations of solid, plug-like portions the deposits. The weathered surfaces of the brecciated portions are stained a deep orange, red or blue-to-black color. In contrast, many of the non-brecciated plugs are pale tan or pink. Deposits are up to 200 meters thick and often make up entire hills (such as near locations F8 and L11 in Figure 2.1). Bedding planes are rare while flow foliation planes are common. The collapse-breccia nature of the deposits suggests that these are proximal deposits and have not been reworked. Jigsaw cooling cracks on the margins of large boulders also imply that these rocks landed hot and have not traveled since that time. A few small (100-200-m-diameter), local basalt flows within *Tmd<sub>tomb</sub>* are mapped with this unit.

*Tmd<sub>tomb</sub>* is deposited unconformably upon Group 2 rocks and is unconformably overlain by one of the other Group 3 units (*Tmb<sub>kc</sub>*) as well as by rocks from Groups 5 and 6. Contact relationships between *Tmd<sub>tomb</sub>* and the third unit in Group 3 (*Tmb<sub>lol</sub>*) are not exposed in the field area. At location G11, the planar, brecciated, lower contact of *Tmd<sub>tomb</sub>* is well-exposed where it dips gently to the north over *Tmr<sub>bio</sub>*. In many places the basal breccia of *Tmd<sub>tomb</sub>* can be difficult to discern from the overlying, marginal brecciated portions of the deposit since in many places only brecciated outcrops are preserved. In some localities the unit overlies a 1-2-m-thick sedimentary deposit which in turn overlies *Tmvs*. The sedimentary deposits consist primarily of fine- and coarse-grained sand and pebble layers, and preserve lamination and cross-bedding which suggest a fluvial environment. The beds dip up to 30° to the southwest or northwest; these variations probably reflect local drainage conditions/directions, or perhaps tectonic tilting.

In the absence of the intervening sedimentary layer, the contact between *Tmd<sub>tomb</sub>* and *Tmvs* can be difficult to discern. Some of the key differences between the two units include rounded clasts within brecciated *Tmvs* versus predominantly angular clasts in *Tmd<sub>tomb</sub>* breccias, the paler colors of both the matrix and the clasts within *Tmvs* versus the red and black-stained *Tmd<sub>tomb</sub>*, and the larger average clast size of *Tmd<sub>tomb</sub>* (commonly 10-40 cm, but up to > 1 meter) in comparison to *Tmvs* (3-10 cm). At the contact, clasts in

uppermost *Tmvs* can be altered to bright yellow and red in color as a result of the emplacement of overlying *Tmd<sub>tomb</sub>*.

Fresh hand samples of *Tmd<sub>tomb</sub>* are pale pink, pale brick-red to deep brick-red, or black. Igneous intrusive lithic fragments make up 1-2% of the rock, average 3-4 cm, and are commonly surrounded by black reaction rims. In some areas rounded granitic xenoliths up to 20 cm are present in *Tmd<sub>tomb</sub>*. Plagioclase phenocrysts make up 5-10% of this rock and are commonly 3-5 mm, making them clearly visible in hand samples. Green orthopyroxenes are distinct and also visible in hand samples (maximum: 2 mm) as are black, altered hornblende (maximum: 2.5 mm).

A shallow, andesitic intrusion mapped with *Tmd<sub>tomb</sub>* near location K7 (Figure 2.1) is approximately 20 meters thick. Fresh hand samples have a speckled cherry red (glassy matrix) and white (devitrified matrix) appearance. Black, elongate, light-reflecting hornblende phenocrysts (3-5%) are visible in hand samples; the felsic phenocrysts are best seen with the aid of a hand lens.

#### *Petrographic description:*

The many flows which are included in *Tmd<sub>tomb</sub>* exhibit a range of mineralogy. Phenocryst content ranges from 10-25% commonly in a fine-grained trachytic groundmass with feldspar microphenocrysts. Both pilotaxitic and hyalopilitic textures exist. The most common phenocryst assemblage is amphibole ([hornblende] and cummingtonite  $[(Mg_{0.52}Fe^{2+}_{0.48})_7Si_8O_{22}(OH)_2]$ )  $\approx$  plagioclase (andesine  $[Ab_{49-64}An_{33-49}Or_{2-8}]$ )  $>$  orthopyroxene (bronzite  $[(Fe^{2+}_{0.21}Mg_{0.79})SiO_3]$ )  $\approx$  quartz with trace amounts of Fe oxides  $\pm$  olivine  $\pm$  biotite. Hornblende phenocrysts are commonly altered to black oxides in both the groundmass and the lithic fragments, and plagioclase phenocrysts generally have mottled rims (glass inclusions?). Some samples show trace amounts of disequilibrium quartz while others show quartz apparently in equilibrium. Lithic fragments are principally igneous intrusive xenoliths such as granite (hornblende, biotite, plagioclase, and quartz) and hornblendite (?) (hornblende  $>$  plagioclase  $>$  biotite). Gneissic clasts are also present. The andesitic intrusion

near location K7 (Figure 2.1) is a pyroxene-hornblende-plagioclase-phyric andesite with 17-27% phenocrysts of labradorite [ $\text{Ab}_{38-49}\text{An}_{56-61}\text{Or}_1$ ] > amphibole ([hornblende] and grunerite [ $(\text{Fe}^{2+}_{0.71}\text{Mg}_{0.29})_7\text{Si}_8\text{O}_{22}(\text{OH})_2$ ]) > orthopyroxene (hypersthene [ $(\text{Fe}^{2+}_{0.30-0.31}\text{Mg}_{0.69-0.70})\text{SiO}_3$ ]) > clinopyroxene (augite [ $(\text{Na}_{0.03}\text{Ca}_{0.82}\text{Fe}^{2+}_{0.14}\text{Mg}_{0.84}\text{Fe}^{3+}_{0.06}\text{Ti}_{0.02})(\text{Al}_{0.23}\text{Si}_{1.85})\text{O}_6$ ]) and minor potassium feldspar and Fe oxides in a cryptocrystalline groundmass.

#### <sup>40</sup>Ar/<sup>39</sup>Ar geochronology:

Plagioclase separates from seven samples of *Tmd<sub>tomb</sub>* from seven different localities yielded a range of isochron ages between  $15.5 \pm 0.4$  Ma and  $16.7 \pm 0.5$  Ma.

#### Group 4 - *Tmr<sub>sf</sub>*

##### *Tmr<sub>sf</sub>*

An important stratigraphic unit in the regions to the north of Santa Isabel Wash is the pyroclastic flow deposit recently designated the Tuff of San Felipe (*Tmr<sub>sf</sub>*) (Stock et al., 1996; 1997b). This crystal-rich, strongly indurated, lithic-lapilli pyroclastic flow deposit is exposed discontinuously in only a few places in the western portion of Santa Isabel Wash and is commonly between 5 and 15 meters thick (but up to 40 m thick). It unconformably overlies either Group 2 rocks (*Tmvs*) or Group 3 rocks (*Tmd<sub>tomb</sub>*) and its basal contact can be at a high angle where it was deposited against pre-existing topography. *Tmr<sub>sf</sub>* is in both conformable and unconformable contact with overlying pyroclastic flow deposits from Group 6; in one locality it is overlain by breccias of Group 5 (*Tma<sub>toro</sub>*).

A distinct basal vitrophyre characteristically grades upward from 20-30 cm of brown glass with black lithophysae into a small zone of reddish brown glass and then up to 1 meter of red and black glass with an upward increase in size and abundance of spherulites. Spherulites are colored red and orange and average 0.5 cm. Large, white feldspar crystals (3-6%) are clearly visible in the glass matrix. In some localities the basal vitrophyre overlies up

to 50 cm of grey, lithic ash. Stony, densely welded  $Tmr_{sf}$  which overlies the vitrophyric base is a pale reddish-purple, cliff-forming unit with shiny anorthoclase phenocrysts visible in hand samples. Abundant lithophysae form a prominent eutaxitic foliation. Millimeter-size lithic fragments (maximum: 2 cm) make up 1-3% of the rock and include trachytic and porphyritic volcanic rocks such as hornblende-phyric andesite. The unit weathers orange and is densely welded. Where the top of  $Tmr_{sf}$  is preserved, it is a 3-5-m-thick, less densely welded deposit which weathers a distinct sky-blue color. Hand samples are porcelaneous in character and lack the abundant lithophysae present in lower sections. Fresh surfaces are pale purple-grey.

*Petrographic description:*

Both the vitrophyre and overlying portions of  $Tmr_{sf}$  contain 6-15% phenocrysts of anorthoclase (two populations:  $[Ab_{56}An_3Or_{41}]$  and  $[Ab_{66-68}An_{5-6}Or_{26-28}]$ ) >> trace amounts of orthopyroxene, amphibole, quartz, and Fe oxides in a glassy, eutaxitic-textured matrix of welded pumice and shards. The matrix is devitrified and shows evidence of vapor phase crystallization except in the fresh, glassy basal vitrophyre. The anorthoclase phenocrysts average 1-2 mm (maximum: 5 mm). The orthopyroxene is green in plane light, and the pleochroic amphibole is pale tan to brown. The matrix of the upper, unwelded portion is composed of devitrified glass shards.

*$^{40}Ar/^{39}Ar$  geochronology:*

Anorthoclase separates from  $Tmr_{sf}$  yielded an isochron age of  $12.7 \pm 0.3$  Ma. This age determination is in good agreement with four dates determined for  $Tmr_{sf}$  in other areas, but differs with two other dates which yield slightly younger ages. The regional correlation section at the end of this chapter briefly mentions the results of these other studies. See Chapter III for a complete discussion and comparison of geochronologic results from these various studies.

## Group 5 - *Tmato*

### *Tmato*

Pico del Toro is a local peak of 700 meters elevation in the Santa Isabel Wash region (location G10 in Figure 2.1). The rock which makes up this peak is a hornblende-phyric andesite named the Pico del Toro Andesite (*Tmato*). The deposit is approximately 200 meters thick and covers about 0.25 km<sup>2</sup> in map view. It unconformably overlies Group 2 rocks (*Tmd<sub>tomb</sub>*) and Group 3 rocks (*Tmvs*). In one locality (F11 in Figure 2.1) the marginal breccia eroded from the slopes of *Tmato* overlies Group 4 rocks (*Tmr<sub>sf</sub>*). The lower contact of *Tmato* is generally not discernible since much of the unit is covered with slope wash, and is thus located approximately. *Tmato* also forms a 0.1 km<sup>2</sup> dome 3 km to the east of Pico del Toro (location K12 in Figure 2.1). This plug-like exposure is 90-100 meters thick, pale tan, and steep-sided.

Fresh hand samples have a light brown to greyish-brown sugary matrix with needle-like hornblende phenocrysts up to 3 mm in length. The hornblende is commonly altered to a deep purple or red and is thus clearly visible in hand samples in contrast with the paler matrix. Weathered surfaces are bright orange or white. A distinguishing feature on some, but not all, samples is steel-blue flow banding. Bands are up to 0.5 cm wide and give the rock a distinct striped appearance.

#### *Petrographic description:*

*Tmato* is a trachytic andesite with a cryptocrystalline groundmass comprised of 30-45% distinctly equant (or stubby), euhedral plagioclase (andesine [Ab<sub>50</sub>An<sub>48</sub>Or<sub>2</sub>] and labradorite [Ab<sub>41-47</sub>An<sub>52-58</sub>Or<sub>1</sub>]) laths which average 1/8-1/4 mm on an edge. Amphibole ([hornblende]) phenocrysts are up to 3 mm in length and make up 3-5% of the rock. Trace amounts of Fe oxides (hematite [(Mg<sub>0.03</sub>Fe<sup>3+</sup><sub>1.96</sub>Ti<sub>0.02</sub>)O<sub>3</sub>]) are also present. The presence of hornblende phenocrysts as the exclusive mafic mineral in this unit makes *Tmato*



lithologically distinct in the study area. Rare quartz phenocrysts up to 5 mm show no evidence for disequilibrium melting, suggesting that perhaps this rock is compositionally closer to dacite rather than andesite.

*<sup>40</sup>Ar/<sup>39</sup>Ar geochronology:*

An isochron age of  $9.3 \pm 0.4$  Ma was determined on plagioclase separates from *Tma<sub>toro</sub>*.

**Group 6 - *Tmr<sub>siw</sub>*, *Tmb<sub>new</sub>*, *Tmr<sub>3</sub>*, *Tmr<sub>3-4</sub>*, *Tmr<sub>4</sub>*, *Tmr<sub>ao</sub>*, *Tmr<sub>ec</sub>*, *Tmr<sub>bs</sub>*, *Tmr<sub>fp</sub>***

*Tmr<sub>siw</sub>*

The colorful, crystal-rich, pumice- and lithic-lapilli pyroclastic flow deposits which comprise the Tuffs of Santa Isabel Wash (*Tmr<sub>siw</sub>*) are readily recognizable in the study area. These weakly indurated, distal outflow sheets are thickest in the northern parts of the study area (up to 100 m at location H4 in Figure 2.1) where they apparently filled a topographic low, and bank against higher topography to the south. They are up to 140 meters thick at location N9 (Figure 2.1) and are also fairly thick (up to 70 m) near the head region of Santa Isabel Wash. They are unconformably deposited upon rocks from Groups 2, 3, and 4 and are conformably overlain by other Group 6 units (either *Tmb<sub>new</sub>* or *Tmr<sub>3</sub>*). In contrast to the overlying ash-flow tuffs, the upper surface of *Tmr<sub>siw</sub>* is not always planar and thus cannot be used as a reliable indicator of paleohorizontal. In one locality on the east side of Santa Isabel Wash (near location E9 in Figure 2.1), lower *Tmr<sub>siw</sub>* contains a 1.5<sup>+</sup>-m-thick horizon of lithic breccia composed of well-rounded, spherical, porphyritic volcanic clasts averaging 10-15 cm. Some granitic clasts are also present. The lithic fragments were probably entrained in the pyroclastic flow deposit from the local substrate by a mechanism such as that described by Buesch (1992) for distal portions of the Peach Springs Tuff in California which contain locally derived lithic fragments. The rounded lithic fragments within *Tmr<sub>siw</sub>* are most likely

from older stream deposits, suggesting the presence of a Miocene “paleo-drainage” in the same locality as the present-day arroyo.

In general the lowermost portion of *Tmr<sub>siw</sub>* is yellow to orange in color while the upper portions grade into red and pink. In some localities at least 4 cooling breaks are evident while in others the contacts are gradational. In some cases a white, air-fall (?) and/or reworked (?) pumice-rich deposit is preserved below *Tmr<sub>siw</sub>* and is mapped with it. *Tmr<sub>siw</sub>* is thus further divided into 5 cooling units labeled *t1* (the discontinuous, pumice-rich deposit at the base) to *t5* (the uppermost cooling unit). It is not clear how much time occurred between the deposition of the various cooling units; however, paleomagnetic analysis on cooling units *t2* through *t5* (see Chapter V for details) shows that each of these four cooling units preserves the same remanent magnetization direction and thus they were probably deposited in a relatively short period of time.

The following descriptions are of the thick, primarily non-welded variety of the *Tmr<sub>siw</sub>* cooling units since those deposits contain the most variation. A brief description of the thin, densely welded exposures of these ash-flow tuffs will be included afterwards.

Cooling unit *t1* is a pumice-rich deposit up to 30-m-thick which could be proximal air fall and/or a surge deposit, and in some locations is interpreted to be water-reworked. It is not always exposed at the base of *Tmr<sub>siw</sub>* suggesting that erosion occurred prior to the deposition of the following cooling units. Alternatively, since some of *t1* is perhaps reworked, it was probably not deposited everywhere in the area but only in certain environments such as fluvial channels. It is usually white to blue-grey, moderately sorted (poorly sorted at base to laminated and thinly bedded near top), and occasionally cross-bedded. In some exposures stratified silts occur above and below cooling unit *t1*. Where it is best preserved (location F14 in Figure 2.1) the deposit is about 3 meters thick and consists of two beds. The lower bed is a non-stratified, < 1-m-thick, plinian (or fallout) deposit of pumice-lapilli (> 50%) and is a characteristic “skim-milk blue” color. This bed pinches out to the north unconformably against underlying Group 2 rocks (*Tmvs*). The upper bed is a 2-3-m-thick, tan, water-reworked deposit with meter-scale cross-beds which are truncated at the upper horizontal

contact by the next cooling unit (*t2*). Cooling unit *t1* contains 10-20% of poorly-sorted, subangular lithic fragments (1 mm-1 cm) as well as obsidian (up to 5 mm) and pumice averaging 1 cm (maximum: 10 cm).

Yellow to orange *t2* is one of the two cooling units (the other is *t5*) which is almost always present and thus characteristic of the *Tmr<sub>siw</sub>*. The pumice is generally darker orange than the rest of the deposit, and unaltered, grey centers of freshly broken larger pieces indicate that the discoloration is a result of alteration. In some places the pumice is altered to a dark pea-green color, or the unit is black and ashy with dark green and black pumice. These particular deposits were perhaps altered in sub-aqueous conditions. This cooling unit is up to 15 meters thick. Where exposures are thicker than a few meters, *t2* commonly forms vertical cliffs. A typical unwelded to slightly welded outcrop consists of 15% orange, rounded or elongate pumice lapilli and blocks averaging 2-3 cm (maximum: 15 cm), 1% rounded and angular obsidian clasts averaging 1-2 mm (maximum: 6 cm), 7-10% other sub-angular lithic fragments (principally fine-grained, pale purple and pale blue-grey volcanic rocks (juvenile clasts?)) averaging 1-2 cm, and 1% phenocrysts of feldspar within both the ashy matrix and the pumice lapilli and blocks.

Cooling unit *t2* is overlain by a similar unwelded cooling unit, *t3*, usually colored pink to pale orange. It does not form distinct cliffs. This unit can be up to 20 meters thick but is not present in all localities. Cooling unit *t3* commonly has vertical (or SW plunging) gas-escape structures near the top. Pumice elongation, if any, is perpendicular to these structures. This cooling unit contains up to 5-15% pink or orange pumice averaging > 1 cm, 7-10% sub-angular, pale blue and pale purple, fine-grained volcanic rocks from 1-50 mm, 1% sub-rounded obsidian from 1-5 mm, and 1% feldspar phenocrysts.

Bright red or grey cooling unit *t4* overlies *t3* (or *t2*, if *t3* is missing). The cooling unit is up to 7-10 meters thick. It is sometimes difficult to locate the upper and lower cooling breaks as they seem to merge with the overlying and underlying cooling units in some places. A distinct, lithic-rich (10-15%) central portion of *t4*, up to 3-5 meters thick and usually with a brick-red to orange matrix, is slightly welded and contains almost no pumice. Concentrated lithic-rich zones can contain up to 30% clasts which is a distinguishable characteristic of this

cooling unit. The lithic fragments average 1-2 cm and include grey, white, and red, fine-grained volcanic rocks and granite. Feldspar phenocrysts (6-8%) can be seen in the matrix with the aid of a hand lens. Below the red indurated zone the unit is non-welded, white to grey with 3-5% white and orange-altered pumice from 2-20 mm, 3-5% lithic fragments which are primarily fine-grained volcanic rocks (juvenile clasts?), 3% feldspar phenocrysts, and < 1% obsidian (altered orange around rims) from 1-3 mm. A similar unwelded, pumiceous layer overlies the central indurated layer for another 3-4 meters.

The uppermost cooling unit of *Tmr<sub>siw</sub>* is the red to purple, moderately to densely welded *t5*. Cooling unit *t5* can be up to 50 meters thick where non-welded. In some places a thin (< 1 meter) grey or purple ashy layer occurs between this cooling unit and underlying *t4*. Cooling unit *t5* usually contains a characteristic basal portion which is a red and black to dark grey, densely welded zone from 1-5 meters thick with well-developed eutaxitic foliation and, in some places, spherulitic zones. Knobby weathered surfaces have a perlitic (devitrified) texture. This welded zone commonly forms cliffs and can have fiamme up to 10 cm in length. Red glassy patches are present throughout the rock (especially surrounding lithic fragments and phenocrysts) and are interpreted to be regions of intense devitrification. Grey-blue volcanic rocks and porphyritic dacite (*Tmd<sub>tomb</sub>*?) lithic fragments make up 5-10% of the rock and are < 1 cm on average. Feldspar phenocrysts can be seen with a hand lens.

The upper portion of cooling unit *t5* has a devitrified purple matrix with red, glassy lithophysae which form bands between 2 and 8 mm thick. It contains 5-10% phenocrysts of feldspar and pyroxene and < 1% mm-size lithic fragments. In some exposures the unit grades upwards into a 1.5-m-thick, purple ash which is in turn overlain by 0.5-5 meters of an orange, non-welded, pumice-flow deposit with > 50% pumice-lapilli (note: except for the color, this is an identical deposit to lower *t1*). This uppermost tephra layer is indurated but friable. It consists of orange pumice in an orange glassy matrix. The matrix is commonly black on weathered surfaces which contrasts with the orange pumice and thus gives the deposit a distinctive appearance in the field. Phenocrysts of feldspar (3-5%) are clearly visible in hand samples.

Where  $Tmr_{SiW}$  bank and thin against pre-existing topography, they are moderately to densely welded. Pumice pieces are commonly strung out as black, glassy fiamme, thereby forming measurable eutaxitic foliation parallel to the basal contact. The deposit can thin from 40 meters to ~1 meter over a horizontal distance of less than 200 meters, although densely welded sections can be up to several tens of meters thick. The cooling breaks are no longer distinguishable; commonly only units classified as  $t2$  and  $t5$  are discernible. In outcrop appearance the unit can change over as little as 1.5 (vertical) meters from yellow or salmon-colored with flattened orange or brown pumice near the base, to brownish-red at the top with > 30-cm-long spherulitic lithophysae. The unit generally contains ~10% angular lithic fragments up to 5 cm.

*Petrographic description:*

The most distinctive features of the phenocryst mineralogy in  $Tmr_{SiW}$  are the general absence of quartz, hornblende, or significant amounts of biotite, and the presence of disequilibrium olivine. The unit consists of 10-20% phenocrysts of plagioclase (andesine [ $Ab_{57-68}An_{27-41}Or_{2-5}$ ] and oligoclase [ $Ab_{70-73}An_{20-25}Or_{5-7}$ ]) and anorthoclase ([ $Ab_{63-70}An_{6-11}Or_{19-31}$ ]) >> olivine  $\approx$  clinopyroxene (ferroaugite [ $(Na_{0.02}Ca_{0.80-0.83}Fe^{2+}_{0.73-0.87}Mg_{0.25-0.41}Fe^{3+}_{0.01}Ti_{0.01})(Al_{0.03-0.04}Si_{1.98-1.99})O_6$ ] and [pigeonite])  $\approx$  Fe oxides (hematite [ $(Mn_{0.03}Fe^{2+}_{0.12}Mg_{0.02}Fe^{3+}_{1.66}Ti_{0.17})O_3$ ])  $\pm$  trace biotite. The olivine is altered black or red around the edges and internally along fractures, and in some crystals a prismatic habit is well-defined. The orthopyroxene is distinctly green (but not pleochroic) in plane light. Some olivine and orthopyroxene phenocrysts are imbedded in larger plagioclase phenocrysts up to 4 mm, suggesting that the country rock through which this unit erupted may have been a coarse-grained gabbro and that these are in fact xenocrysts. Some of the feldspars are mottled (glass inclusions?). The groundmass consists of vitric glass spicules and pumice which are usually colorless but can be bright yellow or pale brown in plane light; it can also have a devitrified cryptocrystalline texture. The bright yellow variety of groundmass glass is most common in cooling units  $t2$  and  $t3$ . Lithic fragments (10-15%) average a few mm to a few cm and include fine-grained,

trachytic-textured volcanic rocks, hornblende-phyric andesite ( $Tmd_{tomb}$ ), granite, and pieces of devitrified tuff. The general absence of hornblende, biotite, and quartz suggests a more anhydrous (hotter) parent magma than other tuffs bearing hydrous phases.

*<sup>40</sup>Ar/<sup>39</sup>Ar geochronology:*

Mixtures of plagioclase and anorthoclase crystals from cooling unit  $t2$  yielded an isochron age of  $6.5 \pm 0.2$  Ma, from cooling unit  $t5$  yielded an isochron age of  $6.7 \pm 0.2$  Ma, and from densely welded  $Tmr_{siw}$  at two locations yielded ages of  $6.6 \pm 0.3$  Ma and  $5.7 \pm 0.2$  Ma. This last age is anomalous given the agreement between the other three ages as well as the ages of overlying deposits. Normal magnetic polarity measured in these cooling units (see Chapter V) suggests that the units were probably deposited during Subchron C3An.2n ( $6.269 - 6.567$  Ma) (Cande and Kent, 1995).

*Tmb<sub>new</sub>*

A 70-120-m-thick, basaltic lava flow covers  $\sim 3$  km<sup>2</sup> at location O10 (Figure 2.1) and is in unconformable contact with underlying  $Tmr_{siw}$ . It is depositionally overlain by a sedimentary breccia/conglomerate, up to 40 meters thick, which contains a variety of clasts including pieces of  $Tmr3$ . It is named the New Year's Mountain Basalt ( $Tmb_{new}$ ) and is a glomeroporphyritic olivine(?)–pyroxene–plagioclase basalt. This is the only known locality where any unit is present between  $Tmr_{siw}$  and overlying  $Tmr3$  and testifies to at least some period of time between their deposition.  $Tmb_{new}$  has a 2-4-m-thick, scoriaceous basal breccia which overlies the uppermost orange tephra layer of  $Tmr_{siw}$ . The basal breccia is overlain by up to 120 meters of stony lava. This dark, tabular lava flow can easily be seen in cross-section from most of the field area. The basalt is a steel grey to black color with green and white glomerocrysts up to 5 mm. They are clearly visible in hand samples and comprise  $\sim 10\%$  of the rock. Individual smaller, white, euhedral feldspar phenocrysts are also clearly visible in

hand samples. The matrix is dense and stony and can be highly vesiculated. Weathered surfaces are usually orange, white, or black.

*Petrographic description:*

$Tmb_{new}$  contains 12-18% phenocrysts of plagioclase (bytownite  $[Ab_{17}An_{83}]$ , andesine  $[Ab_{56-60}An_{36-41}Or_{3-4}]$ , and labradorite  $[Ab_{42}An_{56}Or_2]$ ) > clinopyroxene ([pigeonite] and augite  $[(Na_{0.02}Ca_{0.78}Fe^{2+}_{0.42}Mg_{0.73}Fe^{3+}_{0.02}Ti_{0.01})(Al_{0.06}Si_{1.96})O_6]$ ) > olivine (clear and surrounded with orange in thin section?)  $\approx$  ilmenite  $[Mn_{0.01}Fe^{2+}_{0.81}Mg_{0.06}Fe^{3+}_{0.24}Ti_{0.88})O_3]$  granules. Glomerocrysts of plagioclase and pyroxene are in a fine-grained groundmass with both an intergranular and intersertal texture. Plagioclase laths in the groundmass exhibit slight alignment (i.e., show a slightly trachytic texture). Some of the euhedral to subhedral plagioclase phenocrysts are severely embayed and possibly contain glass inclusions.

*$^{40}Ar/^{39}Ar$  geochronology:*

This unit was not dated but its deposition is tightly constrained by  $^{40}Ar/^{39}Ar$  results from the underlying ( $Tmr_{siw}$ ) and overlying ( $Tmr3$ ) tuffs to be between 6.3 and 6.6 Ma.

*Tmr3*

Conformably overlying  $Tmr_{siw}$  is a sequence of up to four weakly indurated cooling units comprising the crystal-rich, pumice- and lithic-lapilli pyroclastic flow deposit  $Tmr3$ . It is also unconformably deposited upon rocks from Groups 2 and 3 in a few localities, and is conformably overlain by  $Tmr_{3-4}$  or  $Tmr4$  (if the former is missing). The label is taken from Stock (1989; Miocene Rhyolite #3). It is the most extensive ash-flow tuff in the study area and is generally thicker (commonly > 100 meters) than other tuffs from Group 6.  $Tmr3$  fills topography and its upper surface is usually planar and thus is a fairly good indicator of paleohorizontal. Although the four cooling units which comprise  $Tmr3$  can be very similar in outcrop appearance, paleomagnetic results show that one of the cooling units, which is

deposited/preserved only in the western part of the study area (locations H4, E4, and D10 in Figure 2.1), records a unique remanent magnetization direction in comparison to the other three (see Chapter V). This fourth cooling unit (referred to as (*Tmr3 (type I)*)) underlies the other three cooling units (*Tmr3 (type II)*). As discussed in Chapter IV in conjunction with the structural history of the area, the restriction of this lowest cooling unit to the area just east of the E-dipping Santa Isabel fault system (location C5-D16 in Figure 2.1) suggests that it may have been deposited along a region of structural downwarp, or reverse-drag, associated with pre-6 Ma motion along this structure. If this is the reason for its geographic restriction, it seems most likely that the unit could be deposited further north or northwest of Santa Isabel Wash (e.g., Sierra San Felipe), but probably not to the northeast (e.g., Sierra San Fermín). This will become important in Chapter V where the interpretation of paleomagnetic results between these various areas depends upon precise lithologic correlation between the four *Tmr3* cooling units sampled in each study. Slight variations in the outcrop appearance of these four cooling units of *Tmr3* are summarized here.

The lowest cooling unit (*Tmr3 (type I)*) is typically non-welded and commonly contains pumice averaging 5-10 cm in length (maximum: > 40 cm). It is between 10 and 25 meters thick, and as mentioned above can be missing altogether from the *Tmr3* sequence. The matrix is typically pink to light brown and the fibrous pumice are silver-grey. Small, black obsidian wisps can be seen throughout the matrix of some samples with the aid of a hand lens. Anorthoclase phenocrysts make up 5% of the rock and are readily visible in hand samples. Lithic fragments make up 2-5% of the rock and are principally red or grey fine-grained volcanic rocks. In one location this cooling unit is replaced by a 10-20-cm-thick, plinian, anorthoclase-bearing, non-stratified air-fall deposit of coarse pumice and lithic fragments.

The second *Tmr3* cooling unit from the bottom is a 20-25-m-thick, massive, slightly welded, tan to brown, cliff-forming tuff with 5-10% pale buff pumice. The pumice in this cooling unit is distinctly fibrous and averages < 1 cm in some areas and much larger (tens of cm) in others (maximum: > 50 cm). It is from this cooling unit that anorthoclase crystals were separated from one large piece of pumice and used as an internal standard for the  $^{40}\text{Ar}/^{39}\text{Ar}$



geochronology presented in Chapter III. Weathered surfaces are slightly more orange-brown than fresh surfaces. One characteristic feature is that the unit commonly weathers to form large caves. Lithic fragments include ~ 3% red and grey volcanic rocks averaging 1 cm (maximum: 10 cm). Anorthoclase phenocrysts make up 1-5% of the rock.

The third cooling unit from the bottom is moderately welded and up to 30-35 meters thick. The upper half of this unit forms sheer cliffs while the lower half forms less-pronounced slopes. This cooling unit has a bright white, ashy matrix which weathers orange and contains 5-7% white pumice averaging 1-2 cm. Dark red and grey, angular, fine-grained volcanic lithic fragments (10-12%) are distinct within the white tuff and average 1-3 cm (maximum: 30 cm). Other lithic fragments include yellow ash-flow tuff and granite. Large (> 5 mm) anorthoclase phenocrysts (3-4%) are clearly visible in hand samples.

The moderately welded uppermost cooling unit is slightly more welded than the underlying cooling unit and is up to 40-50 meters thick. It consists of a pink, ashy matrix which weathers to white or orange and contains 7-10% devitrified and spherulitic elongate pumice. The pumice are typically silvery-grey and average 5 cm in length, making this cooling unit very similar in appearance to the lowermost *Tmr3* cooling unit. The unit contains 2-3% lithic fragments averaging 1-2 cm, which are compositionally granites, red and grey, fine-grained volcanic rocks, and a white ash-flow tuff. The unit contains 1-2% feldspar phenocrysts visible in hand sample. Eutaxitic foliation is well-developed.

Overlying *Tmb<sub>new</sub>*, a clast-supported, heterolithologic breccia/conglomerate occurs in the stratigraphic position of *Tmr3*. The deposit is up to 40 meters thick and contains a large variety of well-rounded clasts up to 1 meter in diameter of granite, pieces of *Tmr3* (which, in turn, contains significantly larger lithic fragments (5-6 cm) than normally observed of a variety of lithologies), vitrophyre, and other volcanic rocks. Clearly the breccia/conglomerate post-dates the deposition of *Tmr3* since it contains pieces of this tuff within it.

*Petrographic description:*

In thin section the matrix of *Tmr3* is pale brown (in plane light), devitrified, and cryptocrystalline. There are usually 5-15% phenocrysts, which include anorthoclase ([Ab<sub>63</sub>.

${}_{66}\text{An}_{1-2}\text{Or}_{32-36}] \gg$  quartz > trace orthopyroxene and Fe oxides  $\pm$  trace olivine (very altered)  $\pm$  trace hornblende  $\pm$  trace plagioclase. The quartz (average 1 mm) and anorthoclase (up to 2-3 mm) are characteristically embayed (glass inclusions?). Plagioclase is generally rare in the groundmass. The orthopyroxene is distinctly bright green and pleochroic in plane light. The deposit contains up to 15% lithic fragments of a variety of compositions, including hornblende-phyric andesites, porphyritic basalt, volcanoclastic breccia (*Tmvs?*), trachytic volcanic rocks (groundmass commonly altered to black), and granite (containing biotite, hornblende, feldspar, quartz, and sphene). These xenoliths are probably the source of the trace amounts of hornblende and plagioclase in *Tmr3*.

#### ${}^{40}\text{Ar}/{}^{39}\text{Ar}$ geochronology:

Ten separate packages of anorthoclase crystals from a single piece of pumice from *Tmr3* were analyzed. Isochron ages among the packages range from  $6.2 \pm 0.1$  Ma to  $6.7 \pm 0.2$  Ma. The results from these ten samples were combined for each of two lab measurement sessions and thus yielded two average isochron ages of  $6.2 \pm 0.1$  Ma (four packages) and  $6.4 \pm 0.2$  Ma (six packages). See Chapter III for details. Normal polarity magnetization preserved in *Tmr3* (see Chapter V) implies that deposition most likely occurred during Subchron C3An.2n (6.269 - 6.567 Ma) (Cande and Kent, 1995).

#### *Tmr3-4*

*Tmr3-4* is a thin (1-2-meters-thick), weakly indurated, crystal-poor, lithic-lapilli pyroclastic flow deposit in conformable contact with underlying *Tmr3* and overlying *Tmr4*. When present, *Tmr3-4* has been mapped with *Tmr4*. A separate description of *Tmr3-4* is given here since a unique remanent magnetization direction was measured in this unit in the paleomagnetic analysis described in Chapter V. *Tmr3-4* is slightly welded and is similar to *Tmr4* in outcrop appearance but can contain 1-2% glassy lithic fragments commonly up to several cm (maximum: 10 cm). These include red glassy rhyolites, basalts, and granites, and

give the unit a “butterscotch chip” appearance. The unit is rosy pink or tan on fresh surfaces and a slightly darker shade on weathered surfaces. The matrix is sugary and sparkles due to its vitric nature. Elongate fiamme of black welded obsidian are commonly < 1 cm in length, and many smaller fiamme are visible with a hand lens in some samples. Where devitrified the black obsidian alters to a mustard yellow-brown color. Some obsidian pieces are spherical instead of welded and flattened. Pumice are whitish-grey, fibrous, and make up 1-2% of the unit. Some pumice is altered to an orange color. The pumice are slightly elongate and vary in length from a few mm to a few cm. Rare phenocrysts are visible with a hand lens.

*Petrographic description:*

In thin section this unit is an unwelded to moderately welded, vitric ash-flow tuff with < 1% phenocrysts of feldspar and pyroxene. The phenocrysts average < 1 mm and the pyroxenes are characteristically green in plane light. The groundmass consists of glass spicules and pumice. Lithic fragments include altered trachytic volcanic rocks consisting primarily of plagioclase laths.

*Tmr4*

Conformably overlying *Tmr<sub>3-4</sub>* (or *Tmr<sub>3</sub>* if the former is missing) is a crystal-poor, weakly indurated, pyroclastic flow deposit called *Tmr4*. The label is taken from Stock (1989; Miocene Rhyolite #4). *Tmr4* is also deposited unconformably upon Group 2 rocks (*Tmvs*) in Arroyo Oculito. It is conformably overlain by *Tmr<sub>ao</sub>* (where present) and, more commonly, *Tmr<sub>ec</sub>*. It commonly has a planar base and top making it a tabular shape. The diagnostic base consists of up to 1 meter of dark brown vitrophyre containing 1-2% orange, welded pumice with a maximum length of 1 cm. This grades upwards to an orange then cherry red partially welded tuff which in some places has blue, pink or orange, large (from < 1 cm to > 10 cm) lithophysae filled with spherulites. The spherulitic lithophysae can be pink, blue, purple, or orange but are commonly a different color from the groundmass. The uppermost portions of

*Tmr4* change from pink to purple and densely welded with lithophysae. In most parts of the Santa Isabel Wash region *Tmr4* is 3-5 meters thick; however, thicker sections (10-20 m), which include a 2-4-m-thick spherulitic base, occur in the southern parts of the field area where the unit apparently filled topographic lows. A 4-5-m-thick spherulitic base also occurs on the north side of the hills at location L7 (Figure 2.1). Very thick sections (up to 70 meters thick) occur in Arroyo Oculito and have a characteristic planar, resistant, upper surface which forms pronounced “shelves” below the more recessive units above it.

Hand samples have a very uniform, porcelaneous or glassy texture and characteristically break conchoidally. The matrix appears sugary textured on fresh surfaces. Phenocrysts are generally too small to see in hand samples although rare feldspar phenocrysts up to several mm in size exist. Volcanic lithic fragments make up < 1% of the rock and are < 1 cm.

*Petrographic description:*

This densely welded ash-flow tuff contains < 1% of small (average 1/8-1/4 mm) feldspar and clinopyroxene phenocrysts in a spherulitic, devitrified groundmass. Lithophysae contain vapor phase crystals of tridymite (?) and some calcite infilling.

*Tmr<sub>ao</sub>*

The crystal-poor, weakly indurated, pumice- and lithic-lapilli pyroclastic flow deposit which conformably overlies *Tmr4* is named the Arroyo Oculito Tuff (*Tmr<sub>ao</sub>*). It has a distinctive, bright white, weathered surface color where it is exposed at location S7 (Figure 2.1). It is conformably overlain by *Tmr<sub>ec</sub>*, and in some exposures the uppermost 2 meters are ashy, soft, and fractured with zones of zeolites. The thickness of this partially to densely welded ash-flow tuff varies greatly in the mapped area. In Arroyo Oculito it is 20-30 meters thick and varies laterally to include a 2-3-m-thick, grey, densely welded, cliff-forming zone in its central portion. This interior zone is devitrified and contains lithophysae with vapor phase crystallization. In other areas it can be missing or only 1-2 meters thick (e.g., location H4 in

Figure 2.1) and sandwiched between layers of calichified breccia. In these localities fresh surfaces are light orange-brown (unwelded) to purplish-grey (partially welded), and the unit is partially devitrified. Pumice make up 5% of the unit and sub-rounded dacite clasts (1-2%) are usually < 1 cm. Granitic clasts are present in exposures in Arroyo Oculto. Phenocrysts are rare (< 1%) and cannot easily be seen without a hand lens.

*Petrographic description:*

Thin section examination reveals that some samples of *Tmr<sub>AO</sub>* are glassy while others are devitrified. *Tmr<sub>AO</sub>* contains a maximum of 2% phenocrysts of feldspar (plagioclase and anorthoclase (?)) and orthopyroxene. The densely welded versions are devitrified and exhibit vapor phase crystallization. Calcite cement is common in vugs, and rare glass spicules in vitric samples are yellow or brown. One quartz phenocryst was found in one thin section. Lithic fragments include altered trachytic volcanic rocks and porphyritic volcanic rocks which may be pieces of *Tmd<sub>tomb</sub>* (from Group 3). One sample has a lithic fragment which is apparently from unit *Tma<sub>toro</sub>* (Group 5).

*<sup>40</sup>Ar/<sup>39</sup>Ar geochronology:*

An inverse isochron age determined on plagioclase separates from *Tmr<sub>AO</sub>* yielded 6.4 ± 0.1 Ma.

*Tm<sub>rec</sub>*

A densely welded, strongly indurated, crystal-rich, lithic-lapilli pyroclastic flow deposit is correlated to a series of deposits mapped to the north and east known as the Tuff of El Canelo (Stock et al., 1991; Martín-Barajas et al., 1995) (*Tm<sub>rec</sub>*). *Tm<sub>rec</sub>* generally caps the mesa tops of the PVP in the mapped area unless erosion has exposed *Tmr<sub>4</sub>*, *Tmr<sub>AO</sub>*, or *Tmr<sub>3</sub>* below it. It is between 1 and 2 meters thick on the mesa tops in the western and southern parts of the field area and is stained orange, dark red or black on weathered surfaces. The tuff is

devitrified and fresh surfaces can have a white and glassy-red matrix, or a purple to chocolate brown matrix. Sub-horizontal, darker-colored fiamme are weathered-out at exposures along the mesa edges thus giving the unit a distinct foliated appearance. In some cases these vugs are filled with secondary crystallization. In both cases plagioclase phenocrysts sparkle distinctly.

*Tmr<sub>ec</sub>* is conformably overlain by either *Tmr<sub>bs</sub>*, *Tmr<sub>fp</sub>*, or *Tmr<sub>can</sub>* in the eastern parts of the mapped field area. *Tmr<sub>ec</sub>* apparently filled a topographic low in the vicinity of location R8 (Figure 2.1) where it was subsequently dissected by NW-flowing drainages. In this locality it is up to 80 meters thick and contains (in its upper half) steeply dipping foliation planes with down-dip lineations suggesting syn- or post-compaction flow. Rotated (or folded?) fiamme and tension cracks also suggest down-dip movement. These kinematic indicators show flow to the northwest. Repeated variations occur in the steepness of the foliation planes from horizontal to up to 60° over a distance of roughly 10 meters. The general sequence, from back to front (with respect to flow direction), is a fairly flat foliation plane region, a massive and spherulitic portion, and then a steep foliation plane section. In places where the thicker deposits apparently flowed over steep topography, the upper portions are strongly lineated and have brown, deeply etched, weathered surfaces which emphasize the lineations. Fresh surfaces are pale pink and have a sugary, devitrified appearance. Plagioclase phenocrysts sparkle distinctly but are best seen with a hand lens. In a few localities the uppermost several meters are completely devitrified, massive, white and grey with some remnant, red, glassy fiamme.

Significant topographic variations (1-3 meters) in the upper surface of the thicker exposures of *Tmr<sub>ec</sub>* (location R8 in Figure 2.1) give the unit a hummocky appearance. The variations might be the result of rheomorphism over irregular topography, for example over a step-like series of normal fault scarps. However, given the thickness of the unit (80 meters), it seems unlikely that underlying topographic variations would affect the top of the flow. In addition, such variations in foliation orientation are not observed at the base of the unit. It is perhaps more likely, especially given other rheomorphic evidence, that these variations are genetically similar in formation to pressure ridges and tumuli which can develop on the

chilled upper crust of pahoehoe lava flows. Pressure on the solidified, upper surface from the still-fluid underlying tuff might cause the upper surface to buckle. The geometry of these topographic variations does not appear to record information regarding transport direction.

Basal  $Tmr_{EC}$ , where the deposit is greater than a few meters thick, is brick red on fresh surfaces with long, thin, white, continuous, sub-horizontal fiamme. The fiamme can be up to a few mm wide and make up 5-10% of the rocks thus giving it a characteristic striped nature. Ductile deformation of the fiamme indicates post-compaction flow. This lower portion of  $Tmr_{EC}$  forms a resistant layer along which drainages flowed (location R8 in Figure 2.1), and the foliation planes are weathered into a platy, stair-step appearance. Colorless feldspar phenocrysts (~5%) are clearly visible in hand samples. A densely welded, upper flow unit occurs in the northeast (e.g., locations S3, R5, and S5 in Figure 2.1), is up to 40 m thick, and resembles the striped, basal, stair-like outcrops. The presence of an additional cooling unit is consistent with the multiple flows seen in other localities within the Tuff of El Canelo (Stock et al., 1991).

*Petrographic description:*

$Tmr_{EC}$  contains 3-10% phenocrysts of predominantly feldspar (oligoclase [ $Ab_{71-74}An_{19-23}Or_{5-7}$ ] and anorthoclase [ $Ab_{50-58}An_{3-5}Or_{37-47}$ ]) >> orthopyroxene  $\approx$  Fe oxide granules (magnetite [ $(Fe^{2+}_{1.27}Mg_{0.04}Fe^{3+}_{1.35}Al_{0.03}Ti_{0.31})O_4$ ]). Amphibole [hornblende] was also identified with the electron microprobe but not observed in thin section. Some of the altered minerals may be of this composition. The feldspars, which are up to 2.5 mm, are distinct in thin section from feldspars described in other units in this study because they almost always contain brittle fractures or veins filled with a high birefringence material (calcite?). The pleochroic orthopyroxene is green and pink and can be altered to black around the rims. The groundmass is partially to completely devitrified, densely welded, microcrystalline with secondary vapor phase quartz (tridymite?) in the lithophysae, and most samples contain secondary calcite (?) cement. Lithic fragments are rare; a 1.5 mm lithic clast in one thin section was completely altered to black and retained no identifiable features.

*<sup>40</sup>Ar/<sup>39</sup>Ar geochronology:*

Plagioclase separates yielded an isochron age of  $6.1 \pm 0.3$  Ma.

*Tmr<sub>BS</sub>*

The Bighorn Sheep Tuff (*Tmr<sub>BS</sub>*) is a weakly indurated, crystal-rich, lithic-lapilli pyroclastic flow deposit. It is located in the eastern portion of the map area conformably overlying *Tmr<sub>EC</sub>* and conformably underlying either *Tmr<sub>FP</sub>*, *Tma<sub>gem</sub>*, or *Tma<sub>ugl</sub>*. The deposit is moderately welded and is usually 1-3 meters thick although it can be up to 15 meters thick. It is discontinuously preserved on the hummocky upper surface of *Tmr<sub>EC</sub>*. Weathered surfaces of *Tmr<sub>BS</sub>* are bright orange to black. The matrix of fresh samples is usually pale pink/purple or yellow, devitrified and vapor phase altered with grey, orange, or red elongate devitrified pumice making up 10-15% of the rock. A grey matrix with pale grey pumice is also common. The average length of the pumice is 1-3 cm. Feldspar phenocrysts within the matrix are not always visible in hand samples. Lithic fragments, which average 2-3 cm in length (maximum: 30 cm) and make up 1-2% of the rock, include flow-banded volcanic rocks, glassy obsidian, and very altered volcanic rock (dark grey with a red, altered matrix).

*Petrographic description:*

In thin section the welded groundmass of *Tmr<sub>BS</sub>* is microcrystalline with microphenocrysts of feldspar and Fe oxide granules. The rock is devitrified and contains vapor phase crystallization of quartz in the lithophysae. There are 5-10% phenocrysts of feldspar (plagioclase and anorthoclase (?)) > Fe oxides with trace amounts of altered mafic phenocrysts (pyroxene?).



*Tmr<sub>fp</sub>*

The densely welded, strongly indurated Flag Pole Tuff (*Tmr<sub>fp</sub>*) contains abundant, flattened, lithophysae which have the interiors weathered-out and give the deposit the appearance of being riddled with holes. It is a crystal-rich, lithic-lapilli pyroclastic flow deposit. Deposits are up to 6-7 m-thick (most commonly < 0.5 m), extremely discontinuous, and limited to the northeastern portion of the mapped area. *Tmr<sub>fp</sub>* is deposited conformably on *Tmr<sub>bs</sub>*, or *Tmr<sub>ec</sub>* in places where the former is missing, and is conformably overlain by *Tma<sub>ugt</sub>*. The unit looks very similar in outcrop appearance to tabular, PVP-capping *Tmr<sub>ec</sub>* and is the mesa-capping unit where present. At a relatively thick exposure it consists of a basal breccia (< 1 meter) overlain by 2 or 3 purple and brown glassy, crystal-poor vitrophyric layers (commonly 40-50 cm thick). This is overlain by 0.5 meters of the lithophysae-rich zone, which in turn is overlain by 2-3 meters of a stony version which is densely welded and contains ~1% altered lithophysae. In a 6-7 m-thick outcrop, the basal 4-5 meters contains abundant, elongate, lithophysae cavities below a solid, stony upper portion. The more common thinner deposits consist of ~5 cm tan, basal ash, a 10-20-cm-thick red, black, pink and brown basal vitrophyre, and up to 1 m solid, brown tuff and overlying lithophysae rich portions. The unit weathers to a dark brown color.

*Petrographic description:*

*Tmr<sub>fp</sub>* is a densely welded, devitrified tuff with 4-9% phenocrysts of plagioclase and anorthoclase feldspars > Fe oxides > orthopyroxene with trace amounts of altered olivine (?). Lithic fragments (~1%) include very altered porphyritic volcanic rocks which average 1-1.5 mm.

## Group 7 - *Tmagem*, *Tmrcañ*, *Tmaugl*, *Tmahem*

Suggested vent locations for Group 7 lava flows are shown in Figure 2.3.

### *Tmagem*

A local, ~ 625-m-elevation peak named informally here Pico de los Gemelos (location T5 in Figure 2.1) is made up of a diopside-bronzite-plagioclase-phyric andesite named the Los Gemelos Andesite (*Tmagem*). It covers ~ 1.5 km<sup>2</sup> and, as with all lithologic units in Group 7, occurs only on the eastern side of the mapped area in the vicinity of Arroyo Oculito. It is 200-250 meters thick and conformably overlies *Tmrbs*, or *Tmrec* where the former is missing. The relationship between *Tmagem* and *Tmaugl* is not clearly exposed; however, they are adjacent to each other in the field and are in the same stratigraphic position, thus they may be contemporaneous. Differences in their mineralogy suggest that they are not separate portions of the same lava flow. The base of *Tmagem* consists of a series of red, 1-2-m-thick breccia layers alternating with layers of steel-grey, 1-2 meters thick, foliated (flattened vugs), stony lava. This outcrop pattern suggests a succession of initial lava flows with autobrecciated bases which were deposited prior to the main lava flow which comprises most of *Tmagem*. Fresh hand samples of *Tmagem* have a fine-grained, purplish-grey to black matrix with flattened, sub-parallel vesicles (up to 5 mm in length). Green pyroxene phenocrysts (1-2%) are barely visible and smaller plagioclase phenocrysts (1-2%) can be seen with the aid of a hand lens.

In some localities *Tmagem* is underlain by 1-2 m of black basaltic agglutinate or spatter. The black, and occasionally red, sharp, angular clasts average 1-3 cm (maximum: 30 cm) and roughly define bedding (approximately horizontal). The matrix is minor and consists of tan ash. Lineations on some clasts supports the interpretation that they were transported through the air while still hot such as might occur during fire-fountaining. In a

few localities the agglutinate is capped by up to 4 meters of N-dipping, basaltic air fall deposit. These deposits have been mapped with *Tmagem*.

*Petrographic description:*

In thin section *Tmagem* is a seriate-textured andesite with 13-16% phenocrysts of stubby plagioclase laths (labradorite  $[\text{Ab}_{32-35}\text{An}_{64-68}\text{Or}_{0-1}]$  and bytownite  $[\text{Ab}_{20}\text{An}_{80}]$ ) > orthopyroxene (bronzite  $[(\text{Fe}^{2+}_{0.17-0.21}\text{Mg}_{0.79-0.83})\text{SiO}_3]$ ) and clinopyroxene (diopside and augite  $[(\text{Na}_{0.02}\text{Ca}_{0.79-0.83}\text{Fe}^{2+}_{0.15-0.21}\text{Mg}_{0.87-0.92}\text{Fe}^{3+}_{0.04-0.05}\text{Ti}_{0.02-0.03})(\text{Al}_{0.11-0.14}\text{Si}_{1.89-1.91})\text{O}_6]$ ) > Fe oxides. The plagioclase averages 1/4-1 mm and the pyroxenes are commonly 2 mm (maximum: 4 mm). Some samples have a trachytic texture with sub-parallel alignment of feldspar microphenocrysts in a fine-grained groundmass. The groundmass glass can be altered to red or black. The pyroxene phenocrysts are also altered around the rims and within fractures.

*<sup>40</sup>Ar/<sup>39</sup>Ar geochronology:*

Irradiated plagioclase separates did not contain enough measurable radiogenic <sup>40</sup>Ar and thus could not be used to determine a crystallization age for this unit.

*Tmr<sub>can</sub>*

The Picacho Canelo Rhyolite lava flows (*Tmr<sub>can</sub>*) as defined here are a series of plagioclase-phyric rhyolite flows which make up the local topographic peak (elevation ~ 765 meters) known as Picacho Canelo. These flow-banded lava flows should not be confused with the Tuff of El Canelo, described above. They conformably overlie *Tmagem*, or *Tmr<sub>ec</sub>* where the former is not deposited. The flows span ~460 meters in elevation. In the mapped area *Tmr<sub>can</sub>* covers 2 km<sup>2</sup>; however, it undoubtedly extends beyond the map area to the north and east.

A well-exposed basal section of *Tmr<sub>can</sub>* consists of ~1 meter of roughly laminated airfall containing rhyolite lithic fragments, pumice, and ash, overlain by 2-3 meters of an

obsidian-rich, perlitized, matrix-supported breccia. The perlite boulders average 50-80 cm within a yellow ashy matrix. The overlying solid portions of *Tmr<sub>can</sub>* are weathered dark red and flow-banded. Stratigraphically higher in the section, additional brecciated horizons occur within the unit suggesting a composite series of lava flows. These flows are grouped together as one unit based upon outcrop appearance and mineralogy. *Tmr<sub>can</sub>* consists of a partially or completely devitrified glassy matrix which is red and powdery-white with 3-4% plagioclase phenocrysts. Some portions of *Tmr<sub>can</sub>* contain small (<1 cm) spherulites.

A distinct feature within *Tmr<sub>can</sub>* is the presence of juvenile (?) and xenolithic clasts (from pebble-size to ~20 cm). Lithic clasts make up 2-3% of the unit. Folded flow structures around these clasts provide directional flow indicators.

*Petrographic description:*

*Tmr<sub>can</sub>* contains 3-8% phenocrysts of feldspar (oligoclase [ $\text{Ab}_{69-71}\text{An}_{20-22}\text{Or}_9$ ]) > Fe oxides (magnetite [ $(\text{Fe}^{2+}_{1.25}\text{Mg}_{0.04}\text{Fe}^{3+}_{1.26}\text{Al}_{0.16}\text{Ti}_{0.29})\text{O}_4$ ] and ilmenite [ $(\text{Mn}_{0.01}\text{Fe}^{2+}_{0.68}\text{Mg}_{0.03}\text{Fe}^{3+}_{0.55}\text{Ti}_{0.73})\text{O}_3$ ])  $\geq$  clinopyroxene (augite [ $(\text{Na}_{0.01-0.02}\text{Ca}_{0.84-0.87}\text{Fe}^{2+}_{0.19-0.24}\text{Mg}_{0.85-0.88}\text{Fe}^{3+}_{0.00-0.01}\text{Ti}_{0.01})(\text{Al}_{0.04-0.10}\text{Si}_{1.94-1.98})\text{O}_6$ ]) and orthopyroxene (bronzite [ $(\text{Fe}^{2+}_{0.19}\text{Mg}_{0.81})\text{SiO}_3$ ]). Notably the lava flow lacks quartz phenocrysts. The feldspars are up to 2.5 mm and are commonly mottled (glass inclusions?) and the orthopyroxene can be altered black around the rims and along fractures. The pyroxene phenocrysts are generally < 0.5 mm in size, in marked contrast to larger pyroxene phenocrysts in *Tma<sub>hem</sub>* and *Tma<sub>gem</sub>*. The unit has a cryptocrystalline to microcrystalline, seriate-textured matrix of feldspar microphenocrysts in a fine-grained, glassy groundmass. The rock is usually devitrified, and spherulitic halos are present in many of the thin sections. Secondary calcite commonly fills fractures and vugs. Also common in this unit are pockets filled with interstitial-textured needles of feldspar and needle-like mafic phenocrysts. Gabbroic xenoliths up to several cm make up < 1% of the rock and consist of labradorite [ $\text{Ab}_{31-33}\text{An}_{67-69}$ ], bronzite [ $(\text{Fe}^{2+}_{0.23-0.24}\text{Mg}_{0.76-0.77})\text{SiO}_3$ ] and minor clinopyroxene.

*<sup>40</sup>Ar/<sup>39</sup>Ar geochronology:*

Plagioclase mineral separates from two outcrops of *Tmr<sub>can</sub>* separated by about 180 meters in elevation were analyzed. One sample, from the peak of Picacho Canelo, yielded an isochron age of  $6.0 \pm 0.2$  Ma, and a stratigraphically lower sample gave an isochron age of  $5.9 \pm 0.4$  Ma.

*Tma<sub>ugl</sub>*

A steep, black, local peak is informally named here Ugly Mountain (location U6 in Figure 2.1) and is made up of a glomeroporphyritic orthopyroxene-plagioclase andesite named the Ugly Mountain Andesite (*Tma<sub>ugl</sub>*). The lava flow is  $\sim 0.5$  km<sup>2</sup> in area, is about 120 meters thick, and is located at the northeastern corner of the mapped area. It conformably overlies *Tmr<sub>fp</sub>* or *Tmr<sub>bs</sub>* where the former is missing. As described above, its relationship with nearby *Tma<sub>gem</sub>* is unclear although it is in the same stratigraphic position. *Tma<sub>ugl</sub>* has a 5-6-m-thick red (oxidized) basal breccia below the main flow. Weathered surfaces are brick red to orange. Fresh surfaces are sugary-textured and principally red (altered) glass with phenocrysts of feldspar and 1-2% clumps of black, altered minerals. Powdery white, devitrified material (calcite cement?) is common throughout the rock.

*Petrographic description:*

*Tma<sub>ugl</sub>* consists of 9-16% phenocrysts of euhedral plagioclase > orthopyroxene > Fe oxides in a microcrystalline groundmass with an intersertal texture. Glomerocrysts of all three phenocryst types are up to 5 mm but are fairly uncommon. Some of the groundmass is altered to red (in plane light), and some of the pyroxene phenocrysts have red or black altered rims. Many of the plagioclase phenocrysts are extensively mottled (glass inclusions?).

*Tmahem*

At slightly greater than 1000 meters elevation, Los Heme is the highest peak in the mapped area. It is located in the southeast, just east of the head waters of Arroyo Oculito, and rises approximately 300 meters above surrounding mesas of the PVP. The Los Heme Andesite (*Tmahem*) is a diopside-bronzite-plagioclase-phyric andesite. The circular outcrop pattern, which covers roughly 4 km<sup>2</sup> in map view, resembles a solid volcanic neck or plug, and consists of sheer vertical cliffs on most sides. *Tmahem* unconformably overlies Group 2 (*Tmvs*) and Group 6 (*Tmr3* and *Tmr<sub>ec</sub>*) rocks. Thickness varies from about 300 meters on the southwest side to about 500 meters on the northwest side. The eastern portions of *Tmahem* were not mapped in this study. The lava flow is 6 km away from the other two andesite flows within Group 7, but since it is in the same stratigraphic position as the others and is petrographically identical to *Tmagem*, it is tentatively correlated to that Group. *Tmahem* has a thick (up to tens of meters), sub-horizontal basal breccia which is well-exposed in Arroyo Oculito. Hand samples are typically steel grey with marbled pink patches on fresh surfaces; plagioclase phenocrysts are easily discernible and pyroxene phenocrysts, commonly up to 5 mm, are clearly visible in hand specimens and have a characteristic green color.

*Petrographic description:*

*Tmahem* is an intersertal-textured andesite with 10-30% euhedral to subhedral phenocrysts of plagioclase (labradorite [Ab<sub>37-38</sub>An<sub>61-62</sub>Or<sub>1</sub>] and bytownite [Ab<sub>16</sub>An<sub>84</sub>]) > orthopyroxene (bronzite [(Fe<sup>2+</sup><sub>0.17-0.29</sub>Mg<sub>0.71-0.83</sub>)SiO<sub>3</sub>] > clinopyroxene (diopside [(Na<sub>0.02</sub>Ca<sub>0.85-0.87</sub>Fe<sup>2+</sup><sub>0.12-0.14</sub>Mg<sub>0.91-0.93</sub>Fe<sup>3+</sup><sub>0.02-0.03</sub>Ti<sub>0.01</sub>)(Al<sub>0.09-0.10</sub>Si<sub>1.94-1.95</sub>)O<sub>6</sub>]). The groundmass consists of microphenocrysts of feldspar and interstitial glass. The clinopyroxene and orthopyroxene phenocrysts make up one-third of the phenocrysts and in many cases the largest phenocrysts (up to 5 mm) appear to be composites of several grains. A pumiceous, pyroclastic version of *Tmahem* found among the float on the southern slope of Los Heme contains the same distinct, green, pyroxene phenocrysts and shows the same mineralogy in thin section with 8-

12% phenocrysts. Some of the plagioclase phenocrysts in this pumiceous rock are severely embayed.

*<sup>40</sup>Ar/<sup>39</sup>Ar geochronology:*

Irradiated plagioclase separates did not contain enough measurable radiogenic <sup>40</sup>Ar and thus could not be used to determine a crystallization age for *Tmahem*.

2.5. *Regional lithologic correlations*

Groups 2 and 3

*Tmvs*

Andesite-bearing, volcanoclastic deposits similar to those found in the Santa Isabel Wash and Arroyo Oculito regions (*Tmvs* of Group 2) exist along most of the eastern side of the Baja California peninsula. These deposits are interpreted to be the alluvial aprons shed from the Miocene, subduction-related, andesitic magmatic arc.

Dissected remnants of the arc are preserved on the eastern margin of Baja California Sur and, less continuously, in northern Baja California, on the northwest coast of Sonora, and on islands within the Gulf of California (Rossetter, 1973; Gastil and Krummenacher, 1977; Gastil et al., 1979; Hausback, 1984; Neuhaus et al., 1988; Sawlan, 1991; Martín-Barajas et al., 1995). A hornblende andesite belt in Baja California Sur, interpreted to be part of the core of the volcanic arc, spans 22-18 Ma (Gastil et al., 1979; Hausback, 1984). Dated, pre-rift, andesitic volcanism spans ~20-15 Ma in northern Baja California (Barnard, 1968; Gastil et al., 1979; Martín-Barajas et al., 1995; Lee et al., 1996) [Footnote: Barnard (1968) lists a biotite age of  $15.3 \pm 0.8$  Ma which Gastil and others (1979) list as a whole rock age of  $15.0 \pm 2.0$  Ma], 21-18 Ma (but including one  $14.0 \pm 3.0$  Ma age) along the northwestern margin of Sonora (Gastil and Krummenacher, 1977), and spans 15-23 Ma on Isla Tiburón (Gastil and Krummenacher, 1977; Neuhaus et al., 1988; Neuhaus, 1989). Note that these are crystallization ages of andesitic vents or core facies and not ages of deposition of the

volcaniclastic deposits in which the clasts are found. Clearly, however, they provide a constraint on the upper ages of such deposits.

Andesitic vents south of Mesa Cuadrada (Stock et al., 1991; Stock, pers. comm.) which are 17-20 Ma are probably the closest vent facies to the study area (~10 km northwest of Santa Isabel Wash). Another remnant, andesitic lava close to the Santa Isabel Wash region which could be a source for *Tmvs* is located in Arroyo Los Heme ~ 25 km to the southeast of the mapped area. The 4-km-diameter volcanic center is labeled Tma by Martín-Barajas and others (1995), consists of 400-m-high volcanic necks and surrounding epiclastic deposits, and yields  $^{40}\text{Ar}/^{39}\text{Ar}$  ages of  $15.9 \pm 0.2$  and  $16.3 \pm 0.1$  Ma. (As discussed below, an alternative possibility is that Tma is coeval with the more proximal *Tmd<sub>tomb</sub>* facies, which postdates *Tmvs* deposition in Santa Isabel Wash.) Other peaks composed of Miocene andesite to the west of the Santa Isabel Wash area such as Pico Matomí (20 km to the west) (Gastil et al., 1971, 1975) are candidates as well. Still others may have been eroded and/or buried by later volcanism associated with the development of the PVP.

Deposits of the volcaniclastic aprons to the west of this ancient arc are far more voluminous than remnants of the arc itself. They consist of both proximal and distal (deposited further west) facies; however, since the deposits examined in this study (*Tmvs*) are clearly proximal, the remaining discussion will be confined to similar, proximal facies found in other locations. In Baja California Sur, these deposits are part of the Miocene Comondú Formation as redefined by Hausback (1984). The proximal deposits are up to 600 meters thick (San Juan de la Costa area) and are continuously exposed from La Paz north to the 28th parallel in a 10-40-km-wide swath. In northern Baja California, less continuous exposures of similar, proximal deposits are up to 250 m thick in the southern Valle Chico (Stock, 1989), up to 200 m thick in the Sierra San Fermín (Lewis, 1994), and up to 75 m thick in north central Baja California (specifically, about 60 km due south of the town of Puertecitos) (Dorsey and Burns, 1994). Dorsey and Burns (1994) also show that deposits thicken from west to east across the Baja California peninsula.

One stratigraphic difference between all three of these localities in northern Baja California and the deposits preserved in Santa Isabel Wash is the absence of any underlying



nonmarine sedimentary deposits between the volcaniclastic deposits and underlying basement rocks in Santa Isabel Wash. Such underlying deposits are up to ~ 200 m thick in north central Baja California (Mesa Formation of Dorsey and Burns, 1994), from 0 to 70 m thick in the southern Valle Chico ( $T_c$  and  $T_s$  of Stock, 1989), and up to 100 m thick in the Sierra San Fermín ( $T_s$  of Lewis, 1996). The deposition of this unit is interpreted to be the result of a combination of regional, base level rise related to isostatic uplift of previously thickened arc crust and thermal subsidence which resulted in a regional transgression (Dorsey and Burns, 1994). The absence of such deposits in the one basement exposure in Santa Isabel Wash suggests that this exposure was probably a topographically high point around which the later units filled.

The age of the Comondú Formation in Baja California Sur is generally between 25 and 15 Ma (Gastil et al., 1979; Hausback, 1984) although andesite flows as young as 12.5 Ma which unconformably cap the formation in the northern part of Baja California Sur are included in the formation (Hausback, 1984). In northern Baja California the ages of these deposits are slightly younger, ranging from 16.7-12.7 Ma in the southern Valle Chico (Stock, 1989), between 21.2 and 11 Ma (but maybe 12.5 Ma; see Chapter III for discussion of revised geochronology for  $T_{mr,sp}$ ) in the Sierra San Fermín (Lewis, 1996), 17-16 Ma in the Sierra Juarez (Lee et al., 1996), and 20-15 Ma in various localities north of these regions (Gastil et al., 1979). Deposits in Sonora are between 21 and 14 Ma (Gastil and Krummenacher, 1977) and within the gulf on Isla Tiburón are ~23 Ma (Gastil and Krummenacher, 1977).

As determined in this study,  $T_{mvs}$  of the Santa Isabel Wash region is up to 500 meters thick and was deposited prior to 17 Ma. This thickness is on the high side given the thickness of similar deposits in some of the other areas discussed above, and suggests that perhaps the Santa Isabel Wash region was closer to one or more andesitic volcanoes than the areas 20-30 km to the north. Alternatively, local subsidence could explain the thicker deposits. The pre-17 Ma age determined in this study overlaps with other ages of deposition in most of the localities discussed above with the potential exception of the southern Valle Chico where deposition primarily occurred later. In general it appears that the deposition of  $T_{mvs}$  in the

Santa Isabel Wash region ended earlier than in most other nearby regions and was replaced by the deposition of near-source-facies volcanism ( $Tmd_{tomb}$ , discussed below).

### *Tmr<sub>bio</sub>*

On the basis of thin section examination, *Tmr<sub>bio</sub>* (in Group 2 of this study) is probably correlative with one of the biotite-bearing tuffs of Toronja Hill in Arroyo Matomí south of the Sierra San Felipe (Stock, 1989). *Tmr<sub>bio</sub>* is deposited upon *Tmvs* in Santa Isabel Wash, while the tuffs of Toronja Hill overlie Stock's *Tmvs* (15-17 Ma volcanic breccias interpreted to be the proximal facies of the intermediate *Tmvs* facies). This suggests that prior to 17 Ma, Santa Isabel Wash was at a position farther from the source area of the volcanoclastic breccias than the region a few km to the north.

### *Tmd<sub>tomb</sub>*

The deposition of the voluminous, 15.5-17 Ma dacite lava flows of Group 3 (*Tmd<sub>tomb</sub>*) postdates *Tmvs* deposition in Santa Isabel Wash based upon stratigraphic relationships. These extensive, brecciated lava flows do not appear to have correlatives in nearby areas such as the southern Valle Chico (Stock, 1989), the Sierra San Fermín or the southern Sierra San Felipe (Lewis, 1996). On the basis of age constraints on *Tmvs* deposition in Santa Isabel Wash and nearby localities, these dacite flows were probably extruded in the study area synchronously with *Tmvs* deposition in the north (e.g., southern Valle Chico), and again may illustrate lateral facies change between more proximal and distal deposits. The andesite and dacite complex in the eastern PVP mentioned above as a potential source of *Tmvs* deposits (ages of  $15.9 \pm 0.2$  and  $16.3 \pm 0.1$  Ma.) and labeled Tma (Martín-Barajas and Stock, 1993; Martín-Barajas et al., 1995) covers  $\sim 15$  km<sup>2</sup> and could in fact be contemporaneous with *Tmd<sub>tomb</sub>* volcanism instead of preceding it.

Groups 4 and 5*Tmr<sub>sf</sub>*

The middle Miocene Tuff of San Felipe (*Tmr<sub>sf</sub>*) is a new name suggested by Stock and others (1996; 1997b) for a pyroclastic flow deposit (Group 4 in this study) which has been previously referred to as Tmr1 in the Santa Rosa basin (Bryant, 1986), southern Valle Chico, southern Sierra San Felipe (Stock, 1989; Stock and Hodges, 1990), and the Sierra San Fermín (Lewis, 1996). It is an important ash-flow tuff in northeastern Baja California because of its unique age within the regional volcanic stratigraphy and its widespread occurrence. Its distinct brown and black basal vitrophyre and the presence of well-formed anorthoclase phenocrysts facilitate identification in the field.

*Tmr<sub>sf</sub>* is up to 30 m thick in the southern Valle Chico (Stock, 1989), typically 20 m thick in the Sierra San Fermín (Lewis, 1996), up to 80 m thick in the Cañon El Parral region of the southern Sierra San Felipe (Lewis, 1996), and up to 60 m thick in the Santa Rosa Basin (Bryant, 1986). The source is believed to lie below modern alluvium in the Llanos de San Fermín between the northern portion of the Sierra San Fermín and the Cañon El Parral region of the southern Sierra San Felipe (Lewis, 1996). As described above, *Tmr<sub>sf</sub>* is commonly 5-15 m thick, but up to 40 m thick, in Santa Isabel Wash. From base to top, *Tmr<sub>sf</sub>* generally consists of up to 50 cm of white, pumice-bearing (or grey, lithic) ash, a 1-m-thick, brown, basal vitrophyre grading up into a black vitrophyre of similar thickness, and a spherulitic horizon which grades up from the black vitrophyre into densely welded, red to pink, lithophysae-rich rhyolite. In Santa Isabel Wash the upper portion (3-5 m) of the tuff is less densely welded, devitrified, and weathers to a sky-blue color.

Slight variations in mineralogy found between different regions include the presence of plagioclase and augite in exposures from the southern Valle Chico (Stock, 1989), the Sierra San Fermín, and southern Sierra San Felipe (Lewis, 1996) but not in the Santa Isabel Wash region. However, lithic clasts within *Tmr<sub>sf</sub>* found in this study include andesite with hornblende, pyroxene and plagioclase phenocrysts, thus these lithic fragments could be a

source for the plagioclase and augite phenocrysts (which would make them xenocrysts) in the other areas. Electron microprobe results on anorthoclase separates are somewhat varied between samples from Santa Isabel Wash (two populations:  $\text{Ab}_{56}\text{An}_3\text{Or}_{41}$  and  $\text{Ab}_{66-68}\text{An}_{5-6}\text{Or}_{26-28}$ ), the Sierra San Fermín ( $\text{Ab}_{63-65}\text{An}_{1-5}\text{Or}_{30-36}$ ) (Lewis, 1996), the southern Valle Chico ( $\text{Ab}_{63}\text{An}_{10}\text{Or}_{27}$ ) (Stock, 1989), and the Santa Rosa Basin (three populations:  $\text{Ab}_{65}\text{An}_5\text{Or}_{30}$ ,  $\text{Ab}_{58}\text{An}_{17}\text{Or}_{25}$ , and  $\text{Ab}_{47-57}\text{An}_{3-4}\text{Or}_{40-49}$ ). In summary, the total range is  $\text{Ab}_{47-68}\text{An}_{1-17}\text{Or}_{25-49}$ . Although sanidine is more commonly associated with calc-alkalic volcanism than anorthoclase (which is a more common phenocryst in trachytes) (Fisher and Schmincke, 1984), the compositions determined here fall within the anorthoclase field.

Seven age determinations on anorthoclase crystals from *Tmr<sub>Sf</sub>* have been performed with K/Ar and  $^{40}\text{Ar}/^{39}\text{Ar}$  geochronology from these various regions by several different workers (Gastil et al., 1979; Stock, 1989; Lewis 1996; Stock et al., 1997b.; this study). Chapter III gives a complete discussion of the discrepancies between these various studies and also presents the new results from Santa Isabel Wash. To summarize, the ages are  $11.99 \pm 0.50$  Ma and  $10.85 \pm 0.32$  Ma in the southern Valle Chico (Stock, 1989),  $10.6 \pm 0.1$  Ma and  $13.0 \pm 2.0$  Ma in the Sierra San Fermín (Lewis, 1996),  $12.7 \pm 0.3$  Ma in Santa Isabel Wash (this study), and two different ages from Santa Rosa Basin of  $12.53 \pm 0.15$  Ma (Stock et al., 1997b) and  $14.2 \pm 0.9$  Ma (Gastil et al., 1979). The most likely age is presently considered to be about 12.5 Ma. An  $11.2 \pm 1.3$  Ma rhyolite ignimbrite on southwest Isla Tiburón (Gastil and Krummenacher, 1977) might be correlative to *Tmr<sub>Sf</sub>*. This ignimbrite is called Unit 8 by Neuhaus (1989) who describes it as up to 45 m thick and consisting of up to 20% phenocrysts of sanidine, ferro-augite, hornblende, biotite, hypersthene, and plagioclase. Only the presence of biotite makes the mineralogy of Unit 8 on Isla Tiburón different from that of *Tmr<sub>Sf</sub>*. If so, this would be an important constraint on pre-extension paleogeography of this part of the Gulf of California.

*Tma<sub>toro</sub>*

The only other evidence for volcanism in the Santa Isabel Wash area between about 15.5 and 6 Ma besides *Tmr<sub>sf</sub>* is the  $9.3 \pm 0.4$  Ma *Tma<sub>toro</sub>*. This local andesite is interpreted to be post-subduction volcanism based upon its age but also upon criteria discussed by Sawlan (1991) distinguishing subduction-related and post-subduction andesites such as its association with silicic rocks and its isolated, small-volume outcrop nature. This hornblende-phyric andesite has the same mineralogy and is in the same stratigraphic position as unit Tma from the Sierra San Fermín (Lewis, 1996) although an older age ( $11.8 \pm 0.7$  Ma) was determined for that unit in that study (whole rock,  $^{40}\text{Ar}/^{39}\text{Ar}$ ). *Tma<sub>toro</sub>* is also similar in mineralogy and stratigraphic position to Ma2 from the southern Valle Chico (Stock, 1989). This particular unit was not dated. Other andesites which are potentially synchronous with *Tma<sub>toro</sub>* volcanism include a  $8.9 \pm 0.6$  Ma andesite (K/Ar age for hornblende) in the northern Sierra Pinta (McEldowney, 1970; Gastil and others, 1979), a  $15.3 \pm 1.3$  Ma (hornblende age) or  $10.9 \pm 2.3$  Ma (plagioclase age) andesite on Isla Tiburón (Gastil and Krummenacher, 1977), a  $9.9 \pm 1.3$  Ma andesite on Isla Tiburón (Gastil and Krummenacher, 1977), an  $11.3 \pm 1.2$  Ma andesite in western Sonora (Gastil and Krummenacher, 1977), and a  $12.3 \pm 2.9$  Ma andesite northwest of Rancho Buenas Noches in Sonora (Gastil and Krummenacher, 1977).

Group 6

Preferred correlations between the pyroclastic flow deposits of Group 6 and those from nearby localities are presented here based upon comparisons of field descriptions, stratigraphic position, mineralogy, geochronology, and paleomagnetic analyses from several studies. In some cases a lithologic unit defined in one study might be subdivided in another study. Stratigraphic columns showing the preferred correlations with Group 6 rocks and units from other locations are shown in Figure 2.4. The locations of source vents, or calderas, are relatively unknown and are generally inferred to be submerged within the gulf.

*Tmr<sub>siw</sub>*

The oldest pyroclastic flow deposits included in Group 6 (Tuffs of Santa Isabel Wash - *Tmr<sub>siw</sub>*) are in the same stratigraphic position as the Tuffs of Matomí first defined in the southern Valle Chico (Stock, 1989), although field and petrographic descriptions suggest that they are not the same lithologic unit. For example, the Tuffs of Matomí generally contain biotite (Appendix A1 of Stock, 1989), which is characteristically absent from *Tmr<sub>siw</sub>*, and the Tuffs of Matomí are generally white and consist of at least eight individual units. On the other hand, the lithologic description of Tmr3a in the El Coloradito section of the Sierra San Fermín (Appendix C of Lewis, 1996), which is correlated to the uppermost Tuffs of Matomí in that study, includes several features that are similar to those observed for *Tmr<sub>siw</sub>* (although Tmr3a is only one cooling unit as opposed to the series seen in Santa Isabel Wash). Nonetheless, similarities include an upwards grading in color from yellow to orange to reddish brown to dark red (equivalent to *t2* through *t5* of *Tmr<sub>siw</sub>*?), a central, dark red, crystal-rich, densely welded, devitrified zone (equivalent to *t4* or *t5* of *Tmr<sub>siw</sub>*?), several lithic-rich zones (as described for *t2* and *t4* of *Tmr<sub>siw</sub>*?), and an upper bedded tephra layer (equivalent to uppermost *t5* of *Tmr<sub>siw</sub>*?). Tmr3a contains 5-11% phenocrysts of feldspar (mostly anorthoclase?), 3% Fe oxides, < 1% quartz, clinopyroxene, and magnetite, and trace amounts of basaltic hornblende, biotite, epidote, and zircon (Lewis, 1994). The lack of olivine or orthopyroxene and the presence of epidote, hornblende, and biotite make the phenocryst assemblage for Tmr3a different from that of *Tmr<sub>siw</sub>*.

Paleomagnetic declination and inclination values measured in *Tmr<sub>siw</sub>* from Santa Isabel Wash (Chapter V) are different from those measured in Tmr3a in the Sierra San Fermín and Mesa Cuadrada (Lewis and Stock, 1996). This could indicate that the units were not deposited at the same time (and thus are not coeval) or that relative, post-depositional rotations of one lithologic unit have occurred between these sites. If the latter were the case, and tilt-corrections were properly applied (and assuming vertical-axis rotations), the inclination values should be fairly consistent in any given ash-flow tuff regardless of where it

is sampled. Inclination values measured in Tmr3a on Mesa Cuadrada and site sfb in the Sierra San Fermín are 10-15° different from the value recorded in *Tmr<sub>siw</sub>*, and sites sfh and sfi in the Sierra San Fermín are between 5-10° from those within *Tmr<sub>siw</sub>* (Lewis and Stock, 1996; Chapter V). With the exception of site sfb, all of these values overlap within the 95% confidence limits and do not refute lithologic correlation between Tmr3a and *Tmr<sub>siw</sub>*. However, based primarily upon differences in mineralogy described above, and correlations between the Tuffs of Matomí and the unit which stratigraphically overlies *Tmr<sub>siw</sub>* (discussed next), *Tmr<sub>siw</sub>* is interpreted to be a unique package of pyroclastic flow deposits within the Santa Isabel Wash region which was not deposited in the southern Valle Chico to the northwest, the Sierra San Felipe to the north, or the Sierra San Fermín to the northeast.

### *Tmr3*

On the basis of field appearance, the lower 1 to 3 cooling units which comprise *Tmr3* in Santa Isabel Wash (four are discussed in this study) are likely to be correlative to the uppermost Tuffs of Matomí defined in the southern Valle Chico (J. Stock, pers. comm., 1996). The uppermost 1 to 3 cooling units of *Tmr3* from Santa Isabel Wash (*type II*) are probably correlative to Tmr3 as defined in the southern Valle Chico and on Mesa Cuadrada (Stock, 1989), which was renamed Tmr3b in the Sierra San Fermín and Mesa Cuadrada (Lewis, 1996; Lewis and Stock, in review in *Geophys. J. Res.*) (Figure 2.4). Geochronology (listed in Figure 2.4; see also Chapter III and Table 3.4), outcrop appearance, petrography and electron microprobe analyses of anorthoclase separates from all of these localities support these correlations. Phenocryst assemblages vary from 10% (anorthoclase >> augite > quartz > opaques > biotite) in the southern Valle Chico (Stock, 1989) to 9-15% (anorthoclase > plagioclase > quartz; < 1% augite) in the Sierra San Fermín (Lewis, 1996) to 5-15% (anorthoclase >> quartz > trace orthopyroxene and Fe oxides ± trace olivine ± trace hornblende ± trace plagioclase) in the Santa Isabel Wash. One difference is the general absence of plagioclase phenocrysts in *Tmr3* examined in this study but the presence of such phenocrysts in the Sierra San Fermín (Lewis, 1996). Plagioclase-bearing lithic fragments such

as granite within the *Tmr3* deposits examined in this study could be the source of these minerals in the Sierra San Fermín (thus making them xenocrysts).

Although these lithologic correlations seem robust, there is a discrepancy between the paleomagnetic declination values measured within the various *Tmr3* cooling units at different localities which cannot be modeled by simple rotational deformation between sampling sites (inclination values are in general agreement). In Santa Isabel Wash (Chapter V) the same paleomagnetic vector direction has been measured in the upper 3 cooling units (*Tmr3 (type II)*): Dec = 28.5°, Inc = 54.2°,  $\alpha_{95}$  = 2.5°, n = 58, 6 sites) while the lowest cooling unit records a significantly different declination direction (*Tmr3 (type I)*): Dec = 322.7°, Inc = 59.6°,  $\alpha_{95}$  = 6.9°, n=20, 3 sites). If the upper cooling units (*Tmr3 (type II)*) are equivalent to Tmr3b of Lewis and Stock (1996), it implies that the Sierra San Fermín has rotated CW relative to Santa Isabel Wash while Mesa Cuadrada has rotated CCW relative to both the Sierra San Fermín and Santa Isabel Wash. In contrast, paleomagnetic results from the underlying sampled tuffs (*Tmr3 (type I)* in Santa Isabel Wash and Tmr3a in the other localities) imply CW rotation of both of these regions relative to Santa Isabel Wash.

A possible solution to this problem involves changing the lithologic correlations between Mesa Cuadrada and the Sierra San Fermín which are used by Lewis and Stock (1996). Given that *Tmr3 (type I)* is confined to the northwest portion of the Santa Isabel Wash region, which is ~10 km due south of Mesa Cuadrada in contrast to 20-30 km southwest of the Sierra San Fermín, it is possible that the unit on Mesa Cuadrada called Tmr3b by Lewis and Stock (1996) is not actually the same cooling unit as the one preserved in the Sierra San Fermín and labeled Tmr3b. Given the similar field appearances of the four *Tmr3* cooling units described in this study, this confusion is certainly possible. If Tmr3b on Mesa Cuadrada is equivalent to *Tmr3 (type I)* of this study, it conveniently eliminates the paleomagnetic discrepancy by implying that Mesa Cuadrada has rotated CW, and not CCW, relative to Santa Isabel Wash. This result then agrees with paleomagnetic results from overlying *Tmr4* (discussed next). Chapter V presents the details of the paleomagnetic results and discusses the implications of each of these possible lithologic correlations.



To summarize, the uppermost Tuffs of Matomí defined in the southern Valle Chico and Mesa Cuadrada by Stock (1989) (Tmmt) are considered equivalent to Tmr3a on Mesa Cuadrada as divided by Lewis (1994) and Lewis and Stock (in review in J. Geophys. Res.) as well as to Tmr3a in the Sierra San Fermín (Lewis, 1994, 1996; Lewis and Stock, in review in J. Geophys. Res.). *Tmr3 (type I)* in Santa Isabel Wash may be equivalent to Tmmt as initially described by Stock (pers. comm., 1996), or they may in fact be unique to the Santa Isabel Wash region. They are most likely not equivalent to any unit labeled Tmr3a. *Tmr3 (type II)* in Santa Isabel Wash is probably equivalent to Tmr3b in the Sierra San Fermín (Lewis, 1994, 1996) and Mesa Cuadrada (as divided by Lewis and Stock, in review in J. Geophys. Res.) as well as Tmr3 in southern Valle Chico and Mesa Cuadrada by Stock (1989).

#### *Tmr3-4* and *Tmr4*

Comparisons of outcrop and hand sample appearances and petrographic examination imply that *Tmr3-4* of Santa Isabel Wash is the same unit as t2l just south of Arroyo Matomí (~8 km north of Santa Isabel Wash) and that overlying *Tmr4* of Santa Isabel Wash is the same unit as overlying t2u at the same locality (Stock et al., 1991; Stock, unpub. mapping). In addition to descriptions given by Stock (unpub. mapping), samples from south of Arroyo Matomí were collected in this study and cut into thin sections for comparison with units in Santa Isabel Wash. Note that the t2 units are part of the Mpru (Group 5) lithologic unit defined by Stock (1989; 1993).

Field appearance and petrography strongly suggest that *Tmr4* is also equivalent to Tmr4 in the southern Valle Chico, the southern Sierra San Felipe (Stock, 1989), and the Sierra San Fermín (Lewis, 1994; 1996) although biotite phenocrysts identified in both of those studies were not observed in the Santa Isabel Wash exposures. Lithologic correlations between the various localities are very convincing for the distinctive *Tmr4* ash-flow tuff, and thus interpretations based upon paleomagnetic results from this unit are considered to be the most reliable. Paleomagnetic analyses in *Tmr4* imply that at least parts of the Sierra San Fermín have rotated CW relative to Santa Isabel Wash since its deposition. See Chapter V for full discussion of paleomagnetic results.

*Tmr<sub>ao</sub>*

Crystal-poor *Tmr<sub>ao</sub>* is in the same stratigraphic position as t14 in the Mesa El Tábano area (Stock et al., 1991) which is described as extremely crystal-poor with rare plagioclase phenocrysts. In that study t14 is the lowest of three lithologic units which comprise the Tuff of El Canelo and is described as a light pink, lithic-lapilli tuff which is non-welded, altered, and devitrified. Both the field descriptions and mineralogy seem to agree between t14 and *Tmr<sub>ao</sub>*. This tuff could also be correlative with the light purple, extensively devitrified *Tmr5* in the Sierra San Fermín (Lewis, 1994; 1996) which generally contains < 6% feldspar, 1-2% Fe oxides, and trace amounts of clinopyroxene. Finally, *Tmr<sub>ao</sub>* could also be correlative with the 10-15-m-thick, unwelded lithic tuff deposit *Tmc5* (within the unit labeled *Tmc(1-6)* in Figure 2.4) within the Tuff of El Canelo in Arroyo La Cantera of the northeastern PVP (Martín-Barajas et al., 1995).

*Tmr<sub>ec</sub>*

The Tuff of El Canelo (labeled *Tmr<sub>ec</sub>* in this study but also referred to in previous studies as *Tmec* (Lewis, 1996), t9-t12-t14 (Stock et al., 1991), and *Tmc1-Tmc6* (Martín-Barajas et al., 1995)) is one of the better studied pyroclastic flow deposits in this region. Correlations are primarily supported by similar phenocryst content and outcrop appearances from the various localities. Because the stratigraphy in the Santa Isabel Wash and Arroyo Oculito regions is a more complete section than has been preserved in adjacent areas, correlations made in this study are able to accurately place *Tmr<sub>ec</sub>* within the regional stratigraphic sequence for the first time (i.e., relative to other 6 Ma units such as *Tmr3* and *Tmr4*). *Tmr<sub>ec</sub>* is interpreted here to be equivalent with t3 of Arroyo Matomí (Stock et al., 1991), and with other deposits previously identified as the Tuff of El Canelo, including t12, and possibly t9, of Mesa El Tábano (Stock et al., 1991) as well as with *Tmc6* (the uppermost of six cooling units which comprise the Tuff of El Canelo in that region) in the northeastern PVP (specifically Arroyo La Cantera) (Martín-Barajas et al., 1995). (Note that t3 in Arroyo

Matomí is also part of the Mpru (Group 5) lithologic unit defined by Stock (1989; 1993)). The basal unit in Arroyo La Cantera (Tmc1) yielded a  $^{40}\text{Ar}/^{39}\text{Ar}$  age of  $6.44 \pm 0.02$  Ma (Martín-Barajas et al., 1995) which is not inconsistent, within uncertainties, with the  $6.1 \pm 0.3$  Ma age for  $Tmr_{ec}$  determined in this study nor the dates determined here for underlying tuffs  $Tmr_3$  and  $Tmr_{siw}$ . Lewis (1996) suggests that the Tuffs of Dead Battery Canyon in the Sierra San Fermín (Tmr5-Tmr8) may be correlative to the Tuff of El Canelo. The presence of oligoclase [ $\text{Ab}_{73}\text{An}_{19}\text{Or}_7$ ] in unit Tmr7 from that study agrees with microprobe results from this study, and a  $^{40}\text{Ar}/^{39}\text{Ar}$  age of  $6.4 \pm 0.3$  Ma also supports the correlation. Field observations suggest that the vent for the Tuff of El Canelo may have been located south of the Sierra San Fermín in the vicinity of Arroyo Matomí and Arroyo El Canelo (3-4 km south of Arroyo Matomí) (Martín-Barajas et al., 1995; Lewis, 1996).

#### *Tmr<sub>bs</sub>*

It is possible that the  $Tmr_{bs}$  is the same as the upper unit (t9) of the Tuff of El Canelo as described in the Mesa El Tábano region (Stock et al., 1991). Both units contain around 10% feldspar and Fe oxide phenocrysts, are moderately welded, weather to an orange color, and contain pumice and volcanic lithic fragments.

#### Group 7

Because lava flows are less regionally distributed than pyroclastic flow deposits, regional correlations between units from Group 7 of this study and those described by others are made with the assumption that the various lava flows are coeval, but not necessarily the exact same unit as was inferred for Group 6 ash-flow tuffs. Because the stratigraphic position is not constrained by overlying units for two of the andesite flows in this study ( $Tma_{ugl}$  and  $Tma_{hem}$ ), their position relative to the other units is ambiguous, as depicted in Figure 2.5.

*Tma<sub>gem</sub>*, *Tma<sub>ugl</sub>*, and *Tma<sub>hem</sub>*

Nearby andesitic volcanism which might be coeval with the three andesite flows of Group 7 near Arroyo Oculito (*Tma<sub>gem</sub>*, *Tma<sub>ugl</sub>*, and *Tma<sub>hem</sub>*) includes several hundred meters of flows in the southeastern Sierra San Fermín (Tpa of Lewis, 1996). Tpa contains up to 25% phenocrysts of plagioclase >> alkali feldspar > hypersthene > augite >> magnetite and other Fe oxides >> biotite with glomeroporphyritic masses of plagioclase and pyroxene (Lewis, 1994). This differs mineralogically from the three andesite flows in this study primarily by the presence of alkali feldspar and biotite; glomerocrysts were noted only in *Tma<sub>ugl</sub>*. The Tpa andesite and debris flows yield a whole rock  $^{40}\text{Ar}/^{39}\text{Ar}$  age of  $5.7 \pm 0.2$  Ma (Lewis, 1996); however, field relationships indicate that they overlie the 3 Ma Tuffs of Mesa El Tábano in the southeastern Sierra San Fermín, and thus Tpa is interpreted to be younger than 3 Ma (Lewis, 1996). Interestingly, Tpa had very low yields of radiogenic argon (Lewis, 1996) as did the two andesite samples unsuccessfully measured in this study (*Tma<sub>gem</sub>* and *Tma<sub>hem</sub>*) (see Chapter III). Lewis (1996) interprets Tpa to be coeval with a  $0.9 \pm 0.6$  Ma olivine-bearing basalt (or basaltic andesite) in Arroyo Matomí (Mb6 of Stock et al., 1991; age given by Martín-Barajas et al., 1995).

Since Tpa is < 3 Ma, it cannot be coeval with *Tma<sub>gem</sub>* which is overlain by 6 Ma *Tmr<sub>can</sub>*. Although *Tma<sub>ugl</sub>* and *Tma<sub>hem</sub>* are petrographically similar to *Tma<sub>gem</sub>*, it is possible that they are significantly younger and potentially correlative with Tpa since they are not overlain by any other units such as is the case with *Tma<sub>gem</sub>*. A more likely correlative deposit is an andesitic dike and associated basaltic andesite lava flow in Arroyo Los Heme which yields a whole rock  $^{40}\text{Ar}/^{39}\text{Ar}$  age of  $5.1 \pm 0.3$  Ma and contains 10-50% microphenocrysts of plagioclase (labradorite cores and andesine rims), clinopyroxene (augite), and orthopyroxene (bronzite) (Tba of Martín-Barajas et al., 1995). This is mineralogically similar to all three of the Group 7 andesite flows (*Tma<sub>gem</sub>*, *Tma<sub>ugl</sub>*, and *Tma<sub>hem</sub>*). Its age is also in better agreement with the 6 Ma age inferred for *Tma<sub>gem</sub>*.

*Tmr<sub>can</sub>*

The basal, ashy, perlite-bearing breccia and overlying solid portions of the Picacho Canelo rhyolite lava flows (*Tmr<sub>can</sub>*) described in this study are very similar in character to rhyolite flows examined in the southeastern Sierra San Fermín (*Tmr9* of Lewis, 1994; 1996). These flows are located about 10 km northeast of Picacho Canelo. Lewis (1994) describes “a basal block and ash layer containing [sic] dark grey to black perlite and yellow-weathering ash” grading up into “a welded breccia of dark red, devitrified, and flow-foliated rhyolite” overlain by 20-200 m of “dark reddish-purple or purple and white banded, flow-foliated, largely devitrified rhyolite.” These features are similar to those of *Tmr<sub>can</sub>* mapped in this study, although undoubtedly they are fairly common characteristics of rhyolitic lava flows in general. *Tmr9* contains < 1% phenocrysts of plagioclase and Fe oxides and trace amounts of orthopyroxene, clinopyroxene, and alkali feldspar (Lewis, 1994) whereas *Tmr<sub>can</sub>* contains 3-8% phenocrysts of oligoclase > magnetite and ilmenite ≥ clinopyroxene (augite) and orthopyroxene (bronzite). Neither of these rhyolite flows contains quartz phenocrysts. Except for the quantity of phenocrysts, the mineralogy is fairly similar between these two lava flows. Stratigraphically they both overlie ash-flow tuffs interpreted to be equivalent to *Tmr<sub>ec</sub>*. A range of 6-8 Ma is assigned to the *Tmr9* rhyolite domes in the southern Sierra San Fermín (Lewis, 1996) which is in agreement with geochronology determined in this study (Chapter III) for *Tmr<sub>can</sub>* ( $5.9 \pm 0.4$  Ma;  $6.0 \pm 0.2$  Ma).

Lewis (1996) interprets the *Tmr9* lava flows to be coeval with rhyolite/dacite flows designated f4 in Arroyo Matomí (Stock et al., 1991) which is located roughly half the distance between Picacho Canelo and the lavas in the southern Sierra San Fermín. These flows contain feldspar >> opaques = clinopyroxene >> hornblende (Stock et al., 1991) and thus their mineralogy differs only in the presence of trace hornblende from the lavas described above. The f4 flows are in the same stratigraphic position as *Tmr<sub>can</sub>* (i.e., overlying *Tmr<sub>ec</sub>*). Unpublished mapping (Stock; see also Stock et al., 1991) south of Arroyo Matomí to within a few km of Picacho Canelo indicates that f4 flows crop out at the limits of that mapped area (about 1.5 km east-northeast of Picacho Canelo). *Tmr<sub>can</sub>* is thus most likely continuous with

the f4 package. Another series of rhyolite lava flows which overlie *Tmr<sub>ec</sub>* is located in Arroyo La Cantera and Valle Curbina in the eastern PVP (~ 10 km east of Picacho Canelo). These flows are labeled Tmru by Martín-Barajas and others (1995) and yield a  $^{40}\text{Ar}/^{39}\text{Ar}$  whole rock age of  $5.80 \pm 0.03$  Ma. Phenocrysts include < 5% plagioclase (oligoclase to andesine), clinopyroxene (ferroaugite), and opaque minerals, which makes Tmru petrographically similar to *Tmr<sub>can</sub>*. However, since Tmru underlies 5.1 Ma Tba (discussed above), which is tentatively correlated to the three Group 7 andesites, Tmru could only be correlative with *Tmr<sub>can</sub>* if *Tma<sub>gem</sub>*, the one andesite directly overlain by *Tmr<sub>can</sub>*, is older than *Tma<sub>ugl</sub>* and/or *Tma<sub>hem</sub>* and thus not coeval with Tba.

The preferred interpretation for Group 7 rocks is shown in the lower half of Figure 2.5, and involves the correlation of *Tmr<sub>can</sub>* with Tmru of the northeastern PVP and Tmr9 of the Sierra San Fermín. All of the rhyolite lava flows discussed above (*Tmr<sub>can</sub>*, Tmr9, f4, Tmru) are considered to be part of a field of latest Miocene rhyolite domes in the northeastern PVP as previously noted by Martín-Barajas and others (1995).

## 2.6. Summary

The 7 lithologic Groups defined and mapped in the Santa Isabel Wash and Arroyo Oculito regions can be summarized from oldest to youngest as follows:

Group 1 consists of pre-Miocene batholithic and pre-batholithic rocks of probable Mesozoic and Paleozoic age, respectively.

Group 2 rocks are thick (up to at least 500 meters), bedded, volcanic epiclastic deposits interpreted to be derived from the high-standing slopes of the mid-Miocene, subduction-related andesitic arc. They represent intermediate-source facies deposition. Bedding dips vary between 10-40° generally to the west or north. The nearest, dated andesitic centers which could have been a source of the andesite clasts include 17-20 Ma andesitic vents south of Mesa Cuadrada (10 km north of the northwestern limit of the map area) and a 16 Ma complex in Arroyo Los Heme (eastern PVP) (25 km southeast of the southeastern

limit of the map area). On the basis of overlying dated units, Group 2 rocks are pre-17 Ma in age.

Group 3 consists of a voluminous package of ~ 15.5-17 Ma dacites and minor basalt flows which are also interpreted to be subduction-related on the basis of their age and local extent. These lavas are probably in place around small vents throughout the field area (i.e., near-source facies), although identifiable vent features are no longer preserved. Group 3 rocks formed highly irregular topography upon which subsequent units were deposited.

Group 4 consists of one ~ 12.5 Ma pyroclastic flow deposit, the Tuff of San Felipe, with a thick, well-preserved basal vitrophyre. The unit was deposited against irregular topography and is preserved in only a few places in the field area. The tuff is important because it is correlated to a pyroclastic flow deposit to the north which is more continuously exposed, has an identified source region, and is a key marker bed for dating the initiation of continental extension.

Group 5 consists of a hornblende-phyric andesite which occurs at two localities. Although volumetrically minor, its mineralogy and age (~ 9 Ma) make it unique in the field area. On the basis of its age and minor volume, this unit is interpreted to represent post-subduction volcanism.

Group 6 consists of up to 300 meters (more commonly < 150 m) of ~ 6-7 Ma pumice- and lithic-lapilli, rhyolitic pyroclastic flow deposits. The deposition of these silicic units is interpreted to mark a period of significant extension-related, subaerial volcanism. The relatively flat upper surface of this series of tuffs constitutes the top of the PVP plateau in this area. In general the tuffs are thicker (and have basal contacts at lower elevations) in the northeastern parts of Santa Isabel Wash.

Group 7 is a set of porphyritic andesite and rhyolite flows overlying Group 6 rocks in the eastern part of the study area (Arroyo Oculito). Some of these units are considered to be continuous with units mapped immediately to the northeast (Stock et al., 1991; Stock, unpub. mapping).

Figure 2.1. Simplified geologic map of Santa Isabel Wash.



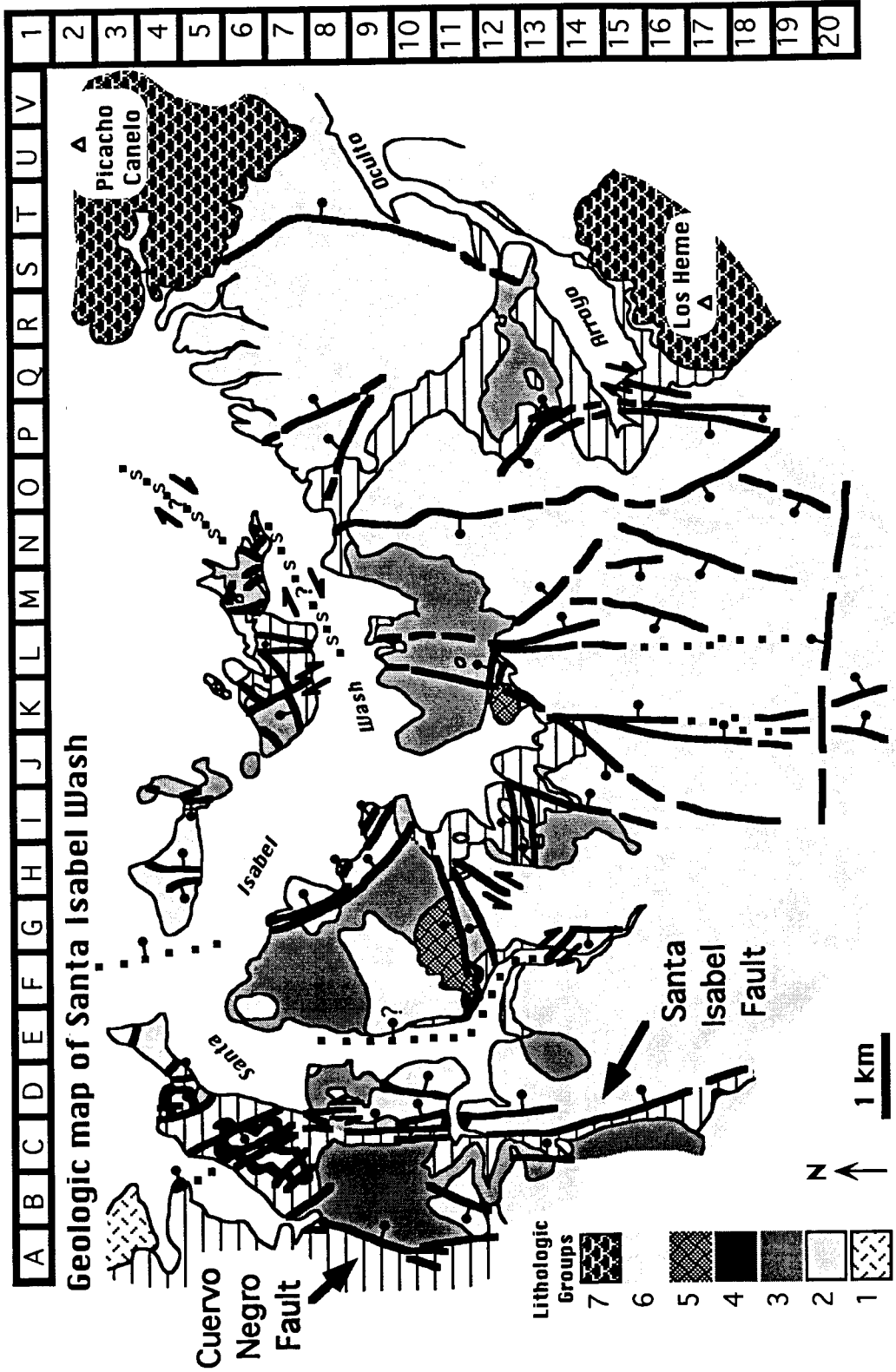

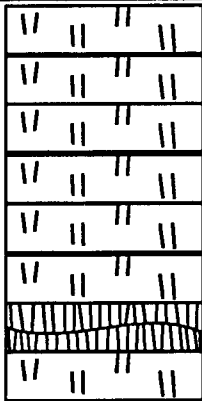


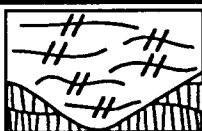
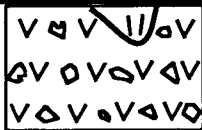

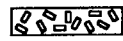
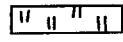
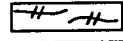

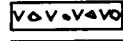



Figure 2.2. Stratigraphic column from Santa Isabel Wash.

# STRATIGRAPHY OF SANTA ISABEL WASH

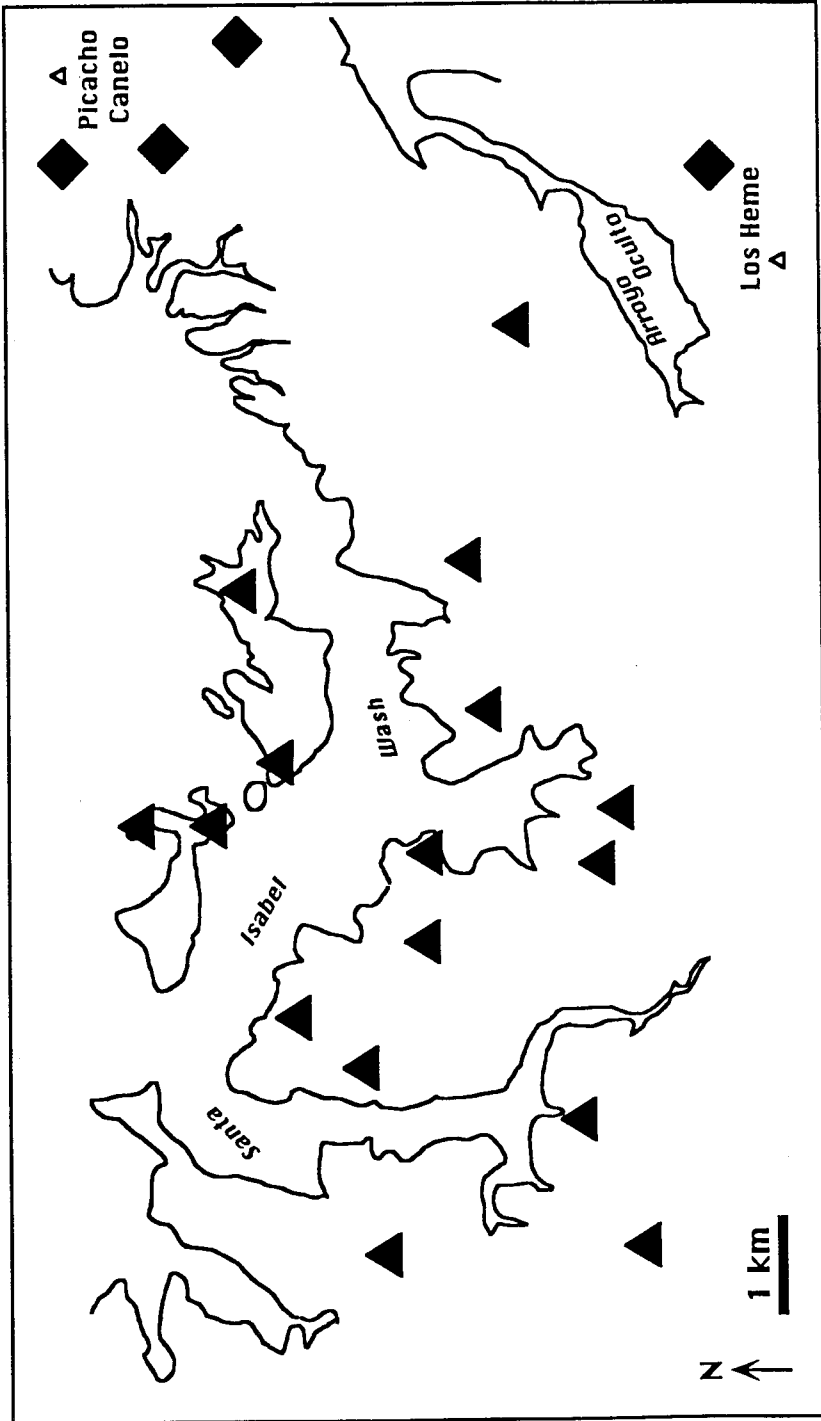
Group:			
7		<i>Tmr<sub>can</sub></i> <i>Tma<sub>hem</sub>, Tma<sub>ugl</sub>, Tma<sub>gem</sub></i>	Picacho Canelo rhyolite* Los Heme andesite* Ugly Mountain andesite* Pico de los Gemelos andesite*
6		<i>Tmr<sub>fp</sub></i> <i>Tmr<sub>bs</sub></i> <i>Tmr<sub>ec</sub></i> <i>Tmr<sub>ao</sub></i> <i>Tmr<sub>4</sub></i> <i>Tmr<sub>3</sub></i> <i>Tmb<sub>new</sub></i> <i>Tmr<sub>siw</sub></i>	Flag Pole tuff* Bighorn Sheep tuff* Tuff of El Canelo Arroyo Oculito tuff* Miocene rhyolite #4 Miocene rhyolite #3 New Year's Mountain Basalt* Tuffs of Santa Isabel Wash*
5		<i>Tma<sub>toro</sub></i>	Pico del Toro andesite*
4		<i>Tmr<sub>sf</sub></i>	Tuff of San Felipe
3		<i>Tmd<sub>tomb</sub></i> <i>Tmb<sub>lol</sub>, Tmb<sub>kc</sub></i>	Tombstone dacite* Land of the Lost basalt* Klondike Canyon basalt*
2		<i>Tmr<sub>bio</sub></i> <i>Tmvs</i>	Biotite tuff*
1		<i>Pz, Mzg</i>	

**Lithologic patterns:**

-  porphyritic andesite
-  ash-flow tuff
-  silicic lava flows
-  basaltic lava flows
-  volcanoclastic breccia
-  batholithic basement

\* indicates new name assigned in this study

Figure 2.3. Possible vent localities for Group 3 and 7 lava flows in Santa Isabel Wash.



▲ Probable locations of Group 3 vents (15.5-17 Ma)

◆ Probable locations of Group 7 vents (6 Ma)

Figure 2.4. Stratigraphic columns showing preferred correlations between Group 6 rocks mapped in Santa Isabel Wash and Arroyo Oculito (this study) and those described by other workers in nearby localities. In some cases the stratigraphy shown for studies other than this one has been simplified by listing only the lithologic units relevant to Santa Isabel Wash and Arroyo Oculito correlations. Stratigraphic order is preserved in all cases. Ages are given in Ma with  $1\sigma$  uncertainties. Note that units t3, t4, t2u, and t2l in Arroyo Matomí (Stock et al., 1991; Stock, unpub. mapping) are defined as Mpru in Stock (1989, 1993).

# Stratigraphic columns showing preferred lithologic correlations between Group 6 rocks of this study and nearby localities

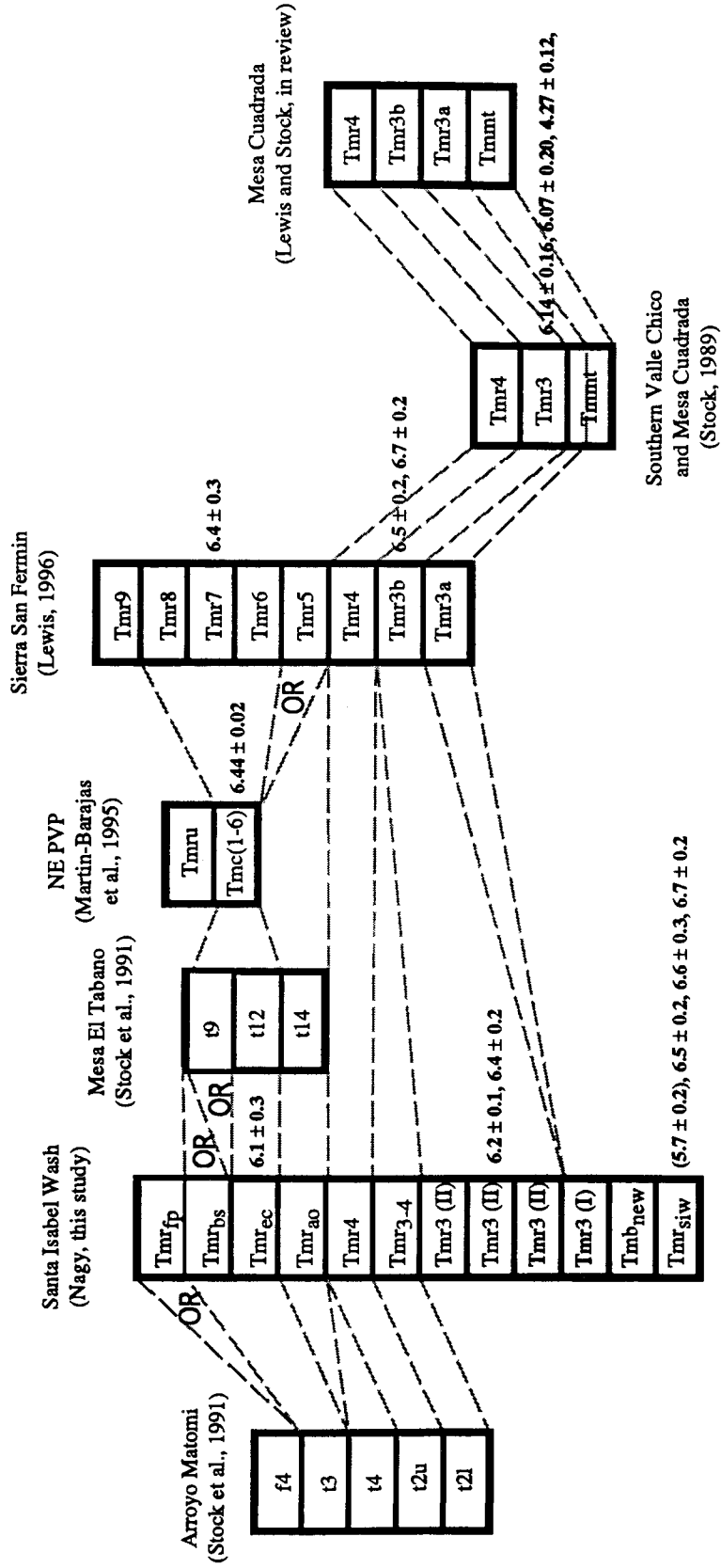
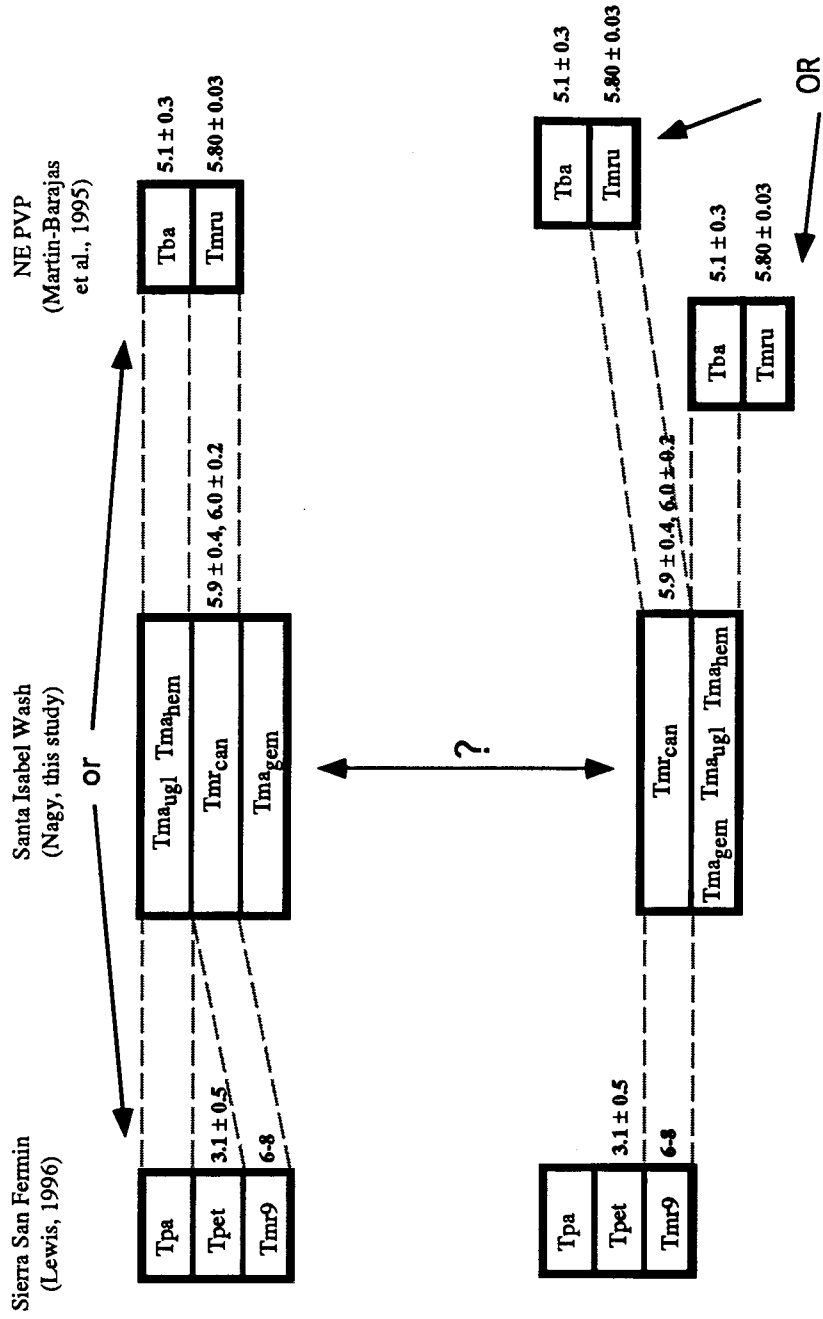


Figure 2.5. Possible stratigraphic correlations for Group 7 rocks from this study and units described by other workers in nearby localities. Two possibilities are shown for the relationship between *Tmr<sub>can</sub>* and two of the andesite lava flows, *Tma<sub>hem</sub>* and *Tma<sub>ugl</sub>*. Although it is not shown here, *Tmr<sub>can</sub>* is considered to be continuous with f4 of Stock (unpub. mapping; also, Stock et al., 1991). The preferred correlation for Group 7 rocks is depicted in the lower part of this figure and involves the correlation of *Tmr<sub>can</sub>* with Tmru of the northeastern PVP and Tmr9 of the Sierra San Fermín.



# Stratigraphic columns showing possible lithologic correlations between Group 7 rocks of this study and nearby localities



## Chapter III

 $^{40}\text{Ar}/^{39}\text{Ar}$  geochronology of lithologic units in Santa Isabel Wash3.1. *Introduction*3.2. *Basic theory of  $^{40}\text{Ar}/^{39}\text{Ar}$  geochronology*3.3. *Laboratory techniques*A. *Basic mineral separation procedures*B. *Non-conventional mineral separation procedures - exposure to  $^{137}\text{Cs}$* C. *Packaging and irradiation*D. *Analytical methods - overview*E. *Heating methods and analysis details*F. *Data analysis*3.4. *Results and Interpretations*A. *Measurement precision*B. *Flux monitors and J-factors*C. *Internal standard*D. *Samples exposed to  $^{137}\text{Cs}$* E. *All other samples*3.5. *Discussion*A. *Volcanism and structural implications*B. *Other geochronologic studies of same units*3.6. *Conclusions*

### 3.1. *Introduction*

Neogene volcanism on the eastern side of peninsular Baja California is primarily associated with the development of the Gulf Extensional Province (GEP) (see Chapter I for further discussion). The North America-Pacific plate boundary is presently located within the GEP (see Figure 1.1 in Chapter I) and is made up of a series of spreading centers and transform faults within the Gulf of California. The western portion of the GEP is subaerially exposed along the eastern side of Baja California and has a sharp western boundary (Main Gulf Escarpment). Along the northern third of the peninsula the subaerial portion of the extensional province averages 50 km in width perpendicular to the coast. Datable volcanic and marine deposits exposed along the margins of the GEP are offset by high angle normal faults and thus can provide timing constraints on the initiation and development of continental extension. See Table 3 of Lee and others (1996) for a summary of evidence for the timing of extension on both sides of the GEP along the entire length of the Gulf of California.

The volcanic units dated in this study are located in northeastern Baja California within, and along the northern margin of, the Puertecitos Volcanic Province (PVP). The PVP is a large (2600 km<sup>2</sup>) volcanic field of Miocene and Pliocene age (Gastil et al., 1975) located near latitude ~30°N and longitude ~115° (southwestern edge). A map of the western portion of the GEP in the region of northeastern Baja California and the entire PVP was presented in Figure 1.5 (Chapter I). The PVP occurs just south of a distinct Basin and Range-type extensional province. From west to east the southernmost latitude of this extensional province includes the southern Valle Chico (“basin”), the Sierra San Felipe (“range”), Llanos de San Fermín (“basin”), and the Sierra San Fermín (“range”) (Figure 1.6 of Chapter I). An unextended, topographically high mountain range, the Sierra San Pedro Mártir, borders the extensional province on the west. A WNW-ESE trending accommodation zone separates the extensional province from the significantly less extended PVP to the south (Dokka and Merriam, 1982; Stock and Hodges, 1990). Most of the samples analyzed in this study were collected south of, or within, the accommodation zone in the northern Sierra Santa Isabel.

The study area, informally named here Santa Isabel Wash, contains numerous N-S striking normal faults related to extensional plate boundary deformation. A detailed geologic map is presented and discussed in conjunction with structural features in Chapter IV. A simplified geologic map of the study area was presented in Chapter II (Figure 2.1). UTM coordinates (Table 3.1) correspond to the collection locations of geochronology samples analyzed and discussed here.

Complete lithologic descriptions of the geologic units defined in this study, including rock classification scheme, field and thin section descriptions, and electron microprobe results, are given in Chapter II. A simplified stratigraphic column was presented in Figure 2.2 in Chapter II and includes both the names assigned to the various units and the unit abbreviations used throughout this text. The Miocene units are divided into six Groups based upon lithology, stratigraphic position, and age (as determined from data presented here). They unconformably overlie pre-Miocene metasediments (*Pz*) and granites (*Mzg*) which constitute Group 1. From oldest to youngest the Miocene Groups are as follows: Group 2: volcanoclastic breccias and sedimentary rocks (*Tmvs*), and a local rhyolite ignimbrite (*Tmr<sub>bio</sub>*); Group 3: dacitic to basaltic lava flows and associated epiclastic breccias (*Tmb<sub>kc</sub>*, *Tmb<sub>lol</sub>*, *Tmd<sub>tomb</sub>*); Group 4: a rhyolitic ash flow tuff (*Tmr<sub>sf</sub>*); Group 5: andesite lava flows (*Tma<sub>toro</sub>*); Group 6: a series of rhyolitic (to dacitic?) ignimbrites (oldest to youngest: *Tmr<sub>siw</sub>*, *Tmr<sub>3</sub>*, *Tmr<sub>3-4</sub>*, *Tmr<sub>4</sub>*, *Tmr<sub>ao</sub>*, *Tmr<sub>ec</sub>*, *Tmr<sub>bs</sub>*, *Tmr<sub>fp</sub>*) including a local basalt flow (*Tmb<sub>new</sub>*) deposited between *Tmr<sub>siw</sub>* and *Tmr<sub>3</sub>*; and Group 7: rhyolite and andesite lava flows (*Tma<sub>gem</sub>*, *Tmr<sub>can</sub>*, *Tma<sub>ugl</sub>*, *Tma<sub>hem</sub>*).

The ages of these lithologic units are clearly important for deciphering the tectonic evolution of this portion of the plate boundary. Many studies document the usefulness of <sup>40</sup>Ar/<sup>39</sup>Ar geochronology for dating volcanic rocks (Stock 1989; Cheilletz et al., 1992; Conrad et al., 1993; Spell and Harrison, 1993; Martín-Barajas et al., 1995; McConnell et al., 1995; Zumbo et al., 1995; Lewis, 1996; Spell et al., 1996; Conway et al., 1997) and to confirm correlations between isolated exposures of a given volcanic deposit (e.g., Pringle et al., 1992;

Best et al., 1995). Both K/Ar and  $^{40}\text{Ar}/^{39}\text{Ar}$  techniques have been used to date the volcanic rocks in the western GEP.

$^{40}\text{Ar}/^{39}\text{Ar}$  data for rock samples from each Group (except Group 1) are presented in this study. These analyses include some challenging aspects. In particular, most samples lack potassium feldspar and thus plagioclase was selected for analysis. Samples therefore contain a relatively small amount of  $^{40}\text{K}$ -derived argon, and furthermore, given the young ages of most units (late Miocene), they contain small amounts of radiogenic argon relative to total argon. Fusion of large amounts of sample (up to  $\sim 1.5$  mg) alleviated some of this problem, but variables such as the mass discrimination of the mass spectrometer and background correction values used in the age calculations had to be evaluated quite carefully. For example, using daily averages of extraction line blanks for line blank corrections, instead of fitting curves to daily variations (and extrapolating for measured samples), has a significant effect on the results because the low argon signals of these K-poor phenocrysts are extremely sensitive to these corrections. This is in contrast to background corrections made when measuring K-rich phenocrysts, which generally have very strong argon signals which are relatively unaffected by small variations in background values for the various argon isotopes.

### 3.2. Basic theory of $^{40}\text{Ar}/^{39}\text{Ar}$ geochronology

The  $^{40}\text{Ar}/^{39}\text{Ar}$  technique is a variant of the classic K-Ar method whereby  $^{39}\text{Ar}$  is produced from naturally present  $^{39}\text{K}$  during neutron bombardment (Merrill and Turner, 1966; for details, see McDougall and Harrison, 1988). Radiogenic  $^{40}\text{Ar}$  (or  $^{40}\text{Ar}^*$ , the symbol \* denotes radiogenic as opposed to nonradiogenic argon) is one of the naturally occurring daughter products of the radioactive isotope  $^{40}\text{K}$  ( $t_{1/2} = 1.28 \times 10^9$  years). In volcanic systems, rapid cooling upon eruption at the surface initiates the retention of  $^{40}\text{Ar}^*$  such that the  $^{40}\text{Ar}^*/^{40}\text{K}$  ratio is potentially proportional to age. Argon diffusion, which can play an important role in rocks which have undergone thermal disturbances, is assumed to be insignificantly small at ambient temperatures (Fechtig and Kalbitzer, 1966). Closure temperature for the retention of radiogenic argon within plagioclase phenocrysts is estimated

to be ~200-250°C (McDougall and Harrison, 1988). The fundamental assumption in both approaches (K-Ar or  $^{40}\text{Ar}/^{39}\text{Ar}$ ) is that all non-radiogenic  $^{40}\text{Ar}$  present is atmospheric in origin. Correction for the presence of atmospheric Ar is made on the basis of known isotopic ratios for the three naturally occurring argon isotopes ( $^{40}\text{Ar}$ ,  $^{38}\text{Ar}$ , and  $^{36}\text{Ar}$ ), which are constant in the earth's atmosphere. However, it needs to be noted that this is not necessarily true of argon dissolved in crustal fluids (Ozima and Podosek, 1983).

During neutron bombardment of a sample in the core of a nuclear reactor, one of the principal reactions is the conversion of  $^{39}\text{K}$  into  $^{39}\text{Ar}_k$  (the subscript  $_k$  denotes  $^{39}\text{Ar}$  derived from  $^{39}\text{K}$  during irradiation). This makes it possible to make mass spectrometric measurements of both  $^{40}\text{Ar}$  and  $^{39}\text{Ar}$  on a single aliquot of sample gas, a significant advantage over traditional K/Ar dating methods which require two different measurement procedures to be performed on separate aliquots of the sample. Argon is extracted from the sample by heating, either in a furnace or by laser. After purification to remove active species, argon contained within gas liberated from the sample is ionized by electron bombardment and accelerated down the flight tube by applying a constant high voltage. Systematic variation of the magnetic field permits each of the argon isotopes to be successively focused upon the collector. The mass spectrometer is calibrated to yield true isotopic ratios from the results of measurements performed with purified atmospheric argon. The correction factors for mass discrimination assume that the isotopic composition of atmospheric argon is constant: 99.600% of  $^{40}\text{Ar}$ , 0.063% of  $^{38}\text{Ar}$ , and 0.337% of  $^{36}\text{Ar}$ .

After correction for line blanks and  $^{40}\text{Ar}$  produced by  $^{40}\text{K}$  during irradiation, correction for non-atmospheric  $^{40}\text{Ar}$  is conventionally performed by assuming that all  $^{36}\text{Ar}$  remaining after correction for line blanks, mass discrimination, and interfering nuclear reactions is atmospheric in origin. A model age for crystallization of a K-bearing mineral can thus be calculated knowing the decay rate ( $\lambda$ ) and the ratio of parent ( $^{40}\text{K}$ ) to daughter ( $^{40}\text{Ar}^*$ ) in a given sample. Since the measured ratio of  $^{40}\text{Ar}^*/^{39}\text{Ar}_k$  in an irradiated sample is proportional to  $^{40}\text{Ar}^*/^{39}\text{K}$ , which in turn is proportional to  $^{40}\text{Ar}^*/^{40}\text{K}$  since  $^{39}\text{K}/^{40}\text{K}$  is essentially constant in nature (McDougall and Harrison, 1988), the ratio of  $^{40}\text{Ar}^*/^{39}\text{Ar}_k$  is proportional to the age. The age equation is:

$$t = \frac{1}{\lambda} * \left( \ln \left[ 1 + J \left( \frac{{}^{40}\text{Ar}^*}{{}^{39}\text{Ar}_K} \right) \right] \right) \quad (3.1)$$

where  $t$  is the age in Ma,  $\lambda$  is  $5.543 \times 10^{-4} \text{ Ma}^{-1}$ , and  $J$  is a dimensionless irradiation parameter which accounts for variables such as length of irradiation, neutron flux density in the reactor, and capture cross section of the target atoms (calculation of  $J$  is described below).

Several other argon isotopes are produced as a result of the neutron bombardment in the reactor. Most notably  ${}^{40}\text{Ca}$  produces  ${}^{36}\text{Ar}$  and  ${}^{37}\text{Ar}$ ,  ${}^{42}\text{Ca}$  produces  ${}^{39}\text{Ar}$ , and  ${}^{40}\text{K}$  produces  ${}^{40}\text{Ar}$  (McDougall and Harrison, 1988). These nuclear reactor interference products are corrected for by measuring the  ${}^{36}\text{Ar}/{}^{37}\text{Ar}$  and  ${}^{39}\text{Ar}/{}^{37}\text{Ar}$  ratios of a K-free, calcium salt, (typically  $\text{CaF}_2$ ,) included in the irradiation tube. From the salt sample, the correction factors  $[{}^{36}\text{Ar}/{}^{37}\text{Ar}]_{\text{Ca}}$  and  $[{}^{39}\text{Ar}/{}^{37}\text{Ar}]_{\text{Ca}}$  ( $_{\text{Ca}}$  subscript denotes derived from calcium) can be derived by measuring the relative proportions of these isotopes produced during irradiation. Note that a correction for the decay of  ${}^{37}\text{Ar}_{\text{Ca}}$  to  ${}^{37}\text{Cl}$  must also be performed ( $t_{1/2} = 35.1$  days). Similarly,  ${}^{40}\text{Ar}_K$  produced from  ${}^{40}\text{K}$  is accounted for by including a pure potassium salt ( $\text{K}_2\text{SO}_4$ ) in the irradiation tube. Again a correction for radioactive decay of  ${}^{39}\text{Ar}$  ( $t_{1/2} = 269$  years) must be applied.

### 3.3. Laboratory techniques

#### A. Basic mineral separation procedures

Rocks chosen for  ${}^{40}\text{Ar}/{}^{39}\text{Ar}$  geochronology satisfied two criteria: relevance to the establishment of a local, dated stratigraphy and sufficient amount and type of datable phenocrysts as determined petrographically in thin section analysis. Dated from 21 (originally 24) different rock samples were 11 (originally 13) different lithologic units. The three samples which did not yield dates had too little radiogenic argon to measure (<1%

radiogenic yield). Detailed mineral separation techniques are described in Appendix C; a brief summary is given here.

Hand samples were crushed by hand and pulverized in a disk mill taking care to avoid contamination. The resulting material was then sieved to yield #30 (0.59 mm), #60 (0.25 mm), #80 (0.177 mm), and #100 (0.149 mm) size fractions. Chosen sieved fractions (usually the #30-#60 fraction) were then repeatedly washed and decanted by hand, and then cleaned ultrasonically to eliminate ultra-fine particles adhering to grains. After the removal of strongly magnetic material with a hand magnet, quartz and feldspar were concentrated using a Frantz isodynamic separator. The non-magnetic fractions of each sample were again washed in de-ionized water and placed in the ultrasonic bath for approximately 30 minutes to break off any glass from the mineral grains. Use of HF was avoided due to the risk of incongruent dissolution which potentially leaves a K-precipitate. The presence of such a precipitate on a mineral grain, when irradiated, can artificially reduce the age of the sample.

Following ultrasonic treatment, further concentration of the feldspars was attempted through the use of heavy liquids. Mixtures of acetylene tetra bromide (ATB; density of 2.96 g/cm<sup>3</sup>) and acetone (0.7848 g/cm<sup>3</sup>) were calibrated to separate minerals differing in density. Separations were generally started with a liquid of the same density as quartz and the first fraction removed prior to adding acetone to the liquid to decrease its density. In general, few crystals sank during the initial step, suggesting that much of the plagioclase in these samples is of an albitic composition. Between 2 and 5 fractionations were made using the heavy liquids for each sample. Fractions were dried using acetone as described above for washed samples.

Following heavy liquid separation, feldspar concentrates were placed in an ultrasonic bath in 10% HCl for 10 minutes, washed three times with de-ionized water, and dried with acetone to remove any carbonate encrusted on the grains. At this stage, feldspar grains were hand-selected using a binocular microscope. Immersion oils were occasionally used to verify the composition of selected grains; the actual grains placed in the oils were discarded. The mass of final plagioclase separates ranged between 45 to 150 mg for a given sample; anorthoclase samples ranged between 40 to 50 mg.



*B. Non-conventional mineral separation procedures - exposure to  $^{137}\text{Cs}$*

Quartz and feldspars overlap in their magnetic susceptibilities (quartz- from diamagnetic up to  $30 \times 10^6 \text{ emu/cm}^3$ ; orthoclase -  $< 10 \times 10^6 \text{ emu/cm}^3$ ; albite - diamagnetic) and are thus concentrated together when using the Frantz isodynamic separator. The use of heavy liquids is consequently an essential step for efficient separation prior to time-consuming hand-selection. Although the specific gravities of quartz and feldspars also overlap, this method has proven to be effective at concentrating alkali feldspar from a sample. The toxicity of heavy liquids make their use less than desirable, and further, their use requires several hours per sample. Subsequent hand-picking is still complicated by the fact that one must look carefully at mineral cleavage to distinguish the various, similar-looking minerals.

Rose and others (1994) have described how  $\gamma$ -radiation of minerals using a  $^{137}\text{Cs}$  source produces diagnostic color changes that can be helpful for mineral separation. Specifically, exposure to the  $^{137}\text{Cs}$  source imparts a smoky hue to quartz and a yellow tint to sanidine but leaves plagioclase crystals relatively unchanged. The change in color generated in this procedure depends upon the  $\text{Al}^{3+}$  content as it is these ions, substituting for  $\text{Si}^{4+}$  with a nearby 1+ ion, which give up an electron during irradiation and produce the change in color (Rose et al., 1994). The procedure does not alter the chemical or oxygen isotope compositions of minerals tested (Rose et al., 1994).

In order to test the usefulness of this method for  $^{40}\text{Ar}/^{39}\text{Ar}$  analysis, aliquots of four samples separated using conventional techniques (prior to the heavy liquid step) were each split into two sub-samples. One of each sub-sample was exposed to a  $^{137}\text{Cs}$  source for 4-5 days (receiving 1.06 Mrad/day of  $\gamma$ -radiation) while the other half of each sub-sample was further separated using the heavy liquid treatment described above. Quartz grains did indeed become a smoky color and anorthoclase phenocrysts had a subtle yellow tint. Grains from each of the sub-samples were hand-selected following the procedure outlined above. Pairs of sub-samples remained separate (i.e., treated like two samples) during the entire measurement procedure in order to compare any differences in the measured  $^{40}\text{Ar}/^{39}\text{Ar}$  systematics (Table 3.3).

### *C. Packaging and irradiation*

Mineral separates for each sample were wrapped in commercial grade aluminum foil and formed into roughly cylindrical packages small enough to fit into a quartz glass irradiation tube. Aliquots of a flux monitor of known age (the 27.8 Ma Fish Canyon Tuff sanidine (FCT-1; Cebula et al., 1986), and an internal, or secondary, standard (anorthoclase from a single pumice block from pyroclastic flow deposit *Tmr3*), were interspersed with the rest of the samples as illustrated in Figure 3.1. The internal standard was divided into three packages per irradiation tube. In general, samples believed to be similar in age were placed adjacent to each other in the sample tubes to minimize the effects of neutron flux variations. Similarly, pairs of samples used for the  $\gamma$ -radiation test were always placed adjacent to each other. The mass of each sample is included in Tables 3.2 and 3.4 (a, b).

The quartz tubes were sealed under low vacuum ( $10^{-2}$  Torr) and shipped to the Ford Reactor at the University of Michigan for neutron irradiation. Samples were irradiated in two separate batches. In the first irradiation (designated as UOFM#75T1) a single tube was irradiated for three hours in the L67 position on 12/20/94 (fast neutron fluence of  $5 \times 10^{12}$  neutrons/cm<sup>2</sup>/s; thermal neutron fluence of  $12 \times 10^{12}$  neutrons/cm<sup>2</sup>/s). The samples were measured in January and February of 1995 at UCLA (referred to hereafter as Lab Session 1). In the second irradiation, two tubes (designated UOFM#82T1 and UOFM#82T2) were irradiated for 5 hours on 10/17/95 in the same reactor site. These samples were measured in November of 1994 and March of 1995 (Lab Session 2). A longer irradiation time was chosen for the second batch of samples in an attempt to increase the  $^{39}\text{Ar}_k$  production, and thereby optimize the  $^{40}\text{Ar}^*/^{39}\text{Ar}_k$  ratio needed for accurate age determination (Turner, 1971a).

### *D. Analytical methods - overview*

Argon isotopic analyses were performed at UCLA  $^{40}\text{Ar}/^{39}\text{Ar}$  facility. A continuous 5W Coherent Ar-Ion laser was used to heat the samples. Crystals were arranged in a copper tray

with eight pie-shaped regions separated by ~5 mm-high walls of copper. Individual sanidine and anorthoclase grains were placed into small wells while plagioclase grains were spread uniformly in a single layer within an entire segment to facilitate analysis of multiple grains. Flux monitors and internal standards were included in each tray and measured periodically to ensure that any long-term changes of the measurement system (over time periods anywhere from hours to weeks) could be identified.

Following laser heating of sample or standard crystals, sample gas was purified using two SAES ST101 alloy getter pumps operated at 250°C (50 l/s) and 400°C (10 l/s), respectively. Gas transfer was via expansion with the total quantity of argon reaching the mass spectrometer recalculated for 100% delivery. Analysis of purified sample gas was carried out with a VG3600 Rare Gas mass spectrometer. An ion pump attached to the mass spectrometer pumped out the flight tube between sample analyses while a turbo vacuum pump is used to remove residual sample gas in the extraction line. The VG 3600 utilizes a Nier-Bright source yielding an Ar sensitivity of  $6 \times 10^{-4}$  A/Torr at a mass resolving power (MRP) of 450. Ion intensities were measured using a Daly electron multiplier operated in analogue mode at  $^{40}\text{Ar}$  sensitivity of  $1.85 \times 10^{-17}$  mol/mV with 2% uncertainty. When configured in this manner, the abundance sensitivity of the VG3600 is  $< 5$  ppm while the mass discrimination is  $0.994 \pm 0.001$  (this particular value, calculated from successive atmospheric Ar measurements, is assigned to a two month bracket during Lab Session 2). Representative total system blanks for a typical procedure involved laser heating for 1-3 minutes of ~0.5 to 1.5 mg aliquots of plagioclase and gettering for 5-10 minutes were:  $5 \times 10^{-16}$  moles,  $2 \times 10^{-18}$  moles,  $1 \times 10^{-18}$  moles,  $1 \times 10^{-17}$  moles, and  $7 \times 10^{-18}$  moles for m/e 40 through 36, respectively. A detailed description of procedures is given in the next section.

#### *E. Heating methods and analysis details*

The method of laser heating varied depending upon the argon content of material being analyzed. Heating times varied from 1 to 5 minutes depending on how many crystals needed to be fused to obtain a signal of sufficient intensity to measure reliably. An aliquot of

plagioclase, for example, required 10-30 grains while aliquots of sanidine or anorthoclase required between 1 and 3 grains, an obvious consequence of their respective potassium contents.

Two types of sample fusion techniques were employed to check for excess  $^{40}\text{Ar}$  and to help define a spectrum of isotopic ratios between atmospheric and radiogenic components. The standard technique used a focused laser beam at ~5 W to fuse all grains in the aliquot. Alternatively, the power setting was varied so that gas could be liberated from the sample in two steps. In the first step, a defocused beam (~ 3-4 mm in diameter) with a power setting of 2 W was used to extract low-temperature gas from the aliquot. In the second step, a focused 5 W beam was employed to fuse the same aliquot. Ideally the gas released in the first of the two steps is enriched in atmospheric  $^{40}\text{Ar}$  relative to K-derived  $^{40}\text{Ar}^*$ , and thus atmospheric contamination should be reduced in the second step and result in a higher radiogenic yield. Pringle and others (1992) found this kind of “low temperature cleaning” useful for removing nonradiogenic argon contamination in Quaternary plagioclases from the Taupo volcanic zone in New Zealand. Their results were comparable to results from resistance-furnace experiments also performed in that study.

Each measurement of an aliquot fused with the defocused 2 W beam is listed in bold in Appendix D. The subsequent step listed is the focused, 5 W fusion step. Because the plagioclase crystals are spread on the tray in a sheet, instead of within individual wells, it is likely that some crystals did not contribute to both analyses. If the defocused step gives an older model age it is likely that the sample contains excess  $^{40}\text{Ar}^*$ . None of the samples measured in this study exhibit compelling evidence for excess  $^{40}\text{Ar}^*$ .

Because variable amounts of material were fused, the duration of gas cleanup also varied between 5-10 minutes. Extraction line blanks were measured periodically while mass spectrometer backgrounds were measured prior to each analysis. A routine, previously calibrated procedure was employed to split sample gas between different sections in the extraction line in order to govern the amount of gas delivered to the mass spectrometer (maximum of 56%). Equilibration times for transferring gas were a minimum of 20 seconds. A typical measurement cycle generally involves 5 cycles of two or more measurements for

each mass. Over 50% of the counting time was devoted to measurement of  $^{36}\text{Ar}$  and baseline readings.

During Lab Session 1, dynamic background measurements for the flight tube were taken at the beginning of each measurement session while extraction line blanks were measured after every 8-10 analyses. Measurement of the extraction line blanks consisted of two measurements. First, a dynamic blank reflecting zero equilibration time with the getters was measured. Then, a static blank representing 10 minutes of equilibration time with the getter pumps was obtained. From these measurements, line blanks appropriate for arbitrary periods of getting were calculated. As 8-10 analyses were generally obtained for each sample, a set of background measurements was taken at least once per sample. During Lab Session 2, a slightly different approach was used to reflect the use of more standardized analysis routines. Blank and static mass spectrometer measurements were combined and performed after every third sample measurement.

#### F. *Data analysis*

With the aid of an in-house computer program at UCLA called AGEAL (M. Grove and O. Lovera, unpub. software, 1996), the  $^{40}\text{Ar}^*/^{39}\text{Ar}_k$  ratio was calculated for each aliquot measured during Lab Session 1. For samples measured during Lab Session 2, these calculations were performed with a modified version of the AGEAL program (X. Quidelleur, unpub. software, 1997) which better estimates variations in the line blanks by fitting polynomials to the values measured at regular intervals throughout the day, and using extrapolated values for each measurement's line blank correction. From the  $^{40}\text{Ar}^*/^{39}\text{Ar}_k$  ratio a model age is calculated for each aliquot assuming atmospheric trapped argon ( $^{40}\text{Ar}/^{36}\text{Ar}$ ) equal to the present-day value of 295.5. The  $^{40}\text{Ar}^*/^{39}\text{Ar}_k$  ratios and model ages are listed in Appendix D for all measurements. Also listed in Appendix D are  $^{40}\text{Ar}/^{39}\text{Ar}$ ,  $^{38}\text{Ar}/^{39}\text{Ar}$ ,  $^{37}\text{Ar}/^{39}\text{Ar}$ , and  $^{36}\text{Ar}/^{39}\text{Ar}$  ratios (corrected for non-atmospheric backgrounds, atmospheric line blanks, mass discrimination, abundance sensitivity, and radioactive decay but not for atmospheric argon or interfering nuclear reactions), moles of K-derived  $^{39}\text{Ar}$ , and  $\%^{40}\text{Ar}^*$ .

Individual errors ( $1\sigma$  analytical uncertainty) are calculated for the  $^{39}\text{Ar}/^{40}\text{Ar}$  ratios and the  $^{36}\text{Ar}/^{40}\text{Ar}$  ratios for each measurement. For a single-stage cooling history all of the data points from a given sample will fall on a linear array between two-end-members. The gas released should be a mixture of purely atmospheric ( $^{39}\text{Ar} = 0$ ) and purely radiogenic ( $^{36}\text{Ar} = 0$ ) argon. All measurements from a given sample are thus linearly regressed using the equations of a best fit line (York, 1969). The error of the fit to an inverse isochron is given by the Mean Squared Weighted Deviate (MSWD) which should be approximately 1 when deviations from the regression line are within analytical error (Wendt and Carl, 1991). Mahon (1996) shows that the skewed nature of the MSWD probability distribution function for a small number of degrees of freedom results in median MSWD values not equal to one. He calculates 95% confidence intervals around median MSWD values on the basis of degrees of freedom (i.e., number of samples minus 2). The 95% range of “critical MSWD values” is listed in the right-hand column of Tables 3.2 and 3.4 (a, b) for each sample given the number of aliquots used in the age calculation.

The  $^{39}\text{Ar}_k/^{40}\text{Ar}^*$  intercept is inverted and used in the age equation (Eq. 3.1) with the appropriate J-factor to calculate the age. The  $^{36}\text{Ar}/^{40}\text{Ar}$  intercept should ideally be equal to 0.00338 (i.e., the atmospheric ratio). Uncertainties ( $\sigma_i$ ) for each  $^{40}\text{Ar}^*/^{39}\text{Ar}_k$  isochron age are calculated using the following equation from McDougall and Harrison (1988):

$$\sigma_i^2 = \frac{(J^2\sigma_F^2 + F^2\sigma_J^2)}{\lambda^2(1 + FJ)^2} \quad (3.2)$$

where  $\sigma_i$  is 1 sigma standard deviation in the calculated age ( $t$ ),  $J$  is the J-factor (discussed below),  $\sigma_J$  is the standard deviation of the J-factor (which is assigned a 2% uncertainty),  $F$  is the  $^{40}\text{Ar}^*/^{39}\text{Ar}_k$  intercept,  $\sigma_F$  is the standard deviation of the  $^{40}\text{Ar}^*/^{39}\text{Ar}_k$  intercept, and  $\lambda$  is the decay rate. The standard error of the best fit line ( $\sigma_F$ ) is calculated as suggested by Mahon (1996). Summaries of statistical results for each sample are given in Tables 3.2 and 3.4 (a, b).

In cases where the MSWD values are outside the range of “critical MSWD values” discussed above, it is likely that the simple two-end-member mixing model is not appropriate.

In these cases it is most likely that a heterogeneous crystal population exists, or the analytical uncertainties have been poorly estimated, or both. In addition to an isochron age, a mean weighted age ( $\mu$ ) can be calculated for each sample using the equation:

$$\mu = \frac{\sum (x_i / \sigma_i^2)}{\sum (1 / \sigma_i^2)} \quad (3.3)$$

where the model age for each sample aliquot ( $x_i$ ) is weighted inversely by its own variance ( $\sigma_i^2$ ) in the sum. The  $1\sigma$  uncertainty about the mean ( $\sigma_\mu$ ) is estimated by:

$$\sigma_\mu^2 \cong \frac{1}{\sum (1 / \sigma_i^2)} \quad (3.4)$$

Weighted mean ages are listed in Tables 3.2 and 3.4 (a, b) for all samples. Because individual model ages assume a  $^{40}\text{Ar}/^{36}\text{Ar}$  intercept equal to 295.5, this assumption also goes into the weighted mean age calculations.

Inverse isochron plots showing all measured aliquots are given in Figures 3.3 and 3.4 (a-i). These plots ( $^{39}\text{Ar}/^{40}\text{Ar}$  versus  $^{36}\text{Ar}/^{40}\text{Ar}$ ) illustrate the two-end-member model used to interpret the results. The  $^{36}\text{Ar}/^{40}\text{Ar}$  intercept represents only atmospheric argon and should ideally have a value of  $1/295.5$  (0.003384). Similarly, the  $^{39}\text{Ar}/^{40}\text{Ar}$  intercept represents solely radiogenic argon from the sample and is used to calculate the age as given in Eq. 3.1. The linear distribution of analyses between these end-members results from different proportions of atmospheric and radiogenic argon released in a given aliquot.

### 3.4. Results and Interpretations

#### A. Measurement precision

The precision of the measurements presented here varies from sample to sample. In general, relatively poorer precision is the result of individual measurement deviations from a linear fit along an isochron. Isochron ages for plagioclase phenocrysts in this study yield values for precision ( $1\sigma$ ) of  $\pm 2-7\%$  with one exception (sample PHO-94-86 with  $\pm 14\%$  precision for the isochron age but  $\pm 2\%$  precision for the weighted mean age), while isochron ages for samples of anorthoclase crystals have a precision of  $\pm 2-4\%$ .

On the basis of instrumental precision,  $^{40}\text{Ar}^*/^{40}\text{K}$  ratios can presently be measured to within  $\pm 0.1\%$ , although intersample precision is more commonly  $\pm 1\%$  (Roddick, 1983; Samson and Alexander, 1987). The most significant variables which limit intersample precision in  $^{40}\text{Ar}/^{39}\text{Ar}$  geochronology are vertical neutron flux gradients within reactors, the uniformity of the  $^{40}\text{Ar}^*/^{40}\text{K}$  ratio within the standard, and corrections of interference reactions from K-, Ca-, and Cl-derived argon (Roddick, 1983).

Measurement precision is also partly a function of the K content in the minerals analyzed. Consequently, precision is generally poorer for analyses of plagioclase feldspar relative to K-feldspar for a given age material (e.g., Pringle et al., 1992; Spell et al., 1996). Some typical values reported for measurement precision on plagioclase crystals include about  $\pm 2-5\%$  from Quaternary ash-flow deposits in the Taupo volcanic zone in New Zealand (Pringle et al., 1992), about  $\pm 1.5-12\%$  from Early Pliocene and Plio-Pleistocene volcanic units from Afar, Republic of Djibouti (Zumbo et al., 1995),  $\pm 1.2-1.9\%$  (laser fusion) and  $\pm 15\%$  (step-heating) from Pliocene volcanics in Baja California, Mexico, (Martín-Barajas et al., 1995),  $\pm 1.2-10\%$  from Plio-Pleistocene volcanics of the Jemez volcanic field in New Mexico (Spell et al., 1996), and about  $\pm 1-5\%$  for altered Cretaceous plagioclase crystals from the Paraná volcanic field in Brazil (Kelley et al., 1994). Measurement precision for analyses of K-feldspars can be  $< \pm 1\%$  (e.g., Lanphere, 1988; Féraud et al., 1990; Spell et al., 1996).



Cheilletz and others (1992) present results for sanidine phenocrysts from Miocene ash-flow tuffs with about  $\pm 1.5\text{-}5\%$  precision.

In several instances, one or more aliquot was removed from the age calculation of a given sample. In some cases, such data points were clearly outliers on the inverse isochron plots (see Figures 3.3 and 3.4), probably from incomplete gettering, and their removal brought the MSWD values closer to unity. In other cases, a very small amount of  $^{36}\text{Ar}$  gas (e.g.,  $< 10^{-15}$  moles) was released at a time when background and blank measurements were unusually high, which overwhelmed the ability to discern the sample signal.

### B. Flux monitors and J-factors

Flux monitor minerals of known age are used to calculate the irradiation factor “J” at each flux monitor position in each sample tube. By definition (but not in practice) J is determined by the following equation (from McDougall and Harrison, 1988):

$$J = (\lambda / \lambda_e) (^{39}\text{K} / ^{40}\text{K}) \Delta T \int \varphi(\varepsilon) \sigma(\varepsilon) d\varepsilon \quad (3.5)$$

where  $\lambda_e$  is the decay constant of  $^{40}\text{K}$  for electron capture,  $\lambda$  is the total decay constant of  $^{40}\text{K}$ ,  $^{39}\text{K}$  is the number of atoms of this isotope in the irradiated sample,  $^{40}\text{K}$  is the initial number of  $^{40}\text{K}$  atoms,  $\Delta T$  is the length of irradiation,  $\varphi(\varepsilon)$  is the neutron flux density at energy  $\varepsilon$ , and  $\sigma(\varepsilon)$  is the capture cross section of  $^{39}\text{K}$  for neutrons having energy  $\varepsilon$ . The latter two variables are integrated over the entire energy spectrum ( $\varepsilon$ ) of the neutrons. In practice, J is calculated by using Eq. 3.1 with the flux monitor minerals of known age.

The J-factor distributions are shown in Figure 3.2 for the first (Figure 3.2a) and second (Figures 3.2b and 3.2c) irradiation sessions. J-factor scales differ for each irradiation session. At each position, 3 to 6 aliquots were measured. The calculated J-factor values are plotted with open circles (the number of aliquots measured is given in the parentheses to the left of each group for clarity). Average J-factor values are shown with solid symbols. Each

data set is fit with a polynomial, and J-factors for each sample of unknown age are extrapolated on the basis of sample position. The coefficients for the polynomials are given for each sample tube in Figure 3.2. Extrapolated J-factor values for the unknown samples are listed in Tables 3.2 and 3.4 (a, b). The J-factor for the flux monitor between the 4 and 5 cm positions in Figure 3.2a varies significantly from the rest of the samples in that tube. Agreement between the ages of four internal standards distributed in this tube (next section), which were calculated using the interpolated J-factors (Table 3.2), suggests that this variation is real and accounted for properly.

### *C. Internal standard*

The internal standard of unknown age, which was divided into three packages per irradiation tube and distributed throughout them (Figure 3.4), was used to confirm that the J-factors have been calculated correctly from the flux monitors of known age. All anorthoclase crystals from the internal standard used in this study were extracted from one large block of pumice. A summary of the  $^{40}\text{Ar}/^{39}\text{Ar}$  measurements for each individual package, including the individual weighted mean and isochron ages, is shown in Table 3.2. Average isochron ages from each Lab Session are also listed.

Inverse isochron plots of the data from both Lab Sessions are shown in Figure 3.3. Isochron ages of packages from different positions (labeled “A-F,” and “gamma” in the case of the sample exposed to  $\gamma$ -radiation) show good agreement in a given irradiation tube, and the averages from the two Lab Sessions overlap within the  $1\sigma$  uncertainty limits. The two methods of calculating an age (isochron and weighted mean ages) show better agreement for samples measured during Lab Session 1 than for measurements made during Lab Session 2. This is partly due to the slightly lower  $^{40}\text{Ar}/^{36}\text{Ar}$  intercept values for samples from Lab Session 2 (all  $< 290$ ), which in turn leads to a slightly younger age since weighted mean ages assume  $^{40}\text{Ar}/^{36}\text{Ar}$  equal to 295.5.

In summary, the average isochron ages from each Lab Session ( $6.2 \pm 0.1$  Ma and  $6.4 \pm 0.2$  Ma) are considered to be the best estimates of the age of the anorthoclase from pyroclastic flow deposit *Tmr3*.

#### D. Samples exposed to $^{137}\text{Cs}$

A summary of samples exposed to the  $\gamma$ -radiation source is given with isochron ages and  $1\sigma$  uncertainties in Table 3.3. A portion of each sample not exposed to the  $\gamma$ -radiation source (separated with heavy liquids in the traditional manner) was also measured to ensure that the  $^{40}\text{Ar}/^{39}\text{Ar}$  systematics had not somehow been disturbed. Phenocrysts from one of the pairs of samples (WIN-94-38 and WIN-94-38 $\gamma$ ) did not contain enough radiogenic argon to measure. The other three samples show reasonable agreement between the sub-samples. For each of these samples a combined  $^{40}\text{Ar}/^{39}\text{Ar}$  isochron age is calculated (final column of Table 3.3) by performing a York regression on the combined data from both sub-samples and using an average value for the J-factors. Since sample pairs were always placed adjacent to each other in the sample tubes, the J-factors are very similar for each sample in a pair (J-factors for these samples are included in Tables 3.2 and 3.4b).

An isochron age of  $6.2 \pm 0.1$  Ma for the  $\gamma$ -irradiated anorthoclase sample from the internal standard (INF-94-53 $\gamma$  in Table 3.2) is identical to the value determined for the non- $\gamma$ -irradiated sample (INF-94-53C in Table 3.2). As seen in Figure 3.3, there is good distribution along the isochron of the aliquots measured for both of these samples. Due to this result, determined during Lab Session 1, all anorthoclase separates used as the internal standard during Lab Session 2 were exposed to the  $^{137}\text{Cs}$  source to facilitate mineral separation.

The  $\gamma$ -irradiated anorthoclase sample from *Tmr<sub>sf</sub>* (LCR-94-72 $\gamma$  in Table 3.4b ( $12.5 \pm 0.5$  Ma)) also shows very good agreement with the non- $\gamma$ -irradiated sample (LCR-94-72 in Table 3.4b ( $12.6 \pm 0.3$  Ma)). The result of combining both data sets is a slightly older age ( $12.7 \pm 0.3$  Ma); however, it overlaps with the individual ages within  $1\sigma$  uncertainty. The MSWD of the combined samples is 0.45, slightly less than the MSWD of each sub-sample, but

it still falls within the permissible range of “critical MSWD values” for 6 degrees of freedom (0.207-2.400; Mahon, 1996). There is relatively little spread along the isochron for either sub-sample (Figure 3.4d).

The third pair of samples consists of plagioclase phenocrysts from *Tmd<sub>tomb</sub>*. The non- $\gamma$ -irradiated sample (PHO-94-86 in Table 3.4b) yields an isochron age of  $15.7 \pm 2.2$  Ma, which agrees within  $1\sigma$  uncertainty with the isochron age of  $16.9 \pm 0.8$  Ma from the  $\gamma$ -irradiated sample (PHO-94-86 $\gamma$  in Table 3.4b). For both samples the MSWD is outside of the 95% critical range. Interestingly, the combined isochron age (using an average J-factor) of  $16.4 \pm 0.7$  Ma yields an MSWD of 1.36 which is within the 95% critical range for 11 degrees of freedom (0.347-1.991; Mahon, 1996). Evidently the two sub-samples define a better isochron when combined. The sub-sample exposed to the  $\gamma$  source consistently yielded a more radiogenic component than the non- $\gamma$ -irradiated sample (Figure 3.4c). This could be the result of selecting higher quality (i.e., less fractured or discolored) grains from the  $\gamma$ -irradiated population versus the non- $\gamma$ -irradiated sub-sample. Finally, the combined age of  $16.4 \pm 0.7$  Ma agrees within  $1\sigma$  uncertainty with dates determined from six other *Tmd<sub>tomb</sub>* rock samples (see Figure 3.4c), especially with one (PHO-94-10) taken from a nearby locality and measured during the other Lab Session.

From these few tests it appears that exposure to a  $\gamma$ -radiation source is a useful mineral separation technique which does not affect  $^{40}\text{Ar}/^{39}\text{Ar}$  isotope systematics of anorthoclase and plagioclase separates.

#### E. All other samples

The same  $^{40}\text{Ar}/^{39}\text{Ar}$  parameters described in Table 3.2 for the internal standard are given in Tables 3.4a (Lab Session 1) and 3.4b (Lab Session 2) for all other samples, and inverse isochron plots for each sample are given in Figures 3.4 (a-i). The plots are arranged from the oldest lithologic unit (Figure 3.4a) to the youngest (Figure 3.4i). There are no data listed or plots shown for the samples listed on the bottom of Table 3.4b which could not be successfully measured.

Of the remaining 18 samples not yet specifically discussed, eight of them have MSWD values outside of the 95% critical range. Six of these 8 have weighted mean ages which agree with the isochron ages within the  $1\sigma$  uncertainties, thus the anomalous MSWD values could be the result of underestimating uncertainties associated with individual measurements. The age discrepancy of the two samples which have significantly different isochron and weighted mean ages, KC-95-19 (Figure 3.4b) and SUN-94-30 (Figure 3.4f), is likely the result of the low  $^{40}\text{Ar}/^{36}\text{Ar}$  intercept values. Note that these two samples have MSWD values between 2.1 and 2.4, which in some studies are considered to be acceptable (e.g., Spell and Harrison (1993) accept MSWD values  $< 2.5$  as evidence for a homogeneous crystal population). One of these two samples (KC-95-19) is a basalt which shows general age agreement with other Group 3 lithologic units, which includes another basalt (Figure 3.4b) and seven dacite samples (Figure 3.4c), thus its isochron age of  $17.1 \pm 1.1$  Ma is interpreted to be the best estimate. In contrast, the other sample (SUN-94-30), from  $Tmr_{SiW}$  in Group 6, yields an anomalously young age ( $5.7 \pm 0.2$  Ma) in comparison to three other samples from the same series of pyroclastic flow deposits (6.5-6.7 Ma; Figure 3.4f). Additionally,  $^{40}\text{Ar}/^{39}\text{Ar}$  ages of 5 overlying units within Groups 6 and 7 constrain these tuffs to be pre-6.5 Ma in age (Figure 3.5). Alteration of the plagioclase phenocrysts in this tuff is rare, and thus loss of radiogenic argon from alteration products, which would result in an anomalously low age, is unlikely to have occurred. Sample SUN-94-30 was taken from the brown, glassy base of densely welded  $Tmr_{SiW}$ , in contrast to the other three samples from this tuff which were taken higher in the section. It is possible that the glass matrix adhering to the phenocrysts was not completely removed, thereby providing material more susceptible to radiogenic argon loss due to hydration and submicroscopic devitrification than the phenocrysts (McDougall and Harrison, 1988).

Those measurements in which an initial, low wattage ( $\sim 2$  W), partial fusion step was performed (boldface rows in Appendix D) resulted in data points which plotted closer to the  $^{36}\text{Ar}/^{40}\text{Ar}$  intercept because primarily atmospheric argon was released in these initial fusions (i.e., these steps had low radiogenic yields). Interestingly, these partial fusion steps give consistently younger model ages than the rest of the measurements for a given sample, perhaps indicating partial  $^{40}\text{Ar}^*$  loss at or near grain surfaces. The partial fusion

measurements were retained in the final analyses in order to better define the isochron for each sample. Some inverse isochron plots of such samples are shown in Figure 3.4 (c, e, f, and g); the partial fusion measurements in these plots are shown with filled squares.

Renne and Basu (1991) and Renne and others (1992) found similar low-temperature discordances for plagioclase samples using an incremental laser heating technique. They attribute their low apparent ages to argon loss through minor reheating ( $\leq 150^{\circ}\text{C}$ ) or alteration of the volcanic rocks. Since partial fusion with a laser is somewhat analogous to the low temperature steps in step-heating experiments, one can also examine studies in which anomalously young ages were found during the initial heating steps to better understand the nature of the anomalous "partial fusion" ages found in this study. Common explanations include loss of  $^{40}\text{Ar}^*$  from less retentive mineral sites due to a thermal disturbance such as post-crystallization heating (Turner, 1971b) or surface features such as lattice defects and microfissures (Geyh and Schleicher, 1990, p. 68), or argon diffusion during slow cooling ( $\sim 5^{\circ}\text{C}/\text{Ma}$ ) over the range of  $^{40}\text{Ar}^*$  retention temperatures (Berger and York, 1981; Harrison and McDougall, 1982). Slow cooling and/or post-crystallization heating seem unlikely for the volcanic lavas and pyroclastic flow deposit examined here. Although emplacement temperatures of volcanic units are well above the range of closure temperatures for argon, the author knows of no studies in which it was shown that the emplacement of a lava flow or pyroclastic flow deposit upon an older volcanic unit disturbed the argon retention in the underlying unit. This is probably due to the short period of time that the overlying unit remains at the high emplacement temperature. For the samples examined in this study, minor surface alteration seems to be the most likely reason for the anomalously young ages found during the low wattage fusion steps. As discussed by Durrance (1986, p. 290), both weathering and ground water interactions can promote argon loss.

The measured aliquots of most samples exhibit a wide range of values for radiogenic yield (Appendix D). This is likely due to the presence of cracked or altered plagioclase phenocrysts. Kelley and others (1994) found a range of values for atmospheric argon content (35-78%) for similarly altered plagioclase phenocrysts which they associate with significant variations in Ca/K ratios within these altered crystals. Their study of pristine (i.e., colorless and

transparent) plagioclase crystals resulted in greater, less variable, radiogenic yields and a smaller range of Ca/K values.

About half of the samples have a  $^{40}\text{Ar}/^{36}\text{Ar}$  intercept which deviates significantly from the present-day atmospheric value of 295.5. In general, the intercepts are less than 295.5. There could be a geologic explanation for the consistently low  $^{40}\text{Ar}/^{36}\text{Ar}$  intercepts, such as isotopic mass fractionation of atmospheric argon prior to, or even after, eruption of the rock to produce a trapped component which has a  $^{40}\text{Ar}/^{36}\text{Ar}$  ratio lower than the present-day, atmospheric value (e.g., Krummenacher, 1970; Kaneoka, 1980; Lippolt et al., 1990).  $^{40}\text{Ar}/^{36}\text{Ar}$  ratios are generally  $> 2000$  for volcanic rocks from the mantle as determined on MORB glasses (e.g., Ozima, 1975; Dymond and Hogan, 1978; Ozima and Podosek, 1983; Allègre et al., 1987) and  $> 10,000$  in mantle xenoliths (Dunai and Baur, 1995); thus, it is unlikely that mixing with a mantle reservoir would produce anomalously low  $^{40}\text{Ar}/^{36}\text{Ar}$  ratios.

It is also unlikely that variables related to the analytical technique might have produced the anomalously low  $^{40}\text{Ar}/^{36}\text{Ar}$  intercept values. For example, because most samples analyzed in this study are not very radiogenic, the  $^{40}\text{Ar}/^{36}\text{Ar}$  intercept value is very dependent upon the mass discrimination of the mass spectrometer. Uncertainty in the mass discrimination is  $\pm 0.11\text{-}0.18\%$  (M. Grove, pers. comm.), which translates to a  $2\sigma$  uncertainty of  $\pm 0.001$ . The effect on sample ages is a change of  $< 1\%$  (i.e., smaller than the measurement precision) for reasonable uncertainties in the value for the mass discrimination. Uncertainties in other variables such as the Ca and K correction factors have an even less pronounced effect on calculated ages. For example, a  $0.1\%$  change in the value of the Ca correction factor changes typical sample ages by  $< 0.5\%$ . These correction factors are known to  $0.01\%$ . Finally, given the large amount of material fused for each measurement, incomplete getting of the gas could also be the cause of the low intercept values. Hydrocarbon contamination could yield isobaric interference with  $^{36}\text{Ar}$ , and thus lower the  $^{40}\text{Ar}/^{36}\text{Ar}$  ratio.

### 3.5. Discussion

#### A. Volcanism and structural implications

A stratigraphic column with the  $^{40}\text{Ar}/^{39}\text{Ar}$  isochron ages determined in this study is shown in Figure 3.5. One sample date out of stratigraphic order (shown in parentheses) is interpreted to be the result of glass contamination (from the sample matrix) which perhaps lost radiogenic argon due to hydration and submicroscopic devitrification (McDougall and Harrison, 1988). Based upon the geochronologic results determined in this study and the relative volume that each lithologic unit represents in the field area, major pulses of volcanism occurred at ~ 15-17 Ma and ~ 6-7 Ma. Minor pulses of volcanism at ~ 12.5 and ~ 9 Ma are also documented. A younger pulse of primarily andesitic volcanism represented by Group 7 rocks is poorly dated in this study (two of the samples in this group,  $Tma_{hem}$  and  $Tma_{gem}$ , were discarded due to lack of measurable radiogenic argon). Rhyolite flows ( $Tmr_{can}$ ) from Group 7 which yielded two ages around 6 Ma overlie at least one of these andesite flows ( $Tma_{gem}$ ), thereby constraining at least some lava flows in Group 7 to be part of the ~ 6-7 Ma pulse of volcanism as well.

The results found here constrain the timing of deposition of  $Tmvs$  (in Group 2) in Santa Isabel Wash to ~ pre-17 Ma. These volcanoclastic breccias and debris flows are up to 500 meters thick and interpreted to be the products of catastrophic sedimentation from high-standing, unstable slopes of the early and middle Miocene, subduction-related volcanic arc (e.g., Gastil et al., 1979). Correlative deposits exist in many places along eastern and central Baja California (Hausback, 1984; Stock, 1989; Dorsey and Burns, 1994; Lewis, 1996). In some of these localities, the age of deposition is constrained to be younger than 16 Ma (see Chapter II for details). It thus appears that the deposition of  $Tmvs$  in Santa Isabel Wash ended earlier than in nearby areas and was replaced by eruption of near-source-facies deposits ( $Tmd_{tomb}$  of Group 3).



On the basis of structural evidence, most extensional deformation in the area post-dates the deposition of the ~6-7 Ma Group 6 and 7 rocks. However, some evidence exists for pre-6 Ma deformation. Several faults which do not offset Group 6 rocks cut underlying Group 2 and 3 rocks (15-17 Ma), and in one locality Group 4 (~12.5 Ma) and 5 (~9 Ma) rocks as well. Some of these faults could have been active any time between 15 Ma and 6 Ma, while others were clearly active between 9 Ma and 6 Ma. Additionally, Group 6 pyroclastic flow deposits bank and fill against a significant paleo-topographic slope interpreted to be an accommodation zone (see Chapter IV). The development of this structure is consequently constrained to pre-6 Ma time. A complete discussion of the history of deformation is given in Chapter IV and incorporates additional details not discussed here such as amount and direction of extension.

#### B. *Other geochronologic studies of same units*

Two of the pyroclastic flow deposits dated in this study have also been dated in adjacent areas. The results are summarized in Table 3.5. A late Miocene ignimbrite first defined in southern Valle Chico (*Tmr3* of Stock (1989)) is correlative with the lithologic unit from which the internal standard was separated in this study (*Tmr3*). This unit has also been correlated and mapped in the Sierra San Fermín (Lewis, 1996). Correlations are made on the basis of outcrop appearance and stratigraphic position, thin section analysis, and electron microprobe results of feldspar compositions. Geochronologic results from anorthoclase crystals separated from samples collected in these areas are listed with the results from this study in the top half of Table 3.5. Also shown are recent results from Stock (unpub. data) in which a portion of the mineral separate used here for the internal standard (INF-94-53) was measured at a different lab (MIT - Cambridge Laboratory for Argon Isotopic Research).

Both of the  $^{40}\text{Ar}/^{39}\text{Ar}$  ages determined in the Santa Isabel Wash for *Tmr3* (this study) are in general agreement with values obtained in the Sierra San Fermín (Lewis, 1996). They also overlap (within  $2\sigma$  uncertainty) with two dates determined via K/Ar measurements in the southern Valle Chico (Stock, 1989) and with Stock's unpublished data. The  $4.27 \pm 0.12$  Ma

K/Ar age from the Southern Valle Chico is considered to be less reliable than the other two ages determined in that study because the argon gas extraction was performed at a temperature below 1650°C and thus may not have completely released all of the argon gas (Stock, 1989).

In summary, the results from these independent studies suggest an age between 6.1 and 6.7 Ma for pyroclastic flow deposit *Tmr3*. Paleomagnetic studies of *Tmr3* from Santa Isabel Wash (this study; see Chapter V) and the Sierra San Fermín and Sierra San Felipe (Lewis, 1994; Lewis and Stock, in review) indicate that the unit preserves normal polarity magnetization. The age of deposition is thus further constrained to have occurred most likely during normal polarity Subchron C3An.2n between 6.269 and 6.567 Ma (Cande and Kent, 1995).

Also shown in Table 3.5 are geochronologic results from an older pyroclastic flow deposit collected from four different locations (*Tmr1* of Bryant (1986), Stock (1989), and Lewis (1996), but called *Tmr<sub>sf</sub>* (Tuff of San Felipe) in this study after Stock et al., 1996; 1997). Chapter II gives detailed criteria for lithologic correlation between these localities. Geochronologic results from this unit are more variable than those determined for *Tmr3*. An exposure of *Tmr<sub>sf</sub>* in Santa Rosa Basin (~40 km to the north of this study area; see Figure 3.2) yields a whole rock K/Ar age of  $14.2 \pm 0.9$  (Gastil et al., 1979) which is slightly older than the age reported here ( $12.7 \pm 0.6$  Ma). The age calculated in this study agrees with one date out of two from both the Southern Valle Chico (Stock, 1989) and the Sierra San Fermín (Lewis, 1996). The  $10.85 \pm 0.32$  Ma age from the Southern Valle Chico (Stock, 1989) and  $10.6 \pm 0.1$  Ma age from the Sierra San Fermín (Lewis, 1996) are younger than the other geochronologic results. Stock (pers. comm., 1994) believes that the  $^{40}\text{Ar}/^{39}\text{Ar}$  total fusion age determined for the Southern Valle Chico sample may be unreliable due to incomplete sample fusion. Lewis (1996) suggests that the  $10.6 \pm 0.1$  Ma age from the Sierra San Fermín is a more reliable date than the older date found in that study on the basis of paleomagnetic analysis and mapping. However, it is possible that this relatively younger age (in comparison to the others in Table 3.5) could be the result of using 5% HF for etching during mineral separation (Lewis, 1996). As mentioned above, this can result in a younger age.

In summary, the age of pyroclastic flow deposit  $Tmr_{sf}$  is almost certainly between 10.5 and 14 Ma. The preferred age determined in this study is  $\sim 12.5$  Ma. Reversed polarity magnetization preserved in  $Tmr_{sf}$  in the Sierra San Fermín and Sierra San Felipe (Lewis, 1994; Lewis and Stock, in review) is interpreted here to imply that deposition probably occurred during reversed polarity Subchron C5An.2r (12.401-12.678 Ma; Cande and Kent, 1995).

### 3.6. Conclusions

Crystallization ages have been successfully determined with  $^{40}\text{Ar}/^{39}\text{Ar}$  geochronology for plagioclase and anorthoclase crystals extracted from middle to late Miocene volcanic lavas and pyroclastic flow deposits from the northern margin of the PVP (northern Sierra Santa Isabel) in northeastern Baja California, Mexico (locally in the Santa Isabel Wash). Measurement precision was  $\pm 2\text{-}7\%$  for plagioclase samples (with one exception of  $\pm 14\%$ ) and  $\pm 2\text{-}4\%$  for anorthoclase separates. Twenty-one rock samples yield ages spanning  $\sim 17\text{-}6$  Ma. Major pulses of volcanism occurred at  $\sim 15\text{-}17$  Ma and  $\sim 6\text{-}7$  Ma with minor pulses at  $\sim 12.5$  Ma and  $\sim 9$  Ma. Detailed mapping and stratigraphy suggest that one of the 21 sample dates (from lithologic Group 6) is too young (perhaps due to radiogenic argon loss in some glassy matrix contaminant), but all other samples show excellent consistency with the stratigraphic sequence. Two of the tuffs dated in this study ( $Tmr3$  and  $Tmr_{sf}$ ) have also been dated independently by other workers from nearby localities using K/Ar and  $^{40}\text{Ar}/^{39}\text{Ar}$  techniques. In general, there is good agreement in age determinations between these different studies.

The results of this study help constrain the timing of extensional deformation in Santa Isabel Wash. Most extensional faulting post-dates the deposition of a series of  $\sim 6\text{-}7$  Ma tuffs and lava flows. However, the tuffs were deposited against a significant paleo-topographic slope interpreted to be a structural accommodation zone, thus the development of this structure must have been prior to 7 Ma. Some pre-6 Ma faulting (post-9 Ma in some places

but in others possibly as old as 15 Ma) is also evident in the area. Chapter IV discusses the history of deformation in detail.

Table 3.1. UTM coordinates of collection locations for geochronology samples.

Sample ID	Lithologic unit	UTM coord. (north)	UTM coord. (east)
INF-94-53	<i>Tmr<sub>3</sub></i>	3362905mN	0701401mE
INF-94-75	<i>Tmr<sub>ao</sub></i>	3362808mN	0701203mE
INF-94-47	<i>Tmr<sub>siw</sub></i>	3362507mN	0703502mE
INN-94-33	<i>Tmr<sub>siw</sub></i>	3365004mN	0698608mE
CHO-94-45	<i>Tmr<sub>siw</sub></i>	3365307mN	0700800mE
INF-94-68	<i>Tma<sub>toro</sub></i>	3362507mN	0703008mE
DIN-94-46	<i>Tmd<sub>tomb</sub></i>	3362807mN	0703509mE
INF-94-52	<i>Tmd<sub>tomb</sub></i>	3363300mN	0701506mE
INN-94-73	<i>Tmd<sub>tomb</sub></i>	3364403mN	0698208mE
WIN-94-32	<i>Tmd<sub>tomb</sub></i>	3365004mN	0699204mE
PHO-94-10	<i>Tmd<sub>tomb</sub></i>	3367102mN	0702305mE
SUN-94-30	<i>Tmr<sub>siw</sub></i>	3365501mN	0699403mE
CAN-95-12	<i>Tmr<sub>can</sub></i>	3367705mN	0709305mE
CAN-95-11	<i>Tmr<sub>can</sub></i>	3367803mN	0709909mE
LCR-94-110	<i>Tmr<sub>ec</sub></i>	3366006mN	0704401mE
LCS-94-72	<i>Tmr<sub>sf</sub></i>	3365807mN	0697809mE
PHO-94-86	<i>Tmd<sub>tomb</sub></i>	3366607mN	0702108mE
INF-94-24	<i>Tmb<sub>lol</sub></i>	3361806mN	0702004mE
LCR-95-08	<i>Tmd<sub>tomb</sub></i>	3365305mN	0703704mE
KC-95-17	<i>Tmr<sub>bio</sub></i>	3362004mN	0698503mE
KC-95-19	<i>Tmb<sub>kc</sub></i>	3362309mN	0699204mE

Table 3.2.  $^{40}\text{Ar}/^{39}\text{Ar}$  results from an internal (secondary) standard (anorthoclase from *Tmr3*) used to confirm the J-factor calculations determined by using flux monitors of known age (external standard). The  $^{40}\text{Ar}/^{39}\text{Ar}$  and  $^{40}\text{Ar}/^{36}\text{Ar}$  intercepts are calculated using a York Regression. Both weighted mean ages, which assume  $^{40}\text{Ar}/^{36}\text{Ar} = 295.5$ , and isochron ages are listed. Inverse isochron plots for each Lab Session are shown in Figure 3.3.

<sup>40</sup>Ar/<sup>39</sup>Ar results of internal standard (anorthoclase) from lithologic unit *Tmr3*

Sample	# of aliquots included in calculation over total #	Total mass (mg)	<sup>40</sup> Ar/ <sup>39</sup> Ar intercept ( $\pm 1\sigma$ )	<sup>40</sup> Ar/ <sup>36</sup> Ar intercept ( $\pm 1\sigma$ )	J-factor	Weighted Mean Age (Ma) ( $\pm 1\sigma$ )	Isochron Age (Ma) ( $\pm 1\sigma$ )	MSWD	95% critical MSWD range (from Mahon, 1996)
<b>Lab Session 1</b>									
<b>Tube 1</b>									
INF-94-53A	6/6	1/3 of 145	8.37 $\pm$ 0.07	292.9 $\pm$ 2.3	0.0004178	6.2 $\pm$ 0.1	6.3 $\pm$ 0.1	4.80	0.121-2.775
INF-94-53B	5/5	1/3 of 145	8.23 $\pm$ 0.06	291.3 $\pm$ 1.4	0.0004215	6.2 $\pm$ 0.1	6.2 $\pm$ 0.1	1.00	0.072-3.117
INF-94-53C	5/5	1/3 of 145	8.29 $\pm$ 0.06	291.8 $\pm$ 2.7	0.0004174	6.1 $\pm$ 0.1	6.2 $\pm$ 0.1	3.19	0.072-3.117
INF-94-53y	4/4	67	8.22 $\pm$ 0.07	291.6 $\pm$ 1.7	0.0004191	6.1 $\pm$ 0.1	6.2 $\pm$ 0.1	1.12	0.025-3.690
average:	20/20						6.2 $\pm$ 0.1		
<b>Lab Session 2</b>									
<b>Tube 2</b>									
INF-94-53A	4/6	1/6 of 132.5	4.38 $\pm$ 0.18	287.1 $\pm$ 3.6	0.0008170	6.0 $\pm$ 0.2	6.4 $\pm$ 0.3	1.29	0.025-3.690
INF-94-53B	5/5	1/6 of 132.5	4.50 $\pm$ 0.11	283.4 $\pm$ 4.6	0.0008275	6.3 $\pm$ 0.1	6.7 $\pm$ 0.2	2.27	0.072-3.117
INF-94-53C	5/5	1/6 of 132.5	4.50 $\pm$ 0.05	286.9 $\pm$ 1.9	0.0008059	6.2 $\pm$ 0.1	6.5 $\pm$ 0.2	0.33	0.072-3.117
<b>Tube 3</b>									
INF-94-53D	4/4	1/6 of 132.5	4.48 $\pm$ 0.07	286.7 $\pm$ 1.5	0.0008066	6.1 $\pm$ 0.1	6.5 $\pm$ 0.2	0.73	0.025-3.690
INF-94-53E	5/5	1/6 of 132.5	4.37 $\pm$ 0.05	289.4 $\pm$ 2.1	0.0008097	6.2 $\pm$ 0.1	6.4 $\pm$ 0.1	0.18	0.072-3.117
INF-94-53F	2/2	1/6 of 132.5	4.50 $\pm$ 0.05	287.8 $\pm$ 1.9	0.0007928	6.3 $\pm$ 0.1	6.4 $\pm$ 0.1	N/A	N/A
average:	25/27						6.4 $\pm$ 0.2		



Table 3.3. Summary of  $^{40}\text{Ar}/^{39}\text{Ar}$  isochron ages for  $\gamma$ -irradiated samples and their non- $\gamma$ -irradiated counterparts. Combined ages were calculated by combining measurements from both sub-samples and regressing the data using an average value for the J-factor. Sample WIN-94-38 did not have enough radiogenic argon to measure.

$\gamma$ -radiation experiment

Sample ID	Lithologic unit	Mineral analyzed	$^{40}\text{Ar}/^{39}\text{Ar}$ isochron age (Ma) $\pm 1\sigma$		
			$\gamma$ -radiation	control (no $\gamma$ -radiation)	combined age
INF-94-53	<i>Tmr3</i>	anorthoclase	6.2 $\pm$ 0.1	6.2 $\pm$ 0.1	6.2 $\pm$ 0.1
LCS-94-72	<i>Tmr<sub>sf</sub></i>	anorthoclase	12.5 $\pm$ 0.5	12.6 $\pm$ 0.3	12.7 $\pm$ 0.3
PHO-94-86	<i>Tmd<sub>tomb</sub></i>	plagioclase	16.9 $\pm$ 0.8	15.7 $\pm$ 2.2	16.4 $\pm$ 0.7
WIN-94-38	<i>Tma<sub>toro</sub></i>	plagioclase	N/A	N/A	N/A

Table 3.4. (next 2 pages)  $^{40}\text{Ar}/^{39}\text{Ar}$  results from all samples of unknown age (with the exception of the internal standard (Table 3.2)). a) 10 samples analyzed during Lab Session 1, b) 12 samples analyzed during Lab Session 2, and 5 samples which did not have enough radiogenic argon to measure.

<sup>40</sup>Ar/<sup>39</sup>Ar results of samples of unknown age (Lab Session 1)

Sample	# of aliquots included in calculation over total #	Total mass (mg)	<sup>40</sup> Ar/ <sup>39</sup> Ar intercept ( $\pm 1\sigma$ )	<sup>40</sup> Ar/ <sup>36</sup> Ar intercept ( $\pm 1\sigma$ )	J-factor	Weighted Mean Age (Ma) ( $\pm 1\sigma$ )	Isochron Age (Ma) ( $\pm 1\sigma$ )	MSWD	95% critical MSWD range (from Mahon, 1996)
INF-94-75	10/13	59	8.45 $\pm$ 0.04	286.5 $\pm$ 1.0	0.0004178	6.2 $\pm$ 0.1	6.4 $\pm$ 0.1	7.77	0.273-2.188
INF-94-47	9/9	129	8.59 $\pm$ 0.12	292.6 $\pm$ 5.3	0.0004191	6.5 $\pm$ 0.1	6.5 $\pm$ 0.2	1.94	0.241-2.286
INN-94-33	8/8	125	8.81 $\pm$ 0.29	289.0 $\pm$ 1.4	0.0004184	5.7 $\pm$ 0.1	6.6 $\pm$ 0.3	0.56	0.207-2.400
CHO-94-45	8/8	119	8.94 $\pm$ 0.09	280.9 $\pm$ 3.7	0.0004180	6.5 $\pm$ 0.1	6.7 $\pm$ 0.2	0.98	0.207-2.400
INF-94-68	13/13	82	12.24 $\pm$ 0.50	288.4 $\pm$ 5.6	0.0004208	8.9 $\pm$ 0.1	9.3 $\pm$ 0.4	4.29	0.347-1.991
DIN-94-46	8/8	118	20.48 $\pm$ 0.25	287.1 $\pm$ 3.0	0.0004218	15.0 $\pm$ 0.1	15.5 $\pm$ 0.4	2.92	0.207-2.400
INF-94-52	12/12	84	21.09 $\pm$ 0.15	286.4 $\pm$ 2.1	0.0004202	15.5 $\pm$ 0.1	15.9 $\pm$ 0.3	1.24	0.325-2.050
INN-94-73	8/8	119	21.03 $\pm$ 0.64	289.4 $\pm$ 3.4	0.0004211	15.0 $\pm$ 0.1	15.9 $\pm$ 0.3	1.01	0.207-2.400
WIN-94-32	8/8	85	21.30 $\pm$ 0.28	280.0 $\pm$ 3.7	0.0004220	15.4 $\pm$ 0.1	16.1 $\pm$ 0.4	0.74	0.207-2.400
PHO-94-10	8/8	98	21.32 $\pm$ 0.25	267.3 $\pm$ 11.3	0.0004218	15.7 $\pm$ 0.1	16.2 $\pm$ 0.4	5.02	0.207-2.400

<sup>40</sup>Ar/<sup>39</sup>Ar results of samples of unknown age (Lab Session 2)

Sample	# of aliquots included in calculation over total #	Total mass (mg)	<sup>40</sup> Ar/ <sup>39</sup> Ar intercept ( $\pm 1\sigma$ )	<sup>40</sup> Ar/ <sup>36</sup> Ar intercept ( $\pm 1\sigma$ )	J-factor	Weighted Mean Age (Ma) ( $\pm 1\sigma$ )	Isochron Age (Ma) ( $\pm 1\sigma$ )	MSWD	95% critical MSWD range (from Mahon, 1996)
SUN-94-30	16/18	103	3.92 $\pm$ 0.12	285.3 $\pm$ 2.2	0.0008084	5.0 $\pm$ 0.1	5.7 $\pm$ 0.2	2.39	0.402-1.864
CAN-95-12	6/7	44	4.07 $\pm$ 0.28	286.5 $\pm$ 8.5	0.0008040	5.5 $\pm$ 0.2	5.9 $\pm$ 0.4	1.89	0.121-2.775
CAN-95-11	17/18	78	4.15 $\pm$ 0.12	267.6 $\pm$ 14.6	0.0008020	5.7 $\pm$ 0.1	6.0 $\pm$ 0.2	1.21	0.417-1.833
LCR-94-110	6/9	44	4.20 $\pm$ 0.15	285.8 $\pm$ 3.6	0.0008087	5.6 $\pm$ 0.1	6.1 $\pm$ 0.3	0.45	0.121-2.775
LCS-94-72γ	4/4	37	8.59 $\pm$ 0.26	287.7 $\pm$ 16.3	0.0008104	12.4 $\pm$ 0.2	12.5 $\pm$ 0.5	0.58	0.025-3.690
LCS-94-72	4/4	47	8.68 $\pm$ 0.12	287.8 $\pm$ 22.9	0.0008100	12.6 $\pm$ 0.1	12.6 $\pm$ 0.3	0.66	0.025-3.690
PHO-94-86	6/6	81	10.51 $\pm$ 1.47	297.7 $\pm$ 19.0	0.0008307	15.9 $\pm$ 0.3	15.7 $\pm$ 2.2	7.30	0.121-2.775
INF-94-24	14/15	82	11.18 $\pm$ 0.28	297.5 $\pm$ 7.0	0.0008120	16.4 $\pm$ 0.1	16.3 $\pm$ 0.5	1.96	0.367-1.942
LCR-95-08	5/5	39	11.21 $\pm$ 0.25	276.5 $\pm$ 12.5	0.0008298	16.3 $\pm$ 0.2	16.7 $\pm$ 0.5	0.64	0.072-3.117
PHO-94-86γ	7/7	85	11.34 $\pm$ 0.46	262.2 $\pm$ 9.2	0.0008290	14.6 $\pm$ 0.2	16.9 $\pm$ 0.8	0.07	0.166-2.560
KC-95-17	13/13	85	11.63 $\pm$ 0.79	286.5 $\pm$ 1.6	0.0008203	11.2 $\pm$ 0.5	17.1 $\pm$ 1.2	1.18	0.347-1.991
KC-95-19	15/18	85	11.77 $\pm$ 0.73	272.8 $\pm$ 7.0	0.0008102	14.3 $\pm$ 0.6	17.1 $\pm$ 1.1	2.11	0.385-1.900

Samples with too little radiogenic argon to measure (< 1% radiogenic yield):

HEM-95-37	149
WIN-94-38I	24
WIN-94-38II	20
WIN-94-38γ	38
GEM-95-49	81

Table 3.5. Comparison of the  $^{40}\text{Ar}/^{39}\text{Ar}$  results from this study with other geochronological results of the pyroclastic flow deposits *Tmr3* and *Tmr<sub>sf</sub>*. Locations are shown in Figure 3.2. Magnetic polarity information (Lewis, 1994; Lewis and Stock, in review; this study (Chapter V)) further constrains deposition of *Tmr3* to have occurred most likely between 6.269 and 6.567 Ma, and that of *Tmr<sub>sf</sub>* to have occurred between 12.401 and 12.678 Ma (ages of geomagnetic polarity boundaries taken from Cande and Kent, 1995). Note that the two ages determined for *Tmr3* in this study combine data from numerous aliquots separately positioned in the reactor and analyzed individually (see text for further details).

**Independent geochronology studies of anorthoclase  
separates from two ash flow tuffs in the vicinity of  
the Puertecitos Volcanic Province**

Unit	Location	Dating method	Age (Ma) $\pm 2\sigma$	Reference
<i>Tmr3</i>	S. Valle Chico	K/Ar	6.14 $\pm$ 0.16	Stock, 1989
<i>Tmr3</i>	S. Valle Chico	K/Ar	6.07 $\pm$ 0.20	Stock, 1989
<i>Tmr3</i>	S. Valle Chico	K/Ar	4.27 $\pm$ 0.12	Stock, 1989
<i>Tmr3</i>	Sierra San Fermin	$^{40}\text{Ar}/^{39}\text{Ar}^{\text{S}}$	6.5 $\pm$ 0.2 $^{\Phi}$	Lewis, 1996
<i>Tmr3</i>	Sierra San Fermin	$^{40}\text{Ar}/^{39}\text{Ar}^{\text{S}}$	6.7 $\pm$ 0.2 $^{\Phi}$	Lewis, 1996
<i>Tmr3</i>	Santa Isabel Wash	$^{40}\text{Ar}/^{39}\text{Ar}^{\text{L}}$	6.2 $\pm$ 0.2 $^*$	Nagy, this study
<i>Tmr3</i>	Santa Isabel Wash	$^{40}\text{Ar}/^{39}\text{Ar}^{\text{L}}$	6.4 $\pm$ 0.4 $^*$	Nagy, this study
<i>Tmr3</i>	Santa Isabel Wash	$^{40}\text{Ar}/^{39}\text{Ar}^{\text{L}}$	6.40 $\pm$ 0.19 $^*$	Stock, unpub. data
<i>Tmr<sub>sf</sub></i>	Santa Rosa Basin	K/Ar <sup>w</sup>	14.2 $\pm$ 0.9	Gastil et al., 1979
<i>Tmr<sub>sf</sub></i>	S. Valle Chico	K/Ar	11.99 $\pm$ 0.50	Stock, 1989
<i>Tmr<sub>sf</sub></i>	S. Valle Chico	$^{40}\text{Ar}/^{39}\text{Ar}^{\circ}$	10.85 $\pm$ 0.32	Stock, 1989
<i>Tmr<sub>sf</sub></i>	Sierra San Fermin	$^{40}\text{Ar}/^{39}\text{Ar}^{\text{L}}$	10.6 $\pm$ 0.1 $^{\omega}$	Lewis, 1996
<i>Tmr<sub>sf</sub></i>	Sierra San Fermin	$^{40}\text{Ar}/^{39}\text{Ar}^{\text{S}}$	13.3 $\pm$ 0.5 $^{\Phi}$	Lewis, 1996
<i>Tmr<sub>sf</sub></i>	Santa Isabel Wash	$^{40}\text{Ar}/^{39}\text{Ar}^{\text{L}}$	12.7 $\pm$ 0.6 $^*$	Nagy, this study
<i>Tmr<sub>sf</sub></i>	Santa Rosa Basin	$^{40}\text{Ar}/^{39}\text{Ar}^{\text{L}}$	12.53 $\pm$ 0.15 $^{\omega}$	Stock et al., 1996

<sup>S</sup>step-heating

<sup>L</sup>laser fusion

<sup>w</sup>whole-rock age

<sup>o</sup>one-step heating

<sup>Φ</sup>plateau age

<sup>\*</sup>isochron age

<sup>ω</sup>weighted mean age

Figure 3.1. Sample and flux monitor distribution in irradiated sample tubes. The label “ $\gamma$ ” indicates a sample exposed to  $^{137}\text{Cs}$  to facilitate mineral separation.



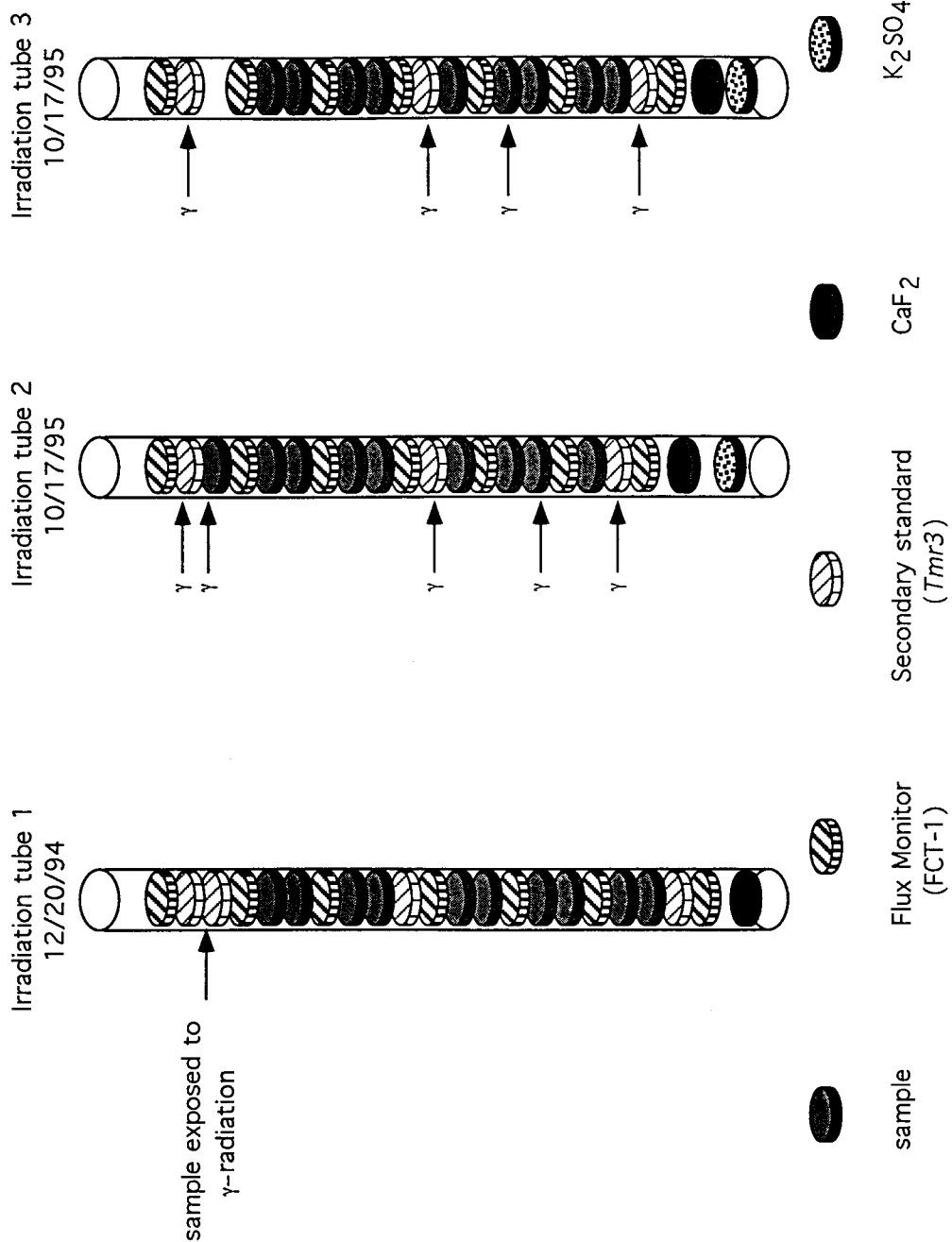
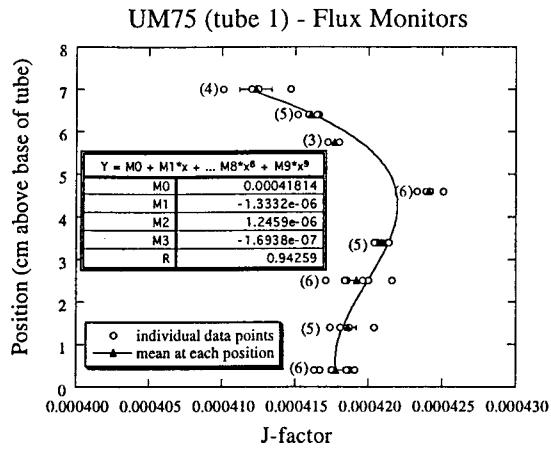
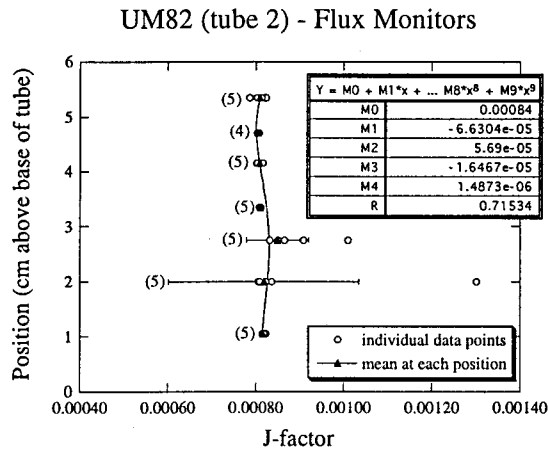


Figure 3.2. Plots of flux monitors of known age (FCT-1) and associated polynomial fits used to interpolate J-factors for samples of unknown age. Individual measurements are shown with open circles, and sample means at each position are shown with a solid triangle and  $1\sigma$  error bar. Number of aliquots measured at each position is also given in parentheses for clarity. Different scales are used for different Lab Sessions. a) One sample tube from Lab Session 1; b, c) two sample tubes from Lab Session 2.

A)



B)



C)

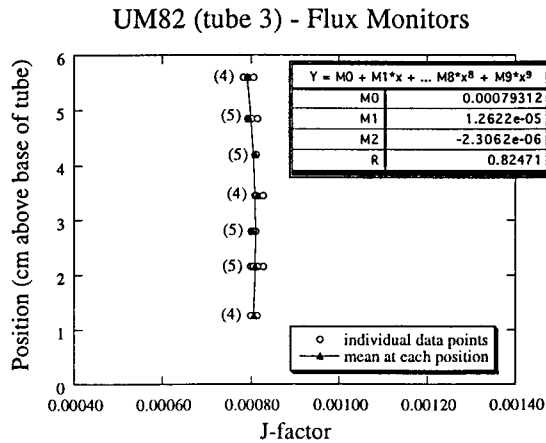
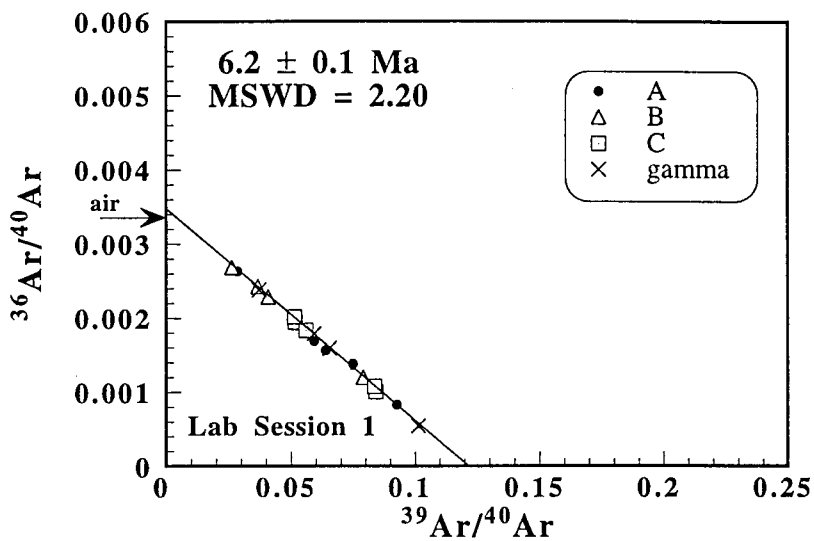


Figure 3.3. Inverse isochron plot of anorthoclase (internal standard) from *Tmr3* (within Group 6). The upper plot shows results from Lab Session 1, and the lower one gives results from Lab Session 2. Letters refer to different positions in the irradiated sample tubes. The sample labeled “gamma” was exposed to a  $\gamma$  source to facilitate mineral separation, and was positioned adjacent to sample “C” in the sample tube. Isochron ages with  $1\sigma$  uncertainty are given.

### Rhyolite #3 (Tmr3)

INF-94-53 (anorthoclase) - secondary standard



### Rhyolite #3 (Tmr3)

INF-94-53 (anorthoclase) - secondary standard

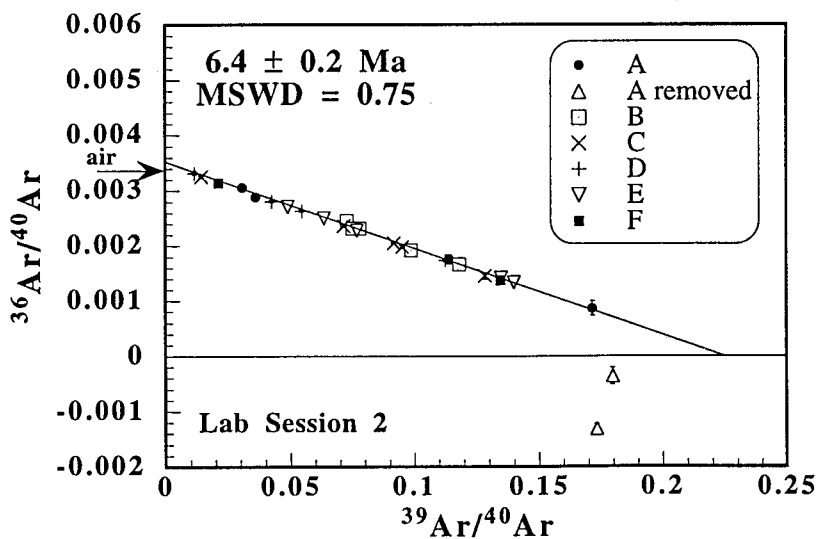
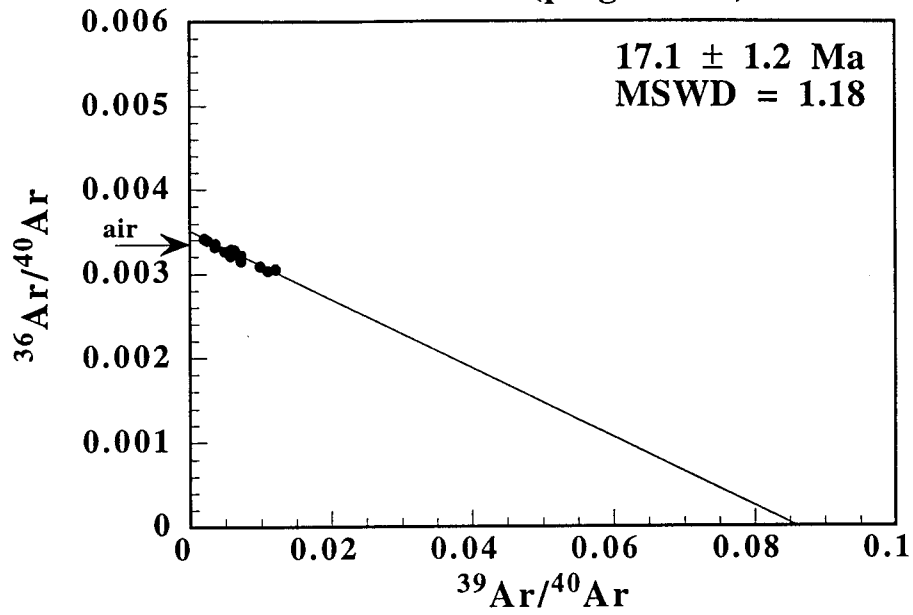
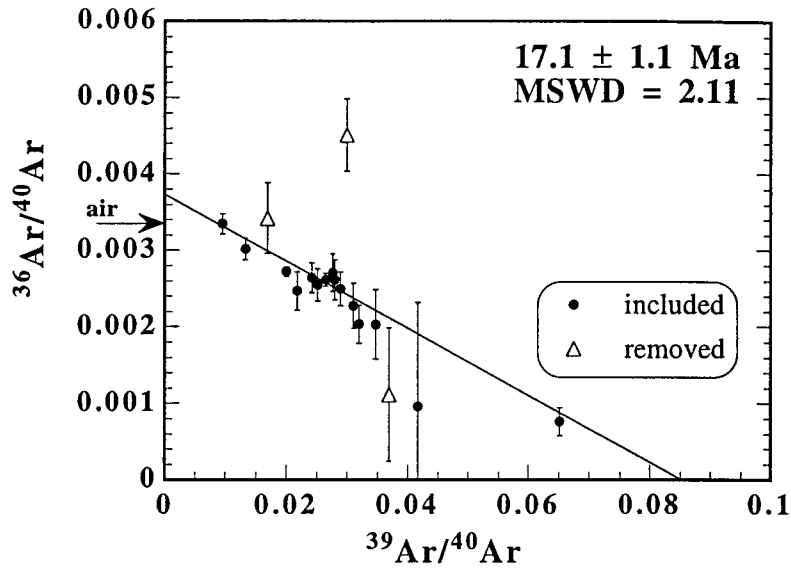


Figure 3.4. (next 10 pages) Inverse isochron plots of all samples of unknown age (not including internal standard). Error bars are  $1\sigma$  uncertainty. Isochron ages are also listed with  $1\sigma$  uncertainties. a) Plagioclase from an ignimbrite (*Tmr<sub>bio</sub>*) within Group 2; b) plagioclase from two different basalt flows (*Tmb<sub>lol</sub>*, *Tmb<sub>kc</sub>*) within Group 3; c) plagioclase from dacite flows (*Tmd<sub>tomb</sub>*) within Group 3 from 7 different localities; d) anorthoclase from an ignimbrite (*Tmr<sub>sf</sub>*) which comprises Group 4; e) plagioclase from a hornblende andesite (*Tma<sub>toro</sub>*) which comprises Group 5; f) plagioclase from the lowest pyroclastic flow deposit of Group 6 (*Tmr<sub>siw</sub>*) sampled at 4 locations; g) plagioclase from an overlying Group 6 pyroclastic flow deposit (*Tmr<sub>ao</sub>*); h) plagioclase from an overlying Group 6 pyroclastic flow deposit (*Tmr<sub>ec</sub>*); and i) plagioclase from 2 locations in a series of rhyolite flows (*Tmr<sub>can</sub>*) within Group 7. Measurements made following a low wattage fusion step (typically 2 W) are shown with solid squares. Measurements not included in the age calculation are identified as well.

***Biotite Tuff ( $T_{mr_{bio}}$ )*****KC-95-17 (plagioclase)**

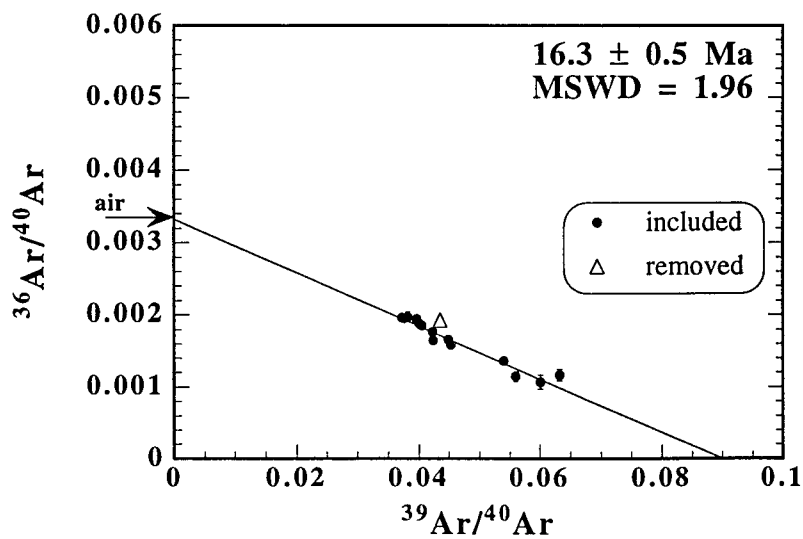
*Klondike Canyon basalt ( $Tmb_{kc}$ )*

KC-95-19 (plagioclase)

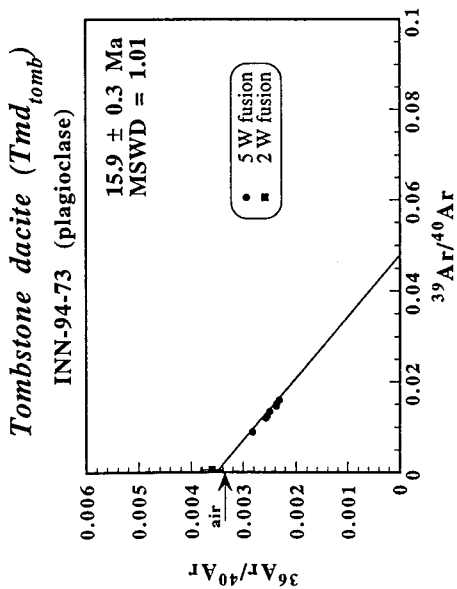
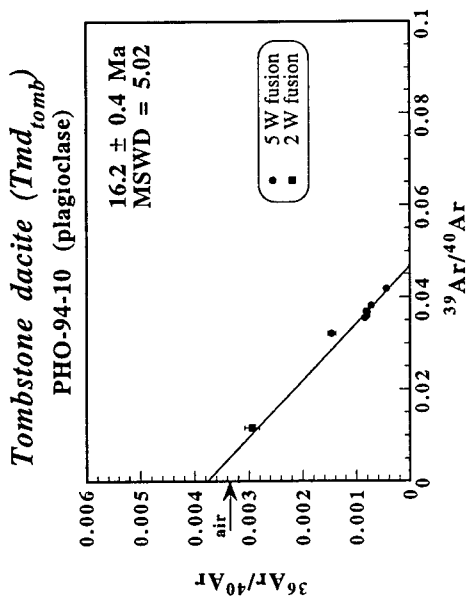
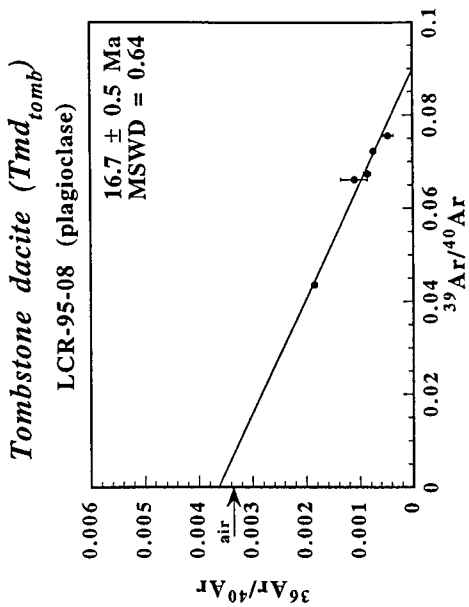
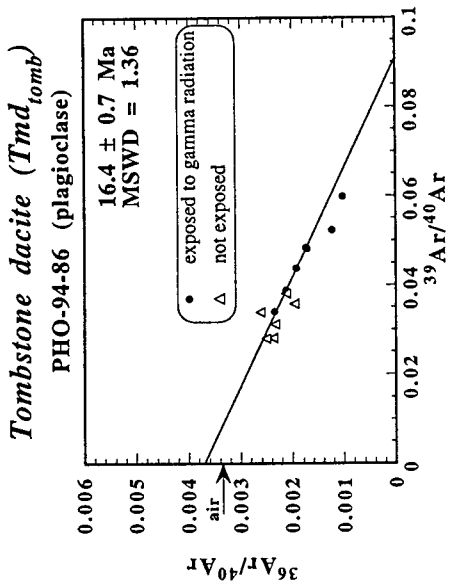


*Land of the Lost basalt ( $Tmb_{lol}$ )*

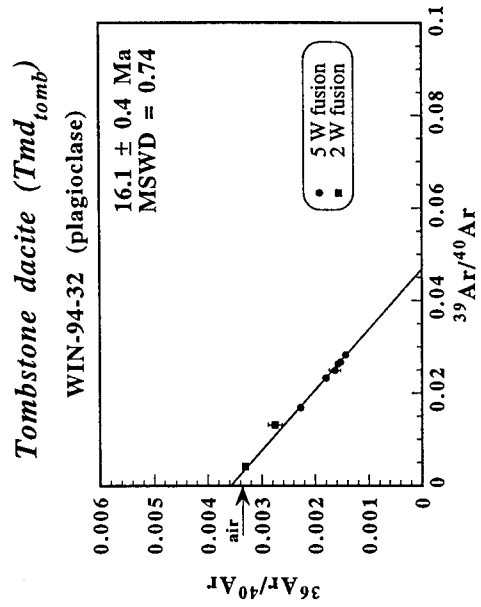
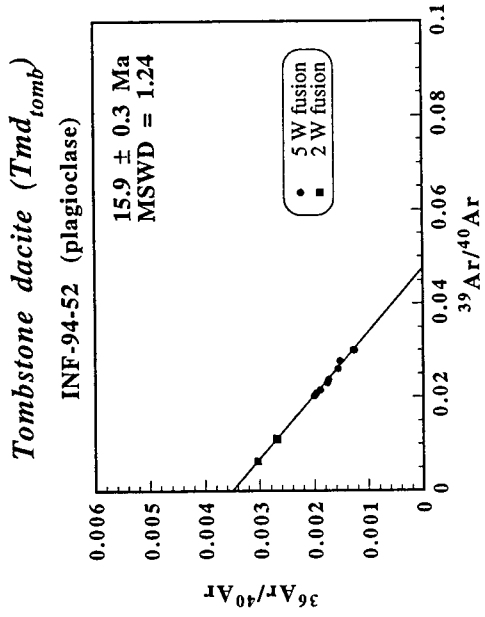
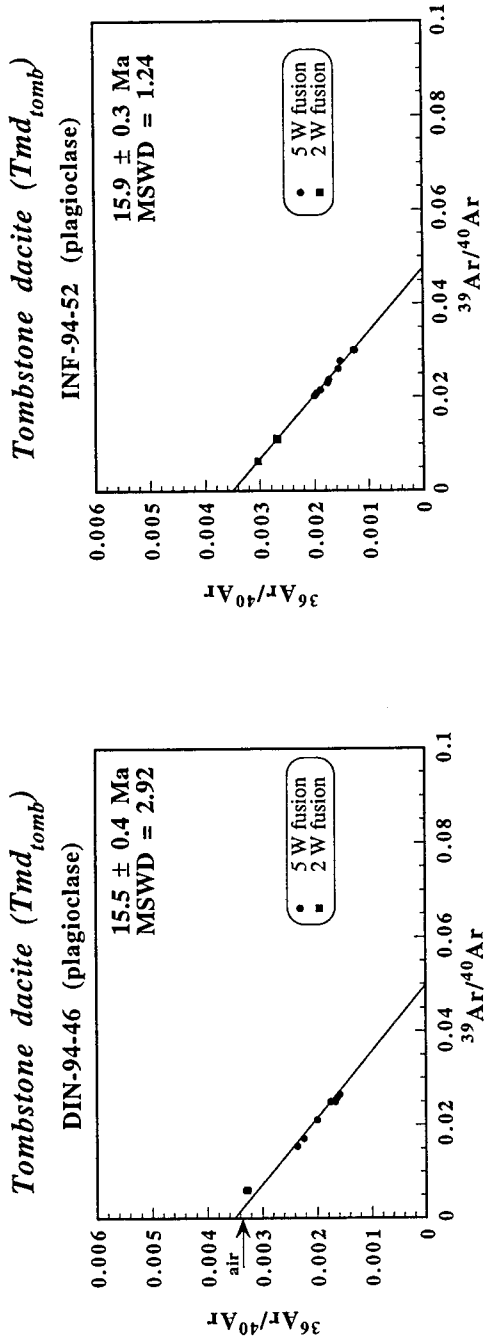
INF-95-24 (plagioclase)





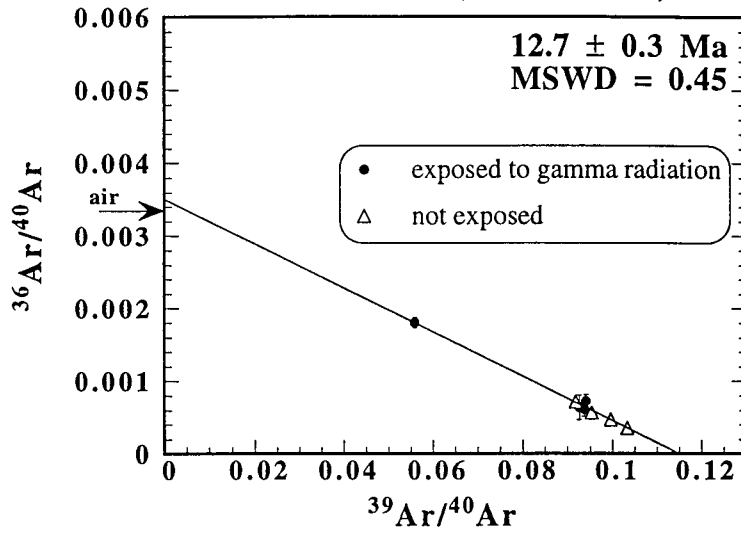


c (continued)



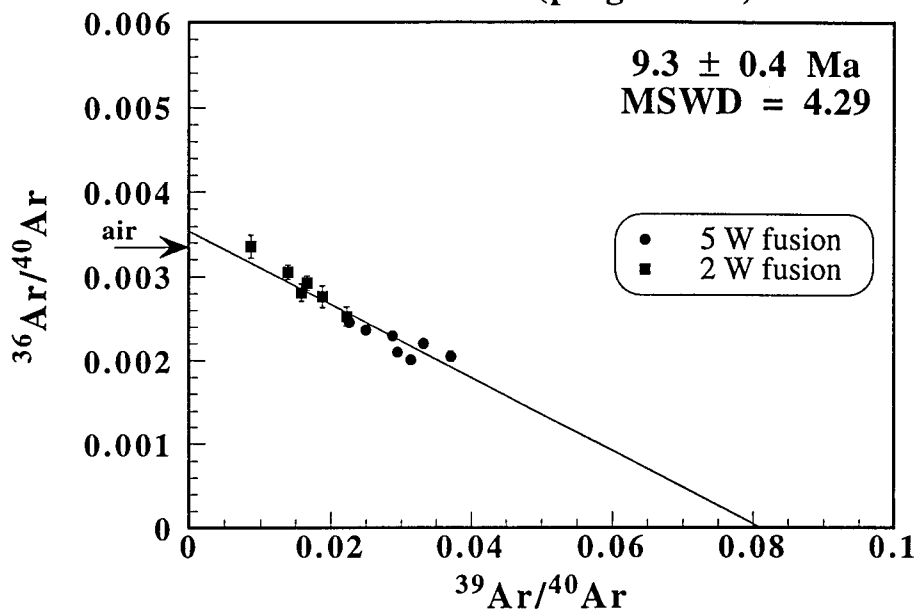
*Tuff of San Felipe ( $T_{mr_{sf}}$ )*

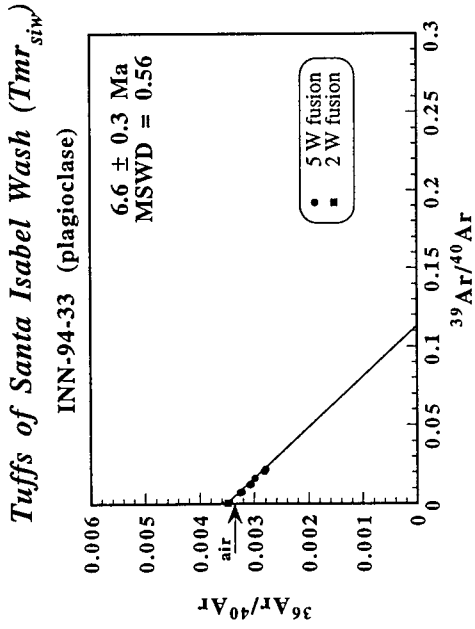
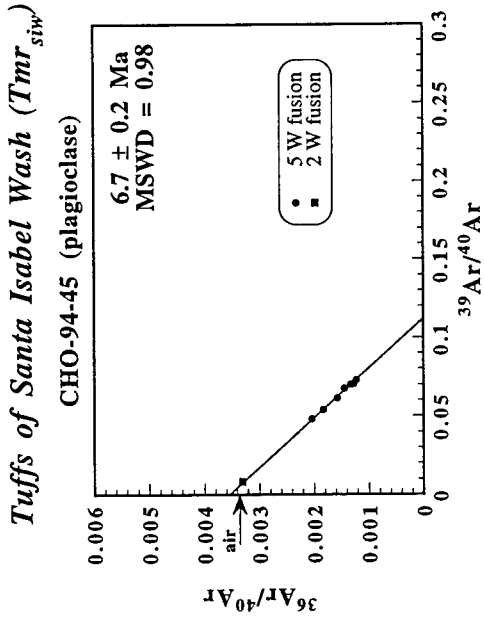
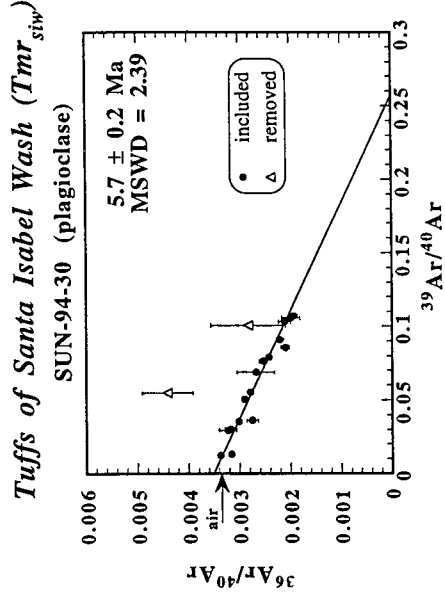
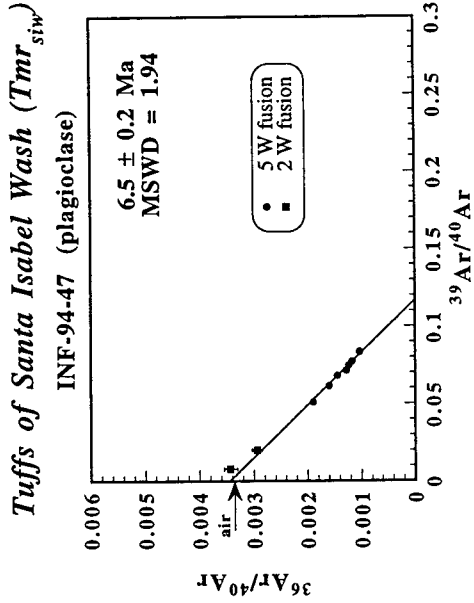
LCS-94-72 (anorthoclase)



*Pico del Toro andesite ( $T_{ma_{toro}}$ )*

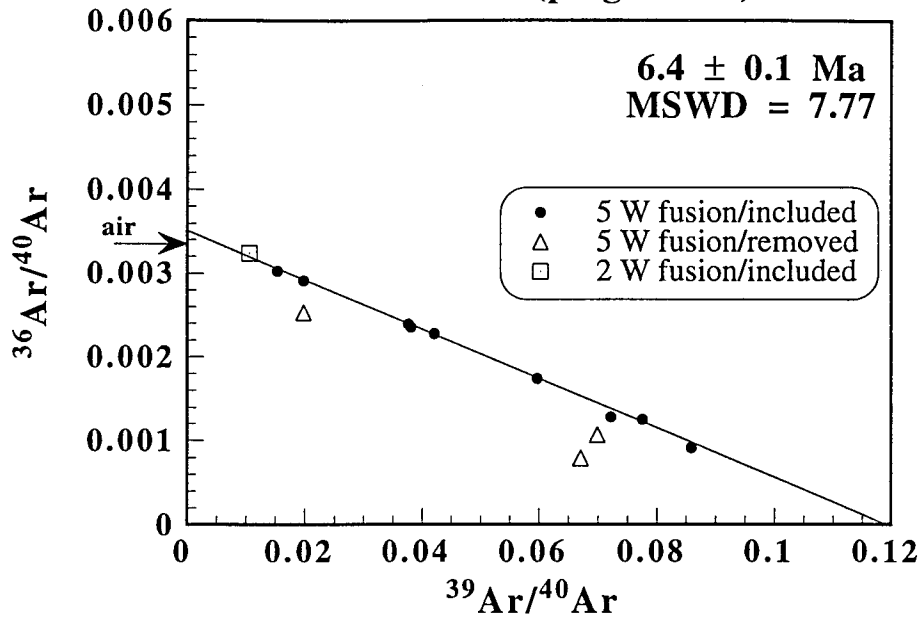
INF-94-68 (plagioclase)





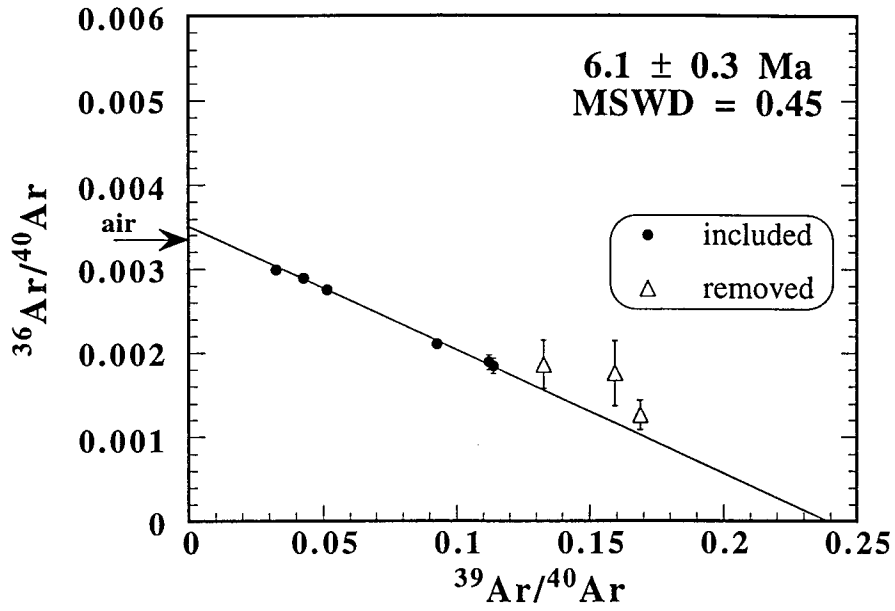
*Arroyo Oculito Tuff ( $T_{mr_{ao}}$ )*

INF-94-75 (plagioclase)



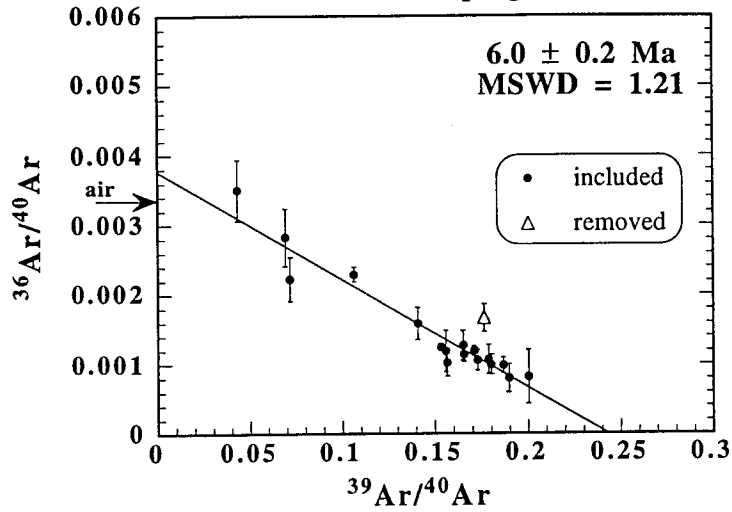
*Tuff of El Canelo ( $T_{mr_{ec}}$ )*

LCR-94-110 (plagioclase)



*Picacho Canelo Rhyolite ( $T_{mr_{can}}$ )*

CAN-95-11 (plagioclase)



*Picacho Canelo Rhyolite ( $T_{mr_{can}}$ )*

CAN-95-12 (plagioclase)

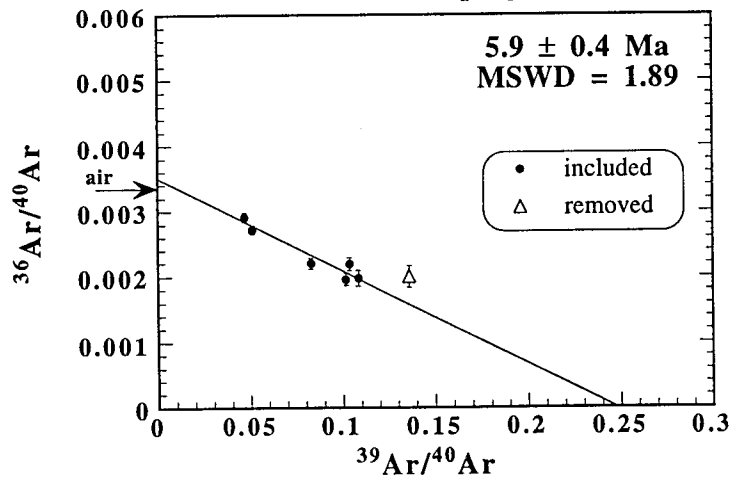
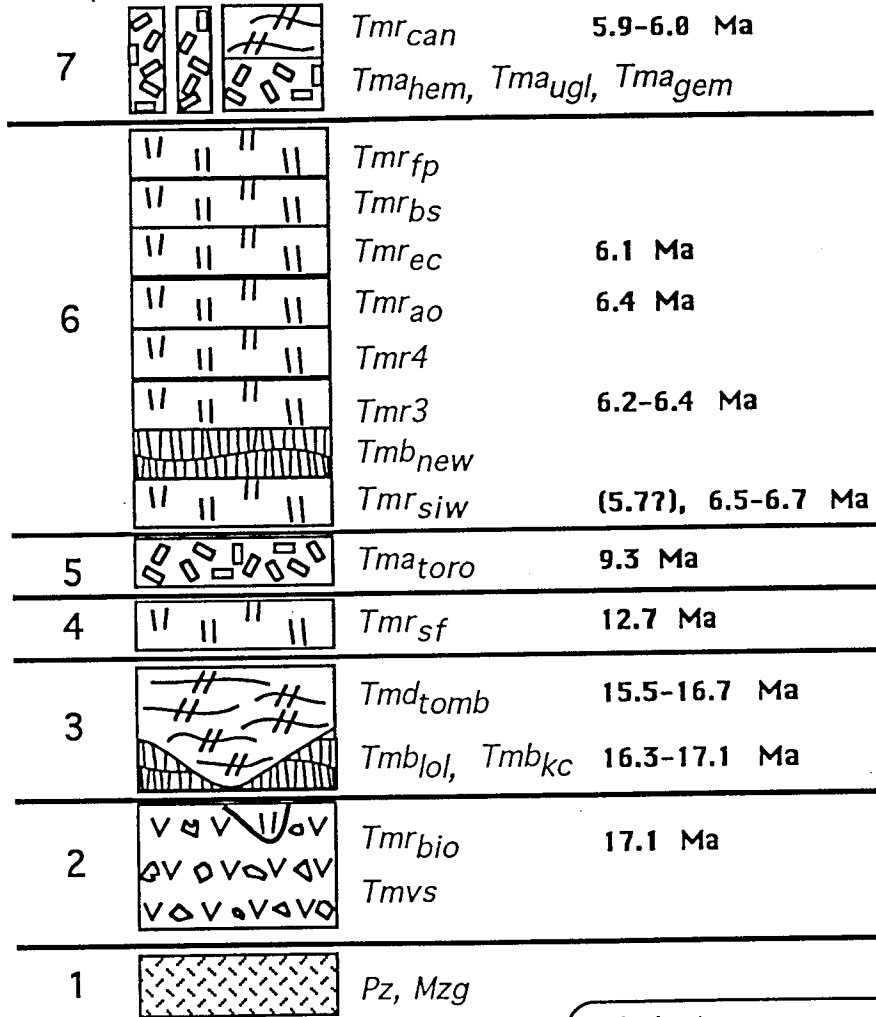




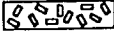
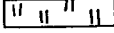


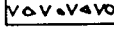
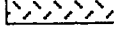
Figure 3.5. Stratigraphic column from Santa Isabel Wash with summary of  $^{40}\text{Ar}/^{39}\text{Ar}$  isochron ages determined in this study. With one exception (shown in parentheses) the ages are stratigraphically consistent. See Tables 3.2 and 3.4 (a, b) for uncertainties.

# STRATIGRAPHY AND <sup>40</sup>AR/<sup>39</sup>AR GEOCHRONOLOGY OF SANTA ISABEL WASH

Group:



**Lithologic patterns:**

-  porphyritic andesite
-  ash-flow tuff
-  silicic lava flows
-  basaltic lava flows
-  volcaniclastic breccia
-  batholithic basement

Chapter IV

Map and structural analysis of Santa Isabel Wash in the northern Sierra Santa Isabel region

4.1. *Introduction*

4.2. *Previous work*

4.3. *1:20000 geologic map and cross section*

A. *Overview*

B. *Thickness changes in 6 Ma pyroclastic flow deposits*

C. *Tilts*

D. *Faults*

i. *Pre-6-7 Ma deformation*

ii. *Post-6 Ma (excluding Quaternary) deformation*

iii. *Quaternary deformation*

4.4. *Structural model*

4.5. *Conclusions*

#### 4.1. *Introduction*

Geologic mapping is clearly one of the most important ways to decipher the history of volcanism and extensional deformation along the subaerially exposed rift margins of the GEP. Although much can be ascertained from air photo studies and reconnaissance field investigations, many important details can be overlooked. For example, previously unidentified changes in the thickness of distal outflow sheets of several pyroclastic flow deposits were documented in this study. These thickness changes suggest a modified structural interpretation for pre-6 Ma time for this region.

Among other things, the geologic map described here will be used to determine the timing, amount, and direction of extension in this region of the GEP. The map was made on a 1:20000 scale topographic base map taken from part of the Puertecitos 1:50000 topographic quadrangle published by the Dirección General de Estudios del Territorio Nacional (DETENAL) de México. Aerial photographs were also available and used to compliment field study. Eight months of detailed mapping and outcrop description, in an approximately 140 km<sup>2</sup> area, included hand sample collection of over 260 rocks for petrographic examination (Chapter II), some of which were subsequently chosen for microprobe analysis (Chapter II) and <sup>40</sup>Ar/<sup>39</sup>Ar geochronology (Chapter III), and collection of 223 rock cores drilled for paleomagnetic analysis (Chapter V).

The location of the study area and surroundings is shown in Figures 1.5 and 1.6 (in Chapter I). Geologic units preserved in Santa Isabel Wash are primarily volcanic and sedimentary rocks. Twenty-one distinct rock units (not including Quaternary alluvium and playa deposits) have been identified and combined into seven Groups on the basis of lithology, age, and stratigraphic position. A summary stratigraphic column is shown in Figure 4.1. The rocks primarily span Miocene and Pliocene times. Geochronologic results (Chapter III) identify significant episodes of volcanic activity around 17-15.5 and 6-7 Ma, and minor volcanism around 12.5 and 9 Ma. Dates are included in the stratigraphic column in Figure 4.1. Uncertainties are not listed here for simplicity but are given in Chapters II, III, and VI as well as in the legend of Plate I.

A simplified geologic map of Santa Isabel Wash is given in Figure 4.2 and shows the distribution of the seven lithologic Groups. Previously named geographic features in the study area include two local peaks: Picacho Canelo in the NE corner of the mapped area and Los Heme in the SE corner of the mapped area. Two washes in the study area are informally named Santa Isabel Wash and Arroyo Oculito. Locations discussed in the text will be identified using the alphanumeric grid outlining Figure 4.2. The complete 1:20000 geologic map given in Plate I differentiates the 21 lithologic units, and three cross sections are shown in Plate II.

Following a brief summary of previous structural interpretations of the northern PVP, this chapter will give a general description of the key structural features in Santa Isabel Wash. These features include significant thickness variations of several pyroclastic flow deposits related to pre-depositional topography, tilts of various sections, and amount and sense of offset along faults. The timing of extensional deformation is divided into pre-6 Ma, post-6 Ma, and Quaternary time periods. Finally, a structural model of Santa Isabel Wash will be given. Chapter VI places these findings into a broader regional context, discussing the relationship between Santa Isabel Wash and the rest of the PVP, the Sierra San Fermín, the Sierra San Felipe, and the southern Valle Chico (see Figure 1.6 in Chapter 1 for locations) as well as within the history of spreading center and transform fault formation in the Gulf of California.

#### 4.2. *Previous work*

The first detailed geologic summary of the PVP and surrounding areas was presented by Dokka and Merriam (1982) on the basis of earlier work by several different authors (principally Hamilton, 1971; Sommer and Garcia, 1970; and Gastil et al., 1975) as well as ground studies, air photo interpretations, and observations from low-flying aircraft. They classified the fault domain which includes the PVP region as one dominated primarily by steep, N-S-striking, west-dipping normal faults bounding eastward-tilted strata, but including a group of N-S-striking, east-dipping normal faults bounding westward-tilted strata in the

western portion of the PVP. The Santa Isabel Wash area is located roughly between these two regions where fault dips change, and is interpreted here to include two of the most significant faults in the east-dipping family noted by these authors. Dokka and Merriam (1982) suggest two intervals of extensional faulting since early Miocene time: a period of relatively intense E-W extension beginning between 17 and 6 Ma until about 3 Ma, and a post-3 Ma period of milder extensional deformation following the same E-W-directed movement as the earlier phase. Note that revised ages (from Martín-Barajas et al., 1995) which are different from the original study by Dokka and Merriam (1982) are used here. In some localities where field checks were performed, a significant component of lateral (strike-slip) motion was noted along some of the faults which they interpret to have accompanied vertical displacement as well. They suggest that structural trends established during the earlier phase of deformation dictated the position of structures accommodating later extension, specifically that the post-6 Ma deformation which pervades the volcanic highlands followed an earlier pattern of basement faulting.

Dokka and Merriam (1982) believe that the style (but not magnitude) of faulting in most of the PVP can be traced into the more highly extended regions to the north. The exception described in their study is in the northeastern portion of the PVP where faults appear to die out northward. They postulate a sinistral, E-W-striking, strike-slip fault near Arroyo Matomí (Figure 1.6 in Chapter I) to explain the disappearance of several N-S-striking faults. Several workers have subsequently examined the entire zone which separates the PVP from the adjacent regions to the north in greater detail (Stock and Hodges, 1990; Stock et al., 1991; Stock, 1993; Lewis, 1994; Lewis and Stock, in review in *J. Struct. Geol.*; Stock, in press, 1997). This structure (the Matomí accommodation zone) was an important structural boundary in Late Miocene time and will be discussed further in Chapter VI in conjunction with results from this study.

### 4.3. 1:20000 geologic map and cross section

#### A. Overview

Although Figure 4.2 is a highly simplified geologic map lacking much of the detail and structural information included in Plate I, several generalizations can be made from it. The pre-Miocene units of Group 1 crop out only in the northwest corner of the map area. As discussed elsewhere (Chapter VI) this locality probably marks a pre-Miocene basement high. Although it is unknown if Group 1 rocks underlie the PVP, the cross sections in Plate II show the minimum depth at which this contact might occur given the thickness of overlying units at this one exposure. Group 2 and 3 rocks are shown in two shades of green to emphasize their similar (early to mid-Miocene) age. Several E-W- to ENE-WSW-striking faults (e.g., localities K7 and I12) that cut these units do not cut the younger rocks, thereby suggesting an early phase of north-side-down deformation. The pyroclastic flow deposit that comprises Group 4 occurs in only a few places on the west side of the field area, and the andesites of Group 5 occur in only two locations (F11 and K12). The thick series of pyroclastic flow deposits of Group 6 covers most of the earlier units except in the footwall of the Cuervo Negro fault at the western edge of the area (labeled in Figure 4.4), and where erosion (in the north and in Arroyo Oculito) has exposed underlying units. The andesite and rhyolite flows of Group 7 occur only in the easternmost portions of the area. Numerous N-S-striking normal faults cut all units. No faults were traced into Group 7 rocks (there was only one fault to trace near S6) although, as described below, the deposition of these units probably predates the episode of pervasive faulting recorded throughout the area. Several faults are inferred to be buried below Quaternary alluvium (shown with dotted lines), and two linear features within the alluvium interpreted to be fault scarps are indicated with dotted lines and the letter “s.”

Some general features of the structural information included on the detailed geologic map (Plate I) and cross sections (Plate II) are mentioned here. As illustrated in the cross sections in Plate II, all faults are interpreted to be planar within the seismogenic upper crust. In the absence of seismic reflection profiles, this interpretation is primarily made on the basis

of focal-mechanism distributions of large normal-fault earthquakes in regions of crustal extension, which suggest that normal faults are approximately planar from the surface to the base of the brittle crust (Jackson, 1987). Strikes and dips of Group 2 rocks were usually measured on fine-grained sandstone layers interbedded with the coarser deposits, and in some cases may reflect the geometry of local drainages rather than the regional dip. The only measurable features within brecciated Group 3 rocks were sub-vertical cooling (?) joints in locations where solid plugs of lava were still preserved. The eutaxitic foliation within the pyroclastic flow deposits generally dips parallel to the underlying topographic slopes. *Tmr<sub>ec</sub>* developed lineations in some areas (e.g., location P8) indicative of gravity-driven rheomorphic flow. The hummocky upper surface of this tuff (described in Chapter II) in the same area yields a wide variety of strike and dip values (up to 60° dips) for the eutaxitic foliation. *Tmr<sub>4</sub>* from Group 6 is absent in some places on the volcanic highlands in the south-central part of the mapped area. The upper two pyroclastic flow deposits of Group 6 (*Tmr<sub>bs</sub>* and *Tmr<sub>fp</sub>*) are very thin (commonly < 1 m) and discontinuous and occur only in the NE portion of the mapped area. Although they usually occur together, there are places where either one can be missing.

#### B. Thickness changes in 6 Ma pyroclastic flow deposits

The change in thickness of the series of 6 Ma pyroclastic flow deposits (Group 6) is significant in several areas. In general the tuffs are relatively thicker north of Santa Isabel Wash (localities E4 and H4, but also H9 south of the wash) and in the region bordering Arroyo Oculito than in the rest of the field area. This observation is interpreted to indicate a pre-6 Ma topographic boundary against which the tuffs banked. A summary of the thickness variations observed in the Group 6 tuffs is given below, followed by an interpretation regarding the nature of the boundary over which they were deposited.

The lowest package of pyroclastic flow deposits in Group 6 is divided into five cooling units and referred to collectively as the Tuffs of Santa Isabel Wash (*Tmr<sub>siw</sub>*). These



tuffs are commonly < 40 m thick and were discontinuously deposited (or preserved?) in topographic lows, attesting to significant relief of pre-existing topography. The upper surface of *Tmr<sub>siw</sub>* appears to be sub-horizontal where the tuffs are relatively unwelded, but in many localities, where they are densely welded and thin to less than a few meters, they preserve a dipping upper surface mimicked in the eutaxitic foliation orientation. They are not exposed in the vicinity of Arroyo Oculito although they could be below the surface. They thicken (up to 100 m) north of Santa Isabel Wash (localities E4 and H4; see also cross section A-A' in Plate II), suggesting a topographic low into which these tuffs filled, and pinch out against Group 3 and 4 rocks south of Santa Isabel Wash (in the vicinity of location H9). Since these pyroclastic flow deposits are distal outflow sheets, and not proximal deposits, it is unlikely that the low which they filled in the north was associated with their source. They also thicken from 40-60 m up to 140 m northwards across a steep topographic slope in underlying Group 3 rocks at location N9.

In contrast to discontinuously deposited *Tmr<sub>siw</sub>*, the overlying series of pyroclastic flow deposits (*Tmr3*) filled topography and probably preserved a relatively planar upper surface. Subsequent Group 6 tuffs were deposited on this planar surface and thus were generally tabular in form. The three tuffs overlying *Tmr3* are thickest (and in some cases exclusive to) the NE section of the area (Arroyo Oculito), again suggesting a topographic low to the NE. These changes are clearly evident in cross section C-C' (Plate II). *Tmr4*, the stratigraphically lowest tuff exposed in Arroyo Oculito (underlying *Tmr3* could be below the surface), thickens from 3-5 m throughout most of the study area up to 70 m in Arroyo Oculito, although the base of *Tmr4* is generally not exposed in Arroyo Oculito and thus the thickness could be greater. Similarly, *Tmr<sub>ao</sub>* thickens from 0-1 m up to 30 m in Arroyo Oculito. The change in the thickness of the overlying Tuff of El Canelo (*Tmr<sub>ec</sub>*) is especially interesting. This tuff has been correlated to (and named after) a portion of the Tuff of El Canelo described in the eastern PVP (south of Arroyo Matomí) where the correlative section is up to 70 m thick (*Tmc6* of Martín-Barajas et al., 1995; see also Stock et al., 1991). As observed in this study, *Tmr<sub>ec</sub>* caps the volcanic highlands (where it is not eroded) with an

average thickness of 1-2 meters and average basal elevation of 600-700 m. This tuff apparently banked towards the west and/or south against a NW-trending topographic break at least 5 km in length extending from O8 to T13 (and perhaps further east of the mapped region). To the NE of this break, the tuff is up to 80 m thick with a basal elevation of about 300 m. This implies a difference in the elevation of the ground surface of 300-400 m at the time of *Tmr<sub>ec</sub>* deposition, and a difference of at least 400-500 m for *Tmr4*. Some, but probably not a significant amount, of the difference in present-day basal elevation across this break may be due to post-depositional faulting.

The nature of some of these pyroclastic flow deposits also changes at the location where the topographic break is postulated to have existed. *Tmr4* develops a thick (several meters) spherulitic base where it banks against the steep paleotopography of underlying Group 2 deposits. Strongly lineated portions of *Tmr<sub>ec</sub>* outcrops suggest post-depositional rheomorphism in the down-slope direction. The lineations generally trend N to NNE and plunge 10-30° to the north. Other features such as tension cracks and sheared fiamme around lithic clasts and feldspar phenocrysts (seen in thin section) also suggest rheomorphic (post-emplacment) flow of *Tmr<sub>ec</sub>*.

The present-day locations of these topographic boundaries, shown with heavy dashed lines in Figure 4.3 (a and b), form two linear, sub-parallel (NW-SE-trending) features labeled "1" and "2" for the following discussion. From the above descriptions there appears to have been a modest topographic drop of 40-80 m across boundary "1" and a much greater change in topography, on the order of 400 m, across boundary "2." It is certainly possible that the topographic low recorded in the northern regions was simply produced by erosion. However, in some areas, post-6 Ma normal faults coincide with the same location where the tuffs previously pinched out (locations G7-H9, which coincides with boundary "1," and O8-P8 which coincides with boundary "2"). The preferred interpretation is thus that these topographic changes mark the localities of pre-6 Ma, NW-striking, NE-side-down normal faults which in some places experienced post-6 Ma reactivation. This interpretation is

depicted in cross section C-C' (Plate II) with queried normal faults at depth which cut Group 2 rocks but not the overlying Group 6 rocks.

If these topographic boundaries formed as a result of normal faulting, there are two scenarios which could explain their relative positions. These scenarios are depicted in Figure 4.3a and 4.3b and assume that motion was contemporaneous along both structures. It is possible that the two segments were at one time a continuous, linear feature, but were subsequently offset from each other along a NE-striking, sinistral strike-slip fault (Figure 4.3a). An alternative scenario could be that the segments formed offset from each other as observed today. In this case some sort of transfer fault would be necessary between them, for example the NE-striking, dextral strike-slip fault shown in Figure 4.3b. Because the change in elevation is significantly greater across "2" than across "1," it seems more likely that the scenario in Figure 4.3b occurred with greater extension NE of segment "2." Additionally, there are no structures in the area which would represent the southwestward continuation of the sinistral fault suggested in Figure 4.3a. The dextral fault in Figure 4.3b is not postulated to exist to the southwest, although if differential extension occurred across it, it must continue at least some distance to the northeast (shown with long dashes in Figure 4.3b). The movement history of the isolated set of hills in the vicinity of location L7 (discussed below) also supports the scenario illustrated in Figure 4.3b. In either case, significant pre-6 Ma NE-directed extension (assuming no oblique motion) is suggested if the topographic breaks were indeed controlled by normal faulting. Additional evidence for a lower elevation in the north early in the history of the region is the pinching out from the north of  $Tmr_{sf}$  on the west side of Santa Isabel Wash (location B7 in Figure 4.2). Other evidence for north- or northeast-side down separation includes the fact that the stratigraphically lowest units exposed in most areas in this part of the peninsula, such as the pre-Miocene batholithic basement and the middle Miocene volcanoclastic deposits (e.g.,  $Tmvs$ ), are not exposed to the northeast of this topographic break in the vicinity of Arroyo Matomí and are probably below the surface.

### C. Tilts

Discerning the regional tilt of the units in Santa Isabel Wash is complicated by several factors. The coarse breccias and conglomerates of Group 2 most likely formed as interfingering lobes of debris flows and thus do not generally preserve measurable bedding representative of paleohorizontal. In some cases crude bedding planes were measured very approximately. Interbedded, fine-grained sands are rare but can easily be measured. Significant variations were recorded but most commonly the beds dip 10-40° to the west or north. Significant exceptions include 20-30° dips to the east near locality C5, and 30-40° dips to the northeast in Arroyo Oculito. No truly consistent pattern emerged from the dips measured in Group 2 rocks.

Lava flows of Groups 3, 5, and 7 do not preserve bedding features and generally have irregular brecciated bases. This leaves the pyroclastic flow deposits as the primary source of tilt information. As discussed in Chapter V in conjunction with tilt-corrections for paleomagnetic study, the eutaxitic foliation preserved in the welded pyroclastic flow deposits of Group 6 often reflects underlying topographic variations and thus is not always a reliable indicator of paleohorizontal. In places where *Tmr3* of Group 6 filled topography and preserved a relatively planar upper surface, measured eutaxitic foliation in the overlying deposits is generally sub-horizontal, suggesting little or no tilt.

There are a few places, however, where a portion of the Group 6 tuffs forming a layered series clearly dip from present-day horizontal, especially when observed from a distance. The most obvious of these are isolated hills north of Santa Isabel Wash consisting of thick sections of *Tmr<sub>siw</sub>* (locations E4 and H4) which dip gently (5-7°) to the west (see cross section A-A' in Plate II). An outcrop on the south side of Santa Isabel Wash (location H9) dips in a similar manner. The tuffs of Group 6 are also shown tilted slightly westward in cross section B-B' (Plate II) within the Santa Isabel fault zone and nearby on either side of Santa Isabel Wash (in the vicinity of locations D11 and F11). The tuffs are not obviously tilted at these particular outcrops, but they are interpreted to be tilted because the *Tmr3/Tmr4* contact at the head of Santa Isabel Wash (locations D12 to F12) tilts about 7° to the west.

One locality where tilt is easy to measure is within the thick section of *Tmr<sub>ec</sub>* to the northwest of Arroyo Oculto. The densely welded base consists of several meters of well-developed, parallel foliation planes which most likely formed horizontally (i.e., perpendicular to the vertical compaction direction) at the time of deposition. However, these foliation planes consistently dip about 10° to the northwest. Also in this region, the contact between *Tmr<sub>ec</sub>* and overlying *Tmag<sub>em</sub>* also dips to the northwest about 20°. These northwestward tilts are attributed to tectonic tilt and will be discussed further below.

#### D. *Faults*

The style, amount, and direction of faulting in Santa Isabel Wash will be described for three different time periods. The first time period pre-dates the deposition of the 6-7 Ma pyroclastic flow deposits of Group 6, the second time period post-dates the deposition of these same units, and the third time period addresses active (Quaternary) features. Some generalities are summarized here first.

The faults in Santa Isabel Wash are generally high-angle (steeply dipping) faults; however, the brecciated nature of the volcanic deposits makes preservation of planar fault surfaces extremely rare. Directional indicators such as slickenlines, or striations, are consequently rare as well. Poor fault plane preservation has been noted elsewhere in similar types of deposits, such as in the Bishop Tuff in northern Owens Valley, California, where a volcanic tableland analogous to the PVP is similarly deformed by extensional faulting (Dawers et al., 1993). A total of 14 faults found in Santa Isabel Wash preserve planar surfaces which could be reliably measured; three of these also preserve slickenlines. The orientations of the 14 measurable fault planes are shown in Figure 4.4. Some faults have been given informal names to be used in the discussion below. Refer to Figure 4.2 for the sense of offset determined along other faults.

Lack of piercing points makes it difficult to assess the absolute sense of offset across many of the faults, and in some cases strike-slip faulting could account for some portion of apparent normal displacement. Consequently, the sense of offset across many of the faults

documented in this study had to be determined somewhat intuitively, and is subject to alternative interpretations. If a significant topographic break is evident across a fault, and a given contact is clearly identified at different elevations on either side of the fault, the fault is then classified as a dip-slip fault. Where there is no significant change in elevation of a contact across a fault, it is interpreted to be a strike-slip fault. It is likely that several faults interpreted in this manner are, in fact, oblique-slip faults which accommodate a combination of both types of motion.

#### i. *Pre-6-7 Ma deformation*

Although most faults in Santa Isabel Wash cut all lithologic units, there are a few places where faults do not appear to cut the 6-7 Ma pyroclastic flow deposits of Group 6. These faults, which generally strike E to ENE and imply N-side-down displacement, are collectively grouped here as “pre-6-7 Ma” structures. In a few localities (e.g., locations K7 and I12 in Figure 4.2) these faults cut the pre-15 Ma Group 2 and 3 rocks ( $Tmvs$  and  $Tmd_{tomb}$ ) but not the overlying Group 6 tuffs, implying an early phase of deformation between 15 and 6-7 Ma. In another location, however, there is a similarly oriented fault which also cuts the 12.7 Ma (Group 4) pyroclastic flow deposit and the 9.3 Ma (Group 5) andesite. This fault is informally named the Pico del Toro fault (Figure 4.4), and it is overlain by undeformed Group 6 tuffs at its westernmost surface expression. Thus, in this case, deformation is constrained to have occurred between 9.3 and 6-7 Ma.

The amount and sense of offset is not readily apparent across these early structures. The contact between Groups 2 and 3 is displaced down to the north across two faults at location I12 between 80-120 m, although the irregular (unconformable) nature of this contact makes this a fairly approximate estimate. If fault-perpendicular, non-oblique, dip-slip motion occurred along these faults, inferred offset directions would be N-S to NNW-SSE. Slickenlines preserved on the Pico del Toro fault plane (Figure 4.4) record a sinistral component of oblique-slip motion, suggesting W- to WNW-directed motion across this structure. Outcrops of  $Tmr_{sf}$  on either side of the Pico del Toro fault are presently at the same

elevation. The ~ 400 m of NE-side-down displacement described above in conjunction with the pre-6-7 Ma paleotopographic slope suggests that this style of deformation (NE-directed extension) dominated over deformation across the E- to ENE-striking faults just described (which suggest W- to WNW-directed extension).

The possibility that the Santa Isabel and/or Cuervo Negro fault systems (described in the next section and identified in Figure 4.4) might have been active prior to Group 6 deposition is suggested by several factors. These include the extremely thin (to absent) nature of *Tmr<sub>siw</sub>* (the lowest Group 6 tuff) to the west of these faults, suggesting perhaps a pre-6 Ma E-facing scarp which acted as a topographic boundary, as well as the geographic restriction of the lowest *Tmr3* cooling unit to the regions immediately east of these faults. As described above, reverse drag would produce a fault-parallel low on the east side of these faults into which the lowest *Tmr3* cooling unit may have been deposited. However, evidence for pre-6 Ma motion across these faults is not extremely convincing and, as described in Chapter VI, other factors suggest that most deformation along them is post-3 Ma.

#### ii. *Post-6 Ma (excluding Quaternary) deformation*

Post-6 Ma faults are common throughout Santa Isabel Wash. Faults generally strike between NNW and NNE (Figure 4.2) and show both west- and east-side-down displacement. Faults clearly exhibiting only strike-slip displacement are rare. On the basis of the amount of offset across faults, surface trace continuity, and spatial geometry, the faults are placed into one of two families. These are (1) a major east-dipping fault system west of Santa Isabel Wash and (2) a collection of smaller synthetic and antithetic faults in the hanging wall of this major system (basically throughout the rest of the area) which are interpreted to terminate against the east-dipping fault plane(s) at depth. The faults which make-up the first group are interpreted to be the principal structures accommodating extension in the Santa Isabel Wash area. The general characteristics of these two families are described here.

Two closely spaced (~ 2 km apart in map view), N-S striking, east-dipping normal faults on the west side of the study area (Cuervo Negro fault and Santa Isabel fault, identified

in Figure 4.4) are the most continuous structures in the mapped area, although NNW-striking splays and cross-structures between them disrupt their continuous nature in the north. These parallel fault systems preserve the thickest outcrops of the oldest (i.e., stratigraphically lowest) lithologic units (Groups 2 and 3) at relatively high elevations in their footwalls. A gentle westward dip of some of the units east of these faults suggests that a listric geometry at depth is possible.

There are two inferred (buried), N-S-striking faults in Santa Isabel Wash itself shown with dotted symbols in Figure 4.2 (see also Plate I) to the east of the Santa Isabel fault. The E-dipping fault at location F4 (Figure 4.2) is geometrically required between two offset, west-dipping outcrops of Group 6 rocks, and may be continuous with the NW-striking faults at location G7. The other fault is shown as E-dipping but queried (location E10 in Figure 4.2). The existence of this fault is postulated on the basis of the west-dipping Lavender Wash fault (Figure 4.4) which offsets the *Tmr3/Tmr4* contact ~40 m down to the west. A southward continuation of this structure was not apparent further south in the wash, and thus displacement is interpreted to die out in this direction. However, the northern end terminates against a NW-striking fault which does not continue across the wash to the west. This fault is inferred to be a dextral strike-slip fault along which displacement from the Lavender Wash fault is translated northwestward. It is postulated that displacement is transferred northward along structures buried by, and perhaps controlling the position of, the present-day wash. These hypothetical structures are dotted in Figure 4.2 and Plate I. The northernmost segment is shown dipping eastward on the basis of minor westward tilt of units to the west described above; however, it could dip westward, antithetic to the Santa Isabel fault but synthetic to the Lavender fault, or it may even die out further south than inferred (e.g., at the head of the wash). The preferred interpretation is to place it within the east-dipping Santa Isabel fault system.

The other family of post-6 Ma faults are interpreted here to be secondary to the Cuervo Negro and Santa Isabel faults on the basis of discontinuous outcrop patterns, smaller amounts of apparent normal offset, and the incipient nature of smaller, sub-parallel structures connected by extensional relay ramps such as described by Larsen (1988) for extensional



regions of relatively low strain. All of these faults are in the hanging wall (to the east) of the Santa Isabel and Cuervo Negro fault systems. In general, these faults are closely spaced (every 1-2 km), strike NNE to NNW, and dip to both eastward and westward (synthetic and antithetic to the Santa Isabel fault system, respectively). If the pre-6-7 Ma topographic slope discussed above and depicted in Figure 4.3 was indeed the result of NW-striking normal faults, several of the post-6 Ma faults appear to have formed along these pre-existing structures (e.g., locations D4, G7, H9, and P8 in Figure 4.2). This reactivation is in agreement with the suggestion by Dokka and Merriam (1982) that post-6 Ma deformation (post-3 Ma deformation according to new geochronology by Martín-Barajas et al., 1995) followed earlier fault patterns.

There were no faults traced into Group 7 (~ 6 Ma) andesite and rhyolite lava flows at the NE and SE corners of the area. Only one mapped structure projects into a Group 7 unit (location S6 in Figure 4.2) and field examination suggested that displacement diminishes at this northern end of the fault. Slope wash from the brecciated base of the Group 7 andesite (*Tmagem*) covers the actual basal contact in this location as well as in many other places, thus poor outcrop exposure precluded the ability to discern small (few m) offsets where the fault projects. Regardless of this ambiguous relationship, it is interpreted here that Group 7 rocks pre-date the episode of deformation which clearly cuts the underlying Group 6 rocks. Lithologic correlation between the 6 Ma rhyolite flows of Group 7 (*Tmr<sub>can</sub>*) and faulted rhyolite flows to the NE of Picacho Canelo (f4 of Stock et al., 1991; J. Stock, unpublished mapping) supports this interpretation.

Variations in the elevation of the relatively planar contacts between some of the Group 6 pyroclastic flow deposits can be useful for determining amounts of normal separation across post-6 Ma faults, assuming that the contacts were at the same elevation everywhere at the time of deposition. As described above, the *Tmr3/Tmr4* contact is one of the most likely features to have been roughly horizontal and located at approximately the same elevation throughout most of the study area at the time of deposition. Again, the exception is in the north and northeast where pre-existing topographic lows are inferred. Contours roughly outlining the present-day elevation of this contact are shown in Figure 4.5.

Elevations of the contact are highest west of Santa Isabel fault (860 m in the south (e.g., location B11 in Figure 4.2) and 660 m in the north where the fault splays (location C7 in Figure 4.2)), and drop to around 600 m in the volcanic highlands to the east (e.g., location I19 in Figure 4.2). The elevation becomes gradually lower further northward to a lowest value (about 400 m) in the hills to the north of Santa Isabel Wash (locations E4 and H4 in Figure 4.2). The drop in elevation of the contact from south to north recorded on both sides of the Santa Isabel fault suggests a component of north-side-down displacement within at least some portions of the study area. In Arroyo Oculito the *Tmr3/Tmr4* contact is below the surface (which within the arroyo is 300 m) which is undoubtedly due to a combination of post-6 Ma faulting and the low elevation of surface upon which the tuffs were deposited (discussed above). Offset across the Cuervo Negro fault system is estimated to be approximately 400 m on the basis of the change in elevation of the contact between Group 2 and 3 rocks (determined from air photo interpretation for the footwall portion).

Unpublished mapping on the high plateau about 10 km WSW of the map area (Stock, Lewis, Salton, and Holt, unpub. mapping) shows the elevation of a contact between two pyroclastic flow deposits interpreted to be correlative to *Tmr3* and *Tmr4* at an elevation of approximately 1000 m. All extensional structures between Santa Isabel Wash and this locality to the west are considered to be part of the Cuervo Negro fault system. These results suggest 400-500 m of post-6 Ma, E-side-down normal separation across both of these fault systems.

The 12.7 Ma pyroclastic flow deposit *Tmr<sub>sf</sub>* (Group 4), although discontinuously deposited in topographic lows, also occurs at significantly different elevations across the area. At the head of Santa Isabel Wash (location F11 and D11 in Figure 4.2), the upper surface is presently at 400 m elevation. To the west of Santa Isabel fault, the upper surface is at 500-600 m elevation in the north (location C7 in Figure 4.2) and 800 m in the south (location D17 in Figure 4.2). To the west of the Cuervo Negro fault, it is at 920 to 940 m (Stock, Lewis, Salton, and Holt, unpub. mapping). These differences also suggest about 500 m of E-side-down separation across the Santa Isabel and Cuervo Negro fault systems. The similarity in the amount of offset for the 12 Ma and 6 Ma deposits argues against significant motion between 6 and 12 Ma along these faults.

In addition to apparent east-side-down displacement, post-6 Ma north- and northeast-side-down displacement is also evident along several faults (e.g., locations G11, G8, M13, and P8 in Figure 4.2). The approximately located (dashed), E-W-striking fault near the southernmost part of the mapped region (location I19 to N20) displaces the *Tmr3/Tmr4* contact about 40 m (north-side-down); however, this fault may also accommodate a significant amount of (dextral?) strike-slip motion. Additional evidence to support north-side-down displacement involves the isolated set of hills in the vicinity of location L7 (Figure 4.2) which consist primarily of Group 2 and 3 rocks. In a few places Group 6 rocks bank against these hills from the north, and their outcrop appearance is much more similar to the sequence found banking against the pre-6 Ma boundary “2” (Figure 4.3) to the east (location O8 to R12) than those banking against boundary “1” to the west (e.g., locations H9, G7, and I5). Specifically, on the hills near location L7, the lowest set of tuffs (*Tmr<sub>siw</sub>*) is not exposed, *Tmr4* has a thick spherulitic base and is 20-30 m thick, and *Tmr<sub>ec</sub>* is up to 40 m thick. On the basis of these features and their present-day elevation, it is postulated that this entire set of hills was located at a higher elevation when the 6 Ma tuffs were deposited, and has subsequently been displaced 80-100 m down to the north (or northeast or northwest). For this reason, the scenario presented in Figure 4.3b is preferred over the one shown in Figure 4.3a. Although the timing is different (pre-6 Ma deformation in Figure 4.3b versus post-6 Ma deformation of the hills at location L7), pre-6 Ma deformation may have initiated the separation of these hills from the south (e.g., from the “gap” in the vicinity of J11) which were subsequently further offset in the same sense (NE-side-down). Restoring these hills to the south requires a N- (NE- ? NW- ?) dipping normal fault located to the south in the Santa Isabel Wash. The preferred interpretation here is that a NW-striking fault (perhaps between locations I7 and J9) from the earlier period of deformation was reactivated, and that a NE-striking dextral fault (similar to the one in Figure 4.3b) accommodated greater extension to the north of it relative to the south. A NE-striking scarp in the alluvium at location M7 (discussed below with Quaternary features) suggests that this geometry of faulting may continue today.

On the basis of the general strike of most faults, the direction of post-6 Ma extension appears to be E-W- to NE-SW-directed if motion is assumed to have been purely dip-slip (fault-perpendicular, non-oblique, motion). Slickenlines preserved on the Santa Isabel fault plane imply oblique motion which is primarily dip-slip with a small sinistral component (Figure 4.4), implying ENE-directed extension. It is certainly possible that many of the smaller faults throughout the area, sub-parallel and synthetic or antithetic to the Santa Isabel fault, have experienced a similar oblique component of motion. Thus it is preferable to use the directional indicators on the Santa Isabel fault as more reliable indicators of extension direction than to simply assume extension occurred perpendicular to fault strikes (i.e., pure dip-slip). On the basis of evidence described above for north-side-down displacement, at least some N-S-directed component of extension appears to be recorded in this area. The most likely common extension direction suggested from these principle structures thus appears to be ENE-WSW-directed. The amount of extension calculated along WNW-ESE-trending cross-section B-B' (Plate II) is ~ 4%, whereas the amount along NE-SW-trending cross section C-C' (Plate II) is ~ 2%. This also suggests that an ~ E-W directed component is dominant over a NE-SW-directed component, but that the latter exists. This somewhat tentative conclusion differs slightly from the local E-W-extension direction determined by Dokka and Merriam (1982) on the basis of tilt patterns and kinematic indicators for this area; however, it is in agreement with extension directions subsequently determined in nearby areas such as southern Valle Chico (Stock and Hodges, 1999) and the Sierra San Fermín (Lewis, 1994; Lewis and Stock, in review in *J. Struct. Geol.*). This will be discussed further in Chapter VI.

A paleomagnetic study performed throughout Santa Isabel Wash on several of the Group 6 tuffs (Chapter V) suggests that there has been no vertical-axis rotational deformation of various fault-bounded blocks, nor wholesale rotation of the entire area relative to geomagnetic north, since 6 Ma. This is in marked contrast to CW rotations documented a few km to the north in the Sierra San Fermín (Lewis, 1994; Lewis and Stock, in review, *J. Geophys. Res.*).

*iii. Quaternary deformation*

Because the youngest rock units in Santa Isabel Wash are 6 Ma, the post-6 Ma extensional deformation described above could be very young. In fact, as discussed in Chapter VI, there is reason to believe that significant deformation began only 2-3 Ma. Several features suggest that active extensional deformation is continuing presently. These include 2-km-long linear features in the active alluvial surface interpreted to be fault scarps (locations M7 and O4 in Figure 4.2) and several sag ponds (or closed basins) probably related to structural downwarping or step-overs between faults (Plate I). As described above, the scarp at location M7 may represent reactivation (or continued deformation) along a pre-6 Ma dextral strike-slip fault postulated in Figure 4.3b. A NW-side-down drop of  $< 1$  m occurs across this scarp which is not well-delineated at the outcrop scale. It is primarily its 2-km-long linear nature, evident on air photos or as viewed from the hills above it, that suggests it might be a fault scarp. The scarp at location O4 is also extremely linear and forms a topographic low into which drainages feed from the southeast and southwest. Evidence is lacking for the sense of motion associated with this scarp. As illustrated in Figure 4.6, if dextral strike-slip motion occurred along it, this could provide a mechanism to explain the presence of the roughly circular, 40 km<sup>2</sup> alluvial plain to the north of Santa Isabel Wash which might have been “opened” along this fault.

Another less obvious feature is an apparent change in the drainage system associated with Santa Isabel Wash. The present location of the wash, as indicated by the position of the label in Figure 4.2 and Plate I, is south of several isolated hills to the north. However, patterns in older alluvial sediments indicate that abandoned drainages at one time passed directly north to northeastwards between these hills. The present-day Santa Isabel Wash appears to be a recently developed topographic low which now directs the flow of sediment from the head region of Santa Isabel Wash to the southeast before turning northward near location O6 in Figure 4.2. The WNW-ESE orientation of most of this wash again suggests a northeast-side-down extension scenario.

The Santa Isabel and Cuervo Negro faults presently have prominent E-facing scarps. Sinistral stream offsets across Santa Isabel fault support the sinistral oblique sense of motion recorded in the slickenlines, thus this major fault is believed to be active today. A prominent feature on air photos is a dark, round volcanic (?) deposit along the fault about 5 km south of the southern extent mapped in this study. Although it is located at quite a distance from easy access, study of the relationship between this unit and the fault, as well as collection of samples for geochronology, would be extremely interesting.

#### 4.4. *Structural model*

A three-dimensional interpretation by Stock and Hodges (1990) of the escarpment fault zone in the vicinity of southern Valle Chico infers a flattening of the zone with depth, and a merging of the synthetic and antithetic faults to the east of the escarpment fault zone into a listric detachment fault. It is possible that this same type of geometry occurs below the PVP. Several features described above support this possibility, which is included in Figure 4.8. Dokka and Merriam (1982) also inferred that downward flattening of the San Pedro Mártir fault and associated synthetic (E-dipping) normal faults, which requires volume compensation, could explain the tilting of strata in the hanging walls.

Cartoon block models of Santa Isabel Wash are presented in Figures 4.7 (pre-6-7 Ma) and 4.8 (post-6 Ma). The major feature in pre-6-7 Ma time (Figure 4.7) is the hypothetical NW-striking faults which accommodate NE-side down displacement of up to 400 m on the basis of subsequently deposited pyroclastic flow deposits. It is possible that this structure marks the southern boundary of the Matomí accommodation zone. Pure dip-slip would imply NE-directed extension, although a dextral component of oblique-slip may have occurred as well. Although motion along the Cuervo Negro and Santa Isabel fault systems may have begun prior to 6 Ma, most evidence suggests that these structures post-date this early period of deformation.

After 6 Ma (probably at 2-3 Ma; see Chapter VI) ENE-directed extension occurred throughout most of the PVP (Figure 4.8). The pre-6-7 Ma fault is shown buried by an

overlying tuff (illustrated with triangles) which thickens to the northeast. North-side-down deformation continues and probably dictates the location of the present-day Santa Isabel Wash. The N- to NNW-striking faults are shown here with an oblique (sinistral) component of slip. The Cuervo Negro and Santa Isabel faults separate a wedge-shaped “rider” segment as described by Gibbs (1984).

#### 4.5 *Conclusions*

An early phase of relatively minor extensional deformation is recorded in Santa Isabel Wash by E- to ENE-striking, north-dipping normal faults which do not cut 6-7 Ma rocks. In one area this faulting post-dates the deposition of a 9.3 Ma andesite flow, while in other places the timing of faulting can only be constrained between 15 Ma and 6-7 Ma. On the basis of the E-W to ENE-WSW strikes of many of these faults, and from preserved slickenlines on one of these faults, a period of extremely speculative ~ N- to NNW-directed extension appears to be recorded. In this case, the timing of faulting is better constrained than the extension direction. On the other hand, a pre-6-7 Ma NE-facing topographic break is apparent from thickness changes in 6-7 Ma pyroclastic flow deposits. It is argued here that this break developed as a result of northeast-side-down normal faulting along NW-striking faults. This region may have been the southern boundary of an accommodation zone between a relatively stable region to the south and an extending region to the north (Chapter VI). Apparent pre-6 Ma vertical separation of ~ 400 m across these structures is significantly greater than the 80-120 m vertical separation inferred across the E-W to ENE-WSW striking faults.

Thus, two types of structures record pre-6 Ma extension in Santa Isabel Wash but suggest significantly different extension directions. There is no clear evidence for early, intense, pre-6 Ma (actually pre-3 Ma from the more recent study of Martín-Barajas et al., 1995) E-W extension as suggested by Dokka and Merriam (1982) for the PVP. As illustrated in Figure 4.5, pre-depositional (i.e., pre-6 Ma) elevations appear to be lower in the north on both sides of the Santa Isabel fault relative to the south.

Santa Isabel Wash consists primarily of post-6 Ma N- to NNW-striking normal faults. One family of structures on the west side of the area consists of the E-dipping Santa Isabel and Cuervo Negro fault systems (Figure 4.4) which are interpreted to be major structures accommodating extension in this area. Similar amounts of E-side-down displacement (~ 500 m) for both 6 and 12 Ma tuffs across the Santa Isabel and Cuervo Negro fault systems implies principally post-6 Ma faulting. As discussed in Chapter VI these faults might represent a significant part of the principle western boundary of the Gulf Extensional Province at this latitude. Projected northward along strike, the larger faults seem to splay within the mapped area. Less continuous faults to the east are synthetic and antithetic to the larger faults and may sole into them at depth. In other words, most of the mapped region is interpreted to be in the hanging wall of the two major fault systems on the west side of the study area. ENE-directed extension is suggested by the most prominent structures in the area, although evidence for NE-directed extension is also present. Some post-6 Ma faults appear to have reactivated earlier structures associated with the NE-facing topographic boundary described above.

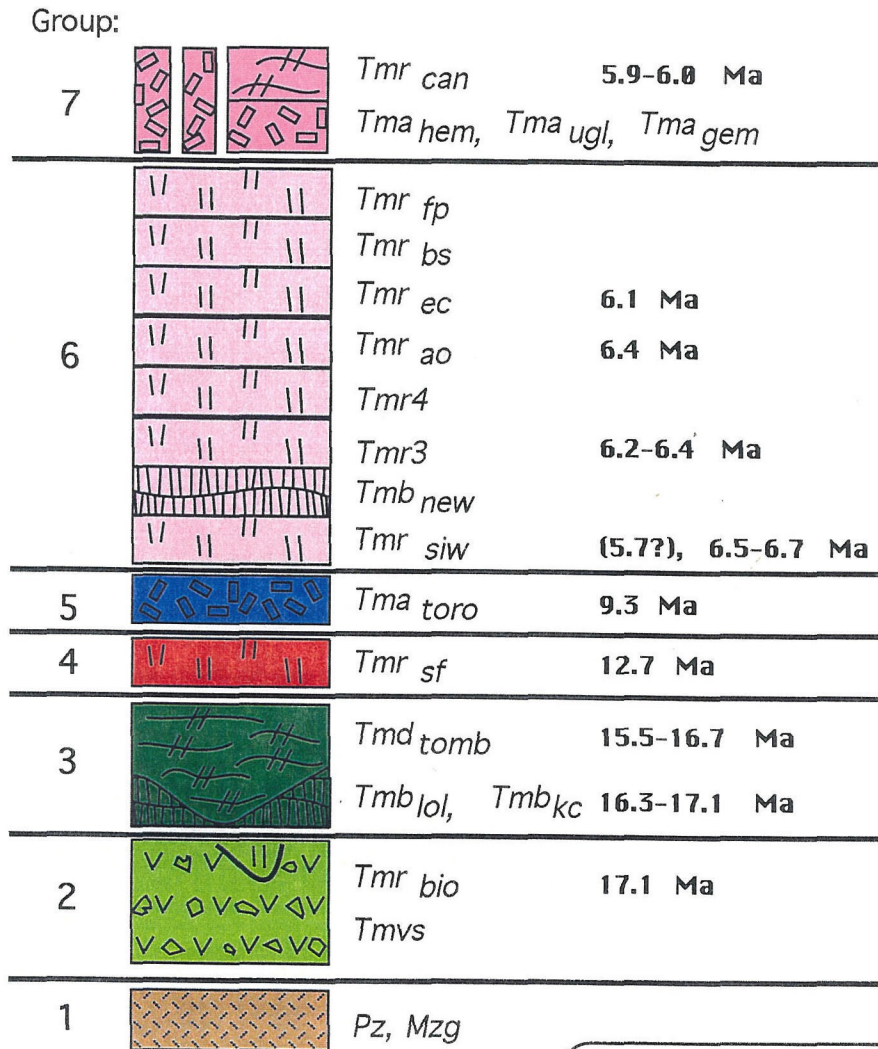
The westward tilting sections observed in some localities in the hanging wall of the Santa Isabel fault could be the result of reverse drag along this fault, suggesting perhaps a listric geometry at depth. If the W-dipping faults in the central portion of the mapped area are indeed antithetic structures within the hanging wall of the Santa Isabel fault, these, too, could be used as evidence for compensation of a listric geometry for the Santa Isabel fault and/or the Cuervo Negro fault.

As discussed in Chapter VI in conjunction with the history of the Gulf of California spreading center system, most deformation probably occurred since 2-3 Ma. Extension is actively continuing in Santa Isabel Wash as evidenced by several Quaternary features such as fault scarps, sag ponds, and stream offsets. One of the most interesting features in the area is that the presently active NNW-striking Santa Isabel fault exhibits a slight sinistral component of motion.



Figure 4.1. Stratigraphic column from Santa Isabel Wash with  $^{40}\text{Ar}/^{39}\text{Ar}$  ages determined in this study.

# STRATIGRAPHY AND <sup>40</sup>AR/ <sup>39</sup>AR GEOCHRONOLOGY OF SANTA ISABEL WASH



### Lithologic patterns:

- porphyritic andesite
- ash-flow tuff
- silicic lava flows
- basaltic lava flows
- volcaniclastic breccia
- batholithic basement

Figure 4.2. Simplified geologic map of Santa Isabel Wash.

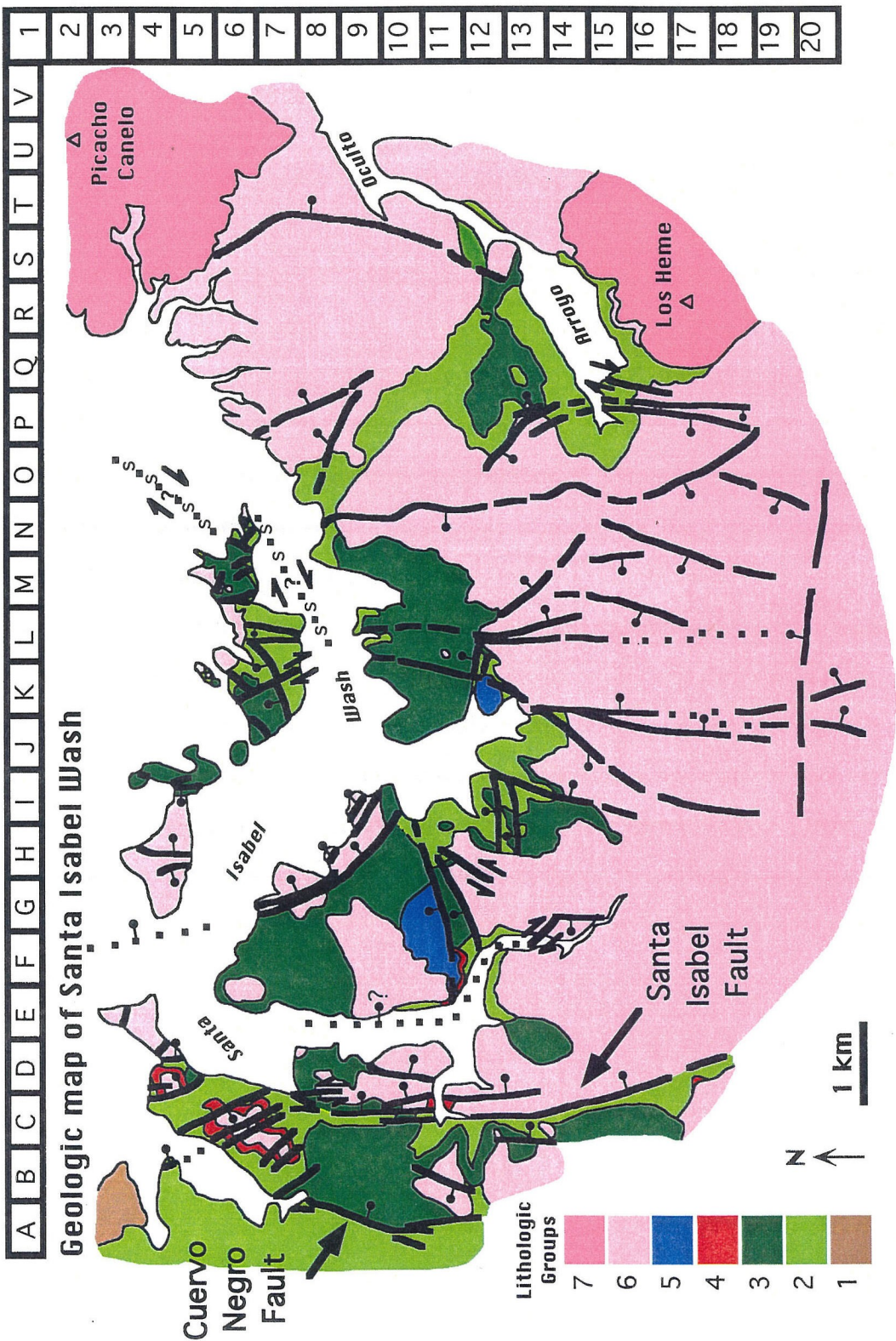
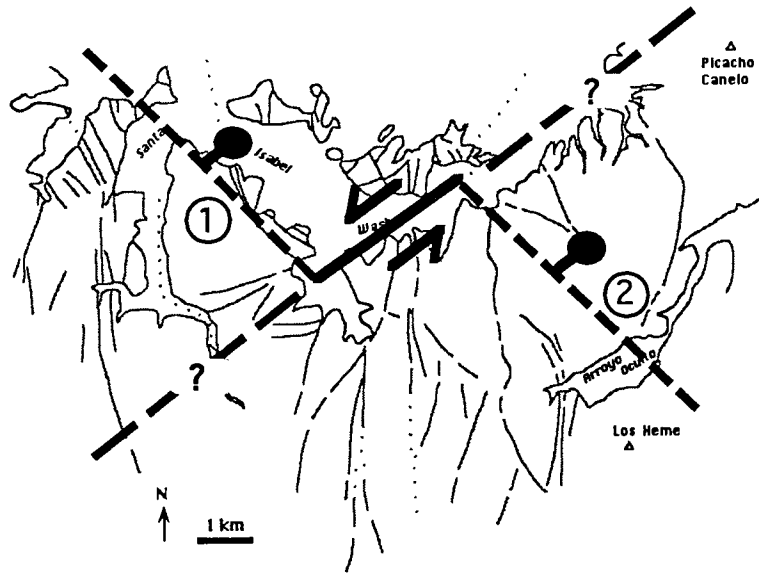


Figure 4.3. Position of topographic boundaries (heavy dashed lines trending NW-SE) against which pyroclastic flow deposits from Group 6 banked. They are numbered “1” and “2” for discussion in text. The tuffs are significantly thicker to the NE of these boundaries than to the SW. Although these pre-6 Ma topographic changes could be the result of erosion, the preferred interpretation is that they mark the positions of NW-striking normal faults (bar and ball symbol on down-thrown side). Two possible scenarios for the relative positions of these sub-parallel boundaries are given in (a) and (b). (a) The boundaries may have been a continuous linear feature which accommodated NE-directed extension but was subsequently offset by a NE-striking, sinistral fault. (b) A relay or transfer structure may have accommodated motion between the originally offset features at the time of NE-directed extension. In this scenario a greater amount of NE-side-down displacement could have occurred along segment “2” (indicated with the longer arrow) which agrees with field observations. As discussed in the text, this latter scenario is the preferred interpretation.

a.



b.

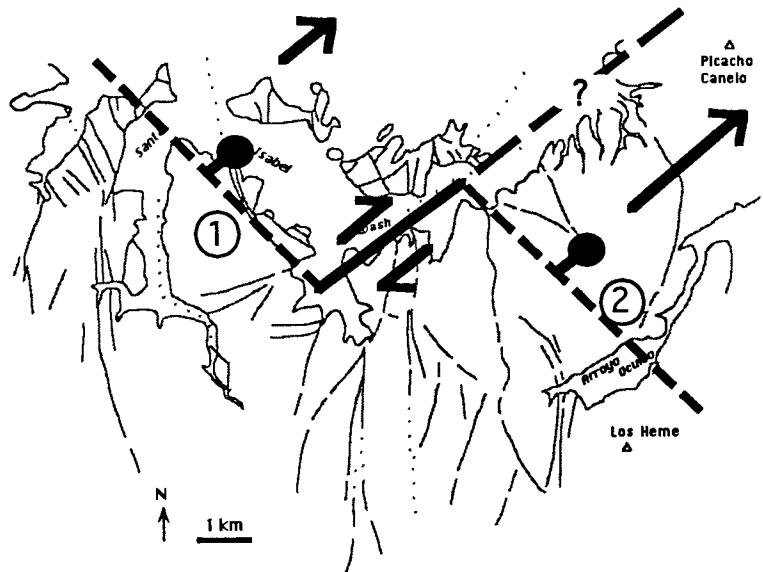


Figure 4.4. Locations and dip values of fourteen measured fault planes in Santa Isabel Wash. The dips of most other faults (see Figure 4.2 and Plates I and II) were inferred on the basis of the surface trace pattern. Three of the measurable fault planes preserve slickenlines which suggest oblique normal faulting with a sinistral component to the motion. Some faults are given informal names used in discussions in the text.

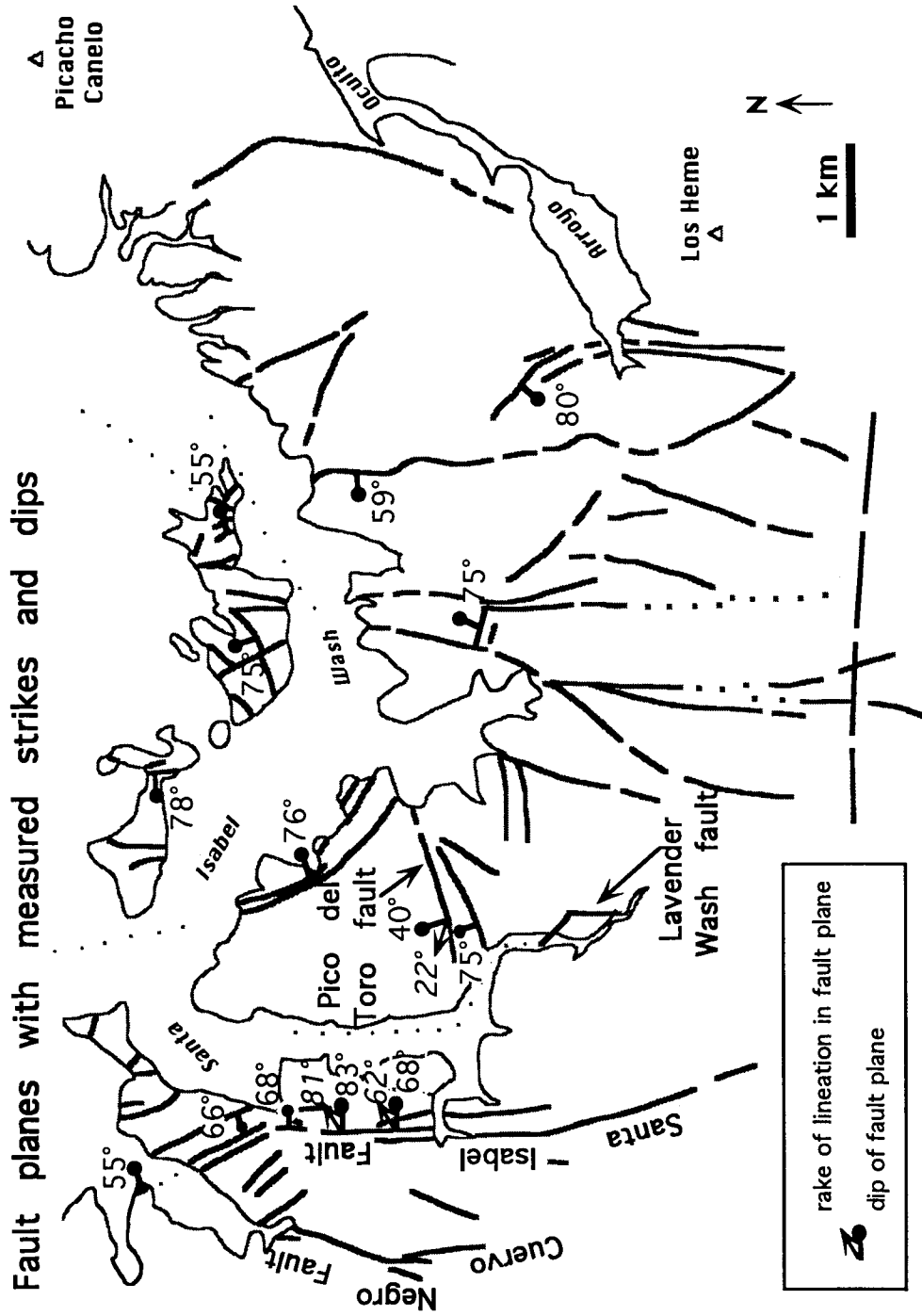
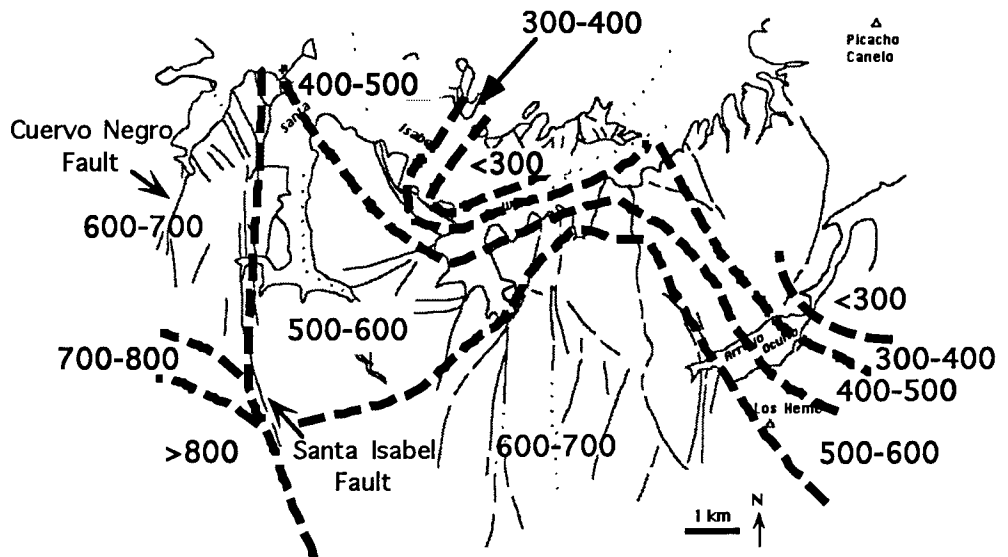




Figure 4.5. Contours roughly outlining the present-day elevation of the *Tmr3/Tmr4* depositional contact in Santa Isabel Wash. The correlative contact is believed to exist at approximately 1000 m elevation about 10 km west of the study area (Stock, Lewis, Salton, and Holt, unpub. mapping) (interpreted to be west of the Cuervo Negro fault system). Approximately 500 m of E-side-down displacement is inferred to have occurred across the Cuervo Negro and Santa Isabel fault systems. Pre-depositional (i.e., pre-6 Ma) elevations appear to be lower in the north on both sides of the Santa Isabel fault relative to the south and are perhaps indicative of an earlier phase of north- or northeast-side-down extensional deformation.



Elevation (in meters) of *Tmr3/Tmr4* contact

Figure 4.6. Location of a NE-striking fault inferred on the basis of a Quaternary fault scarp mapped at its southwestern end within the study area. Dashed lines with filled arrowheads show how modern drainages originate from the southeast and southwest, follow along the topographic low created by the inferred fault, and move off further north. No evidence was found indicating sense of motion along this fault. If dextral strike-slip motion occurred along it, as queried here, this could provide a mechanism for some of the opening of the 40 km<sup>2</sup> alluvial plain to the west of it.

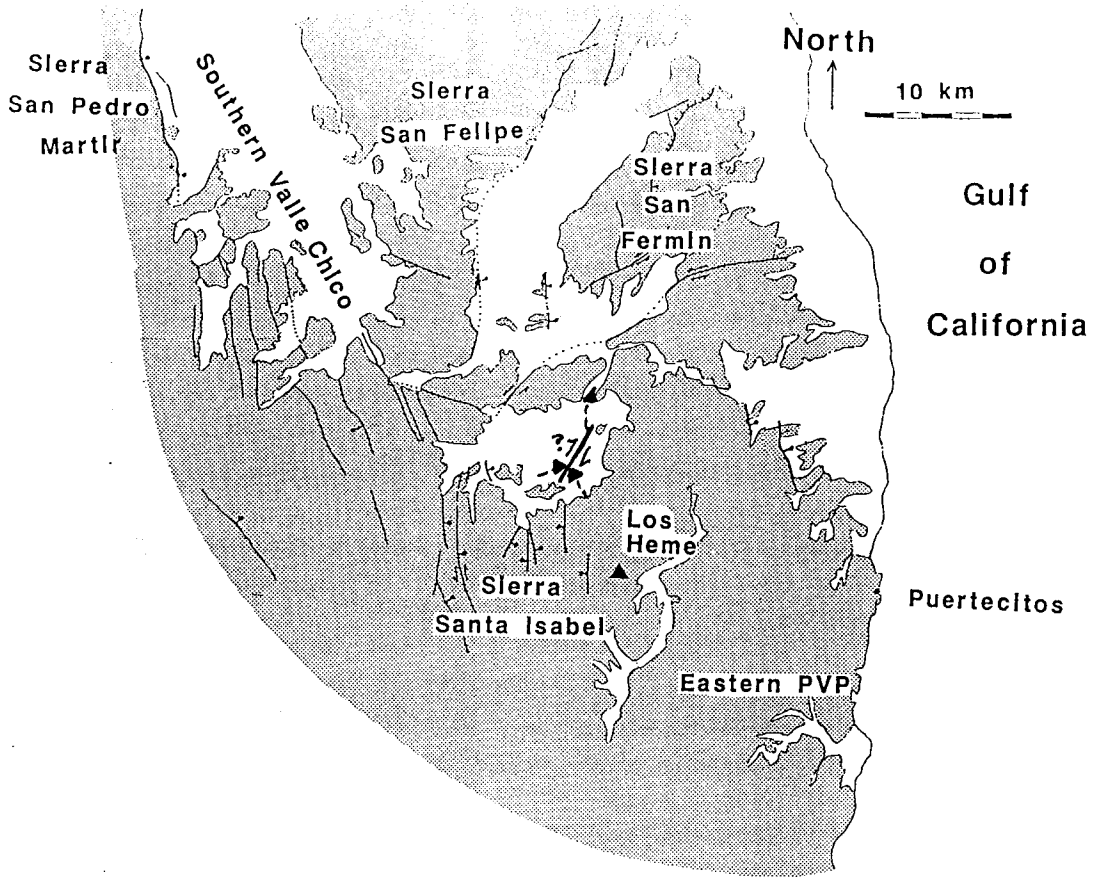


Figure 4.7. Cartoon block model of Santa Isabel Wash prior to deposition of 6-7 Ma Group 6 pyroclastic flow deposits.

PRE - 6-7 Ma

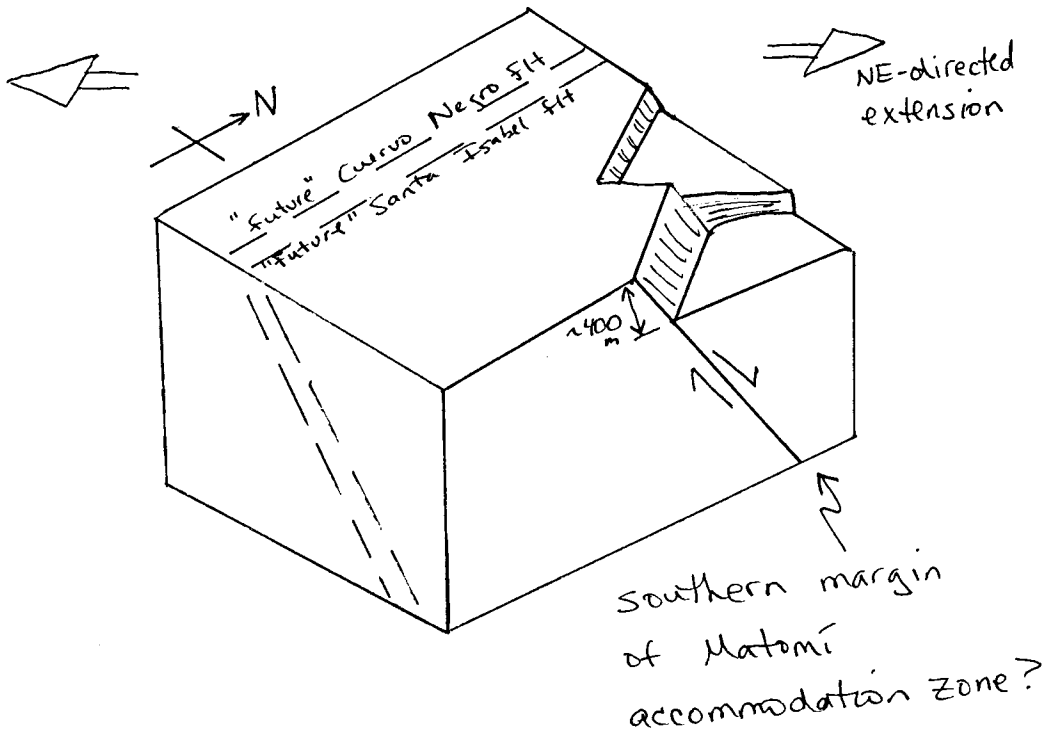
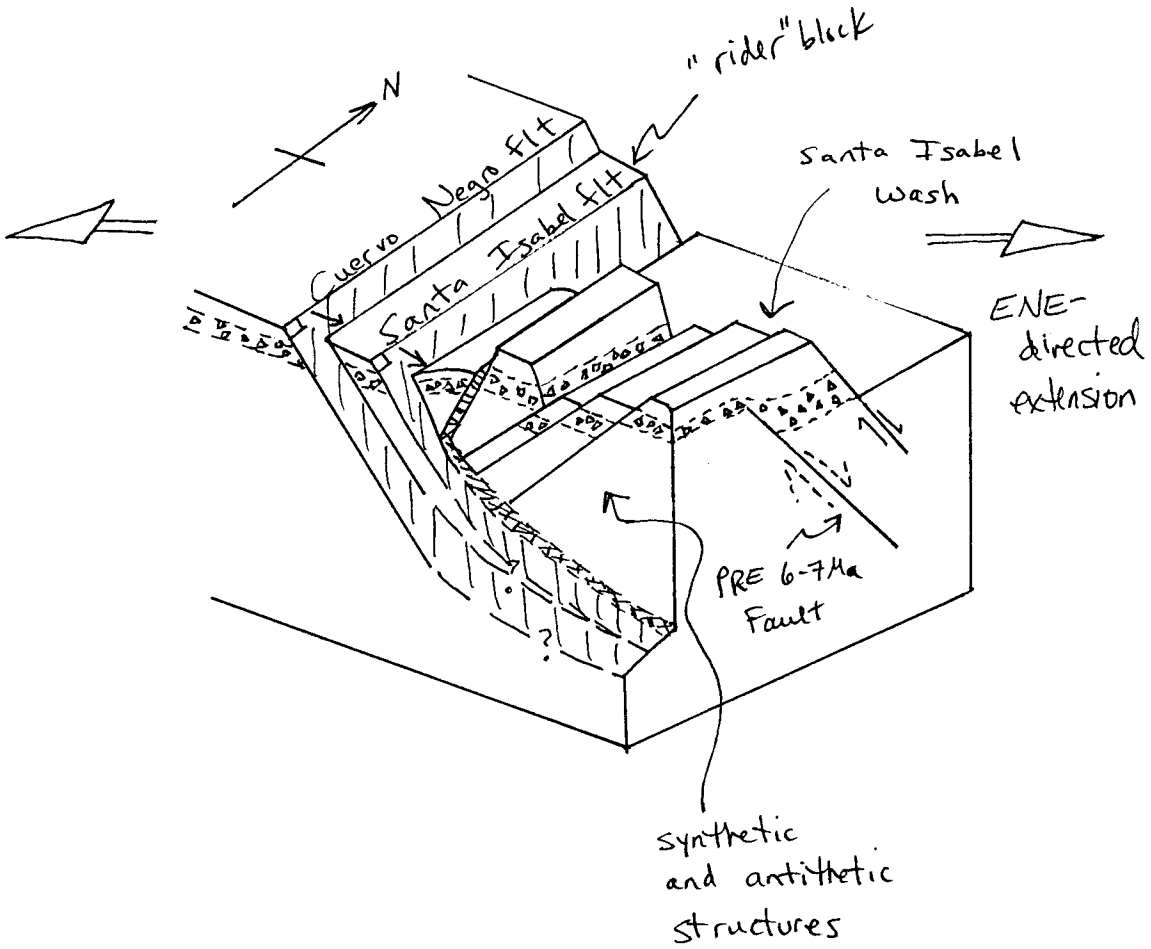


Figure 4.8. Cartoon block model of Santa Isabel Wash after deposition of 6-7 Ma Group 6 pyroclastic flow deposits. Listric geometry is inferred on the basis of tilted blocks in the hanging wall of Santa Isabel fault; however, it is not required. Most faulting is probably post 3-2 Ma (see Chapter VI for discussion).

POST 6 Ma





Chapter V

Paleomagnetic study of 6 Ma volcanic tuffs in Santa Isabel Wash

5.1. *Introduction*

5.2. *Field and laboratory methods*

A. *Sample collection and preparation for measurement*

B. *Demagnetization strategies*

C. *Rock magnetic and magnetic susceptibility tests*

5.3. *Results*

A. *Statistical methods and stability of RM within sites*

B. *Site to site synthesis*

C. *Test for common mean direction*

5.4. *Interpretation*

A. *Group means relative to each other*

B. *Group means relative to geomagnetic north*

5.5. *Comparison of results to Sierra San Fermín and Sierra San Felipe regions*

A. *Lithologic correlations*

B. *Relative rotations*

5.6. *Conclusions*

### 5.1. Introduction

In theory paleomagnetic analysis is well-suited to the task of identifying rotational deformation between discontinuous exposures of the same pyroclastic flow deposit. A consistent Thermoremanent Magnetization (TRM) direction of relatively strong intensity should ideally be preserved throughout a flow following extrusion and rapid, postemplacement cooling (e.g., Hildreth and Mahood, 1985). Within a series of flows deposited in a short period of time, cooling breaks as well as eutaxitic (flattening) foliation should be roughly horizontal, except perhaps at the margins of the deposit, and thus simplify structural corrections. Present-day sampling and laboratory demagnetization techniques are well-established, and the latter can be used to successfully isolate and remove common magnetic overprints found in some samples such as those which result from high-intensity lightning strikes.

Not surprisingly several studies have confirmed that reality is indeed much more complex than such an ideal scenario. Although the majority of paleomagnetic studies of pyroclastic flow deposits report tight clustering (e.g.,  $\alpha_{95} < 5\text{-}10^\circ$ ) of remanent magnetization (RM) directions for a set of cores at a given site (i.e., 3-10 cores collected within a few meters of each other), significant dispersion between different sampling localities in the same pyroclastic flow unit is not uncommon. Anomalous RM directions measured within such deposits have been attributed to postemplacement rheomorphism (Ellwood, 1982; Rosenbaum, 1986; Hagstrum and Gans, 1989), clast rotation induced by hydrocompaction (Hoblitt et al., 1985), syncooling secular variations (Wells and Hillhouse, 1989; McIntosh, 1991), chemical changes associated with devitrification (Geissman, 1980), difficulties in determining paleohorizontal for structural corrections (Hagstrum and Gans, 1989; McIntosh, 1991; Rosenbaum et al., 1991; Best et al., 1995), and sub-blocking temperature emplacement (Rosenbaum, 1993).

Despite these complexities there are studies which document convincing evidence for vertical-axis rotations between structural blocks based on paleomagnetic analysis of one or more pyroclastic flow deposit. Some examples include  $28^{\circ} \pm 12^{\circ}$  CW rotation of the Schell Creek Range relative to the Kern Mountains region in east central Nevada (Hagstrum and Gans, 1989), a range of  $37^{\circ} \pm 9^{\circ}$  CW to  $51^{\circ} \pm 10^{\circ}$  CCW rotations of the Miocene Peach Springs Tuff in the Colorado River extensional corridor (Wells and Hillhouse, 1989),  $7.1^{\circ} \pm 6.6^{\circ}$  CCW rotation of the southwestern Nevada volcanic field relative to the North American craton (Hudson et al., 1994), about  $30^{\circ}$  (no uncertainties given) CW rotation of south Yucca Mountain relative to north Yucca Mountain (Rosenbaum et al., 1991), and  $25^{\circ}$  (no uncertainties given) CCW rotation of Black Butte relative to other sampled localities in the Rio Grande rift (McIntosh, 1991). Given the uncertainties determined in most of these studies, it appears that small rotations (e.g.,  $< 10^{\circ}$ ) are within the noise of the measurement techniques and/or the natural variations preserved within a deposit, and thus cannot be confidently identified.

A recent paleomagnetic study examining vertical-axis rotations in pyroclastic flow deposits in northeastern Baja California found  $31^{\circ} \pm 15^{\circ}$  CW rotation in the Sierra San Fermín (Figure 1.6 in Chapter I) relative to nearby reference sections also measured in that study (Lewis, 1994; Lewis and Stock, in review in *J. Geophys. Res.*, 1997). Paleomagnetic analysis on some of the same deposits is presented here from the northern Sierra Santa Isabel, located ~30 km southwest of the Sierra San Fermín, and compared to the results from the earlier study. Structural differences between the Sierra San Fermín and the northern Sierra Santa Isabel (Nagy et al., 1996) suggest that these two regions, separated by an accommodation zone (see Chapter VI), have undergone different histories of deformation.

The Sierra Santa Isabel is located on the northern margin of the Miocene-Pliocene Puertecitos Volcanic Province (PVP). The study locations discussed here are on the western edge of the Gulf Extensional Province (GEP) and are shown in Figure 1.6 (in Chapter I). In addition to making comparisons with results from the Sierra San Fermín, the paleomagnetic

study described here was designed to support lithologic correlations within Santa Isabel Wash (informally named here) in the northern Sierra Santa Isabel, and to look for local rotations between structural blocks in an  $\sim 140 \text{ km}^2$  mapped area (see Chapter IV) of extensional deformation. The possibility of local rotation is likely given the abundance of mapped and inferred faults in Santa Isabel Wash, and the rotational deformation recorded to the north (Lewis, 1994; Lewis and Stock, in review in *J. Geophys. Res.*, 1997). A detailed geologic map and structural discussion of Santa Isabel Wash are presented in Chapter IV. A simplified geologic map is shown in Figure 5.1.

## 5.2. Field and laboratory methods

### A. Sample collection and preparation for measurement

A continuous stratigraphic package of five  $\sim 6$  Ma pyroclastic flow deposits (further divided into 11 cooling units) was sampled for paleomagnetic analysis at 15 locations in Santa Isabel Wash. From youngest to oldest these tuffs are the Arroyo Oculito Tuff ( $Tmr_{ao}$ ) (one cooling unit),  $Tmr_4$  (one cooling unit),  $Tmr_{3-4}$  (one cooling unit),  $Tmr_3$  (four cooling units), and the Tuffs of Santa Isabel Wash ( $Tmr_{siw}$ ) (four cooling units - labeled  $t5$  (stratigraphically highest) through  $t2$ ). Units  $Tmr_3$  and  $Tmr_4$  were first defined in an earlier study (Stock, 1989). Not all cooling units were present at each sampling site, nor were all cooling units drilled which were present at a given site. These pyroclastic flow deposits are between 1 and 160 meters thick in Santa Isabel Wash. Both welded and unwelded versions were sampled in this study, although in some cases the unwelded tuffs were too soft to drill. Complete lithologic and mineralogical descriptions are given in Chapter II, and  $^{40}\text{Ar}/^{39}\text{Ar}$  geochronology of  $Tmr_3$  and  $Tmr_{siw}$  are presented in Chapter III.

The 11 cooling units are listed in stratigraphic order (youngest at the top) in Table 5.1 with the number of cores collected at each site. Sampling sites are labeled A-P and are

shown schematically in Figure 5.2. In addition, stratigraphic columns of the 11 cooling units are shown adjacent to each sampling site in Figure 5.2, and shaded regions show which cooling units were sampled at each site. This study primarily concentrates on the RM directions preserved in the two oldest deposits, *Tmr3* and *Tmr<sub>siw</sub>*, which include eight cooling units.

In addition to the samples summarized in Table 5.1, oriented block samples were collected from an overlying tuff (one of the Tuffs of El Canelo - *Tmr<sub>ec</sub>*) and cored with a drill press in the lab. Block samples were collected from this densely welded tuff because the rock was extremely difficult to drill, and the amount of gasoline and water needed for field sampling was impractical. These block samples were collected from sampling sites B, C, D, and J (Figure 5.2). The cores drilled from oriented block samples of *Tmr<sub>ec</sub>* did not produce successful results, and they are mentioned here only for completeness. Most samples yielded erratic and unstable demagnetization paths, and two cores from a given block sample often preserved significantly different primary RM directions. Many samples exhibited multi-component behavior that was not resolved into an isolated stable, RM direction. Consequently, all samples from *Tmr<sub>ec</sub>* have been removed from this study. One likely reason for the inconsistent RM directions is post-depositional, rheomorphic flow which is evidenced in *Tmr<sub>ec</sub>* by flow foliation, lineations, and kinematic flow indicators such as tension gashes and sheared fiamme. There are also more opportunities for orientation errors with block samples than for cores drilled in the field. Most samples preserved normal polarity magnetization, although this is not necessarily a reliable result.

The 223 rock cores listed in Table 5.1 were collected using a gasoline powered drill equipped with a 25.4-mm (1") diameter, diamond-tipped drill bit and cooled with water. Between 4 and 8 cores were drilled from a given cooling unit at each site; the 11 samples listed for unit *Tmr3(I)* at site D were collected from two stratigraphic horizons separated by about 60 meters. Appendix E gives a detailed description of sample collection techniques.

In the lab, each core was cut into 22-mm-long segments using a diamond saw. At this length, samples approximate a sphere, the optimum sample shape for paleomagnetic measurement. In some cases individual cores were long enough to be cut into 3 segments. The letter "A" was added at the end of a given sample name for the innermost segment (i.e., furthest from the surface of the rock) to distinguish it from the next segments ("B" and "C"). The core labeling system used in this study is shown in Figure 5.3. Generally "A" segments were used for the demagnetization measurements as they were likely to be affected least by weathering processes at the rock surface. Following sizing of the cores, all samples were placed in a magnetically shielded  $\mu$ -metal room for the duration of the demagnetization procedure. Any broken pieces of core were glued back onto the cores using alumina cement in the shielded room. Note that the five cores shown schematically in Figure 5.3 are oriented in five different orientations. Drilling cores in a variety of orientations provides a good check on possible remagnetization due to the drilling process and/or systematic misorientation of the cores.

### *B. Demagnetization strategies*

Samples were measured at the Caltech Paleomagnetism Laboratory in a computer-controlled cryogenic SQUID (Superconducting QUantum Interference Device) magnetometer in a magnetically shielded  $\mu$ -metal room. The background noise level of the magnetometer is approximately  $5 \times 10^{-12} \text{ Am}^2$  ( $5 \times 10^{-9} \text{ G/cm}^3$ ).

Since all of the rock units sampled in this study are pyroclastic flow deposits, it is most likely that the primary RM preserved in these units is a TRM acquired during rapid, postemplacement cooling of the units from above the Curie temperature. Given Curie temperatures of common magnetic minerals between 575°C and 675°C (e.g., magnetite and hematite, respectively), and pyroclastic flow emplacement temperatures measured as high as

730°C (e.g., Mount St. Helens (Banks and Hoblitt, 1981)), this assumption is probably a sound one.

Laboratory demagnetization techniques have been developed which allow for the removal of secondary overprints and the extraction of the primary RM direction. Secondary magnetization overprints that are possible include 1) Isothermal Remanent Magnetization (IRM), acquisition in a strong magnetic field such as that induced by a lightning strike, 2) Chemical Remanent Magnetization (CRM), acquisition from a magnetic mineral which nucleates and grows in a magnetic field, and 3) an overprint of the present day magnetic field direction known as Viscous Remanent Magnetization (VRM).

Two pilot studies using a total of 46 samples provided an assessment of the most efficient and strategic demagnetization methods for this study. Following measurement of the Natural Remanent Magnetization (NRM), which is the sum of all of the components acquired within a rock throughout its history, 22 samples in pilot group 1 were thermally demagnetized by incremental heating in a magnetically shielded  $\mu$ -metal oven and measured after each step. Remanence is thus analyzed with respect to the spectrum of relaxation times of the magnetic particles. Thermal steps generally used were 100°C, 200°C, 300°C, 375°C, 450°C, 500°C, 530°C, 560°C, 590°C, 620°C, 650°C, and 690°C.

The 24 samples in pilot group 2, following NRM measurement, were subjected to alternating field (AF) demagnetization. In this procedure the magnetic remanence of samples is measured after a weak, decreasing, alternating magnetic field is applied in three orthogonal directions. Sample remanence is measured after each step in a series of field strength increases. In this way the remanence is examined from the coercivity spectra of the magnetic grains in the sample. The AF demagnetization field steps generally used were 2.5 mT, 5.0 mT, 7.5 mT, 10.0 mT, 15.0 mT, 20.0 mT, 25.0 mT, 30.0 mT, 40.0 mT, 50.0 mT, 60.0 mT, 70.0 mT, and 80 mT (1 mT = 10 Gauss). In addition, these samples were subject to thermal demagnetization following the completion of the AF demagnetization to determine if additional components might be discerned. These thermal steps were 100°C, 250°C, 375°C,

475°C, 530°C, 580°C, 610°C, 650°C, and 690°C. Samples from this pilot group will be referred to as the “AF (+ thermal)” demagnetized samples in the following discussion.

In order to compare the two demagnetization methods, the "B" segments (Figure 5.3) of eight cores were thermally demagnetized in pilot group 1 and compared to the "A" segments of the same cores which were treated to the procedures of pilot group 2. Some examples of the demagnetization results of these sister samples are shown in Figures 5.4 (a, b), 5.5 (a, b), and 5.6. The results of progressive demagnetization are illustrated with Zijdeveld plots (horizontal projection in closed symbols, vertical projection in open symbols), lower hemisphere equal area plots, and magnetic intensity plots normalized to the initial magnetic intensity of each sample. The histograms on the normalized intensity plots illustrate the fraction of total intensity removed at a given demagnetization step.

A secondary overprint is evident in a sample from  $Tmr_{siw} (t4)$  shown in Figure 5.4. The sample demagnetized with the AF (+ thermal) technique (Figure 5.4a) shows gradual removal of the secondary component which initially shows a declination value of  $\sim 350^\circ$  and an inclination of  $\sim 20^\circ$ . By the 20.0 mT demagnetization step, a stable TRM direction with a declination value of  $\sim 20^\circ$  and an inclination of  $\sim 25^\circ$  persists for the remainder of the demagnetization procedure until the sample becomes magnetically unstable during the last few steps. In contrast, the thermally demagnetized sample (Figure 5.4b) defines a plane in which both of these components exist; however, the primary RM direction is not resolved. This is most evident in the equal area plot. Comparison of the Zijdeveld plots for these sister samples illustrates how the thermally demagnetized sample (Figure 5.4b) yields declination directions subsequent to the 300°C heating step which clearly have not been cleaned of the overprint.

A similar example is presented in Figure 5.5 (a, AF (+ thermal) demagnetization, and b, thermal demagnetization) for a sample from  $Tmr_{ao}$ . Once again a secondary overprint does not appear to have been successfully removed by the thermal demagnetization process. In both cases there is a greater drop in magnetic intensity with the AF (+ thermal)



demagnetization procedure than with thermal demagnetization only. The samples demagnetized with AF also show a much smoother and more regular drop in intensity than do thermally demagnetized samples.

The relatively consistent RM direction measured for an AF (+ thermal) demagnetized sample from  $Tmr_{siw}$  (t5) in the top of Figure 5.6 (best seen in the Zijdeveld plot) contrasts with the slightly more variable directions measured for a thermally demagnetized sample (bottom of Figure 5.6). This is partly because samples are not removed from the holder between each AF demagnetization step (i.e., the demagnetization coils are in-line with the measurement coils) and thus their positions do not change between steps. The necessity to put samples into the oven during thermal demagnetization requires that the sample be repositioned for each measurement. This positioning error is relatively small as can be ascertained by examining the slight differences and respective uncertainties of the resultant vectors: AF (+ thermal) demagnetized sample [21 steps]: Dec = 22.4°, Inc = 39.6°,  $\alpha_{95}$  = 0.5°; thermally demagnetized sample [14 steps]: Dec = 20.7°, Inc = 40.1°,  $\alpha_{95}$  = 2.3°. Again, the thermal demagnetization did not reduce the magnetic intensity of this sample as much as did the AF (+ thermal) demagnetization procedure.

It is possible that lightning strikes have imparted IRMs on some of the tuffs sampled. The strong NRM intensities ( $\sim 10^{-3}$  mT = 10 A/m) are comparable to NRM values found in other ignimbrites inferred to have acquired high-intensity, lightning-induced IRMs (e.g., McIntosh, 1991). Additionally, the large magnetic intensity drops during the initial AF (but not thermal) demagnetization steps (e.g., Figures 5.4a and 5.5a) could represent the removal of an IRM, since large IRM components are fairly immune to removal with thermal demagnetization techniques but can be readily removed using AF demagnetization (McElhinny, 1973). For this reason, in addition to observations discussed above, AF demagnetization is preferred for sample demagnetization in this study.

In some cases a few thermal demagnetization steps were performed in the middle of the AF demagnetization procedure to check for the presence of goethite. Goethite ( $\alpha$ -

FeOOH) is a naturally occurring iron hydroxide which dehydrates to oxides between 100° and 300°C (McElhinny, 1973). Although it is most common in sediments, it is also considered important in volcanic rocks (J. Kirschvink, pers. comm., 1995). If present, a goethite component can obscure the primary RM vector below the dehydration temperature. The following combination demagnetization scheme was chosen: five initial AF demagnetization steps (2.5 mT, 5.0 mT, 7.5 mT, 10.0 mT, 15.0 mT) followed by two thermal demagnetization steps (200°C and 300°C) and then the remaining AF demagnetization steps (20.0 mT, 25.0 mT, 30.0 mT, 40.0 mT, 50.0 mT, 60.0 mT, 70.0 mT, and 80 mT). Eighty-three samples were demagnetized using this strategy; a typical sample (from *Tmr<sub>siw</sub> (t4)*) is shown in Figure 5.7. As is the case for the sample shown here, it appears that the intermediate thermal demagnetization had little effect on any of the units. The remaining 100+ samples were demagnetized using only AF demagnetization. Cores were typically demagnetized in 13 steps up to 80 mT, but in cases of samples with very strong magnetic intensities as high as 260 mT.

### *C. Rock magnetic and magnetic susceptibility tests*

Rock magnetic experiments performed to discern the nature of the magnetic grains carrying the RM in the rocks included Anhyseretic Remanent Magnetization (ARM) tests and laboratory IRM tests. At least one sample from each pyroclastic flow deposit was measured. The sample was crushed by hand with a mortar and pestle to randomize the magnetic directions, 30 to 50 milligrams were placed into a small plastic epindorph tube, and a small bit of wax was melted over the sample to keep the grains in place during the experiment. Four tests were then sequentially performed in a cryogenic SQUID magnetometer with an IRM generator. First an ARM was incrementally imparted on the sample in a standard 100 mT alternating field from 0.5 to 2 mT (four steps at 0.5 mT increments), and then the ARM was subjected to AF demagnetization from 2 to 199.5 mT

(21 steps). A 100-mT IRM was applied to the sample followed by AF demagnetization of the IRM (same 21 steps). Finally, IRM acquisition was examined beginning with a 2 mT pulse and going as high as 1995.3 mT (31 steps).

A typical example of the results from the rock magnetic tests is shown in Figure 5.8. A predominance of fine-grained (< 10  $\mu\text{m}$ ) single-domain or pseudo-single-domain magnetite is suggested by higher coercivities of the ARM demagnetization curve (AF of ARM) relative to the IRM demagnetization curve (AF of IRM). The IRM acquisition curve suggests domination of the remanence by ferrimagnetic minerals such as magnetite, which typically saturate at peak coercivities of 100 mT, and smaller amounts of antiferromagnetic minerals such as hematite, which saturate at higher coercivities (~ 650 mT) (Tarling, 1983).

Magnetic susceptibility was measured for all samples using a Bartington magnetic susceptibility meter. Those samples heated in the oven were remeasured after heating to try to detect any changes in the properties of magnetic minerals in the samples. Most samples, including heated samples, had mean bulk magnetic susceptibilities (measured at low frequency) between 0.001 and 0.004 (per unit volume in SI units). These values are within the ranges measured in other ash flow tuffs (e.g., Hillhouse and Wells, 1991; Schlinger et al., 1991).

An exception was cooling unit *t2* from *Tmr<sub>siw</sub>* which yielded magnetic susceptibility values > 0.01 and commonly > 0.05. Magnetic grains which are very small (0.001-0.01  $\mu\text{m}$ ) behave superparamagnetically and are evident in susceptibility tests because they have much higher magnetic susceptibilities than stable single-domain grains. Significant changes in susceptibility were noted for these samples when the measurement frequency was changed, supporting the presence of superparamagnetic grains in this cooling unit (Thompson and Oldfield, 1986). An additional rock magnetic test was performed to check for the presence of superparamagnetic grains in cooling unit *t2* (Figure 5.9). The sample was cooled to liquid N<sub>2</sub> temperatures, subjected to a strong IRM pulse, and then measured repeatedly as it was brought up to ambient temperature. This is shown with the thick curve in Figure 5.9. The

sample was then cooled again to liquid N<sub>2</sub> temperatures but not subjected to an IRM pulse, and again measured repeatedly as it was brought up to ambient temperature (thin curve in Figure 5.9). The retention of the magnetic moment for a brief period of time following the IRM pulse supports the presence of superparamagnetic grains; paramagnetic materials do not have the same ability to temporarily retain magnetization after a field is removed. A small change in the slope of the thin curve in Figure 5.9 (indicated with an arrow) around 120° K likely marks a crystallographic transition indicative of single-domain magnetite known as the Verwey transition in which the crystal structure transforms from an ordered cubic form to a lower symmetry (O'Reilly, 1984).

### 5.3. Results

#### A. Statistical methods and stability of RM within sites

RM vectors were calculated using principal component analysis (Kirschvink, 1980) to selected demagnetization steps for each sample. As discussed above (e.g., Figures 5.4a, 5.5a) multiple components of RM may be identified by changes in magnetization direction with progressive demagnetization. For example, a given sample can contain a low coercivity VRM or IRM overprint, a primary TRM direction, and an unstable high coercivity component. An example of a sample from *Tmr<sub>Siw</sub> (t4)* with a significant low coercivity overprint is shown in Figure 5.10. By the 15 mT step, however, the overprint has been removed and a stable RM direction is evident.

The primary RM direction for most of the samples consists of a single component fit with a line in vector space; however, some samples show only partial removal of an overprint and thus the two components (the primary direction and the overprint direction) are best fit with a plane. The RM direction of a sample from *Tmr3 (type I)* (Figure 5.11) moves gradually away from an overprint direction of  $D \approx 130^\circ$  and  $I \approx 15^\circ$  with progressive

demagnetization. However, as demagnetization continues, a stable single component is not clearly resolved, and thus this sample is fit with a plane. Ten of the cores used in this analysis were fit with planes instead of lines.

The sample summary in Table 5.2 lists paleomagnetic results for the 11 cooling units. They are combined on the basis of RM directions into six groups (discussed below). The stratigraphically highest tuff is listed first. Sampling location, bedding strike and dip, number of samples collected ( $N_c$ ) and used ( $N$ ) in the analysis, and primary RM directions in geographic and stratigraphic (tilt-corrected) coordinates are given for each sampling site. A total of five cores out of the original 223 were removed from the study on the basis of poorly preserved RM direction. (The normal polarity preserved in four of these discarded samples agrees with the polarity recorded in the rest of the samples; the fifth sample had a horizontal inclination direction.)

The uncertainties for each site mean (Table 5.2) are calculated using both Fisher and Bingham distribution functions. The Fisher distribution function, which assumes a circularly symmetric distribution, yields concentration parameters  $\kappa$  and  $\alpha_{95}$ . A larger value of  $\kappa$  implies tighter clustering of the data points relative to a smaller value. For multiple samples from a single cooling unit, a grouping of data is usually considered acceptable when  $\kappa$  is large (say  $> 80$ ) and/or when the value for  $\alpha_{95}$  is  $< 5-10^\circ$ . The Bingham distribution function is preferable to the commonly used Fisher distribution function because it can approximate elongate paleomagnetic data sets. In other words, it has the potential to identify and parameterize distributions in which only the declination or inclination values vary significantly while the other varies only slightly (see Onstott (1980) for comparison and complete discussion of these two distribution functions). The concentration parameters for Bingham distributions thus consist of two values of uncertainty related to any elliptical spread in a data set. In Table 5.2 these parameters are listed as  $\kappa_1$  and  $\kappa_2$  with associated  $\alpha_{95}$  values. The Bingham distribution is elliptical in shape when  $\kappa_1 < \kappa_2 \ll 0$  (Onstott, 1980). For both distribution

demagnetization. However, as demagnetization continues, a stable single component is not clearly resolved, and thus this sample is fit with a plane. Ten of the cores used in this analysis were fit with planes instead of lines.

The sample summary in Table 5.2 lists paleomagnetic results for the 11 cooling units. They are combined on the basis of RM directions into six groups (discussed below). The stratigraphically highest tuff is listed first. Sampling location, bedding strike and dip, number of samples collected ( $N_c$ ) and used ( $N$ ) in the analysis, and primary RM directions in geographic and stratigraphic (tilt-corrected) coordinates are given for each sampling site. A total of five cores out of the original 223 were removed from the study on the basis of poorly preserved RM direction. (The normal polarity preserved in four of these discarded samples agrees with the polarity recorded in the rest of the samples; the fifth sample had a horizontal inclination direction.)

The uncertainties for each site mean (Table 5.2) are calculated using both Fisher and Bingham distribution functions. The Fisher distribution function, which assumes a circularly symmetric distribution, yields concentration parameters  $\kappa$  and  $\alpha_{95}$ . A larger value of  $\kappa$  implies tighter clustering of the data points relative to a smaller value. For multiple samples from a single cooling unit, a grouping of data is usually considered acceptable when  $\kappa$  is large (say  $> 80$ ) and/or when the value for  $\alpha_{95}$  is  $< 5-10^\circ$ . The Bingham distribution function is preferable to the commonly used Fisher distribution function because it can approximate elongate paleomagnetic data sets. In other words, it has the potential to identify and parameterize distributions in which only the declination or inclination values vary significantly while the other varies only slightly (see Onstott (1980) for comparison and complete discussion of these two distribution functions). The concentration parameters for Bingham distributions thus consist of two values of uncertainty related to any elliptical spread in a data set. In Table 5.2 these parameters are listed as  $\kappa_1$  and  $\kappa_2$  with associated  $\alpha_{95}$  values. The Bingham distribution is elliptical in shape when  $\kappa_1 < \kappa_2 \ll 0$  (Onstott, 1980). For both distribution

functions, concentration parameters given in Table 5.2 have been calculated using the tilt-corrected declination and inclination values.

All samples record normal polarities.  $^{40}\text{Ar}/^{39}\text{Ar}$  ages determined for *Tmr3* and the various cooling units of *Tmr<sub>siw</sub>* (presented in Chapter III) span  $6.1 \pm 0.6$  Ma to  $6.7 \pm 0.1$  Ma, implying that the units were most likely deposited during Subchron C3An.2n (6.269-6.567 Ma) (Cande and Kent, 1995).

Minor tilt corrections were made at a few localities where the entire series of tuffs clearly dipped; however, most units are interpreted to be horizontal. Eutaxitic foliation measurements were made at all sampling sites where a compaction foliation was evident. With the exception of one sampling locality (site B), where eutaxitic foliations of the drilled outcrop are almost vertical, the dips of the foliations generally vary between horizontal and  $\sim 35^\circ$ . Significant variations in the strikes and dips of the eutaxitic foliation plane were present among sets of cores from some of the sampling sites, and this presented the opportunity to see if tilt-correcting with eutaxitic foliation measurements would increase or decrease the dispersion. The assumption made here is that compaction occurs above the Curie temperature prior to the acquisition of TRM and thus should not affect the preserved RM directions (e.g., Tarling, 1983; Fisher and Schmincke, 1984). This contrasts with the interpretation that eutaxitic foliation planes represent paleohorizontal, and thus can be used for tilt-corrections (e.g., Hagstrum and Gans, 1989; McIntosh, 1991; Rosenbaum et al., 1991; Lewis, 1994). The RM directions at three sampling sites in Santa Isabel Wash in which the bedding is interpreted to be horizontal were recalculated by tilt-correcting with the eutaxitic foliation values (Table 5.3) and compared to the values given in Table 5.2. The three sites chosen had the largest variations in eutaxitic foliation planes among the cores collected. Dispersion clearly increases significantly in all three cases when tilt-corrections are made using eutaxitic foliation values. The eutaxitic foliation in these particular deposits evidently developed at temperatures above the Curie temperature and, at least at these locations, does not represent paleohorizontal.

### B. Site to site synthesis

The 11 cooling units distributed throughout the 15 locations fall into 6 distinct groups on the basis of the preserved RM directions. They are divided as such in Table 5.2 by horizontal lines. As will be discussed further below, this implies that there appear to be no relative rotations between sampling sites within any of the lithologic units. Equal area plots showing the resultant vectors of the cores from each site (for a given cooling unit) are shown in Figure 5.12 (a-f). From youngest to oldest the six groups are  $Tmr_{ao}$  (Figure 5.12a),  $Tmr4$  (Figure 5.12b),  $Tmr_{3-4}$  (Figure 5.12c), two groups from  $Tmr3$  (three stratigraphically higher cooling units (in some localities subdivided into: u-upper, m-middle, l-lower) designated “type II” (Figure 5.12d) and an underlying cooling unit designated “type I” (Figure 5.12e)), and all four cooling units ( $t5-t2$ ) from  $Tmr_{siw}$  (Figure 5.12f). Each equal area plot in Figure 5.12 corresponds to one of the rows in Table 5.2 which lists a mean site direction. Planes are drawn as great circles for samples which were fit to a plane instead of a line. Fisher confidence cones of 95% are also shown. In cases where  $\alpha_{95}$  is very small, such as for  $Tmr_{siw}$  ( $t5$ ) at site E in Figure 5.12f, the confidence circles are partly or completely obscured by the sample points.

In general, data points cluster well at individual sites and commonly have  $\alpha_{95} < 10^\circ$ . This suggests that orientation errors and/or small-scale variations (i.e., over a few meters) in preserved RM direction are minor. Four exceptions to well-clustered sites are samples from  $Tmr_{ao}$  at Site D (Figure 5.12a),  $Tmr4$  at Site D (Figure 5.12b),  $Tmr_{3-4}$  at Site C (Figure 5.12c), and  $Tmr3$  (type I) at Site K (Figure 5.12e) which yield  $\alpha_{95}$  values between  $14.2^\circ$  and  $20.8^\circ$ . The scatter at these four sites includes variations among all of the cores, and is not the result of only one or two outliers. These sites are interpreted to be examples of outcrops with poorly preserved RM direction, perhaps due to incomplete removal of a CRM or IRM overprint. Nonetheless, the results from all four sites were retained in this study.



Combined RM directions with associated uncertainties are calculated for each of the six distinct groups with Fisher and Bingham distribution functions in a manner similar to individual site calculations described above (Table 5.2 and Figure 5.13.) The group means are calculated by treating each data point at each site (i.e., each core) as an individual measurement and calculating the average as if they were all from one site. This contrasts with the commonly used method of taking averages of sites (which are already averages of several cores and each have their own associated concentration parameter.) For example, the combined RM direction calculated for  $Tmr_{siw}$  uses 91 individual samples instead of averaging the 16 site means. The method used here seems more logical if the assumption is that all sites grouped together record the same RM direction, and since there is no way to assign a statistically meaningful uncertainty to a group of samples in which each sample (in this case, each site) already has its own associated uncertainty, it leads to a more statistically meaningful estimate of the uncertainty of the average.

### *C. Test for common mean direction*

Prior to calculating the combined values for the six groups as described above, a straightforward statistical test was utilized to justify combining the data from the various sampling sites for each of the six groups. To test whether two or more Fisher distributions have a common mean when the values for  $\kappa$  are not the same for each group, we can calculate the quantities  $\mathbf{R}$  and  $\mathbf{R}_w$  as follows (from Fisher and others (1993)):

$$\mathbf{R} = \kappa_1 \mathbf{R}_1 + \dots + \kappa_r \mathbf{R}_r \quad (5.1)$$

and

$$x = \kappa_1 R_1 x_1 + \dots + \kappa_r R_r x_r \quad (5.2)$$

$$y = \kappa_1 R_1 y_1 + \dots + \kappa_r R_r y_r \quad (5.3)$$

$$z = \kappa_1 R_1 z_1 + \dots + \kappa_r R_r z_r \quad (5.4)$$

$$R_w = (x^2 + y^2 + z^2)^{1/2} \quad (5.5)$$

where  $R_i = n_i - \{(n_i - 1) / \kappa_i\}$  and  $x_1, y_1$ , and  $z_1$  are the direction cosines from a group  $i$  at a given site containing  $n_i$  samples. A test statistic  $g_r$  is then calculated:

$$g_r = 2(R - R_w) \quad (5.6)$$

and compared to the upper 95% point of the  $\chi^2$  distribution. If  $g_r$  is too large, the hypothesis is rejected that the distributions have a common mean direction.

Unfortunately, this test for estimating the common mean direction of two or more rotationally symmetric sample distributions must have at least 25 individual data points per sample to determine an acceptable confidence cone (Fisher et al., 1993). Sampling sites in this study have between four and eight individual data points (i.e., cores), and thus a bootstrap technique had to be employed to assess the estimate of the test statistic ( $g_r$ , estimated as given above; Table 5.4). A short computer program (modified from the reversal test program of McFadden and McElhinny (1990)) simulates random sub-populations within a Fisher distribution with identical parameters ( $n_i, D_i, I_i, \kappa_i, R_i$ ) of each population being tested and compares the separation between them. The process is repeated 1000 times in order to determine random variation within a single Fisher distribution.

In all cases the test statistic is less than the value found 1 out of 20 times from the simulation (Table 5.4). This means that the hypothesis cannot be rejected (i.e., must be accepted) at the 95% confidence level that the distributions have a common mean. This

approach to estimating the uncertainty of the common mean direction yields a useful quantitative parameter. For example, a group of samples may produce a test statistic which is greater than the bootstrap-generated 5% limit but less than, say, the 10% limit. In this case, the hypothesis of common mean directions cannot be rejected at the 90% confidence level, but must be rejected at the 95% confidence level. The hypothetical group of samples may be interpreted to have common mean directions with 90% confidence, but not with 95% or greater confidence.

This procedure to test for a common mean direction among a group of sites (each of which consists of a number of samples with  $< 25$  individual data points) could help to better quantify similar data sets in future paleomagnetic studies. (In instances where there are  $> 25$  elements per group, successful bootstrap statistical procedures have already been developed (e.g., Tauxe et al., 1991)). Presently, paleomagnetic studies which group results from a number of sites (with  $n < 25$  per site) to determine a mean direction for a given lithologic unit often combine several sites based simply upon visual inspection of how well-grouped the 95% confidence ellipses for each site are relative to each other. In many studies this is not even stated, but the lack of criteria for grouping sites suggests that this is how the decision was made. A slightly more rigorous approach used in some studies is to define a somewhat arbitrary procedure to remove anomalous sites. For example, McIntosh (1991) removed sites from his study with mean directions which were more than  $15^\circ$  away from the unit-mean direction.

To illustrate the potential usefulness of the procedure developed here, several published data sets were examined using this test. In all cases the authors of each study chose to group a number of sites together to calculate a unit-mean. The 15 sampling sites within the Pahrnagat ash flow sheet from the study of Best and others (1995) yield a test statistic ( $g_r$ ) less than the 5% limit generated by that data set and the bootstrap procedure described above, indicating that there is indeed justification to group these sites together to derive a unit-mean direction. Of the four lava flow sequences distinguished by Conway and others (1992) in

Guatemala, three of them (involving either 4 or 14 sampling sites) yield similar results as the previous example. However, the fourth lava sequence (SE sequence - Hb<sub>oldest</sub>) resulted in  $g_r$  for five sampling sites greater than that determined at both the 5% and 10% limits. Thus the hypothesis must be rejected at the 90% confidence level (at least) that the five sites from that lava sequence have a common mean direction. As a final example, the data from the Chiquito Peak and Masonic Park tuffs from the San Juan volcanic field (Lipman and others, 1996) were examined. While  $g_r$  for eight sites within the Masonic Park Tuff is less than the value for the 5% limit, supporting the decision to calculate a unit-mean, the value for  $g_r$  for the 8 sites from the Chiquito Peak tuff is greater than both the 5% and 10% limits. Again, the calculation of a statistically meaningful unit-mean for this example is questionable. When these kinds of results occur, it suggests that perhaps there are other factors contributing to the site-to-site dispersion which need to be addressed. Finally, note that the mean RM directions from the above data sets which yield a value for  $g_r$  less than the generated 5% limit (i.e., thereby justifying grouping multiple sites together) could be recalculated by treating all cores from all sites independently (as done in this study) instead of averaging site means. This should give a better assessment of the uncertainties in the data set since it avoids averaging site means which already have associated uncertainties.

#### *5.4 Interpretation*

Vertical-axis rotations between 15 sampling sites are not evident on the basis of the paleomagnetic results presented here for ~6 Ma pyroclastic flow deposits in Santa Isabel Wash of the northern PVP. Based upon the results of the test for common mean directions, the various sampling sites record the same RM direction within a given deposit with 95% confidence. Slight variations in RM directions between sites in a given deposit preclude detection of small relative rotations of less than about 10°. This amount of uncertainty agrees

with values determined in other paleomagnetic studies of pyroclastic flow deposits (e.g., Hagstrum and Gans, 1989; Wells and Hillhouse, 1989; Hudson et al., 1994).

Absence of post-6 Ma rotational deformation in Santa Isabel Wash is an important result since numerous faults separating the sampling sites could have acted as boundaries of rotating structural blocks. Additionally, as discussed below, post-6 Ma rotational deformation has been documented 20-30 km to the north (Lewis, 1994; see also Lewis and Stock, in review in *J. Geophys. Res.*, 1997). The combined magnetic directions listed for each group in Table 5.2 and illustrated in Figure 5.13 are the values used in the following discussion.

#### *A. Group means relative to each other*

The three youngest groups ( $Tmr_{ao}$ ,  $Tmr_4$ , and  $Tmr_{3-4}$ ) record three directions reasonably close to each other (Figure 5.13), although it is likely that at least some time passed between the deposition of each tuff in order for minor secular variations to have occurred.

In contrast, the two RM directions (*type I* and *type II*) preserved in lithologic unit  $Tmr_3$  are significantly different from each other. This implies a significant amount of time between the deposition of the oldest cooling unit (*type I*) and the three overlying cooling units (*type II*). Given present-day assessments of secular variations of the Earth's magnetic field of  $\sim 0.1^\circ/\text{yr}$  (e.g., Barraclough, 1995; Ultré-Guérard and Achache, 1995), the  $35^\circ$  angular difference between the two preserved RM directions suggests at least 350 years of time between the deposition of the lowest and the upper three cooling units.

The existence of two distinct RM directions preserved in  $Tmr_3$  was an unexpected result, as the four cooling units are very similar in outcrop appearance and samples were consistently drilled at the lowest possible  $Tmr_3$  outcrop overlying  $Tmr_{siw}$ . The three upper cooling units were sampled at Site L and clearly preserve the same (*type II*) RM direction (Figure 5.12d). Two distinct cooling units sampled at site N also gave similar (*type II*) RM

directions. It appears that a cooling unit preserving the *Tmr3 (type I)* RM direction is not present at either of these localities. In fact, there are only three sampling sites which have cooling units with *Tmr3 (type I)* RM directions, and all of these sites are located in the western and northwestern parts of Santa Isabel Wash (Sites A, D, K; Figure 5.2). (Note that *type I* RM occurs in two places at site D within outcrops separated stratigraphically by about 60 meters). Based upon the results of underlying *Tmr<sub>siw</sub>* (discussed next), which shows no differences in RM direction between sites A, D, and K and the other sites, it is improbable that the two types of *Tmr3* RM directions are the result of rotation of the same cooling unit between sites A, D, and K and the rest of the sampling sites. More likely, this lowest *Tmr3* cooling unit was not deposited and/or preserved east or south of sites A, D, and K. Subsequent field checks suggest that the upper cooling units (*type II*) are present in sites A, D, and K overlying the cooling unit preserving the *Tmr3 (type I)* RM direction.

The oldest group, *Tmr<sub>siw</sub>*, consists of four distinct cooling units which record the same geomagnetic field direction. The deposition of this package of pyroclastic flow deposits, which varies in outcrop appearance from 1-2 meters thick and densely welded to 160 meters thick and partially to unwelded, must have occurred relatively quickly in order to preserve the same field direction. The complete lack of evidence for weathering at the cooling breaks also suggests a short time interval.

#### B. Group means relative to geomagnetic north

There are variations between the combined group declinations and geomagnetic north, and between the combined group inclinations and the expected value of  $\text{Inc} = 50^\circ$  at the study latitude ( $\lambda = 30^\circ 30'$ ) given the relationship  $\text{Tan}(\text{Inc}) = 2 \text{Tan}(\lambda)$  (e.g., Tarling, 1983). This raises the possibility that post-depositional rotation and/or translation of the entire area may be documented. If the position of the geomagnetic pole was independently known at the time of deposition of the sampled volcanic deposits, for example via paleomagnetic

records from continuous sedimentary sections spanning the Miocene, then it could be assessed whether or not the values recorded by these volcanic units agree with the direction of the geomagnetic pole at the time of deposition. Unfortunately, continuous records of secular variation do not extend back in time as far as the Miocene so it is necessary to rely on statistical studies of paleosecular variation (PSV).

Quidelleur and Courtillot (1996) calculate and discuss various models of PSV based upon the large database of paleomagnetic data from volcanic sequences from the last 5 Ma. By using either their preferred model (Model C1) or considering only data from their database,  $\alpha_{95}$  confidence limits around the Miocene geomagnetic pole can be calculated given the latitude of the study site and assuming a due north declination direction. The assumption of a due north declination direction is supported by the absence of a significant non-zonal component in the time-averaged field for the last 5 Ma (Quidelleur and Courtillot, 1996). Using this assumption here will test whether or not tectonic rotation of the entire Santa Isabel Wash region relative to due north has occurred. The confidence limits are calculated via:

$$\alpha_{95} \text{ (of DEC)} = (2\sigma D) (\cos (\text{Inc})) \quad (5.7)$$

$$\alpha_{95} \text{ (of INC)} = (2\sigma I) \quad (5.8)$$

where  $\sigma D$  and  $\sigma I$  are taken from Quidelleur and Courtillot (1996) and  $(\text{Inc}) = 50^\circ$ . Values of  $(\sigma D, \sigma I)$  are  $(12.5^\circ, 13^\circ)$  based on Model C1 and  $(15^\circ, 12.5^\circ)$  based upon the database for latitudes between  $30^\circ$  and  $40^\circ\text{N}$ . The  $\alpha_{95}$  confidence limits for both cases are shown in Figure 5.14 centered on  $D = 0^\circ$  and  $I = 50^\circ$ . These confidence ellipses for the geomagnetic pole are shown superimposed upon the combined RM directions of the six groups in Figure 5.15. With one exception (*Tmr3 (type I)*), the entire  $\alpha_{95}$  confidence cone of each of the six groups falls completely within one or both of the ellipses for the geomagnetic pole; the  $\alpha_{95}$  confidence cone of group *Tmr3 (type I)* only partially overlaps with the ellipses. The RM

directions of the six groups thus fall within reasonable secular variations around a geomagnetic pole of  $D = 0^\circ$  and  $I = 50^\circ$ . Of the 38 individual sampling site means, 34 also overlap with the secular variation ellipses (inset in Figure 5.15). Not surprisingly, two sites which do not overlap are from group *Tmr3 (type I)*, and the other two are from *Tmr<sub>siw</sub>*. A hypothesis of rotation of the entire region is thus not strongly supported by the data, and it is concluded that no rotations relative to geomagnetic north can be unambiguously discerned for these samples.

### 5.5 Comparison of results to Sierra San Fermín and Sierra San Felipe regions

The paleomagnetic analysis performed by Lewis (1994; see also Lewis and Stock, in review in *J. Geophys. Res.*, 1997) presented evidence for  $31^\circ \pm 15^\circ$  vertical-axis CW rotations of the Sierra San Fermín relative to the Sierra San Felipe (see Figure 1.6 in Chapter I). This amount of relative (not absolute) rotation is an average value found within ~6 Ma pyroclastic flow deposits in that study. At least one, but perhaps two, of the pyroclastic flow deposits sampled in the Sierra San Fermín and the Sierra San Felipe is correlative with tuffs sampled in Santa Isabel Wash. Comparisons of the preserved RM directions between the two regions are presented here following a discussion of lithologic correlations. Chapter II gives more detailed lithologic descriptions of the units in Santa Isabel Wash. Units *Tmr<sub>ao</sub>* and *Tmr<sub>3-4</sub>* from Santa Isabel Wash are not included in the following discussion, as correlatives either do not exist or were not sampled in the Sierra San Fermín.

#### A. Lithologic correlations

Volcanic stratigraphy defined in the southern Valle Chico and southern Sierra San Felipe (Stock, 1989; 1993) includes a package of ~ 6 Ma pyroclastic flow deposits which have been correlated to deposits in the Sierra San Fermín (Lewis, 1996; Lewis and Stock, in



review in J. Geophys. Res., 1997) and Santa Isabel Wash (this study). These various localities are shown in Figure 1.6 (Chapter I). The sampling location in the Sierra San Felipe is known as Mesa Cuadrada, and will be referred to as such for the remainder of this discussion. In the initial study, the ~ 6 Ma units were defined (youngest to oldest) as Tmr4 (Miocene Rhyolite #4), Tmr3 (Miocene Rhyolite #3), and Tmmt (Miocene Tuffs of Matomí; Stock, 1989; 1993). Isotopic ages determined in that study on anorthoclase ( $Ab_{65}An_3Or_{32}$ ) from Tmr3 are  $6.07 \pm 0.20$  Ma and  $6.14 \pm 0.16$  Ma (see Chapter III for full discussion of geochronologic results from southern Valle Chico). Tmr4 and Tmmt are also interpreted by Stock (1989) to be ~ 6 Ma based on the lack of erosional surfaces between them and Tmr3. Lewis (1996), who found Tmr4 and Tmr3 in the Sierra San Fermín, further divides Tmr3 into an upper cooling unit (Tmr3b) and lower cooling unit (Tmr3a), and correlates Tmr3a with the upper portion of Stock's Tmmt. Isotopic ages for Tmr3b anorthoclase ( $Ab_{65}An_2Or_{33}$ ) from two different locations in the Sierra San Fermín are  $6.5 \pm 0.2$  Ma and  $6.7 \pm 0.2$  Ma (Lewis, 1996).

#### Tmr4

In Santa Isabel Wash one ash flow tuff fits the description of crystal-poor Tmr4 described in both of the earlier studies. This unit is referred to as *Tmr4* in this study. In Santa Isabel Wash *Tmr4* is up to 70 m thick (but more commonly < 5 m thick) and is a distinct orange to purple porcelainous tuff with a characteristic brown glassy base containing 3-5% small (< 1 cm) orange pumice fragments. *Tmr4* contains < 1% phenocrysts of feldspar and clinopyroxene. In the southern Valle Chico Tmr4 is at least 8-10 m thick and contains < 3% phenocrysts (potassium feldspar, biotite, and clinopyroxene) (Stock, 1989), and in the Sierra San Fermín it is up to 50 m thick and has < 3% phenocrysts (plagioclase, clinopyroxene, opaques, and biotite; Lewis, 1994). The principal petrographic difference between these studies is that biotite phenocrysts were not identified in samples from Santa Isabel Wash.

*Tmr3*

The underlying unit called *Tmr3* in this study, which includes four cooling units commonly totaling > 100 m thick, also fits descriptions of *Tmr3* in the southern Valle Chico (up to 80 m thick; Stock, 1989) and *Tmr3b* in the Sierra San Fermín (up to 120 m thick; Lewis, 1996).  $^{40}\text{Ar}/^{39}\text{Ar}$  ages determined in this study on anorthoclase ( $\text{Ab}_{63-66}\text{An}_{1-2}\text{Or}_{32-35}$ ) are  $6.5 \pm 0.1$  Ma and  $6.2 \pm 0.1$  Ma for *Tmr3* (*type II*). Both of these  $^{40}\text{Ar}/^{39}\text{Ar}$  ages are in agreement (within  $2\sigma$  uncertainty) with values obtained for *Tmr3b* in the Sierra San Fermín (Lewis, 1996). The  $6.2 \pm 0.1$  Ma age from this study is also consistent with two dates determined via K/Ar measurements in the southern Valle Chico (Stock, 1989) and with Stock's unpublished  $^{40}\text{Ar}/^{39}\text{Ar}$  date ( $6.40 \pm 0.19$  Ma; see Chapter III for details). The chemical compositions of the anorthoclase phenocrysts are also very similar in all three studies. Phenocryst assemblages vary from 10% (anorthoclase >> augite > quartz > opaques > biotite) in the southern Valle Chico (Stock, 1989) to 10-15% (anorthoclase and plagioclase >> augite > quartz > opaques and trace basaltic hornblende, biotite, hypersthene, muscovite, and zircon) in the Sierra San Fermín (Lewis, 1994; 1996) to 5-15% (anorthoclase >> quartz > trace orthopyroxene and Fe oxides  $\pm$  trace olivine  $\pm$  trace hornblende) in Santa Isabel Wash. Slight differences thus include the absence of biotite, plagioclase, and augite phenocrysts in deposits from Santa Isabel Wash.

Unfortunately, since the two types of paleomagnetic RM directions preserved in *Tmr3* in Santa Isabel Wash imply two distinct times of deposition of tuffs with identical mineralogy and field appearance, it is not clear which ones are correlative to the units in the southern Valle Chico or the Sierra San Fermín. Recall that four cooling units were defined in this study for Santa Isabel Wash. On the basis of field appearance, the lower 1 to 3 cooling units which comprise *Tmr3* in Santa Isabel Wash could even be correlative to the uppermost Tuffs of Matomí (*Tmmt*) defined in the southern Valle Chico (J. Stock, pers. comm., 1996). Between 1 and 3 of the uppermost cooling units of *Tmr3* from Santa Isabel Wash (preserving *Tmr3* (*type*

II) RM directions) are probably correlative to Tmr3 as defined in the southern Valle Chico (Stock, 1989) and Tmr3b in the Sierra San Fermín and Mesa Cuadrada (Lewis, 1996; Lewis and Stock, 1996). The apparent spatial restriction of *Tmr3 (type I)* in the NW region of Santa Isabel Wash suggests that this cooling unit might extend to the southern Valle Chico and/or the southern Sierra San Felipe (Mesa Cuadrada) areas (10-20 km to the NW) but probably not as far as the Sierra San Fermín (30 km to the NE).

### *Tmr<sub>siw</sub>*

*Tmr<sub>siw</sub>* varies between 1 and 160 meters in thickness and generally consists of a basal, white, pumice-flow deposit, including surge deposits which may or may not be present (cooling unit *t1*), overlain by a yellow-to-orange unwelded to densely welded pumiceous lithic lapilli tuff (*t2*), a pink to pale orange, unwelded pumiceous lithic lapilli tuff commonly with vertical gas-escape structures (*t3*), a grey (brick-red-weathering), densely welded, lithic-rich (commonly 10-15% but up to 30-40%) devitrified zone (*t4*), and a purple to pink unwelded to densely welded lithic lapilli tuff which in places has a densely welded, spherulitic, red and black zone with well-developed eutaxitic foliation (*t5*). The unit is usually capped by up to 1 meter of orange, bedded tephra.

It is not entirely clear if the cooling units which comprise *Tmr<sub>siw</sub>* are correlative with any units from the localities to the north; they may be unique to the Santa Isabel Wash region. They are in the same stratigraphic position as Tmmt of southern Valle Chico and Mesa Cuadrada (Stock, 1989) and Tmr3a of the Sierra San Fermín (Lewis, 1994; 1996). Unit Tmmt on Mesa Cuadrada is described by Stock (1989) as a 20-60 meter thick, variable package of unwelded, predominantly white, (but also light brown to orange), pumice lapilli tuffs of pyroclastic flow origin. In the paleomagnetic study of Lewis (1994; see also Lewis and Stock, in review in J. Geophys. Res., 1997) the uppermost major tuff of Tmmt on Mesa Cuadrada is referred to as Tmr3a. Lewis (1996) describes Tmr3a in the Sierra San Fermín as a

poorly to moderately welded, yellow-to-orange-brown weathering, lithic tuff which is < 25 meters thick. Within Tmr3a as described in the El Coloradito section in that study (Appendix C of Lewis (1996)) there is a densely welded, red to brown, crystal-rich, devitrified zone with 10% lithics. The unit is overlain by up to 2 meters of brown-, yellow-, or pink-weathering bedded tephra. These lithologic characteristics of Tmr3a are more similar to the variations observed in the cooling units of *Tmr<sub>siw</sub>* in Santa Isabel Wash than the characteristics of Tmmt described at Mesa Cuadrada, although Tmr3a consists of only one cooling unit.

Phenocryst assemblages in *Tmr<sub>siw</sub>* vary but in general consist of 10-20% phenocrysts of feldspar (andesine, oligoclase, and anorthoclase) >> olivine ≈ clinopyroxene (ferroaugite and pigeonite) ≈ Fe oxides (hematite) ± trace biotite. Thin section descriptions in Chapter II give additional detail. Lewis (1994) describes the phenocryst assemblage of Tmr3a to include 5-11% feldspar (plagioclase and anorthoclase), ≤ 3% iron oxides, < 1% each of quartz, clinopyroxene, and magnetite, and trace amounts of hornblende, biotite, epidote, and zircon. Tmmt from Southern Valle Chico is generally described as biotite-rich, and in some places contains biotite, sanidine, and no quartz (Stock, 1989). The absence of epidote, hornblende, and quartz, the relatively minor amount of biotite, and the presence of olivine, make the phenocryst assemblage for *Tmr<sub>siw</sub>* significantly different from those of Tmr3a and Tmmt.

#### Preferred lithologic correlations

Lithologic units sampled for paleomagnetic analysis from Santa Isabel Wash, the Sierra San Fermín, and Mesa Cuadrada are listed in the first column of Table 5.5. On the basis of significantly different phenocryst contents and differences in outcrop appearances, *Tmr<sub>siw</sub>* is interpreted here to be unique to Santa Isabel Wash and not correlative to any units preserved in the north. Tmr3a in the Sierra San Fermín, which has been correlated to upper Tmmt on Mesa Cuadrada, is in the same stratigraphic position as *Tmr<sub>siw</sub>* of Santa Isabel Wash.

Tmr3b of the Sierra San Fermín and Mesa Cuadrada is lithologically similar to both *Tmr3* (*type I*) and (*type II*) of Santa Isabel Wash. *Tmr4* in all areas is the same ash flow tuff.

### B. *Relative rotations*

Paleomagnetic results from this study and that of Lewis (1994; see also Lewis and Stock, in review in *J. Geophys. Res.*, 1997) are summarized in Table 5.5. Declination and inclination values from individual sites in the Sierra San Fermín (instead of the site averages calculated in that study) are given for units Tmr4 and Tmr3a because the sites from each unit fail the statistical test for a common mean direction described above, and thus should probably not be combined to derive a mean direction. The 5 sites from Tmr3b in the Sierra San Fermín do pass the test and thus the average is retained in Table 5.5. In addition to the data discussed here, Lewis (1994; see also Lewis and Stock, in review in *J. Geophys. Res.*, 1997) also recorded  $\sim 40^\circ$  CW rotation of the Sierra San Fermín relative to Mesa Cuadrada in an underlying,  $\sim 12$  Ma pyroclastic flow deposit. All rotations are interpreted to be at least post-6 Ma, and perhaps post-3 Ma, (Lewis and Stock, in review in *J. Geophys. Res.*, 1997). Comparisons between the new results from Santa Isabel Wash and those from the previous study are discussed below for the various lithologic units in this study.

#### *Tmr4*

Inclination values within *Tmr4* from Santa Isabel Wash and all three sites in the Sierra San Fermín agree with each other within 95% confidence limits. In contrast, two of the three sites in the Sierra San Fermín record declination directions which are  $\sim 34^\circ$  CW of the value recorded in Santa Isabel Wash. These two sites are thus interpreted to be rotated  $\sim 34^\circ$  CW relative to Santa Isabel Wash. The third declination value, from samples collected at a location about 10 km north of the other two sites in the northernmost Sierra San Fermín (site sfb of

Lewis, 1994; see also Lewis and Stock, in review in *J. Geophys. Res.*, 1997), records the same direction as recorded in Santa Isabel Wash within the 95% confidence limits, and it thus appears not to be significantly rotated relative to Santa Isabel Wash.

### *Tmr3 (type II)*

The unit stratigraphically below *Tmr4* in Santa Isabel Wash, *Tmr3 (type II)*, could be correlative with *Tmr3b* in the Sierra San Fermín and Mesa Cuadrada. If this were the case, there would be good agreement between the inclination values from all three localities. The recorded declinations would suggest that both Santa Isabel Wash and the Sierra San Fermín have rotated CW ( $\sim 19^\circ$  and  $\sim 31^\circ$ , respectively) relative to Mesa Cuadrada. However, this would also imply that the Sierra San Fermín has rotated  $\sim 12^\circ$  CW relative to Santa Isabel Wash, which is significantly less than the  $\sim 34^\circ$  CW rotation recorded in the overlying (*Tmr4*) unit. The CW rotation of Santa Isabel Wash relative to Mesa Cuadrada would also be more difficult to understand given the regional interpretation of deformation (see Chapter VI; also Lewis and Stock, in review in *J. Geophys. Res.*, 1997). The declination of one of the *Tmr3b* sites in the Sierra San Fermín (site sfb) is  $28.3^\circ$  (not listed in Table 5.5 since 5 sites are averaged together), virtually identical to that found in the Santa Isabel Wash for *Tmr3 (type II)*. Interestingly, results discussed above for *Tmr4* and this same sampling site in the Sierra San Fermín (sfb) also suggested minor or no rotation between this sampling site and Santa Isabel Wash. Thus if *Tmr3 (type II)* is the same pyroclastic flow deposit as *Tmr3b*, site sfb in the Sierra San Fermín appears to be unrotated relative to Santa Isabel Wash.

### *Tmr3 (type I)*

Instead of the above scenario, it is possible that *Tmr3b* from Mesa Cuadrada and Sierra San Fermín is correlative with *Tmr3 (type I)* from Santa Isabel Wash. Inclination values

agree within 95% confidence for all three of these areas. Recall that *Tmr3 (type I)* appears to be spatially restricted to the northwestern portion of Santa Isabel Wash. Consequently this proposed lithologic correlation with Mesa Cuadrada, which is situated to the northwest of Santa Isabel Wash, appears to be quite plausible, and would imply that Mesa Cuadrada has rotated  $\sim 45^\circ$  CW relative to Santa Isabel Wash. However, it seems less likely that *Tmr3 (type I)*, which is not preserved in the north central part of Santa Isabel Wash, was deposited in the Sierra San Fermín, although the possibility cannot be ruled out. If Tmr3b in the Sierra San Fermín is correlative with *Tmr3 (type I)*, this implies about  $80^\circ$  CW rotation between Santa Isabel Wash and the Sierra San Fermín, which is significantly greater than the amount recorded in the units discussed above.

It is also possible that *Tmr3 (type I)* of Santa Isabel Wash is correlative to Tmr3a in the study to the north. If this were the case, both the Sierra San Fermín and Mesa Cuadrada show evidence of large amounts of CW rotation ( $90^\circ$ - $140^\circ$ ) relative to Santa Isabel Wash. This amount is significantly larger than described above for overlying tuffs. Additionally, there is less consistency of inclination values between *Tmr3 (type I)* and Tmr3a than there is between inclination values of *Tmr3 (type I)* and Tmr3b.

### *Tmr<sub>siw</sub>*

The preferred interpretation for the lowest stratigraphic pyroclastic flow deposits sampled in this study, *Tmr<sub>siw</sub>*, is that they are unique to Santa Isabel Wash and do not correlate with Tmr3a in the Sierra San Fermín or Mesa Cuadrada. If these units were correlative, the recorded declinations in the Sierra San Fermín would be  $30^\circ$ - $80^\circ$  CW of Santa Isabel Wash, and those of Mesa Cuadrada would be about  $30^\circ$  CW of Santa Isabel Wash. Inclination values would agree within 95% confidence limits between Santa Isabel Wash and the other sites except for site sfb (Table 5.5) in the Sierra San Fermín.

Preferred interpretation

The most robust lithologic correlation is that of unit *Tmr4* in both studies. Based upon results from this unit, it appears that the Sierra San Fermín has rotated CW ( $\sim 30^\circ$ ) relative to Santa Isabel Wash since the deposition of this 6 Ma pyroclastic flow deposit. Given the similar appearance of the various *Tmr3* cooling units examined in this study, it is possible that Tmr3b from Mesa Cuadrada is not the same cooling unit as the one in the Sierra San Fermín as interpreted by Lewis (1994; see also Lewis and Stock, in review in *J. Geophys. Res.*, 1997). If this were the case, the interpretation favored here would be to correlate the stratigraphically lower *Tmr3 (type I)* from Santa Isabel Wash with Tmr3b on Mesa Cuadrada, and the stratigraphically higher *Tmr3 (type II)* of Santa Isabel Wash with Tmr3b in the Sierra San Fermín on the basis of the spatial distribution of the various *Tmr3* cooling units in Santa Isabel Wash. In this scenario, the Sierra San Fermín and Mesa Cuadrada record declination directions  $\sim 13^\circ$  CW and  $\sim 48^\circ$  CW, respectively, of those in Santa Isabel Wash. It would be preferable, however, if definitive lithologic correlations could be resolved in some manner independent of the paleomagnetic data. It is certainly possible that none of the cooling units referred to as *Tmr3* in Santa Isabel Wash are correlative to those in the Sierra San Fermín or Mesa Cuadrada. *Tmr<sub>siw</sub>* of Santa Isabel Wash is interpreted to be unique to this study locality and is not correlated to the pyroclastic flow deposit (Tmr3a) in the same stratigraphic position in the other localities.

### 5.6 Conclusions

Paleomagnetic analysis of 218 cores drilled from a stratigraphic succession of 11 volcanic cooling units at 15 locations in Santa Isabel Wash of the northern Sierra Santa Isabel in Baja California has resulted in the identification of six distinct lithologic groups which



record unique RM directions. Eutaxitic, or flattening, foliation within these pyroclastic flow deposits most likely developed at temperatures above the Curie temperature and does not represent paleohorizontal. Normal polarity magnetization and  $^{40}\text{Ar}/^{39}\text{Ar}$  geochronology suggest that deposition of these tuffs occurred during Subchron C3An.2n (6.269-6.567 Ma; Cande and Kent, 1995). A bootstrap method to statistically test for common mean directions between various sites in each group was developed and used 1) to conclude that no relative rotations exist between the various sampling sites for any of the six groups, and 2) to justify grouping some of the cooling units together.

Comparison of the combined group RM directions, calculated by using individual samples from all sites as opposed to site means, to models of PSV (Figure 5.15) shows that each of the six groups falls within permissible bounds (95% confidence) of secular variation of the geomagnetic pole around a declination of present-day north and an inclination of  $50^\circ$  (determined from study latitude). Consequently there is no evidence for wholesale rotation or translation of the units sampled since the time of deposition ( $\sim 6$  Ma).

Lithologic correlations between Santa Isabel Wash, the Sierra San Fermín ( $\sim 30$  km to the NE), and Mesa Cuadrada in the Sierra San Felipe ( $\sim 20$  km to the NNW) suggest that at least one of the cooling units sampled in this study (*Tmr4*) correlates to a deposit sampled for paleomagnetic analysis in the Sierra San Fermín (*Tmr4* of Lewis and Stock, in review in J. Geophys. Res., 1997). This correlation is primarily based upon petrographic descriptions and field appearance. The declination values recorded in this unit in the Sierra San Fermín are  $\sim 30^\circ$  CW of those sampled in Santa Isabel Wash. Lithologic correlations between Mesa Cuadrada and Santa Isabel Wash are ambiguous at this time; however, if the Sierra San Fermín is also rotated  $\sim 30^\circ$  CW relative to Mesa Cuadrada as determined by Lewis and Stock (in review in J. Geophys. Res., 1997), then Santa Isabel Wash and Mesa Cuadrada should record similar RM directions.

Paleomagnetic analysis of a  $\sim 12.5$  Ma ash flow tuff (*Tmr<sub>sf</sub>*) (Stock et al., 1996b; 1997) in the study by Lewis and Stock (in review in J. Geophys. Res., 1997) recorded  $\sim 35^\circ$

CW rotation of the Sierra San Fermín relative to Mesa Cuadrada. Samples have been collected from the same tuff in Santa Isabel Wash and should help resolve some of the ambiguity surrounding the 6 Ma tuffs.

Table 5.1. Number of rock cores drilled at each sampling site in Santa Isabel Wash. Sites are designated A-P and correspond to localities shown in Figure 5.2. Cooling units are listed in stratigraphic order with the youngest unit at the top of the list. Three cooling units (l-lower, m-middle, u-upper) make up unit *Tmr3(II)*. The 11 samples collected within unit *Tmr3(I)* at site D were taken from outcrops separated stratigraphically by about 60 meters (six samples collected from lower outcrop and five samples collected from higher one).

Unit	A	B	C	D	E	F	G	H	I	K	L	M	N	O	P
$Tmr_{ao}$		5	5	5					6						
$Tmr_4$		5		5											
$Tmr_{3-4}$		5	6									7			
$Tmr_3(II) u$											8				
$Tmr_3(II) m$											7		7		
$Tmr_3(II) l$					5				6		7	7	7	4	
$Tmr_3(I)$	5			11						6					
$Tmr_{siw}(t_5)$	5				5	6	6	5	6	6		7	8		
$Tmr_{siw}(t_4)$				5											
$Tmr_{siw}(t_3)$				5											6
$Tmr_{siw}(t_2)$				5			5						7	7	

Table 5.2. (next 3 pages) Summary of demagnetization results grouped by lithology. The stratigraphically highest tuff is listed first. Sampling location, bedding strike and dip, number of samples collected (Nc) and used (N) in the analysis, and primary RM directions in geographic and stratigraphic (tilt-corrected) coordinates are given for each sampling site. Uncertainties for each site mean are calculated using both Fisher and Bingham distribution functions. The 11 cooling units are combined into six distinct groups, and combined RM directions were calculated using all samples from a given unit (as opposed to averaging site means). Each row containing a site mean corresponds to an equal area plot in Figure 5.12 (a-f), and each row listing a combined group value corresponds to an equal area plot in Figure 5.13.

Bedding			Geographic			Stratigraphic			Bingham Stats.			Fisher Stats.	
Location	Strike	Dip	N/N <sub>c</sub>	Dec	Inc	Dec	Inc	$\kappa_1$	$\alpha_{95}$	$\kappa_2$	$\alpha_{95}$	$\kappa$	$\alpha_{95}$
<i>Tmr<sub>40</sub></i> - 1 cooling unit													
Site B <sup>P</sup>	0	0.0	5/5	12.2	51.8	12.2	51.8	-1.4E2	3.8	-0.5E0	4.3	213	5.4
Site C	0	0.0	5/5	4.9	42.7	4.9	42.7	-1.2E3	1.3	-6.4E1	5.6	154	5.5
Site D	187	5.5	5/5	10.8	45.2	5.2	45.6	-1.4E1	12.8	-0.2E0	339.4	12	20.8
Site P	0	0.0	6/6	2.0	42.4	2.0	42.4	-7.7E0	21.0	-0.7E0	27.2	86	7.8
combined:			21/21	7.2	45.6	5.9	45.7	-2.5E1	4.5	-0.4E0	5.0	44	4.9
<i>Tmr<sub>4</sub></i> - 1 cooling unit													
Site B <sup>P</sup>	0	0.0	5/5	6.5	42.4	6.5	42.4	-1.6E2	3.6	-1.0E0	4.6	236	5.4
Site D	187	5.5	5/5	13.9	41.5	9.0	42.0	-6.3E1	5.7	-1.2E1	13.4	24	14.2
combined:			10/10	10.7	41.6	7.8	42.1	-3.1E1	5.8	-0.5E0	6.5	54	6.7
<i>Tmr<sub>3-4</sub></i> - 1 cooling unit													
Site B	0	0.0	5/5	0.8	42.2	0.8	42.2	-2.7E2	2.7	-6.9E1	5.4	140	5.8
Site C <sup>P</sup>	0	0.0	6/6	355.0	30.0	355.0	30.0	-1.3E1	11.7	-0.5E0	13.7	20	15.5
Site M	0	0.0	7/7	352.7	40.0	352.7	40.0	-8.7E2	1.3	-2.5E2	2.4	571	2.3
combined:			18/18	355.9	37.5	355.9	37.5	-2.7E1	4.6	-0.2E0	4.8	48	5.0
<i>Tmr<sub>3</sub></i> (type II) - 3 cooling units													
Site E	250	8.0	5/5	31.2	61.8	21.6	56.3	-2.7E3	0.9	-3.9E2	2.2	872	2.3
Site I	0	0.0	6/6	30.8	66.3	30.8	66.3	-4.0E2	2.0	-2.8E2	2.4	453	2.9
Site L(u)	0	0.0	8/8	29.3	52.1	29.3	52.1	-2.7E2	2.2	-4.6E1	5.3	119	4.8

Site L(m)	0	0.0	7/7	31.6	58.2	31.6	58.2	31.6	58.2	-3.1E2	2.2	-2.0E2	2.7	352	3.0
Site L(l)	0	0.0	7/7	28.2	58.5	28.2	58.5	28.2	58.5	-3.5E2	2.0	-7.3E1	4.4	176	4.2
Site M <sup>p</sup>	0	0.0	7/7	31.1	34.9	31.1	34.9	31.1	34.9	-2.4E1	7.8	-0.3E0	8.6	39	9.9
Site N(u)	0	0.0	7/7	21.3	53.5	21.3	53.5	21.3	53.5	-4.4E2	1.8	-1.8E2	2.8	373	2.9
Site N(l)	0	0.0	7/7	28.5	47.2	28.5	47.2	28.5	47.2	-1.7E3	0.9	-1.0E2	3.7	284	3.3
Site O	0	0.0	4/4	36.2	64.8	36.2	64.8	36.2	64.8	-3.8E2	2.6	-9.6E1	5.1	172	6.1
combined:			58/58	29.4	54.5	28.5	54.2	28.5	54.2	-2.9E1	2.5	-0.3E-1	2.5	55	2.5
<i>Tmr3 (type I) - 1 cooling unit</i>															
Site A <sup>p</sup>	182	6.5	5/5	354.5	67.5	339.6	65.9	339.6	65.9	-6.1E2	2.3	-0.9E0	2.9	219	5.6
Site D(u)	187	5.5	4/5	354.0	66.7	342.4	64.9	342.4	64.9	-1.7E2	3.8	-5.0E1	7.1	87	8.6
Site D(l)	187	5.5	5/6	324.3	72.7	313.8	68.6	313.8	68.6	-3.1E2	2.5	-8.1E1	5.0	164	5.4
Site K	0	0.0	6/6	312.0	43.4	312.0	43.4	312.0	43.4	-2.4E2	2.7	-7.4E0	16.1	18	14.8
combined:			20/22	328.8	61.9	322.7	59.6	322.7	59.6	-1.3E1	6.4	-0.3E0	7.0	24	6.9
<i>Tmr<sub>stiv</sub> - 4 cooling units</i>															
(t5)															
Site A	182	6.5	5/5	18.0	40.7	12.2	42.0	12.2	42.0	-3.5E3	0.8	-3.8E1	7.3	95	7.1
Site E	250	8.0	5/5	20.0	46.4	15.4	40.1	15.4	40.1	-2.7E4	0.3	1.3E3	1.3	3080	1.2
Site F	0	0.0	6/6	28.1	47.2	28.1	47.2	28.1	47.2	-5.1E2	1.8	-2.4E2	2.6	455	2.9
Site G	0	0.0	4/6	20.4	36.1	20.4	36.1	20.4	36.1	-4.2E3	2.4	-5.8E1	6.6	114	7.5
Site H	312	17.0	5/5	13.2	49.2	19.7	33.8	19.7	33.8	-1.5E3	1.1	-1.1E2	4.2	267	4.2
Site I	0	0.0	6/6	31.3	42.7	31.3	42.7	31.3	42.7	-3.4E2	2.2	-6.6E1	5.0	184	5.0
Site K	0	0.0	6/6	9.0	42.3	9.0	42.3	9.0	42.3	-2.3E2	2.7	-5.6E1	5.5	125	5.5
Site M	0	0.0	7/7	7.0	42.0	7.0	42.0	7.0	42.0	-2.2E2	2.5	-4.4E1	5.7	108	5.4
Site N	0	0.0	8/8	25.7	38.9	25.7	38.9	25.7	38.9	-1.3E3	1.0	-1.3E2	3.1	365	2.7
(t4)															
Site D	187	5.5	5/5	26.9	24.8	24.4	26.6	24.4	26.6	-8.4E2	1.5	-1.7E2	3.4	369	3.6





Table 5.3. Three extreme examples of the variations in eutaxitic foliation measured at a given sample locality for a given lithologic unit. Each eutaxitic foliation value corresponds to one drilled core. The Fisher concentration parameters illustrate how tilt-correcting these samples based upon the eutaxitic foliation planes greatly increases the dispersion of the site means. This implies that the eutaxitic, or flattening, foliation developed when these deposits were still above the Curie temperature and does not represent paleohorizontal.

Sampling site	Eutaxitic foliation	Fisher $\kappa$ ("tilt-corrected")	Fisher $\alpha_{95}$ ("tilt-corrected")	Fisher $\kappa$ (from Table 5.2)	Fisher $\alpha_{95}$ (from Table 5.2)
<i>Tmr<sub>ao</sub></i> - Site B	N32°E, 78°NW	2	57.7	213	5.4
	N32°E, 78°NW				
	N43°E, 88.5°SE				
	N34°E, 73.5°NW				
	N43°E, 60°NW				
<i>Tmr<sub>ao</sub></i> - Site C	N2°E, 11°SE	11	21.5	154	5.5
	N82°E, 21°SE				
	N20°W, 4.5°NE				
	N54°W, 27°NE				
	N54°W, 27°NE				
<i>Tmr<sub>3-4</sub></i> - Site M	N82°E, 9°NW	83	6.7	571	2.3
	N82°E, 9°NW				
	N57°W, 36°NE				
	N57°W, 36°NE				
	N57°W, 36°NE				

Table 5.4. Results of a statistical test for common mean direction to justify grouping samples together from different sampling sites for the six groups recording unique RM directions. If the test statistic ( $g_r$ ) is less than the 5% limit (determined from a bootstrap technique modified after the reversal test program of McFadden and McElhinny (1990) and described in text), then the hypothesis that the site distributions have a common mean cannot be rejected. All six groups pass this test, and thus combined values given in Table 5.2 (and illustrated in Figure 5.13) are taken to be the final result for each group.

Lithologic unit	Number of sites	$g_r$	5% limit	Result
<i>Tmr<sub>ao</sub></i>	4	21.225	51.582	cannot reject
<i>Tmr<sub>4</sub></i>	2	0.115	2.058	cannot reject
<i>Tmr<sub>3-4</sub></i>	3	11.276	22.774	cannot reject
<i>Tmr<sub>3</sub> - type II</i>	9	232.559	865.508	cannot reject
<i>Tmr<sub>3</sub> - type I</i>	4	38.008	52.388	cannot reject
<i>Tmr<sub>siw</sub></i>	16	641.766	2154.969	cannot reject

Table 5.5. Summary of paleomagnetic RM directions recorded in pyroclastic flow deposits in Santa Isabel Wash, the Sierra San Fermín, and Mesa Cuadrada of the southern Sierra San Felipe. Locations are shown in Figure 1.6 in Chapter I. Italicized lithologic names in the first column are from Santa Isabel Wash, and names listed in regular type are from the study by Lewis (1994; see also Lewis and Stock, in review in *J. Geophys. Res.*, 1997). Unit *Tmr4* is interpreted to be the same pyroclastic flow deposit in both studies. It is not unambiguously clear whether unit Tmr3b in the Sierra San Fermín and Mesa Cuadrada correlates with *Tmr3 (type I)* or *Tmr3 (type II)* in Santa Isabel Wash. It is possible that none of the cooling units referred to as *Tmr3* in Santa Isabel Wash are correlative to those in the Sierra San Fermín or Mesa Cuadrada. The preferred correlation in this study is between Tmr3b of the Sierra San Fermín with *Tmr3 (type II)* of Santa Isabel Wash, and Tmr3b of Mesa Cuadrada with *Tmr3 (type I)* of Santa Isabel Wash on the basis of the spatial distribution of the various *Tmr3* cooling units in Santa Isabel Wash. Outcrop descriptions and phenocryst content of Tmr3a in the Sierra San Fermín is different to that of *Tmr<sub>siw</sub>*, and thus these stratigraphically lowest units are not correlated. See text for further discussion.

$\S$ Lithologic unit	<i>Santa Isabel Wash</i>	Sierra San Fermín	Mesa Cuadrada
<i>Tmr4</i> , <i>Tmr4</i> (both locations)	D = 7.8°, I = 42.1°, $\alpha_{95}$ = 6.7°, n = 10	D <sup>b</sup> = 15.0°, I = 42.8°, $\alpha_{95}$ = 5.8°, n = 3 D = 42.1°, I = 52.7°, $\alpha_{95}$ = 6.1°, n = 6 D = 42.4°, I = 42.0°, $\alpha_{95}$ = 3.4°, n = 11	
<i>Tmr3</i> (type II)	D = 28.5°, I = 54.2°, $\alpha_{95}$ = 2.5°, n = 58		
<i>Tmr3b</i>		D = 40.1°, I = 54.0°, $\alpha_{95}$ = 7.7°, s = 5*	D = 9.5°, I = 53.9°, $\alpha_{95}$ = 8.9°, n = 3
<i>Tmr3</i> (type I)	D = 322.7°, I = 59.6°, $\alpha_{95}$ = 6.9°, n = 20		
<i>Tmr3a</i>		D <sup>b</sup> = 59.9°, I = 53.6°, $\alpha_{95}$ = 2.1°, n = 3 D = 73.7°, I = 35.6°, $\alpha_{95}$ = 4.9°, n = 7 D = 98.5°, I = 43.6°, $\alpha_{95}$ = 7.5°, n = 3	D = 52.4°, I = 52.2°, $\alpha_{95}$ = 12.9°, n = 3
<i>Tmr<sub>Siw</sub></i>	D = 20.6°, I = 40.0°, $\alpha_{95}$ = 2.1°, n = 91		

$\S$  Lithologic unit names from this study (Santa Isabel Wash) given in italics; names in regular type from Lewis (1994) and Lewis and Stock (in review in J. Geophys. Res., 1997).

\* Mean direction calculated from five site (s) averages (containing 33 samples). All other values listed for the Sierra San Fermín and Mesa Cuadrada represent one sampling site each with (n) samples. Means calculated for Santa Isabel Wash data combine individual samples from a number of sites instead of using average site means. See text for details.

D<sup>b</sup> indicates site sfb in the Sierra San Fermín.

Figure 5.1. Simplified geologic map of Santa Isabel Wash.

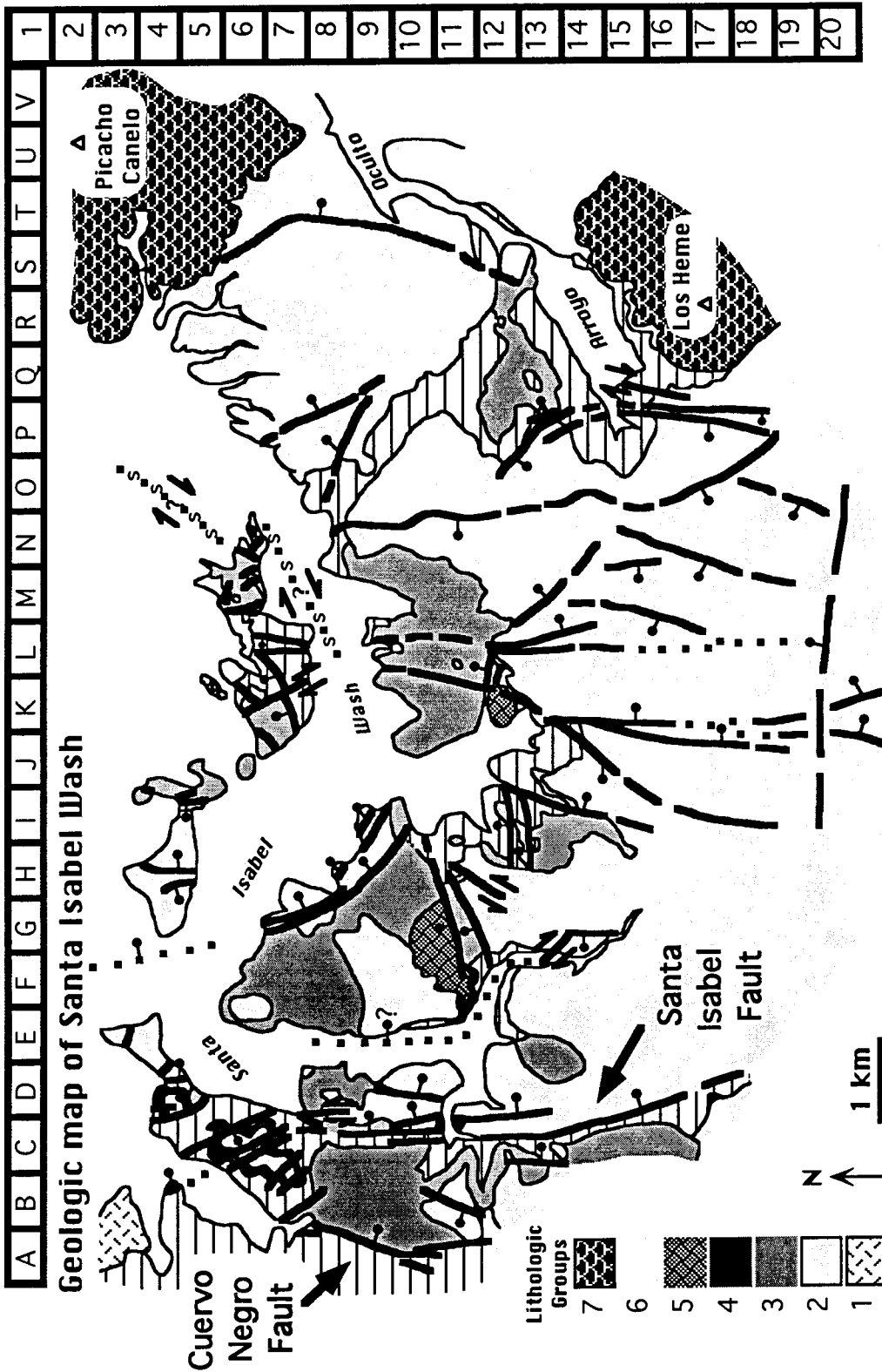




Figure 5.2. Location map of sampling sites for paleomagnetic analysis in Santa Isabel Wash of the northern Sierra Santa Isabel. The stratigraphic columns adjacent to each site indicates (in grey) which cooling units were drilled at each site. Number of cores collected at each site for each lithologic unit is given in Table 5.1. Block samples of an overlying, densely welded unit (*Tm<sub>rec</sub>*) were collected at sites B, C, D, and J.

# Paleomagnetic sampling sites

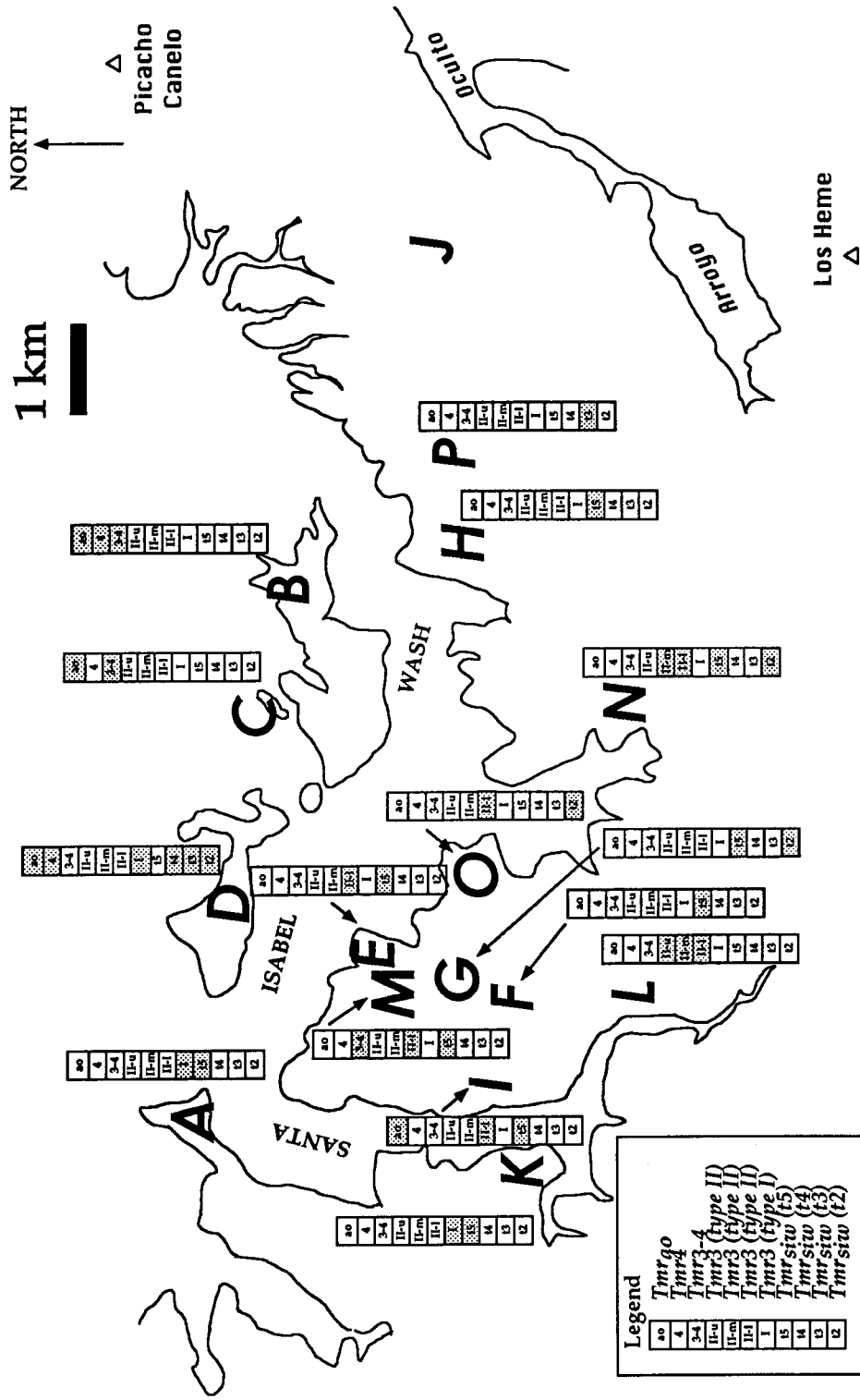


Figure 5.3. Cartoon showing core sample labeling system. In general the “A” segments of cores were demagnetized in this analysis because they were furthest from the effects of weathering at the rock surface. A pilot study testing demagnetization options compared results from “A” and “B” sections from several of cores. As shown schematically here, cores from each site were drilled at a variety of orientations to help detect systematic sampling errors.

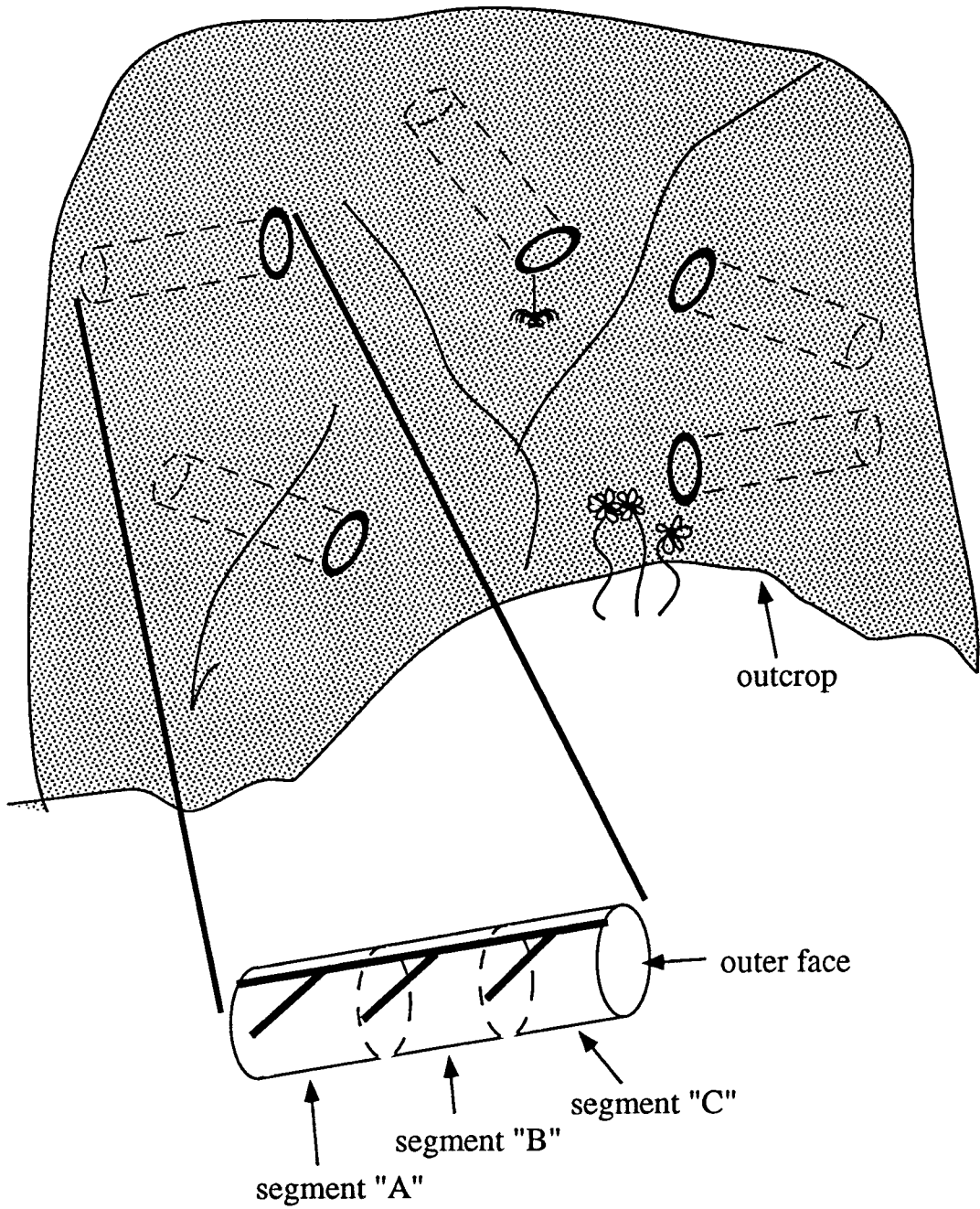
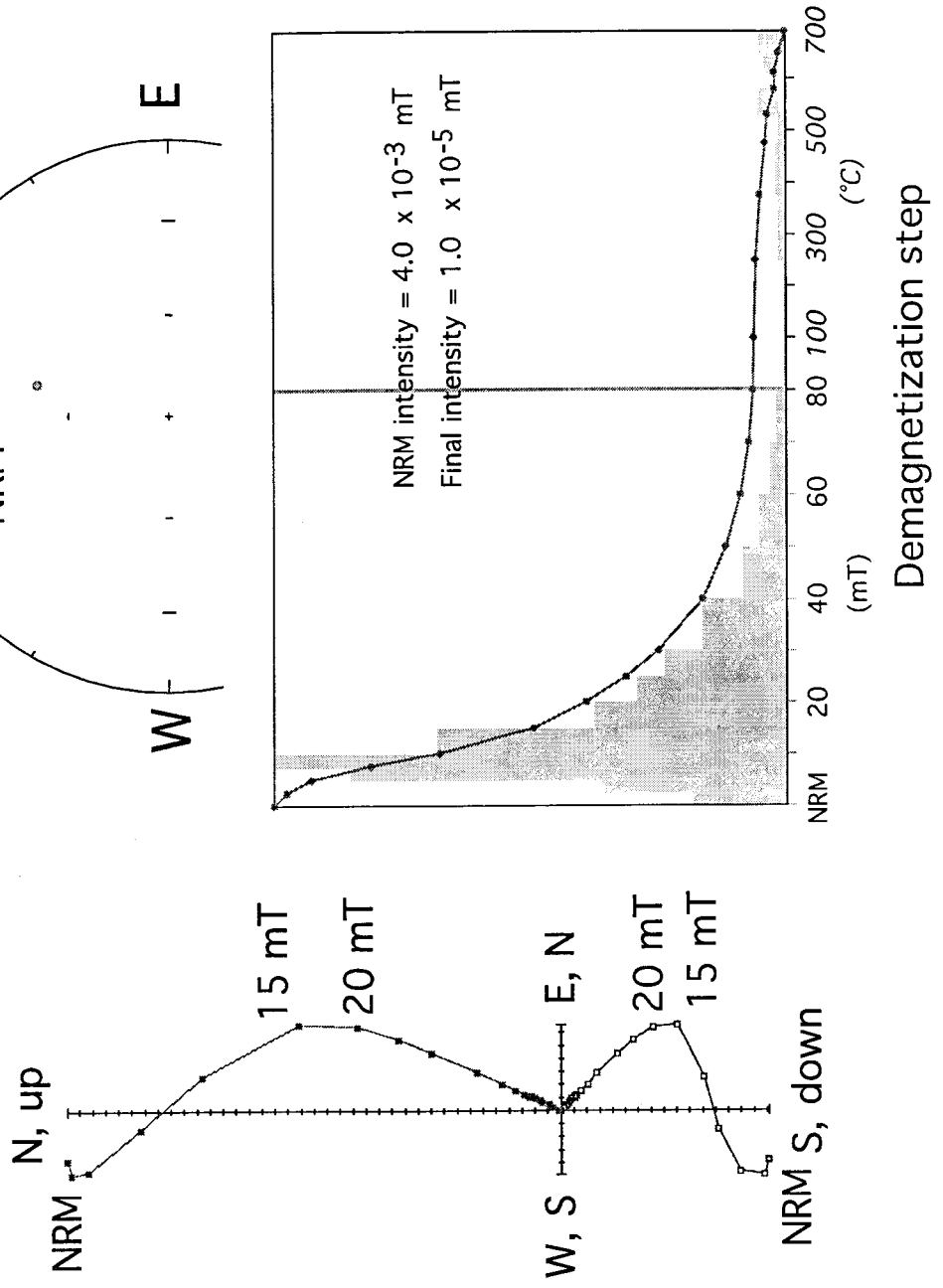


Figure 5.4. (next 2 pages) Two sections of the same core from unit  $Tmr_{siw} (t4)$  measured in the pilot study using a) AF (+ thermal) demagnetization and b) thermal demagnetization techniques. Zijderveld plots (at left) show measured declinations (horizontal projection - closed symbols) and inclinations (vertical projection - open symbols) with progressive demagnetization. Axes labels are for declination, inclination directions, respectively. Various demagnetization steps are labeled including the initial measured values (NRM). Lower hemisphere equal area plots (top right) are also shown (solid points are directed downwards, open points are directed upwards). The present day magnetic field at the sampling locality is shown in these plots with an isolated shaded circle. Normalized magnetic intensity plots (lower right) show magnetic intensity (normalized to the initial intensity) with progressive demagnetization (points connected with curve) and a histogram showing the fraction of the total intensity removed at a given demagnetization step. A secondary overprint which is successfully removed with AF (+ thermal) demagnetization (a) is incompletely removed from the sample demagnetized with thermal techniques only (b). The AF (+ thermal) demagnetized sample (a) exhibits a smooth drop in intensity which is also in contrast with the thermally demagnetized sample (b). These results suggest that AF demagnetization is better suited to these samples than thermal demagnetization.

### Sample from *Tmr<sub>siw</sub>* (t4)



Sample from *Tmr siw (t4)*

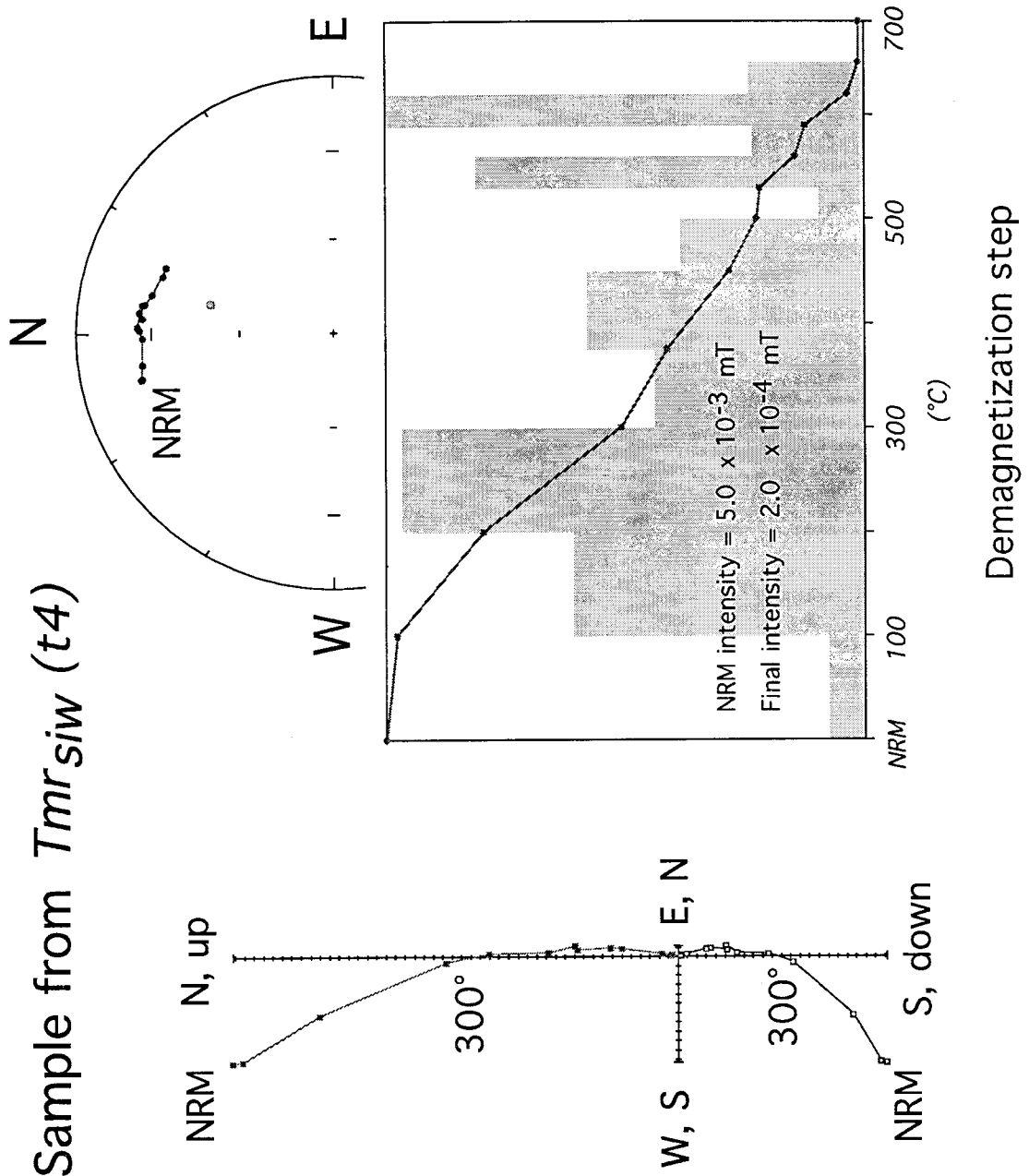
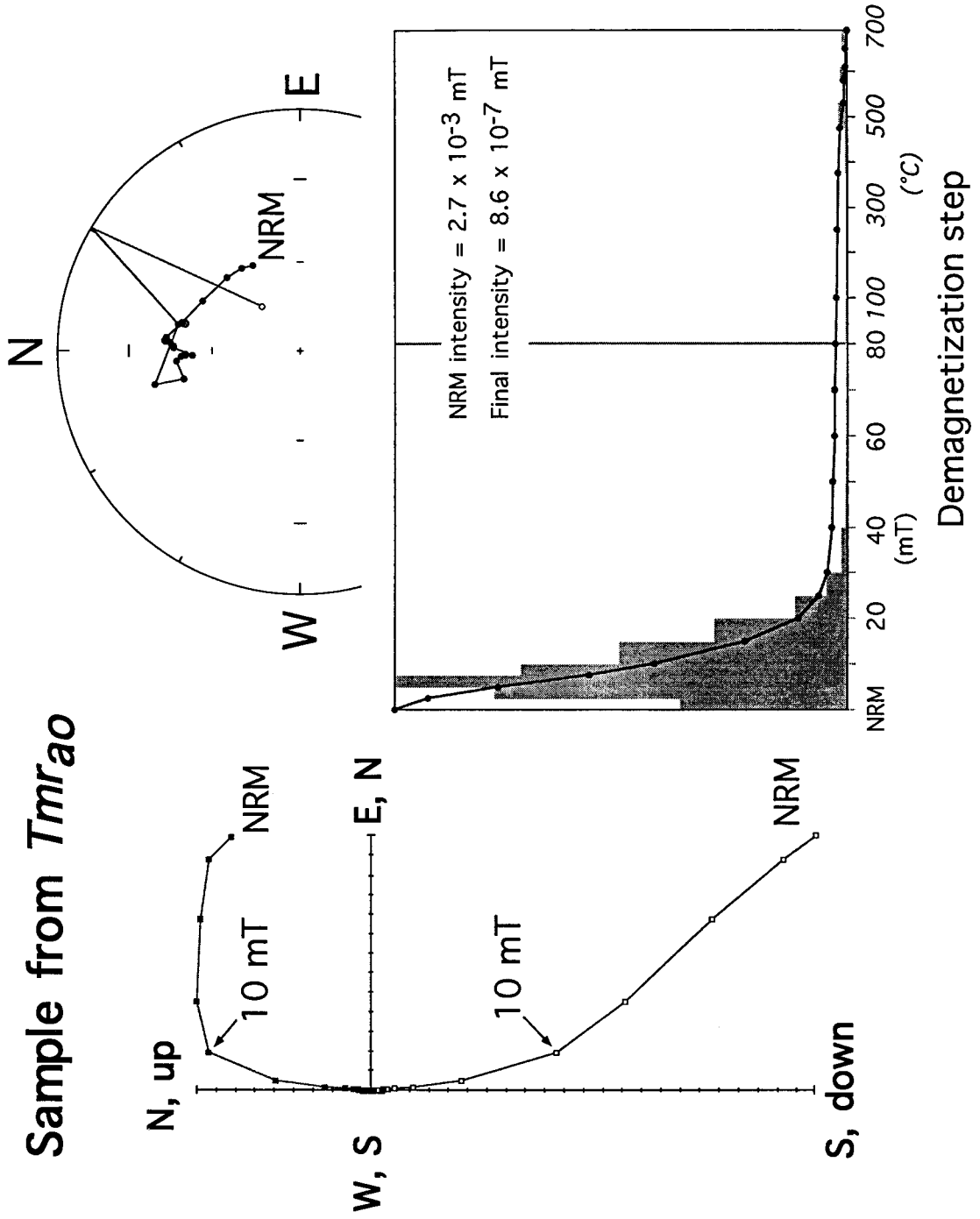


Figure 5.5. (next 2 pages) Two sections of the same core from unit  $Tmr_{ao}$  measured in the pilot study using a) AF (+ thermal) demagnetization and b) thermal demagnetization techniques. Plotting conventions as in Figure 5.4. Results are similar to those found for samples from unit  $Tmr_{siw}$  ( $t4$ ) (Figure 5.4), again suggesting that AF demagnetization is better suited to these samples than thermal demagnetization.



# Sample from Tmrao



# Sample from *Tmr<sub>ao</sub>*

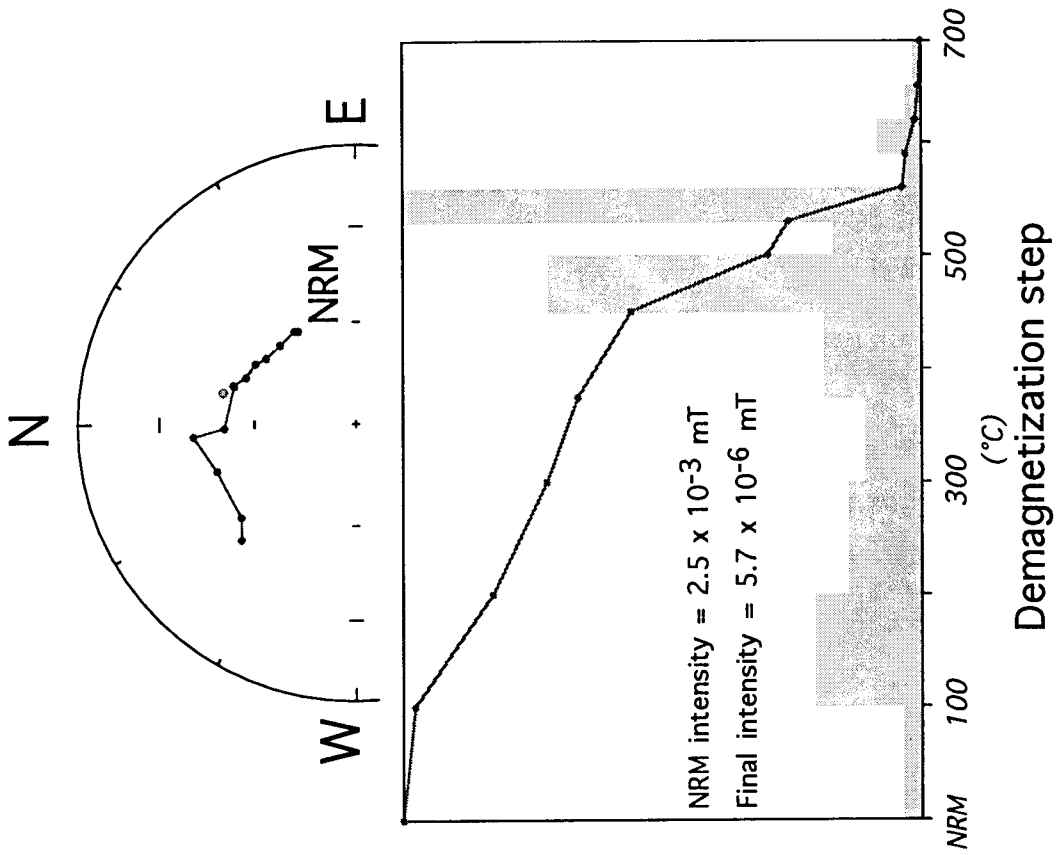
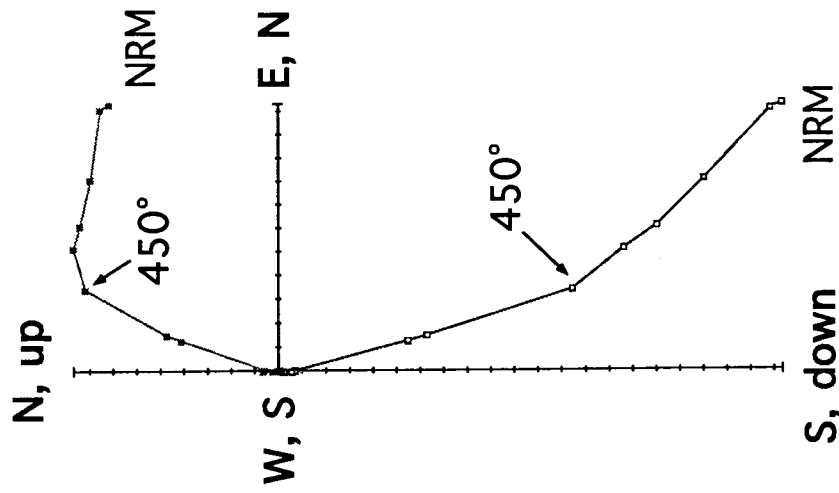


Figure 5.6. Two sections of the same core from unit  $Tmr_{SiW} (t5)$  measured in the pilot study using AF (+ thermal) demagnetization (upper plots) and thermal demagnetization (lower plots) techniques. Equal area plots are not shown. Plotting conventions as in Figure 5.4. The relatively consistent RM direction measured for the AF (+ thermal) demagnetized sample (top) contrasts with the slightly more variable directions measured for a thermally demagnetized sample (bottom). These samples illustrate a slight repositioning error associated with thermal demagnetization techniques that can be avoided with AF demagnetization techniques because samples are not removed from the sample holder during the latter procedure.

### Sample from *Tmr<sub>siw</sub>* (t5)

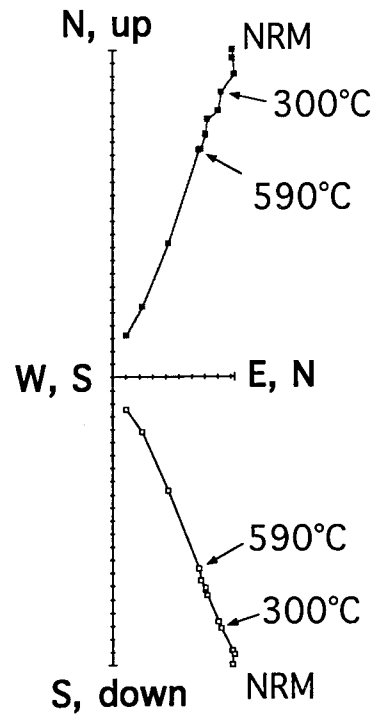
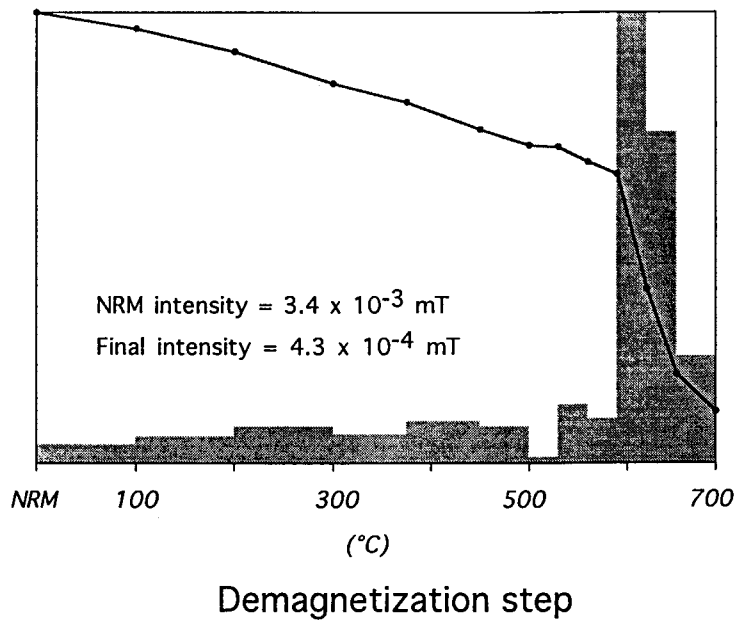
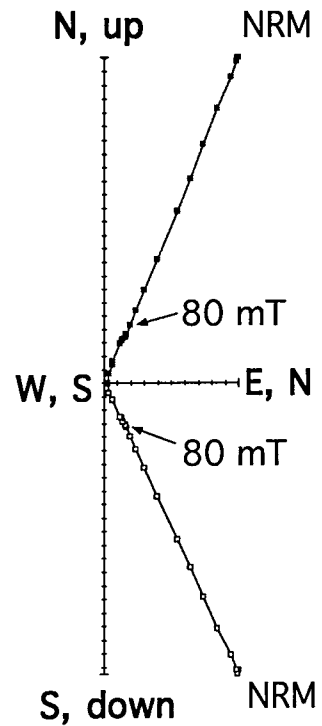
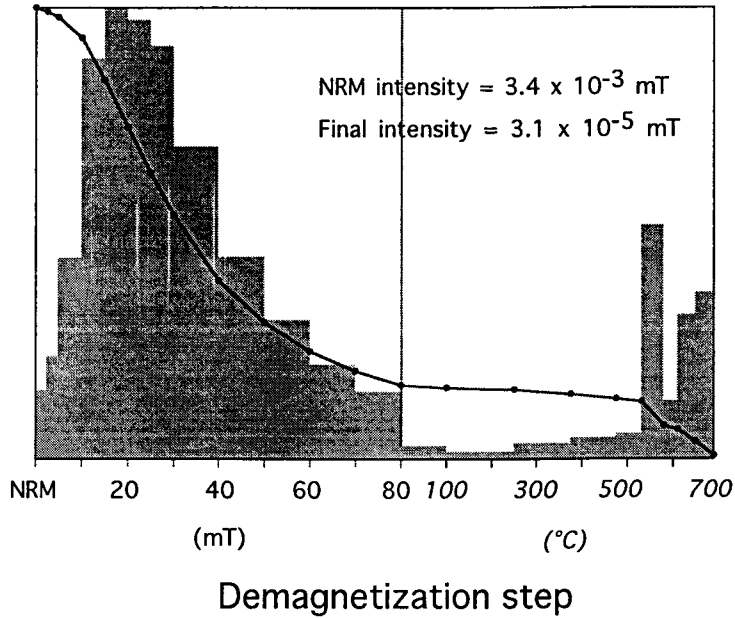


Figure 5.7. Demagnetization scheme combining AF demagnetization and intermediate thermal demagnetization steps. Plotting conventions as in Figure 5.4. Eighty-three samples were demagnetized in this fashion to try to detect the presence of goethite. Results suggest that goethite, which could obscure the primary RM direction below its dehydration temperature of 100°C-300°C, is not present in the pyroclastic flow deposits sampled in this study. The remaining 100+ samples were demagnetized using AF demagnetization only.

Sample from *Tmr siw (t4)*

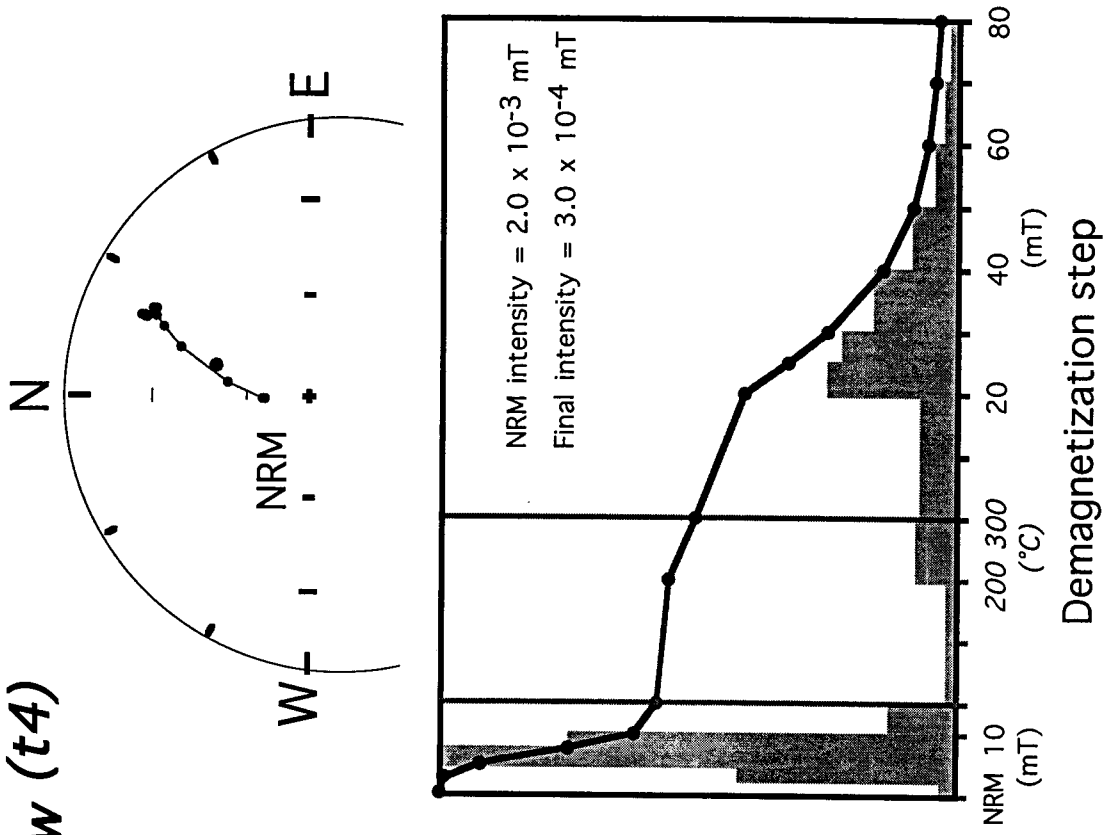
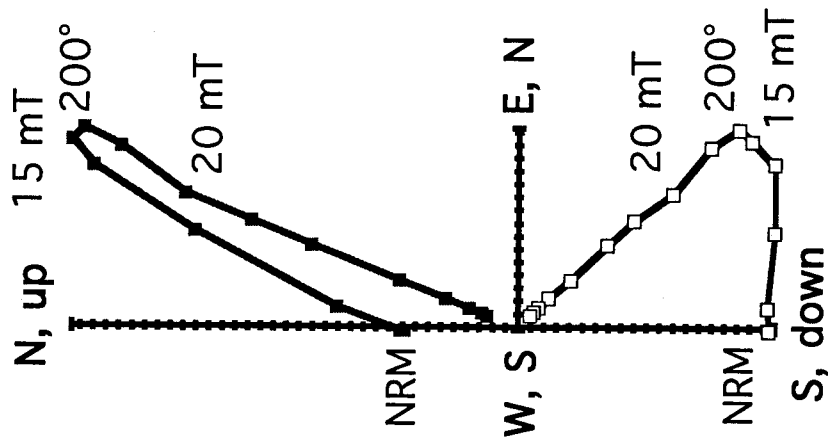


Figure 5.8. Typical rock magnetic experimental results for a sample from Santa Isabel Wash. This particular sample is from unit *Tmr3 (type II)* collected at site I. The curves imply a predominance of ferrimagnetic minerals such as single-domain or pseudo-single-domain magnetite, and smaller amounts of antiferromagnetic minerals such as hematite.

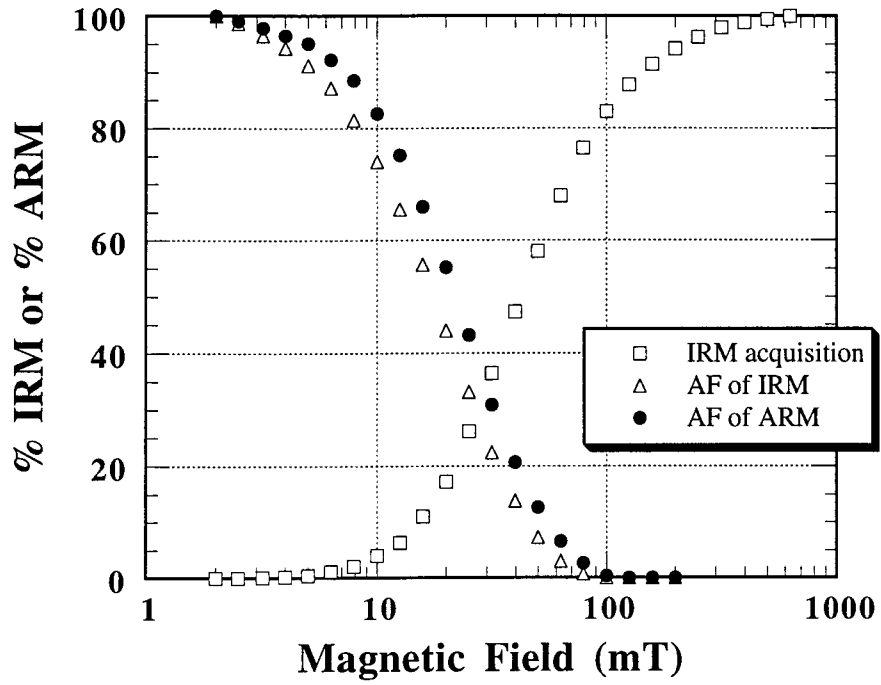
Unit *Tmr3 (type II)* from Site I



Figure 5.9. Results of a rock magnetic test on cooling unit  $t_2$  of  $Tmr_{siw}$ . The thick curve indicates superparamagnetic behavior of the sample following a strong IRM pulse at liquid  $N_2$  temperatures. Progressive measurements are made over time as the sample warms to ambient temperatures. The thin curve shows a similar set of measurements made without an IRM pulse. The arrow indicates a slight bump on the thin curve which probably represents the Verwey transition, a crystallographic transition indicative of single-domain magnetite.

### Rock magnetic test for superparamagnetic grains

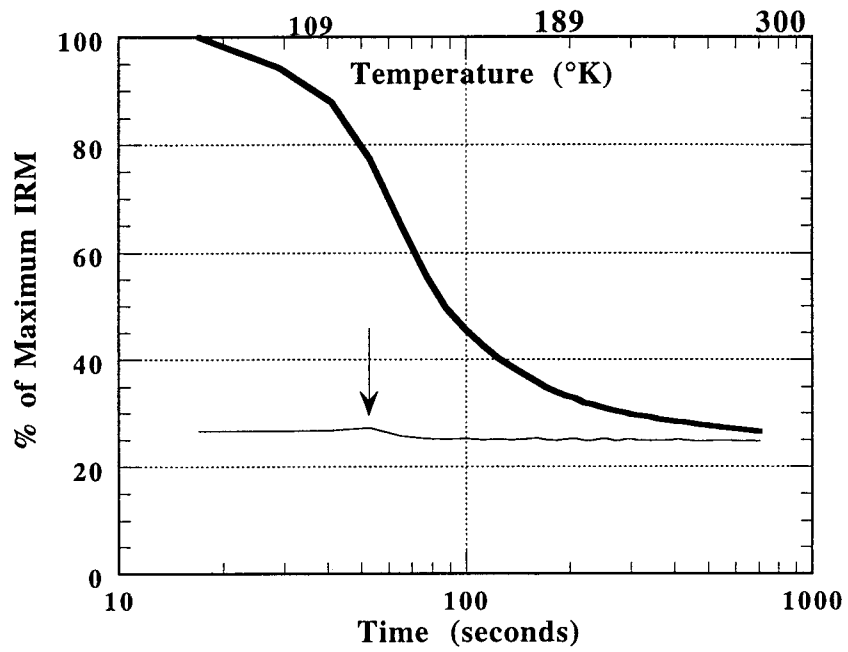


Figure 5.10. Zijderveld and equal area plots of a sample with an upward-directed, low coercivity overprint. The overprint is removed by the 15 mT demagnetization step. Plotting conventions as in Figure 5.4.

Sample from  $Tmr_{siw} (t4)$

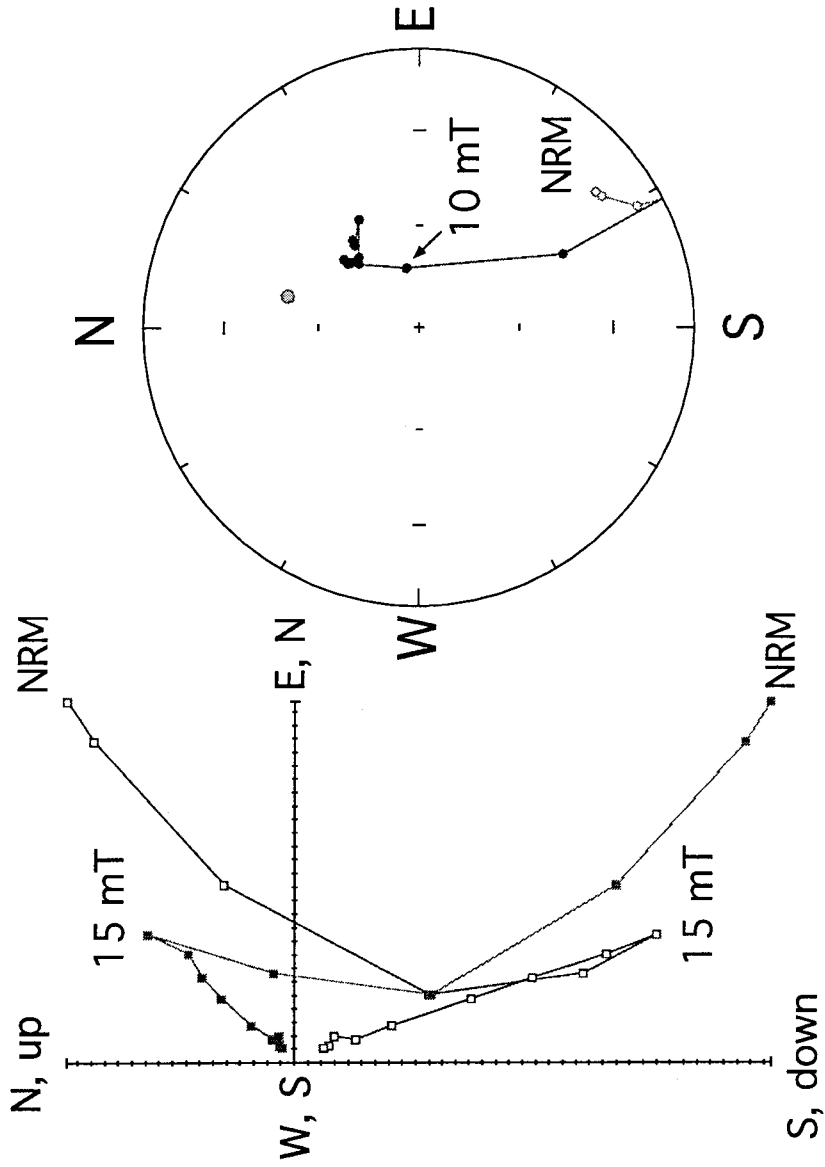


Figure 5.11. Zijderveld, equal area, and normalized intensity plots of a sample with two components of magnetization. Because a primary component is not clearly isolated, the data are fit with a plane which contains both components instead of a line. Plotting conventions as in Figure 5.4. The demagnetization vectors of 10 out of 218 cores were fit with planes instead of lines.

Sample from *Tmr3* (type I)

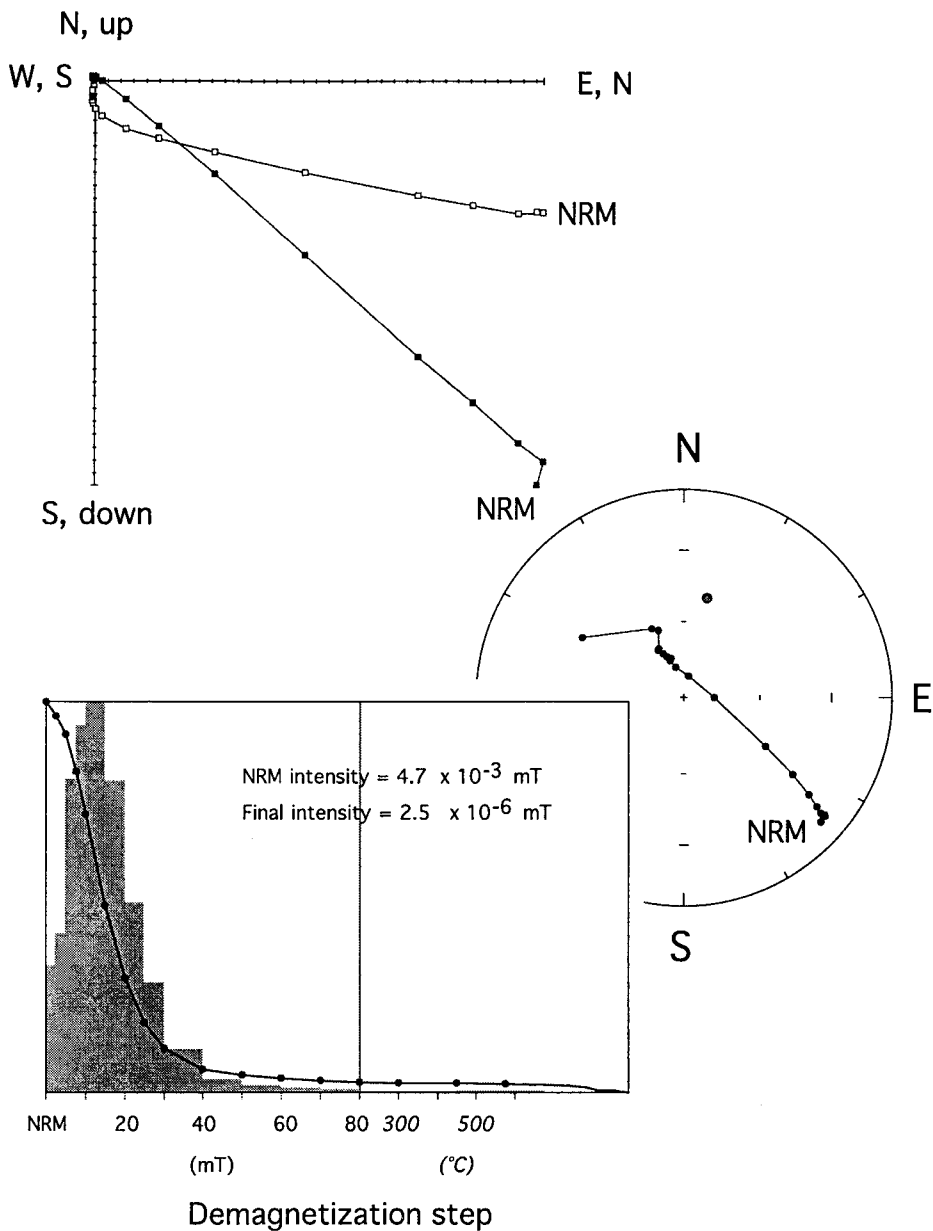
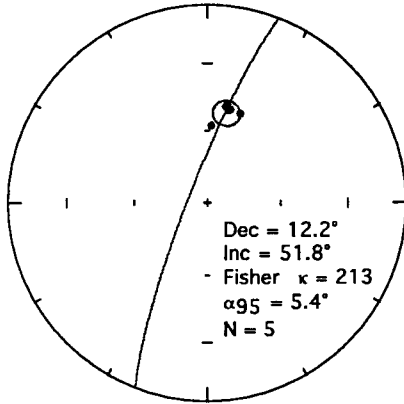


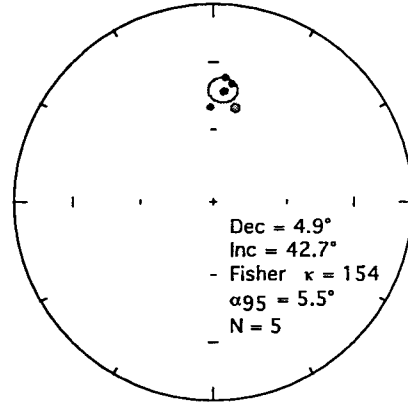
Figure 5.12. (next 10 pages) Equal area plots of primary RM directions for each sample at a given site. Ellipses are  $\alpha_{95}$  Fisher confidence cones centered on the means. Results yield six groups which preserve distinct RM directions: a)  $Tmr_{ao}$ , b)  $Tmr4$ , c)  $Tmr_{3-4}$ , d)  $Tmr3$  (type II) (three cooling units) e)  $Tmr3$  (type I) (one cooling unit), and f)  $Tmr_{siw}$  (four cooling units). Each plot corresponds to one row listing a site mean in Table 5.2. The combined results of each of the six groups (a-f) are shown in Figure 5.13.

*Tmr<sub>ao</sub>*

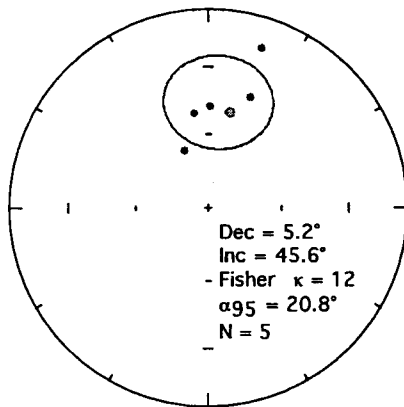
Site B



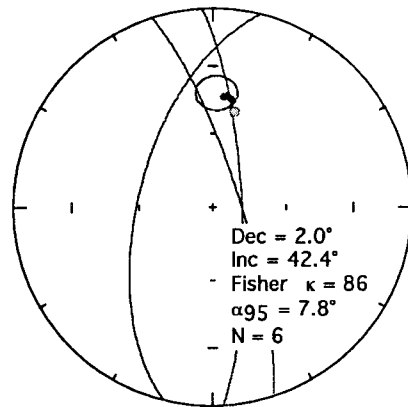
Site C



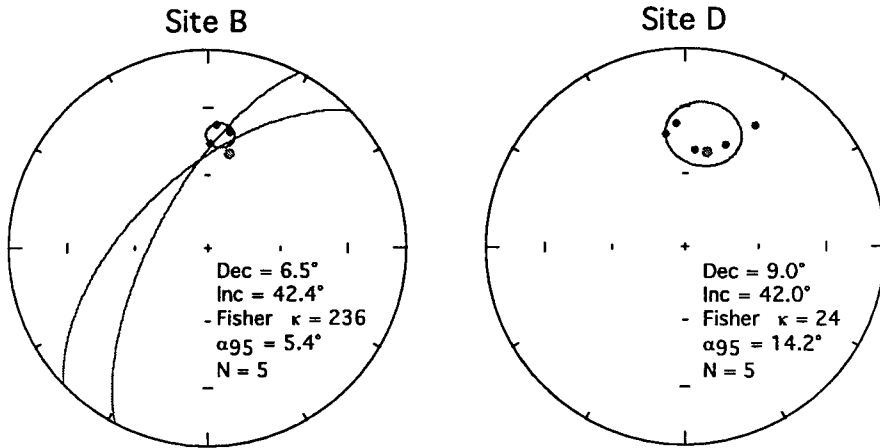
Site D



Site I

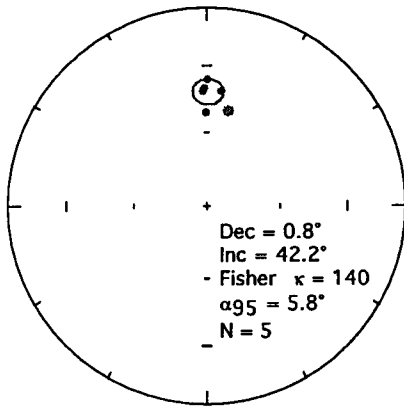




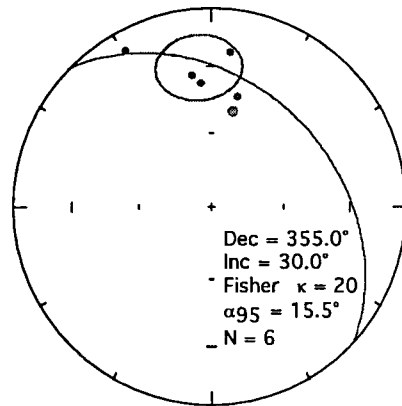
*Tmr4*

# Tmr3-4

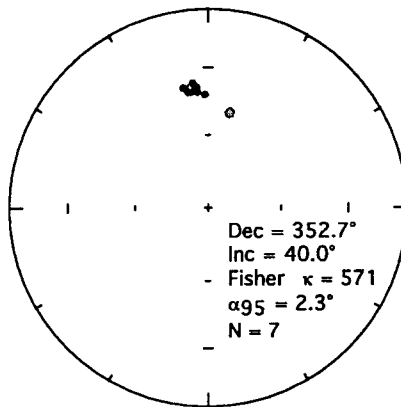
Site B



Site C

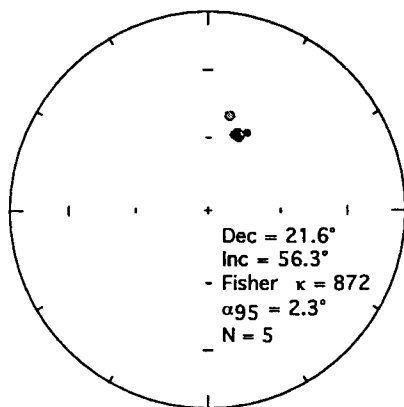


Site M

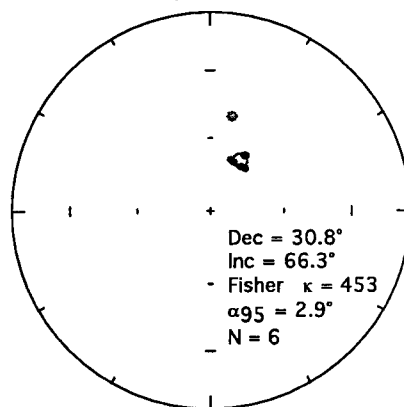


# Tmr3 - type II

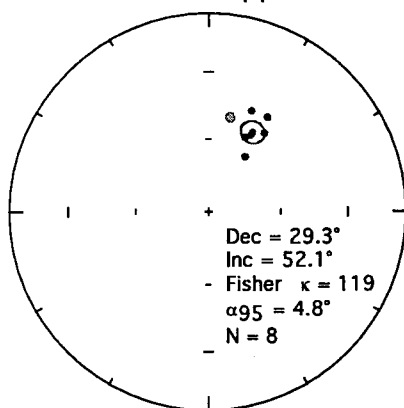
Site E



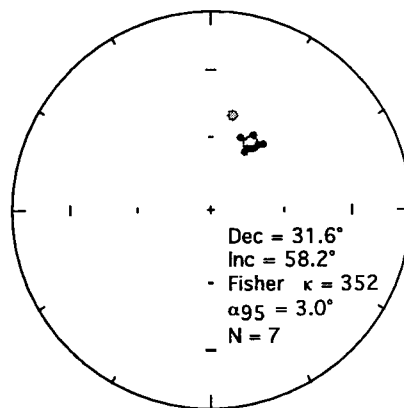
Site I



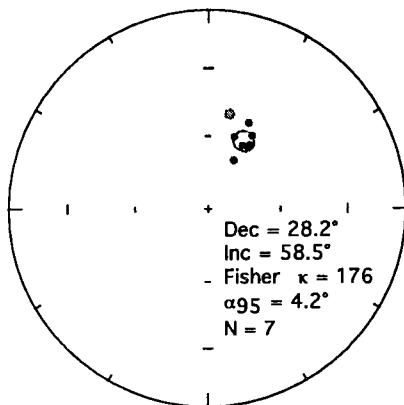
Site L - upper



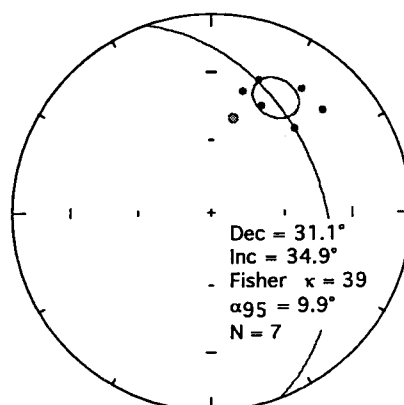
Site L - middle



Site L - lower



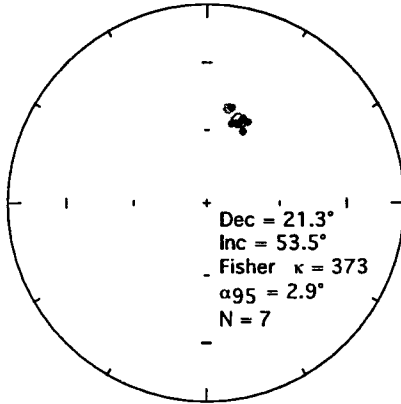
Site M



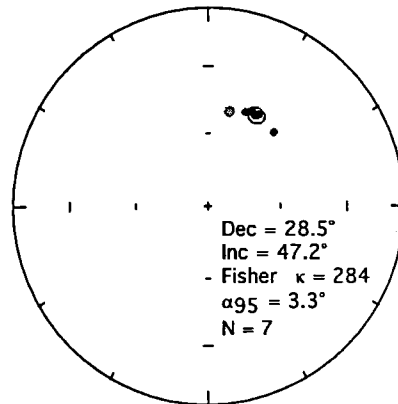
d (continued)

*Tmr3 - type II - continued*

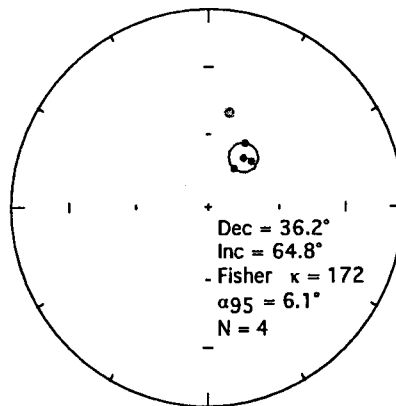
Site N - upper



Site N - lower

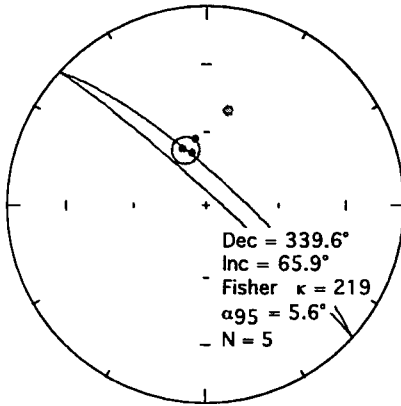


Site O

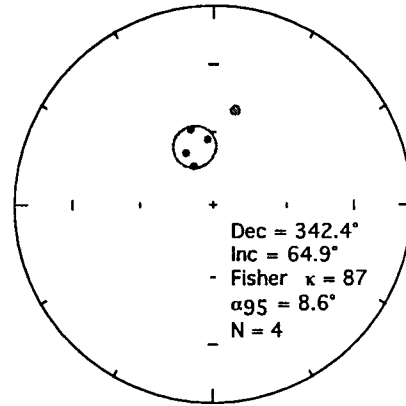


# Tmr3 - type I

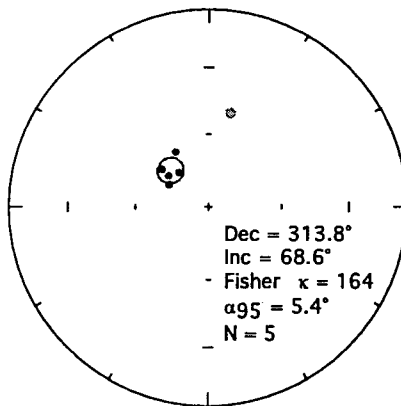
Site A



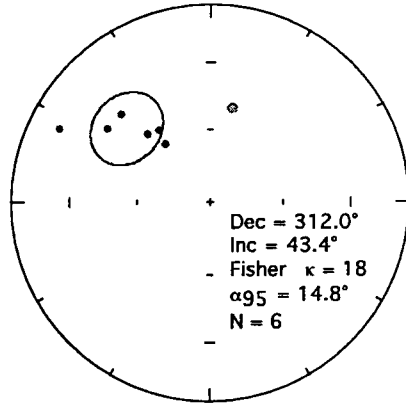
Site D - upper



Site D - lower

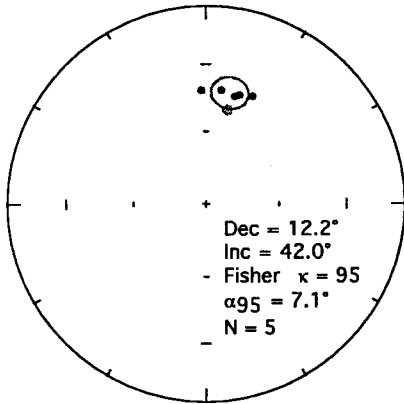


Site K

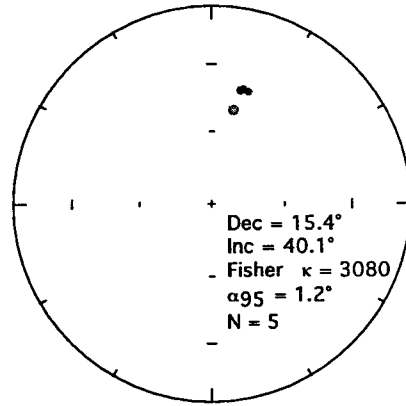


# $Tmr_{siw}(t5)$

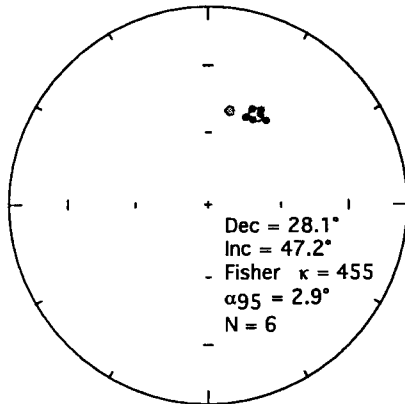
Site A



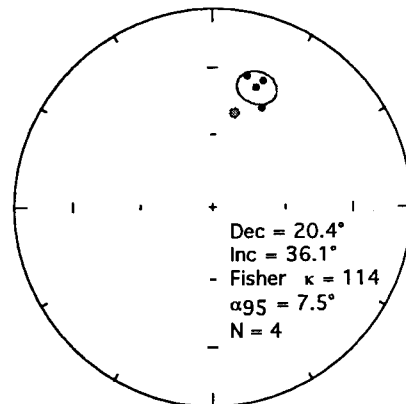
Site E



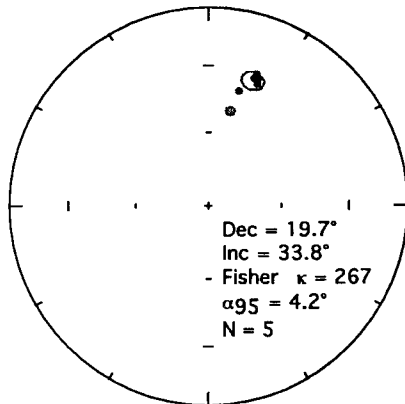
Site F



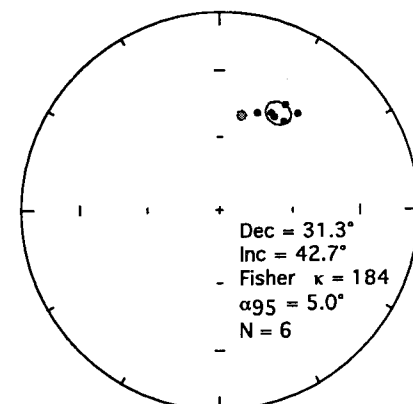
Site G

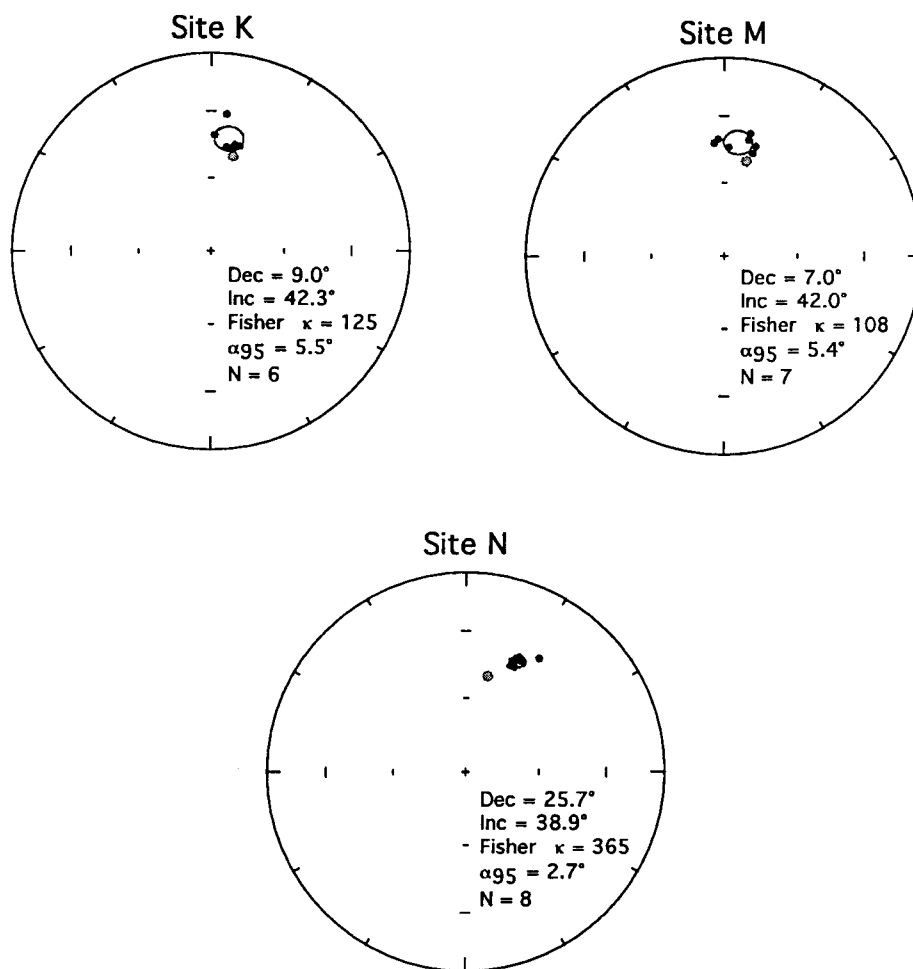


Site H

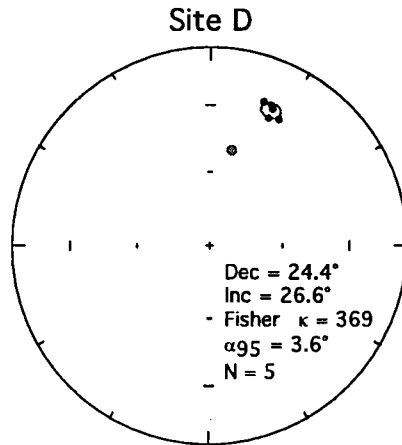


Site I

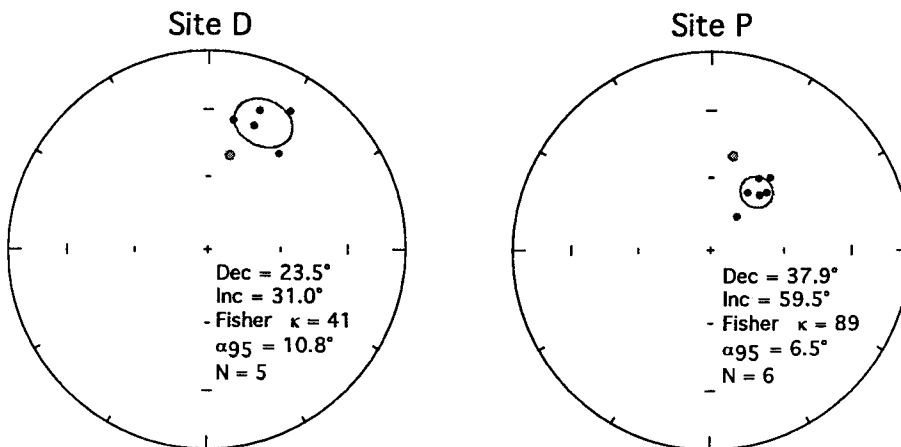


*Tmr<sub>siw</sub> (t5) - continued*

## $Tmr_{siw}(t4)$



## $Tmr_{siw}(t3)$

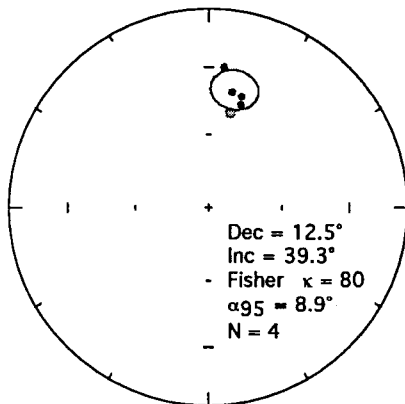




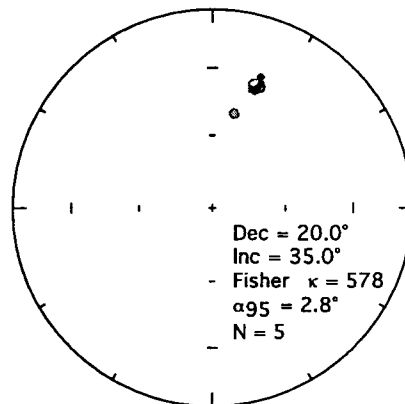
f (continued)

# $Tmr_{siw}(t2)$

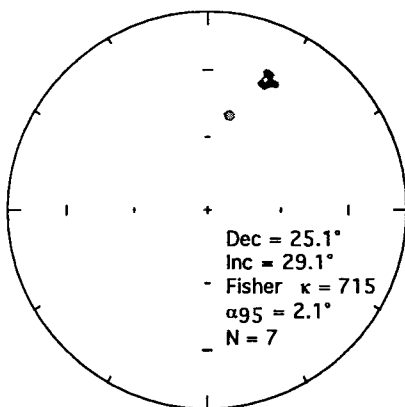
Site D



Site G



Site N



Site O

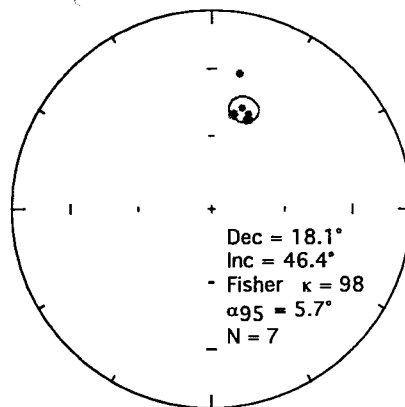
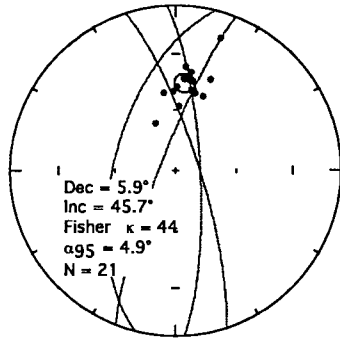
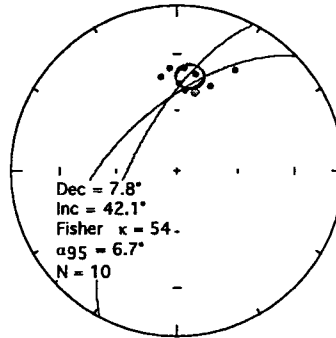


Figure 5.13. Equal area plots for the six groups with distinct RM directions. Each plot corresponds to a combined group value listed in Table 5.2. After passing a test for common mean direction (see text for details), the combined group RM values for each group were calculated by treating each data point at each site (i.e., each core) as an individual measurement and calculating the average as if they were all from one site. For example, the combined RM direction calculated for  $Tmr_{siw}$  uses 91 individual samples instead of averaging the 15 sites.

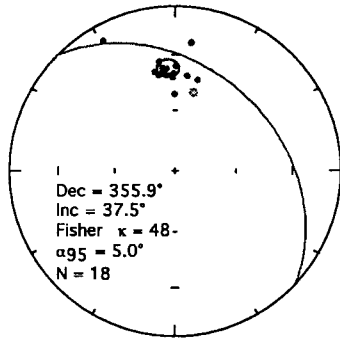
*Tmr<sub>20</sub>* - 4 locations



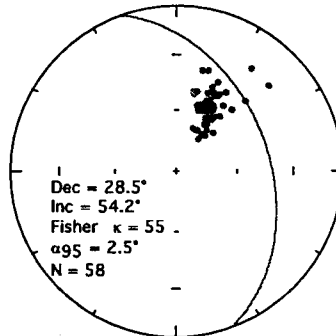
*Tmr4* - 2 locations



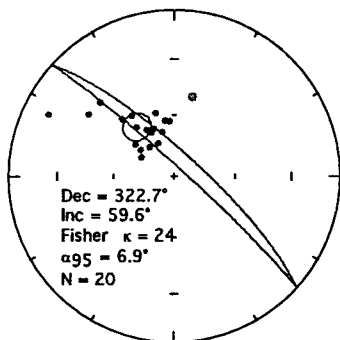
*Tmr3-4* - 3 locations



*Tmr3 - type II* - 9 locations



*Tmr3 - type I* - 4 locations



*Tmr<sub>siw</sub>* - 16 locations

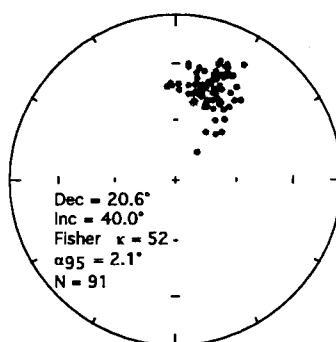
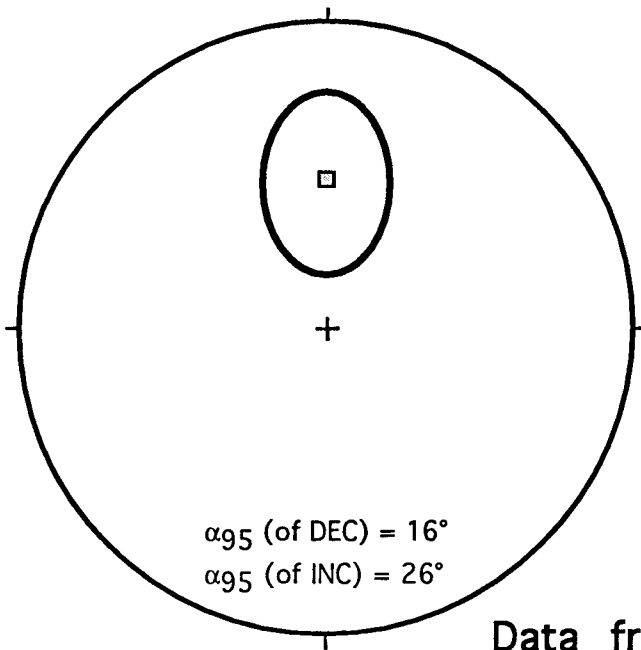


Figure 5.14.  $\alpha_{95}$  confidence ellipses for the geomagnetic pole around the expected position of geomagnetic north at the study locality. The values are determined from PSV models based upon volcanic sequences from the last 5 Ma (Quidelleur and Courtillot, 1996). Confidence limits are shown using the preferred model of Quidelleur and Courtillot (1996) (Model C1) as well as using only data from their database for latitudes between 30° and 40°N.

Model C1



Data from database

Equal Area Projections

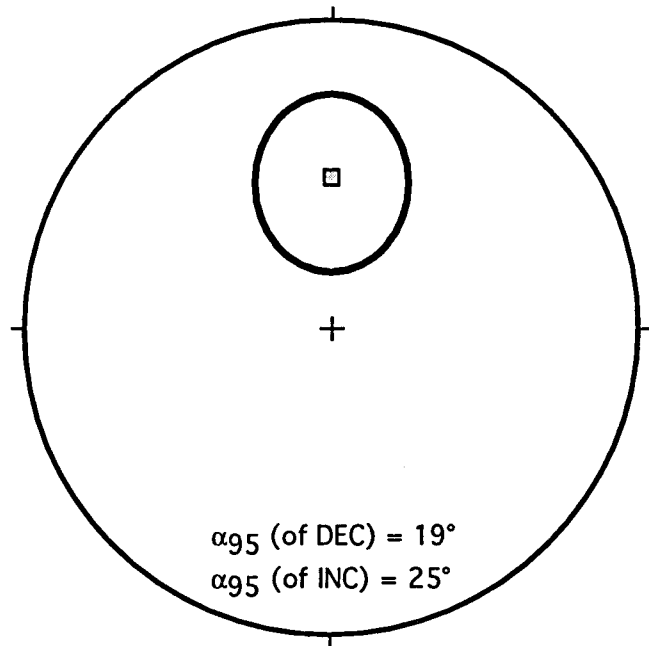
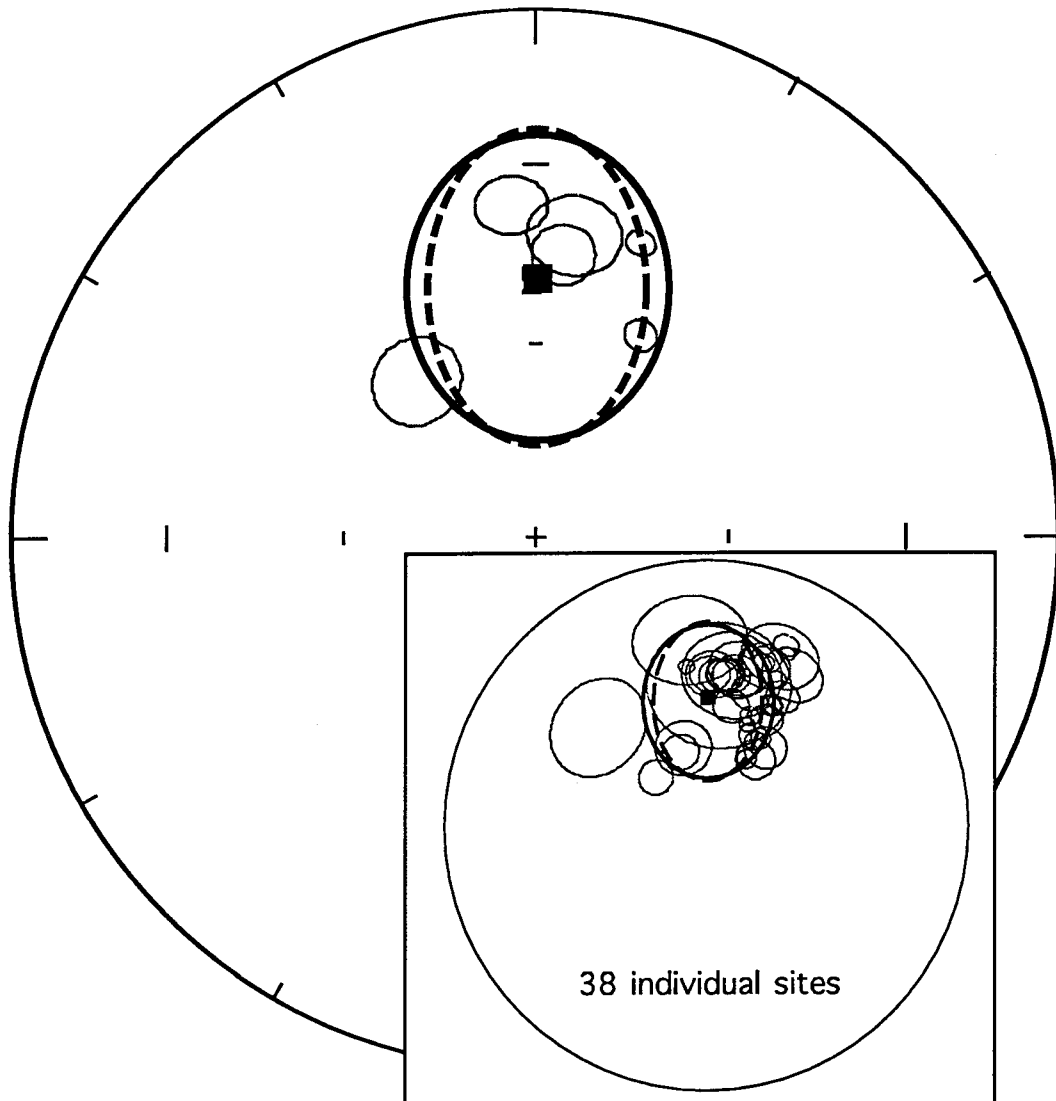


Figure 5.15. Confidence ellipses for the geomagnetic pole from Figure 5.14 superimposed upon the combined RM directions for the six different groups. Model C1 limits are shown with a dashed ellipse and the database limits are shown with a solid ellipse. All six groups fall within or overlap with the 95% boundaries of expected secular variation, suggesting that Santa Isabel Wash as a whole has not undergone rotation relative to geomagnetic north. Inset shows the same ellipses superimposed upon the mean RM directions for the 38 sampling sites. Four sites fail to overlap with the ellipses.

Six lithologic groups with unique RM directions from  
Santa Isabel Wash and  $\alpha_{95}$  confidence ellipses  
for the geomagnetic pole



## Chapter VI

## Regional synthesis and Summary

- 6.1. *Summary of geologic history of Santa Isabel Wash in the northern Sierra Santa Isabel*
- 6.2. *Comparison with adjacent areas (Southern Valle Chico, Sierra San Fermín, PVP) and relationship to Matomí accommodation zone*
- 6.3. *Relationship to Gulf Extensional Province and Gulf of California spreading system*
- 6.4. *Relationship to PAC-NAM plate boundary*
- 6.5. *Model to explain present-day ENE-directed extension in northeastern Baja California, Mexico*
- 6.6. *Implications for the propagation of oceanic rifts into continents*
- 6.7. *Conclusions*



### 6.1. *Summary of geologic history of the northern Sierra Santa Isabel (Santa Isabel Wash)*

The Santa Isabel Wash region (informally named here) of the northern Sierra Santa Isabel provides excellent exposure of the northern margin of the Puertecitos Volcanic Province (PVP) in profile. The location of the PVP in northeastern Baja California and the geology of the surrounding areas are shown in Figure 6.1. The study area location and the names of nearby features included in the following discussion are shown in Figure 6.2. In general the PVP is a flat, plateau-like, volcanic tableland of limited, principally fault-related, topography. Topographic relief on the PVP tableland is typically on the order of 50-100 meters. In some places erosion has cut 100-200 meters below the upper surface of the plateau, which is primarily composed of late Miocene/early Pliocene (Gastil et al., 1975) volcanic tuffs. In Santa Isabel Wash, and the informally named Arroyo Oculito region to the east, up to 700 meters of topographic relief exposes the units which underlie the plateau-forming tuffs, thus providing a window into the pre-late Miocene geologic history. A summary of the history recorded in Santa Isabel Wash is given here beginning with the oldest exposed deposits. The ages given for several units were determined using  $^{40}\text{Ar}/^{39}\text{Ar}$  geochronology (Chapter III). A simplified geologic map of the study area which divides the lithologic units into seven Groups is shown in Figure 6.3 (see Figure 4.2 of Chapter IV for a colored version and Plate I for the actual 1:20000 geologic map).

#### ***Early Miocene***

The steep slopes of early Miocene, subduction-related andesitic volcanoes provided the source material for thick (up to at least 500 m) volcanoclastic deposits (*Tmvs*) of Group 2. The thickest deposits are in the westernmost part of the field area where they form steep cliffs in the footwall of a major E-dipping normal fault named here the Cuervo Negro fault (Figure 6.3). *Tmvs* is essentially the “basement” rock in the area upon which all other units were deposited. An unconformable lower contact is exposed in only one location (NW corner of mapped area) where *Tmvs* is deposited upon pre-Miocene granite and metasedimentary rocks

(Group 1). The pre-Miocene batholithic topography was undoubtedly irregular, and the isolated exposure in Santa Isabel Wash perhaps indicates a basement high around which the volcanoclastic sediments were deposited. Intervening, nonmarine, sedimentary deposits up to 200 m thick are preserved between the batholithic and volcanoclastic deposits in nearby localities (Figure 6.2) such as parts of the southern Valle Chico (Stock, 1989), the Sierra San Fermín (Lewis, 1996), and north central Baja California (Dorsey and Burns, 1994), but not in Santa Isabel Wash, also suggesting that the basement contact exposed here was perhaps topographically high. It is not known if the PVP is underlain by a continuation of the pre-Miocene batholithic rocks, but it is certainly possible. There are no known granitic outcrops in the entire PVP (principally to the west, east and south of the study area). The closest known outcrop of granite just south of the PVP is ~ 30 km southeast of Santa Isabel Wash (Figure 6.1).

The closest Miocene (17-20 Ma) andesitic vents from which the Group 2 deposits may have been derived are located ~ 10 km northwest of Santa Isabel Wash in the southernmost part of Valle Chico (Stock et al., 1991) (Figure 6.2). Other candidates include Miocene Pico Matomí (Gastil et al., 1975), located 20 km west of Santa Isabel Wash, and a ~ 16 Ma andesitic volcanic center in Arroyo Los Heme (Martín-Barajas et al., 1995) approximately 25 km southeast of Santa Isabel Wash (Figure 6.2).

The coarse *Tmvs* deposits generally have sub-horizontal, yet poorly-defined, bedding in Santa Isabel Wash. Fine-grained sandstones are preserved in some places and record a variety of strikes and dips. In general beds dip 10-40° to the west or north. Small pyroclastic flows were deposited synchronously during *Tmvs* deposition and are interbedded within it. A  $17.1 \pm 2.4$  Ma (all errors quoted here are  $2\sigma$ ) biotite-rich pyroclastic flow deposit (*Tmr<sub>bio</sub>*) up to 80 m thick filled an E-W trending paleochannel/paleocanyon, or some other type of steep-sided, topographic low, within upper *Tmvs* over an E-W distance of at least 4 km. The locations of some of these discontinuous outcrops include K12, H11, F12, and E12 in Figure 6.3.

### *Middle Miocene*

Lava flows of Group 3 erupted after *Tmvs* deposition ceased. Basalt flows (*Tmb<sub>lob</sub>*, *Tmb<sub>kc</sub>*) up to 0.5 km<sup>2</sup> erupted in a few places (e.g., locations E13 and I13 in Figure 6.3)  $16.3 \pm 1.0$  to  $17.1 \pm 2.2$  Ma, and voluminous dacitic lavas (*Tmd<sub>tomb</sub>*) erupted throughout the region between  $15.5 \pm 0.8$  and  $16.7 \pm 1.0$  Ma. The thickest dacite flows are approximately 240 m thick. The ages of these lavas suggest that they, too, are associated with subduction-related volcanism, although they represent a more proximal facies relative to the underlying, medial-facies volcanoclastic deposits (*Tmvs*). Volcanism apparently waned following the deposition of *Tmd<sub>tomb</sub>* until a  $12.7 \pm 0.6$  Ma pyroclastic flow deposit (*Tmr<sub>sf</sub>* of Group 4) was deposited discontinuously in the western portion of the mapped area (principally in the vicinity of C6 in Figure 6.3). *Tmr<sub>sf</sub>* has a distinct, basal vitrophyre which is generally at a high angle against irregular underlying topography, and a sub-horizontal upper surface. The thickest exposure (60 meters) pinches out against underlying topography from north to south on the west side of Santa Isabel Wash (location B7 in Figure 6.3).

### *Late Miocene*

Another apparent hiatus in volcanism followed the deposition of *Tmr<sub>sf</sub>* until  $9.3 \pm 0.6$  Ma when a mineralogically distinct hornblende andesite (*Tma<sub>toro</sub>* of Group 5) erupted in at least two areas (locations F11 and K12 in Figure 6.3). These are relatively small (0.1-0.25 km<sup>2</sup>) lava flows.

Post-9.3 Ma normal faulting offsets all of the lithologic units described above. Specifically, an ENE-striking normal fault (the Pico del Toro fault; see Figure 4.4 in Chapter IV) which dips  $\sim 40^\circ$  to the northwest cuts all of these units and preserves slickenlines indicative of sinistral oblique-slip faulting. The amount of offset is not readily apparent. This fault does not cut an overlying series of  $\sim 6$ -7 Ma tuffs of Group 6, thus an “early” period of faulting occurred sometime between  $\sim 6$ -7 and 9.3 Ma. Other faults which cut the pre-15.5

Ma units ( $Tmvs$  and  $Tmd_{tomb}$ ) but not the overlying Group 6 tuffs also strike ENE to E and show north-side-down displacement (e.g., locations K7 and I12 in Figure 6.3). In these locations the faults could be as old as 15.5 Ma, since the 12.7 and 9.3 Ma units are not present.

At some time prior to the deposition of the ~ 6-7 Ma Group 6 pyroclastic flow deposits, which form the plateau-like upper surface of the PVP in the study area, a roughly NW-trending topographic break developed along the northern margin of the region mapped in this study (see Figure 4.3 in Chapter IV for present-day position). Significant changes in the thickness of Group 6 pyroclastic flow deposits across the slope suggest that the region to the northeast was up to 400 m lower than the region to the southwest. Although this topographic change could have been the result of erosion, the preferred interpretation is that it marks the positions of pre-6-7 Ma extensional faults accommodating NE-side down displacement (see Chapter IV for further discussion). As will be developed below, this extension may be related to a NW-trending accommodation zone between regions of differential extension.

The oldest in the series of ~ 6-7 Ma Group 6 pyroclastic flow deposits is an assemblage of five cooling units ( $Tmr_{siw}$ ) believed to be restricted to the Santa Isabel Wash region which were deposited around  $6.5 \pm 0.4$  to  $6.7 \pm 0.4$  Ma. The tuffs filled topographic lows and pinched out, or “plastered,” against higher topography; their upper surface is generally not sub-horizontal. This package is commonly less than 40 m thick but can be up to 140 m thick.

The next overlying pyroclastic flow deposit in Group 6 ( $Tmr3$ ) was commonly thick enough to fill in most of the surrounding irregular topography and consequently has a relatively planar, sub-horizontal, upper surface. The age of  $Tmr3$ , which consists of four cooling units, is between  $6.2 \pm 0.2$  and  $6.4 \pm 0.4$  Ma. The series of cooling units mapped as  $Tmr3$  is commonly > 60-80 m thick, and up to 140 m thick in the southwest portion of the map area. In the south-central and southeast parts of the mapped area (i.e., the PVP highlands), basal  $Tmr3$  is not exposed and thus its thickness cannot be determined. It is at least 40 m thick where the highlands of the PVP are cut at the head region of Arroyo Oculito

and stratigraphic relationships are exposed in profile. Although the four *Tmr3* cooling units look very similar in outcrop appearance, paleomagnetic study (Chapter V) suggests that the lowest cooling unit might be restricted to the northwestern portion of the mapped area. This implies either a pre-6 Ma topographic low in the northwest filled by the lowest *Tmr3* cooling unit, or some other mechanism for geographic restriction of this unit, or rapid erosion of this cooling unit in the east just down to the upper surface of underlying *Tmr<sub>siw</sub>*, which seems highly unlikely. These exposures of the lowest cooling unit are located immediately east of the E-dipping Santa Isabel fault (Figure 6.3). If this fault system were active prior to the deposition of *Tmr3*, a region of hanging-wall downwarp, or reverse drag, could have produced an east-facing scarp and a topographic low adjacent to the fault in the position where this lowest cooling unit is deposited.

The thickness of three subsequently deposited pyroclastic flow deposits in Group 6 changes significantly across the pre-existing topographic boundary described above. The lowest of these (*Tmr4*, which includes a thin, underlying cooling unit *Tmr<sub>3-4</sub>*) is 3-5 m thick in most of the study area but up to at least 70 m thick in the vicinity of Arroyo Oculito (Figure 6.3). This crystal-poor tuff has not been dated. It is overlain by *Tmr<sub>ao</sub>* ( $6.4 \pm 0.2$  Ma), 0-1 m thick in most of the area but up to 30 m thick in Arroyo Oculito, which in turn is overlain by *Tmr<sub>ec</sub>* ( $6.1 \pm 0.6$  Ma), 1-2 m thick in most of the area but at least 80 m thick in Arroyo Oculito. At the location of the pre-6-7 Ma topographic slope, *Tmr4* develops a thick (several meters) spherulitic base, and *Tmr<sub>ec</sub>* is strongly lineated in the down-slope direction. Other features such as tension cracks and sheared fiamme around lithic clasts and feldspar phenocrysts (seen in thin section) also suggest rheomorphic (post-emplacement) flow of *Tmr<sub>ec</sub>* down the paleo-topographic slope.

Following the deposition of the Group 6 pyroclastic flow deposits, thick andesitic and rhyolitic lava flows (Group 7), in some cases preceded by minor mafic spatter eruptions, were deposited in the easternmost part of the field area. A series of rhyolite flows and breccias (*Tmr<sub>can</sub>*) up to 500 m thick was deposited in the northeast corner of the map area  $5.9 \pm 0.8$  to  $6.0 \pm 0.4$  Ma and overlies at least one of the andesite lavas (*Tma<sub>gem</sub>*). Two other andesite

flows ( $Tma_{hem}$ ,  $Tma_{ugl}$ ) are interpreted to be correlative with  $Tma_{gem}$  on the basis of thin section analysis and field relationships although they could be significantly younger. The andesite lavas, most likely composed of numerous flows, are between 120 and 550 m thick and include basal breccias which can be tens of meters thick.

### ***Latest Miocene/Early Pliocene***

Post-6 Ma faults are common throughout the area. Two closely spaced (~ 2 km apart in map view), N-S striking, E-dipping normal fault systems on the west side of the study area (Cuervo Negro fault and Santa Isabel fault; Figure 6.3) are the most continuous structures in the mapped area, although in the north they are disrupted by NNW-striking splays and cross-structures. On the basis of the difference in elevation of the  $Tmr3/Tmr4$  contact (an ~ 6 Ma horizon) between Santa Isabel Wash and a region mapped on the plateau to the west of the Cuervo Negro fault (Stock, Lewis, Salton, and Holt, unpub. mapping), there appears to be about 500 m of E-side-down separation across the entire Santa Isabel and Cuervo Negro fault systems. The elevation difference of outcrops of  $Tmr_{sf}$  ( $12.7 \pm 0.6$  Ma) between these two areas also suggests about 500 m separation, notably indicating that most, if not all, ENE-directed extension is post-6 Ma. These parallel fault systems, which preserve the thickest and oldest lithologic units (Group 2 and 3) of the area at relatively high elevations in their footwalls, are interpreted to accommodate a significant portion of Gulf extension at this latitude (discussed further below). A gentle westward dip of some of the units along the northern margin of the field area suggests that a listric geometry at depth is possible.

Additional post-6 Ma faults are interpreted here to be secondary to the Cuervo Negro and Santa Isabel faults on the basis of discontinuous outcrop patterns, smaller amounts of apparent normal offset, and the incipient nature of smaller, sub-parallel structures. These faults are closely-spaced (every 1-2 km) and strike NNE to NNW. All of these faults are in the hanging wall (to the east) of the Santa Isabel and Cuervo Negro fault systems and show both synthetic and antithetic dips. Many of them have an arcuate outcrop pattern.

A maximum of 4% E- to ENE-directed extension is accommodated across all extensional structures mapped in Santa Isabel Wash. None of these faults were traced into the youngest andesite and rhyolite lava flows (Group 7) at the northeast and southeast corners of the area; however, the 6 Ma age of these lavas suggests that they were deposited prior to the “post-6 Ma” deformation described here (which, as discussed below, is perhaps “post-2-3 Ma” deformation). Lithologic correlation between one of the lava flows (*Tmr<sub>can</sub>*) and faulted rhyolite flows (“f4” of Stock et al., 1991; Stock, unpub. mapping) to the northeast of Picacho Canelo (see Figure 6.3) supports this sequence of events.

### *Quaternary*

Evidence for active deformation in Santa Isabel Wash includes 2-km-long linear features in the active alluvial surface interpreted to be fault scarps (indicated with more than one “s” along the scarp in Figure 6.3), sag ponds, and redirecting of modern drainages inferred to be related to extensional deformation. The Santa Isabel fault has a well-defined, E-facing scarp and appears to offset modern drainages in a sinistral sense. Both of these features confirm the sinistral oblique motion recorded in slickenlines on fault plane surfaces of the Santa Isabel fault. This is an extremely important observation because it implies that ENE-directed extension is presently continuing in the study area.

### *6.2. Comparison with adjacent areas (Southern Valle Chico, Sierra San Fermín, PVP) and relationship to Matomí accommodation zone*

An accommodation, or transfer, zone is a region which separates two areas of differential extension (e.g., Bosworth, 1985) such as might form during the early, “border fault formation” phase of rifting. There may, or may not, be a change in polarity (i.e., transport direction) of the border faults across such a zone. At some time after continental extension began in northeastern Baja California (11-12 Ma), a broad W- to WNW-trending transfer zone (Matomí accommodation zone) developed between two NNW-striking, E-

dipping normal faults which marked the western rift margin of the GEP (Dokka and Merriam, 1982; Stock, in press; see also bottom of Figure 6.4). One of these faults was the early San Pedro Mártir fault (Figure 6.1) to the northwest of the PVP, and the other one, less well-defined, was located to the southeast of the PVP near the present coast in the vicinity of Gonzaga Bay (Stock, in press). The cause of the apparent strike-perpendicular offset between these two structures is unknown, but may have been an original irregularity of the early to middle Miocene arc which was exploited at the time of rift margin development (Stock, in press). The location and position of some accommodation zones along other rift margins, such as in East Africa, appear to have similarly followed preexisting structural discontinuities or zones of weakness (e.g., Bosworth, 1992; Kilembe and Rosendahl, 1992; Scott et al., 1992).

A pre-6 Ma (probably 11-12 Ma) age is suggested for the initiation of the Matomí accommodation zone on the basis of 11-6 Ma faulting to the north (Stock, 1989; Lewis, 1994; Lewis and Stock, in review, *J. Struct. Geol.*) which is not observed south of this structure. The Matomí accommodation zone is made up of WNW-striking oblique-slip faults and NNW-striking normal faults at its western end in the southern Valle Chico (Stock and Hodges, 1990). It manifests itself in the Ultima Esperanza fault zone at the southeast corner of southern Valle Chico (Stock and Hodges, 1990; Stock, 1993) but has not been observed any further southeast, between the region due north of Santa Isabel Wash and the coast (see limits of Matomí accommodation zone indicated in Figure 6.2). The missing southeast segment may have been subsequently offset by younger, NE-striking sinistral faults (Stock, in press) which would place its present location somewhere in the vicinity of Arroyo Matomí. Significant disruption of 6 Ma pyroclastic flow deposits immediately south of Arroyo Matomí (Gastil et al., 1975; Stock et al., 1991), if related to the Matomí accommodation zone, would imply that motion along the zone has occurred since 6 Ma. There is no evidence of disruption of 3 Ma pyroclastic flow deposits in the eastern PVP where this structure could project (e.g., Martín-Barajas et al., 1995), suggesting that motion associated with the Matomí accommodation zone is at least older than 3 Ma.



By simply projecting along the strike observed in southern Valle Chico, the Matomí accommodation zone would have passed approximately 5 km northeast of Santa Isabel Wash (prior to any later displacement by other faults). However, if the Matomí accommodation zone became significantly broad to the southeast, or if there were a step-over of this zone of transfer to the southwest, then the zone could have coincided with the pre-6 Ma topographic break found in the northern part of Santa Isabel Wash interpreted to have accommodated pre-6 Ma NE-side-down displacement. This idea will be expanded upon below.

Oblique rifting occurs when the trend of a rift zone at a plate boundary is at an angle to the relative displacement direction, and as a consequence rift formation is the product of extension perpendicular to the rift trend and shear parallel to this trend (Withjack and Jamison, 1986). The relative amount of each component depends upon the acute angle ( $\alpha$ ) between the trend of the rift zone, which might be dictated by some pre-existing zone of weakness, and the displacement direction. Withjack and Jamison (1986) derived an analytical model based upon oblique rifting experiments using clay over a metal base and metal sheet and simulating extension for various values of  $\alpha$ .

Fault trends predicted by analytical and experimental rifting models for various values of  $\alpha$  show good agreement with the orientation of normal and strike-slip faults along the margins of the Gulf of California (Withjack and Jamison, 1986). In general these predicted and observed fault orientations include N-S-striking normal faults, NW-SE-striking dextral strike-slip faults, and NE-SW-striking sinistral strike-slip faults. Withjack and Jamison (1986) naturally assigned the extension direction to be parallel to PAC-NAM plate motion, which they determined from Gulf of California transform fault azimuths. At least in northeastern Baja California, however, it is clear that NE- to ENE-directed extension has occurred since 11-12 Ma and appears to be continuing today (e.g., Stock, 1989; Lewis, 1994; Lewis and Stock, in review in *J. Struct. Geol.*; this study). Thus, an application of their model assuming ENE-directed extension is used here to see what orientations of structures accommodating extension would be predicted given the apparent orientation (W- to WNW-trending) of the zone of weakness which separated the two orthogonal segments of the rift margin described above (and developed into the NW-striking Matomí accommodation zone).

Although the transfer zone is significantly smaller than plate boundaries modeled by oblique rifting experiments, the models should apply equally well at smaller scales.

The results are shown in Figure 6.4a. If the zone of weakness originally trended WNW-ESE, as suggested by its present-day orientation in southern Valle Chico, the angle  $\alpha$  between it and the extension direction would be  $60^\circ$ . In this case the oblique extension model of Withjack and Jamison (1986) predicts normal faults with strikes oriented  $15^\circ$  CW of the zone of weakness (i.e., NW-SE). This is in excellent agreement with the orientation of the pre-6 Ma topographic break in Santa Isabel Wash. Variations on these oblique extension experiments have been performed using a dry sand medium over plastic and rubber sheets (McClay and White, 1995) and sand over a layer of silicone (Tron and Brun, 1991). For values of  $\alpha$  equal to  $60^\circ$ , both of these studies generally found a similar orientation of normal faults to those determined by Withjack and Jamison (1986).

Given the present-day E-W-trending zone (roughly coinciding with the position of Arroyo Matomí) which separates the northern region of higher extension from the less extended region to the south, it is plausible that the orientation of the zone of weakness which led to the Matomí accommodation zone was originally oriented E-W. If this were the case (Figure 6.4b),  $\alpha$  would equal  $30^\circ$  (given ENE-extension) and the model of Withjack and Jamison (1986) would predict normal faults with strikes oriented  $30^\circ$  CW of the zone (i.e., WNW-ESE). In addition, sinistral strike-slip faults with strikes oriented  $60^\circ$  CW of the zone (i.e., NNW-SSE) are also predicted when  $\alpha$  equals  $30^\circ$ . The model of Tron and Brun (1991) found similar results including a partitioning between oblique dip-slip and strike-slip. The model of McClay and White (1995) did not test  $\alpha$  equal to  $30^\circ$ .

If the late Miocene extension direction in northeastern Baja California were in fact NE-directed (rather than ENE-directed), the model of Withjack and Jamison (1986) would predict the following: for a WNW-trending zone of weakness ( $\alpha = 75^\circ$ ), only normal faults striking  $8^\circ$  CW of the deforming zone (i.e., N $52^\circ$ W) should form, while for an E-trending zone of weakness ( $\alpha = 45^\circ$ ), only normal faults striking  $23^\circ$  CW of the deforming zone (i.e., N $67^\circ$ W) should form. These orientations are in poorer agreement with features in Santa Isabel Wash than those predicted by assuming ENE-directed extension.

The orientation of the structures in Santa Isabel Wash which potentially represent the continuation of the Matomí accommodation zone is in general agreement with those found in southern Valle Chico (WNW-striking oblique-slip faults and NNW-striking normal faults) (Stock and Hodges, 1989; Stock, 1993). If the structures in Santa Isabel Wash are indeed related to the Matomí accommodation zone, results from this study confirm that the zone was not only a pre-3 Ma feature, but in fact a pre-6 Ma feature, bounded to the south by NW-striking faults which showed a significant component of N- to NE-side-down displacement. Pure dip-slip would imply NE extension, whereas dextral oblique-slip along these structures would suggest ENE-directed extension. The relationship between these structures and the ones associated with the Matomí accommodation zone in southern Valle Chico could be explained in one of two ways. If the structures are continuous, the entire Matomí accommodation zone would have been fairly broad east of southern Valle Chico (around 5 km wide). An alternative interpretation is that the Matomí accommodation zone remained relatively narrow, such as seen in southern Valle Chico where the zone is about 2 km wide, but formed an *en-echelon* surface pattern thereby stepping southward into Santa Isabel Wash at A' in Figure 6.2. This case is especially appealing because if dextral oblique-slip motion occurred on these structures, a step-over to the south would open a basin at the location of the roughly circular, 40 km<sup>2</sup> alluvial plain presently located north of Santa Isabel Wash. This scenario is shown in Figure 6.5; the basin which could have developed in such a step-over is labeled "B." A Quaternary fault inferred from a NNE-striking scarp along the southeast side of this alluvial plain (discussed in Chapter IV) could also provide a possible mechanism for partial opening of this basin depending upon the sense of motion along it, which at this time is unknown.

Because the Santa Isabel fault system in Santa Isabel Wash trends N-S to NNW-SSE and exhibits a component of sinistral oblique-slip, it is tempting to attribute the origin of this structure to the obliquity between extension direction and an original E-W-trending zone of weakness as discussed above for the formation of the Matomí accommodation zone. In fact, given the persistence of ENE-directed extension documented in Santa Isabel Wash after 6 Ma, this could have occurred after 6 Ma as well, as long as the E-W-trending zone of weakness

continued to influence the orientation of structures accommodating deformation. Present-day motion along the Santa Isabel fault appears to be primarily dip-slip on the basis of slickenline orientations, however the fault may have initially (pre-6 Ma?) developed as a structure accommodating a more significant sinistral component of motion. This scenario is extremely speculative, and, as described below, the preferred interpretation is that the Santa Isabel fault developed primarily as an E-dipping, post-6 Ma (and perhaps post-3 Ma) structure whose small component of sinistral oblique-slip is the result of present-day ENE-directed extension.

The style and amount of post-6 Ma deformation in Santa Isabel Wash and other portions of the PVP has clearly been different from regions to the north of the Matomí accommodation zone. Because major extensional deformation began 11-12 Ma to the east of the San Pedro Mártir fault, the amount of extension is greater and more developed to the north than in Santa Isabel Wash and the rest of the PVP. Additionally, post-3 Ma CW vertical-axis rotation of the Sierra San Fermín relative to the Sierra San Felipe (Lewis and Stock, in review in *J. Geophys. Res.*) apparently did not affect Santa Isabel Wash (Chapter V). However, the same direction of extension (ENE) appears to be recorded both north and south of the Matomí accommodation zone since 11-12 Ma. These similarities and differences are extremely important for the regional model discussed later in this Chapter.

### 6.3. *Relationship to Gulf Extensional Province and Gulf of California spreading system*

Comparison of the area studied here with portions of the PVP to the west of Santa Isabel Wash examined in previous studies (e.g., Gastil et al., 1975; Dokka and Merriam, 1982; Stock, Lewis, Salton, and Holt, unpub. mapping) suggests that the Santa Isabel and Cuervo Negro fault systems are the principal structures bounding the western edge of the Gulf Extensional Province at this latitude. Their position is about 10 km further east than the southward projection of the Main Gulf Escarpment (San Pedro Mártir fault). As described here in conjunction with the history of transform faulting in the Gulf of California, the development of the Santa Isabel and Cuervo Negro faults was probably not related to these

features in the north, but rather resulted from the Guaymas transform extending northwestward into the southern PVP region around 2-3 Ma (Stock, in press).

The relationship between the late Miocene structures developed on the margins of the GEP and those of the Pliocene/Quaternary spreading center system within the Gulf of California is ambiguous. In Axen's (1995) regional analysis of segmentation and vergence reversal of the Main Gulf Escarpment in Baja California, he assigns the entire PVP region to the role of an accommodation zone separating a footwall segment to the north from a hanging wall segment to the south. The presence of a hanging wall segment to the south of the PVP would require an underlying W-directed detachment surface, such as the one below the Sierra Juárez further north, which would perhaps reach the surface east of the present-day coastline. On the basis of the high angle between several accommodation zones (such as the one postulated to include the PVP) and the Gulf of California fracture zones, the relative ages of the accommodation zones and the Gulf of California spreading system, and the direction of early extension, Axen (1995) believes that there is little relationship between the earlier segmentation and the subsequent geometry of the Gulf of California spreading center system.

On the other hand, Stock (in press) suggests that there is a correlation between several accommodation zones in northeastern Baja California and major transform offsets in the Gulf of California. The most convincing relationship is between the pre-6 Ma Matomí accommodation zone and the (initially) along-strike Tiburón fracture zone. These two potentially continuous structures would have intersected the coast in the vicinity of the town of Puertecitos about 6 Ma (Stock, in press). If the Matomí accommodation zone does indeed pass on the north side of Santa Isabel Wash as suggested above, the position and orientation of the NW-striking structures in Santa Isabel Wash agree with this geometry. Thus if the Matomí accommodation zone and the earliest features of the Tiburón fracture zone were related, this would imply that the former, produced as a result of pre-6 Ma ENE-directed extension (see above discussion), produced a structure at its southeast end which subsequently became a strike-slip transform fault accommodating an entirely different direction of motion associated with NW-SE-directed PAC-NAM relative plate motion. If this is the case, it appears

that the geometry of at least one late Miocene extensional structure (the Matomí accommodation zone) is related to a Gulf of California fracture zone.

#### 6.4. *Relationship to PAC-NAM plate boundary*

The plate boundary in the Gulf of California is unique because it includes a region of tectonic transition between continental transform motion in the north and plate divergence in the south. The oceanic spreading system, which is presently well-developed in the mouth of the Gulf of California, is, in a sense, propagating northwards into the continental crust of the northern gulf and southern California. Greater rates of seismic slip (estimated from seismic moment data) observed in the northern versus southern Gulf of California suggest a stronger coupling of the plate boundary in the north relative to the south (Tajima and Tralli, 1992) due to the different plate boundary natures.

The plate boundary accommodating NW-SE-directed PAC-NAM relative motion (about 50 mm/yr) at the latitude of southern Baja California has been fully established within the Gulf of California since at least 3.5 Ma. This duration comes from magnetic anomalies at the mouth of the Gulf of California (north of the Tamayo fracture zone) where sea floor spreading is recorded since the time of Anomaly 2A (Larson et al., 1968; Curray and Moore, 1984; Lonsdale, 1989). This also agrees with plate reconstructions which show that most plate boundary motion was occurring within the Gulf of California by 3.5 Ma (Stock and Hodges, 1989). North of the mouth of the Gulf of California, the full relative plate motion is believed to be accommodated by the oceanic spreading center system until between 31°N and 32°N latitudes, where some of the relative plate motion is transferred westward along transpeninsular faults such as the Agua Blanca and Elsinore faults (Humphreys and Weldon, 1991). The study area discussed here is located south of this zone of westward transfer near the western edge of the Gulf of California rift margin. There are no known major, active structures to the west of the study area accommodating present-day plate motion.

A reorientation of the relative plate motion direction between about 12 and 5 Ma resulted in partitioning of plate motion accommodation between ENE-directed extension in

the Gulf of California and strike-slip faulting west of the peninsula (Atwater, 1970; Hausback, 1984; Stock and Hodges, 1989; see also discussion in Chapter I). Pre-6 Ma NE-directed extension documented in Santa Isabel Wash (this study) and other places in northeastern Baja California (Stock, 1993; Lewis, 1994; Stock and Lewis, in review, in *J. Struct. Geol.*) are in good agreement with this earlier history of deformation within the Gulf of California.

Curiously, the study area discussed here continues to record ENE-WSW-directed extension, as do the areas to the north between the study area and the Agua Blanca fault. Specifically these areas include the southern Valle Chico, which has been extending to the ENE since about 11 Ma (e.g., Stock and Hodges, 1990), and the Sierra San Fermín, which records NE- to ENE-directed late Miocene extension and Pliocene-Quaternary, ENE-directed extension (Lewis, 1994; Lewis and Stock, in review in *J. Struct. Geol.*). Post-3 Ma CW vertical-axis rotation of the Sierra San Fermín suggests that pre-3 Ma extensional structures may have in fact accommodated an extension direction oriented closer to NE (rather than ENE) prior to the rotations (Lewis and Stock, in review in *J. Struct. Geol.*). In contrast to findings in northeastern Baja California, there are several examples (discussed in Chapter I) in central and southern Baja California where the expected change in extension direction to the ESE or SE has been observed during Pliocene or Quaternary time (Angelier et al., 1981; Bryant, 1986; Zanchi, 1994; Umhoefer and Stone, 1996).

As discussed in Chapter I, there is a slight discrepancy between the direction of present-day PAC-NAM relative plate motion calculated by plate motion models (about 325° whether calculated over the last 3 Ma (DeMets et al., 1990, 1994) or 6 Ma (Minster and Jordan, 1978)) and the orientation of transform faults in the Gulf of California (300°-310°). Earthquake slip vector azimuths recorded along the transform faults (303°-312°) (Goff et al., 1987) are in good agreement with the major bathymetric trends. Stock and Hodges (1989) calculate a PAC-NAM relative plate motion on the basis of plate reconstructions for Baja California for post-5.5 Ma time which is approximately parallel to the 303°-317° ( $\pm 20^\circ$ ) direction determined for the time interval 20-10.6 Ma (see Figure 1.3 in Chapter I), and this also agrees with transform fault orientations. In yet a different study, CCW rotation since 3.5 Ma of the PAC-NAM relative plate motion is interpreted to be the cause of transform fault

reorientations, spreading center break-ups, and the abandonment of old spreading centers and the creation of new ones (Lonsdale, 1989).

How does E- to NE-directed extension in northeastern Baja California fit into the NW-SE-directed relative plate motion between PAC and NAM? One possibility is partitioning of motion between strike-slip and normal faulting (e.g., in a manner analogous to the 12-5 Ma partitioning of the PAC-NAM plate boundary between strike-slip structures west of Baja California and extensional structures east of Baja California (Stock and Hodges, 1989)). Regardless of whether the present-day relative PAC-NAM plate motion is oriented closer to  $300^\circ$  or  $325^\circ$ , the ENE-directed extension recorded in northeastern Baja California is unusual. If ENE-directed extension does indeed accommodate a component of the present-day PAC-NAM plate boundary motion, some other major structure is clearly required to accommodate the rest of the motion. The vector diagram in Figure 6.6a shows the relative PAC-NAM plate motion of 50 mm/yr oriented at  $325^\circ$ . If a component of this plate motion is accommodated by E- to ENE-directed extension in northeastern Baja California (illustrated here at a rate of approximately 10 mm/yr), the remaining motion which needs to be accommodated is about 45 mm/yr oriented slightly more northerly than the actual plate motion vector. This remaining motion could be accommodated in a number of ways (Figure 6.6b). The upper part of Figure 6.6b illustrates how a dextral strike-slip fault striking parallel to the vector could accommodate the motion. Alternatively, accommodation could be partitioned between a combination of, for example, a N-striking dextral strike-slip fault and other dextral strike-slip faults striking NNW to WNW (lower part of Figure 6.6b). Alternatively, a combination of strike-slip and dip-slip (i.e., oblique-slip) along any of these faults would also be a geometrically acceptable solution.

The orientations of potential transform faults and basins at this latitude in the northern Gulf of California are not well known due to rapid sedimentation from the Colorado River which obliterates many features. However, bathymetric contours in this part of the Gulf of California (Figure 6.7 after Dauphin and Ness, 1991), which generally parallel the NW-striking transform faults south of latitude  $30^\circ\text{N}$ , do in fact change to a more northerly trend between latitudes  $30^\circ\text{N}$  and  $31^\circ30'\text{N}$ . This change is paralleled by a similar change in the



orientation of the coastline. Geologic maps (e.g., Fenby and Gastil, 1989) generally interpret this region to contain a N-S-trending spreading center linking the Wagner basin southward to the Consag basin and then intersecting the northwest edge of the Upper Delfín Basin in a poorly defined manner, perhaps across a short transfer fault (as represented in Figure 1.1 of Chapter I). Alternatively, the N-S-trending contours between latitudes 30°N and 31°30'N could in fact mark the position of an anomalously oriented transform fault accommodating dextral strike-slip motion, thereby providing a possible structure for accommodating PAC-NAM relative plate motion partitioned with E- to ENE-directed extension. Possible accommodating structures which include a N-striking dextral strike-slip fault were shown in the lower part of Figure 6.6b. This hypothesis, which suggests that the Wagner basin might actually be the “Wagner transform,” is included in the following model of the evolving PAC-NAM plate boundary along the entire Baja California peninsula.

The rate of extension in northeastern Baja California is poorly known, and the extension rate assumed in Figure 6.6a (10 mm/yr) may be unreasonably high given present-day observations. Several factors could lower the inferred extension rate (i.e., shorten the vector in Figure 6.6a). For example, E-directed extension rather than ENE-directed extension would give a lower extension rate. If the “Wagner transform” actually strikes NNW rather than N, this would also make the extensional component smaller. If the “Wagner transform” is indeed a reactivated normal fault, it may not be vertical and may accommodate oblique-slip. If it were an E-dipping structure, this, too, would lower the amount of plate boundary motion partitioned onto extensional structures in northeastern Baja California.

Earthquake focal mechanisms for 13 earthquakes recorded in the northern Gulf of California (between 1977 and 1994) with  $M_w$  between 5.0 and 6.0 are shown in Figure 6.8. Unfortunately, most of these did not occur within the WTZ and thus cannot be used to support or refute the proposed model. The fault plane solutions shown in Figure 6.8 fall into three categories. Focal mechanisms shown in blue imply the presence of either NW-striking dextral or NE-striking sinistral strike-slip faults, while those in red represent either NNW-striking dextral or ENE-striking sinistral strike-slip faults. Two anomalous focal mechanisms are shown in green. Earthquakes depicted with the blue focal mechanisms are in good

agreement with stresses associated with the PAC-NAM relative plate motion direction and with azimuths of Gulf of California transform faults; most of these are interpreted to be NW-striking dextral strike-slip faults. One of these earthquakes is located in the north-central Gulf of California within the WTZ just west of the region known as the Wagner basin (or “transform”, as suggested here). If the earthquakes associated with the red focal mechanisms occurred along NNW-striking dextral strike-slip fault planes, this would be in agreement with the above discussions regarding reactivation of remnant fault planes formed during late Miocene ENE-directed extension; however, these events occur outside of the WTZ. Within the limits of the WTZ there is an event on the peninsula (represented with a green focal mechanism in Figure 6.8) which implies either SW-side-down motion (with a slight sinistral component) on a steep, NW-striking fault, or a shallowly dipping (to the NW) NE-striking fault exhibiting dextral oblique-slip motion. Motion along either of these fault planes contrasts with inferred fault motion mapped in that vicinity (Sierra San Fermín) where most documented faults are ENE-striking, dip-slip and strike-slip faults with components of sinistral motion (e.g., Ironwood Canyon or El Coloradito fault zones of Lewis and Stock, in review, J. Struct. Geol.).

#### *6.5. Model to explain present-day ENE-directed extension in northeastern Baja California, Mexico*

A six stage model of plate boundary structures accommodating relative PAC-NAM along the Baja California peninsula is sketched in Figure 6.9. These cartoons are intended to summarize the timing and orientation of various structures in a general way, but above all provide a mechanism to explain present-day ENE-directed extension observed in northeastern Baja California in this study and others outlined above. Features at six different times between 20 Ma and the present are shown on maps of the present-day coastline for simplicity, but ideally the extension which has opened the Gulf of California should be removed. Since only features on the Baja California peninsula and within the Gulf of California are discussed, the relative position of the Mexican coastline is somewhat irrelevant

to this discussion. A more rigorous analysis is envisioned in the near future. Each sketch shows the relative PAC-NAM plate direction for the associated time interval as determined by Stock and Hodges (1989). Other references used for various features such as fault orientations and timing throughout the model include Humphreys and Weldon (1991), Lonsdale (1991), Stock and Lee (1994), and Stock (in press). Labels are assigned to various features and explained in the figure caption.

*Stage I.* Until about 20 Ma subduction of the Guadalupe plate beneath NAM occurred west of Baja California (e.g., Atwater, 1970). Relative PAC-NAM plate motion was oriented approximately  $325^\circ$ .

*Stage II.* The Rivera triple junction migrated southward replacing the subducting boundary with a dextral strike-slip zone. This change occurred approximately 20 Ma west of northern Baja California and moved southward until at 13 Ma the triple junction was located west of the central portion of the peninsula (Stock and Lee, 1994). Relative PAC-NAM plate motion remained oriented approximately  $325^\circ$ , parallel to the developing offshore dextral transform fault.

*Stage III.* Subduction ceased simultaneously along the southern half of the Baja California peninsula between 12 and 10 Ma as a result of cessation of spreading between the PAC and Guadalupe plates. At this time, relative PAC-NAM plate motion rotated CCW to approximately  $300^\circ$ , oblique to the San Benito and Tosco-Abreojos transform faults west of Baja California. As a result, plate motion was partitioned between these transform faults and ENE-directed extension, which apparently localized along the thermally weakened, subduction-related arc located in the position of the present-day Gulf of California. NNW-striking normal faults exhibiting pure dip-slip would be the most likely candidates to develop in the absence of pre-existing structures which might dictate structural trends. The San Pedro Mártir fault developed at this time (e.g., Stock, 1989), as probably did the NW-striking Matomí accommodation zone at its southern end (Stock, in press). Middle to late Miocene marine deposits found in the northern and central Gulf of California suggest that extension formed a significant depression in this region (Stock et al., 1996a).

*Stage IV.* Between 10 and 4 Ma several changes occurred. New structures were beginning to form and overprint old structures in an attempt to accommodate the change in plate motion which began during *Stage III* (10-12 Ma). Baja California was in the process of being transferred from the NAM plate to the PAC plate. The transform faults to the west of Baja California were still active but probably accommodated a smaller and smaller portion of the relative plate motion with time as the plate boundary gradually shifted eastward into the Gulf of California. Newly oriented structures nascent to the Gulf of California spreading system began to develop within the central and southern Gulf of California region, including a zone of strike-slip motion (the future Tiburón transform fault) separating Isla Tiburón from Isla Angel de la Guarda. This zone, as discussed above, may have been associated with the pre-6 Ma Matomí accommodation zone. In southern California and northernmost Baja California, faults associated with the modern San Andreas Fault system, including transpeninsular faults such as the Agua Blanca and Elsinore faults, became increasingly active (Humphreys and Weldon, 1991).

It is suggested here that a previously unrecognized zone of structures obliquely oriented to PAC-NAM motion (which was probably in the process of changing to its post-4 Ma orientation of  $325^\circ$ ) existed between the developing Gulf of California spreading center system to the south and the continental transform system to the north. This zone is named here the Wagner transition zone (WTZ). The orientation of the boundaries of the WTZ are drawn with dashed lines approximately perpendicular to PAC-NAM relative plate motion. This orientation was chosen for convenience because, ideally, offsets along structures accommodating plate motion can be summed across any zone perpendicular to the plate motion direction and should consistently yield the same amount of relative motion. The WTZ includes the portion of northeastern Baja California north of (and including) the PVP but south of the eastward projection of the Agua Blanca fault, and the portion of the Gulf of California sea floor which contains the Wagner and Consag basins.

As described above, the present-day N-S trends in the bathymetry in the northernmost Gulf of California suggest a structure oriented obliquely from other transform faults (and inferred spreading centers) both to the north (i.e., Cerro Prieto fault; see Stage V) and to the

south (i.e., Tiburón transform fault). The crucial assumption for the model described here is that this structure is a N- to NNW-striking dextral strike-slip (or oblique-slip) fault, and not a basin (i.e., incipient spreading center) as commonly inferred.

This hypothetical NNW-striking fault, striking sub-parallel to San Pedro Mártir fault, may have developed during earlier (late Miocene) ENE-directed extension. At some point during the transfer of plate boundary motion onto structures located exclusively in the Gulf of California, this structure became reactivated as a dextral strike-slip fault. As described above, motion along such a structure in conjunction with E- to ENE-directed extension could accommodate the WNW-directed PAC-NAM plate motion. This suggests that the 150-200 km wide WTZ in northeastern Baja California might be an important example of a transitional region linking an oceanic spreading system propagating into continental crust.

A zone of divergence is geometrically created along the southeast margin of the WTZ as illustrated in Figure 6.10 (panel "2"). The pulse of effusive 6 Ma volcanism preserved in the PVP and nearby regions could be related to the development of this zone. The orientation of a basin which might result from this divergence, shown here with the long axis oriented perpendicular to the relative plate motion direction, is a direct consequence of choosing the WTZ boundaries to be perpendicular to that same motion. The position and timing of development of this basin agrees with a nascent spreading center (Upper Tiburón Basin) in a 6 Ma reconstruction of the region adjacent to the PVP (Stock, in press).

*Stage V.* A principal change which occurred by 3-2 Ma is shown in Figure 6.10 (panels "3" and "4"). Prior to 3 Ma the Upper Tiburón Basin experienced seafloor spreading which resulted in southeastward displacement of the axis away from the WTZ along the Tiburón fracture zone. At 3 Ma this spreading center became extinct and was replaced by a new one to the northwest (the Upper Delfín Basin), again forming at the zone of divergence on the southeast margin of the WTZ (panel "4" in Figure 6.10). The time it took for this change to occur may have been a function of the rate at which seafloor spreading formed new oceanic floor relative to the rate of overall ENE-extension in the WTZ. Again divergence was probably associated with the eruption of 3 Ma tuffs in the eastern PVP.

At this time the Guaymas transform fault system, just south of the Tiburón fracture zone, propagated to the northwest in response to a westward spreading center jump which formed between Isla Angel de la Guarda and the eastern margin of the PVP (Stock, in press). The new northwest portion of the Guaymas transform intersected the coast at the southern limit of the PVP. This basically created a new position (further westward) for the western edge of the rift system, thereby exposing the PVP region to the same ENE-directed extension that had been occurring to the north since 11-12 Ma. In other words, the PVP was now within the WTZ. Major deformation in Santa Isabel Wash undoubtedly began at this time. The new position of the rift margin also caused an increase in the length of the western edge of the WTZ, and thus may have localized the divergence which created the Lower Delfín Basin (panel "5" in Figure 6.10).

*Stage VI.* As described above, the extension which began to separate Isla Angel de la Guarda from the eastern margin of the PVP during *Stage V* developed into a spreading center (Lower Delfín Basin) by 2 Ma. The spreading center became continuous with the spreading zone to the north of Tiburón fracture zone (Upper Delfín Basin) which had developed in the zone of divergence at 3 Ma. The combined spreading centers formed the continuous Delfín Basin which would later become offset again into the Upper and Lower Delfín Basins. Not surprisingly, the  $2.6 \pm 0.1$  Ma Volcan Prieto is located at the intersection of the Guaymas transform and the zone of divergence of the WTZ (Figures 6.9 and panel "6" in Figure 6.10).

This model explains several puzzling features in the northern Gulf of California. The longer history of extension (which continues today) in the WTZ relative to regions to the south can explain why the northernmost Gulf of California is slightly wider (in a NE-SW direction) than the central and southern Gulf of California. The NNW-striking orientation of late Miocene extensional structures which have not yet been overprinted in the WTZ by new structures dictates the geometry of the present coastline north of 30°N as well as the orientation of bathymetric trends in the northern Gulf of California. As inferred above, the coastline south of PVP is related to the presence and orientation of the Guaymas transform

fault. The intersection of these two very different zone of deformation meet and are reflected in the jog in the coastline at the PVP.

#### *6.6. Implications for the propagation of oceanic rifts into continents*

Similar accommodation of plate boundary motion along preexisting structures may have occurred in regions to the south of the WTZ at various times between 12 and 6 Ma prior to the establishment of the Gulf of California spreading center system. In other words, during the earliest phases of plate boundary establishment within the Gulf of California, relative PAC-NAM plate motion was likely to be accommodated initially onto pre-existing structures reactivated in a favorable sense. Within zones (oriented perpendicular to the component of plate motion direction accommodated in the Gulf of California) of NNW-striking normal faults (e.g., Stage III in Figure 6.9), the plate motion may have been partitioned between continued ENE-directed extension along some structures and dextral oblique-slip along others. Perhaps the faults which dipped closest to vertical were most favorably oriented for the strike-slip component, and the extensional component remained partitioned along shallower structures. As plate motion continued to be accommodated along pre-existing structures, extension matured in conjunction with continued basin subsidence until thinning of the continental crust produced a zone weak enough for newly oriented structures to cut through the pre-existing ones. Middle to late Miocene extensional structures may have thus been gradually overprinted with a new, favorably-oriented system of oceanic transform faults and spreading centers.

In this manner the rift may have propagated northward through continental crust over time by overprinting unfavorably-oriented structures with a favorably-oriented oceanic spreading center system in places where ENE-directed extension had sufficiently thinned the crust. However, it is possible that instead of gradually unzipping Baja California (south to north) from mainland Mexico, the oceanic rift may have developed simultaneously along the entire zone weakened by earlier extension within the southern and central Gulf of California. The presence and position of the WTZ could be the result of thicker continental crust in this

region relative to regions further south which have already been replaced by the oceanic rift system. Regions of relatively thicker crust clearly require a more protracted period of extension relative to regions of thinner crust before they become zones which are weak enough to be overprinted. Since the Gulf of California rift is basically cutting from the edge of a continent towards the interior, it would not be surprising that longer periods of extension would be required to cut through interior sections than sections at the edge of the continent. The region identified here as the WTZ could be likewise thinned and overprinted with structures linked to the oceanic spreading center system in the future.

Many details remain to be worked out regarding this model. For example, the geometry of the boundary between the WTZ and the continental transform system in southern California and northern Baja California is unclear. Post-3 Ma CW rotation and motion along NE-striking sinistral strike-slip faults such as observed in the Sierra San Fermín (Lewis, 1994; Lewis and Stock, in press, *J. Struct. Geol.*) need to be incorporated. The model for rift development can be tested by identifying inactive, NNW-striking structures along the rift margins which may have accommodated partitioned plate boundary motion, and determining the timing and sense of offset along them. The discrete partitioning of plate motion between only two types of structures is undoubtedly an oversimplification of the complexities that might actually exist in the WTZ or similar earlier zones. However, this model offers a new explanation for several unusual features in the northern Gulf of California region and provides many testable hypotheses.

### 6.7. *Conclusions*

The informally named Santa Isabel Wash region of the northern Sierra Santa Isabel is located on the northern margin of the Puertecitos Volcanic Province in northeastern Baja California, Mexico. Detailed mapping,  $^{40}\text{Ar}/^{39}\text{Ar}$  geochronology, and paleomagnetic analysis have been used together to understand the geologic history preserved in this region since early Miocene time. Pre-6 Ma volcanic and volcanoclastic rocks are generally similar to those found in nearby areas; however, pre-6 Ma deformation is significantly different from the



regions a few km to the north. The Matomí accommodation zone separates the PVP from those northern regions, which include the entire area east of the San Pedro Mártir fault which has been extending to the ENE since 11-12 Ma. The southeastern segment of the Matomí accommodation zone may have passed through the study area as evidenced by significant pre-6 Ma NE-side-down extension.

Voluminous 6 Ma pyroclastic flow deposits in the PVP probably originated from the east in association with the development of the Gulf of California spreading center system (Stock, in press). Most of the faults in Santa Isabel Wash cut these tuffs and thus are assigned a post-6 Ma age. The most significant are located on the western margin of Santa Isabel Wash (Santa Isabel and Cuervo Negro fault systems) and exhibit as much as 500 m E-side-down displacement. On the basis of the late Miocene to Recent evolution of the nearby transform faults and spreading centers of the Gulf of California system (Stock, in press), extension along these faults, and the secondary antithetic and synthetic faults in their hanging wall, is interpreted to have begun 3-2 Ma when the Guaymas transform extended northwestward, thereby including the PVP within the rift margin. The direction of extension in Santa Isabel Wash appears to be E- to ENE-directed, similar to the region east of the San Pedro Mártir fault.

A model prompted by the need to explain present-day ENE-directed extension in this portion of northeastern Baja California (south of the Agua Blanca fault and north of, but including, the PVP) has been presented. Among other things, the model can explain the position and jumps of the Tiburón and Delfín spreading centers from 6 Ma to the present, the greater width of the northern Gulf of California relative to the central and southern Gulf of California, the bend in the modern-day coastline, the geometry and pattern of plate motion accommodation between the Agua Blanca fault and the PVP, and bathymetric features in the vicinity of the Wagner and Consag basins. It also illustrates structurally how the oceanic spreading system may have gradually moved into the Gulf of California along earlier extensional structures, and how the transition from continental rifting to oceanic rifting may have proceeded. This transition is still in progress today in a region defined here as the Wagner Transition Zone (WTZ). The WTZ separates a region to the south where PAC-NAM

relative plate motion (oriented approximately NW-SE) is fully accommodated along a simple oceanic spreading system from a region to the north where a complex system of continental transform faults accommodates the motion. Within the WTZ, the relative plate motion is accommodated on NNW-striking faults which developed during middle to late Miocene extension. In the simplest scenario, the plate motion is partitioned between dip-slip faults accommodating ENE-directed extension and one or more N- to NNW-striking dextral strike-slip (oblique-slip?) faults (the “Wagner transform”?) located below the northernmost Gulf of California in the vicinity of the Wagner and Consag basins.

Figure 6.1. Simplified geologic map illustrating the abrupt southward termination of the San Pedro Mártir fault at the Miocene-Pliocene PVP (southern region patterned solid grey but not including the Sierra San Fermín or other regions to the north with similar pattern). The region to the north of the PVP is relatively more extended and consists of Basin and Range-type topography. “SSFf” is Sierra San Felipe fault. (Figure modified from original provided by C. Lewis; geology after Gastil et al., 1975).

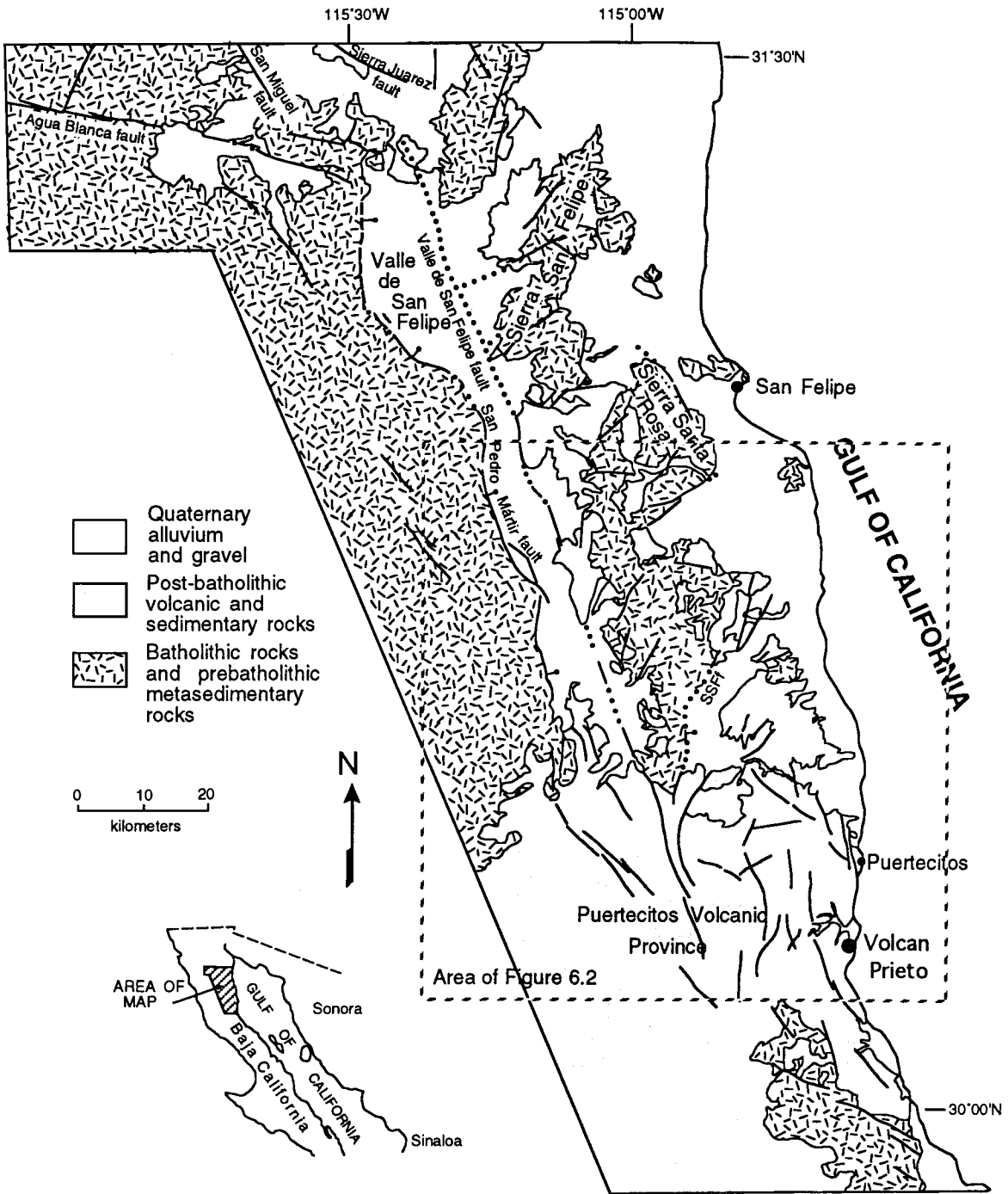


Figure 6.2. Geographic features and names in the vicinity of the study area. Quaternary alluvial deposits, and the Gulf of California, are unpatterned. See Figure 6.1 for the limits of the PVP and the locations of major faults determined from previous studies. A-A' marks the limits of the Matomí accommodation zone as interpreted by Stock (in press, 1997). In addition, Stock (in press, 1997) believes that the accommodation zone has been offset along a NE-striking, sinistral strike-slip fault near position A' and consequently might project eastwards in the vicinity of Arroyo Matomí.

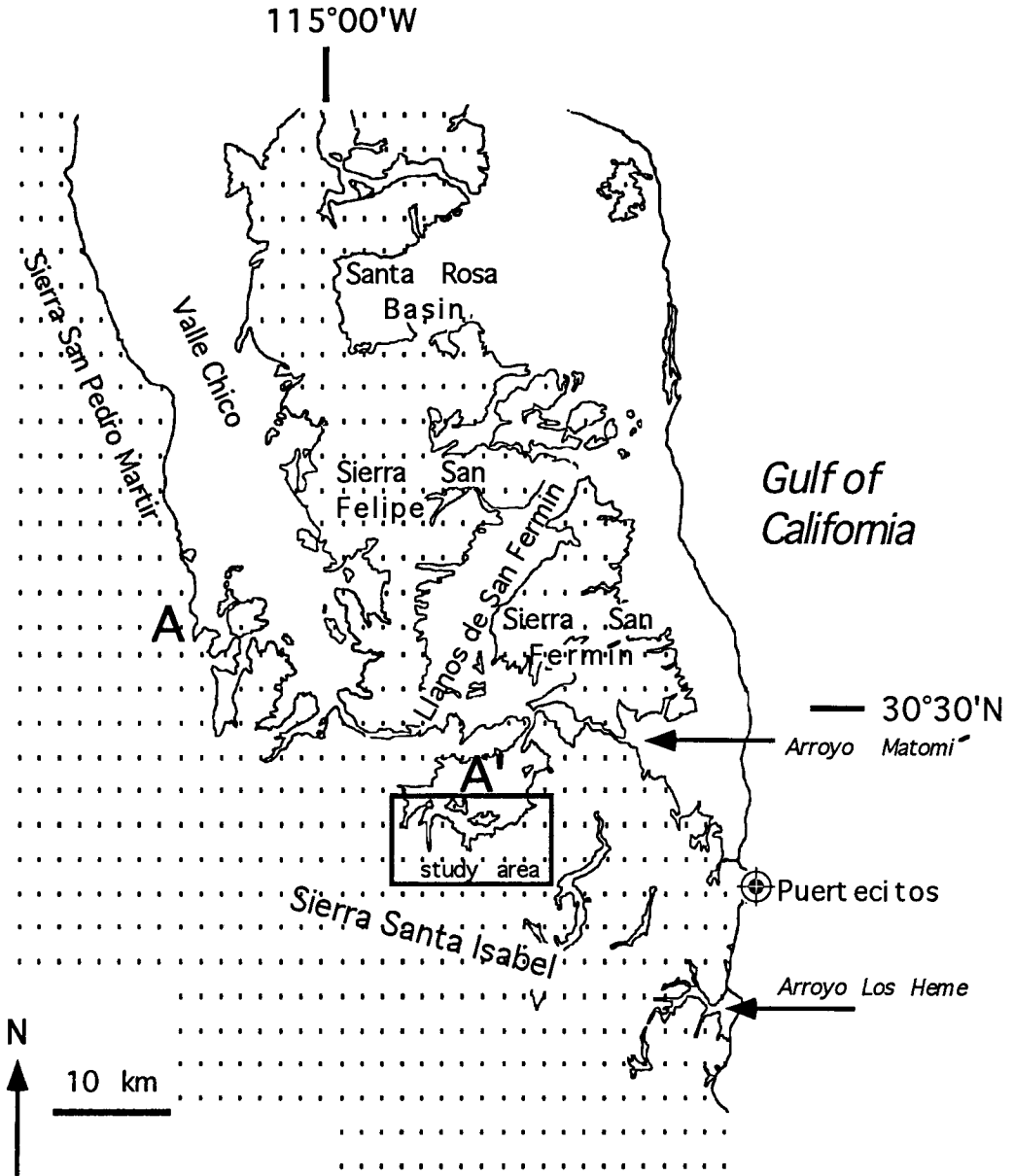


Figure 6.3. Simplified geologic map of Santa Isabel Wash in the northern Sierra Santa Isabel.

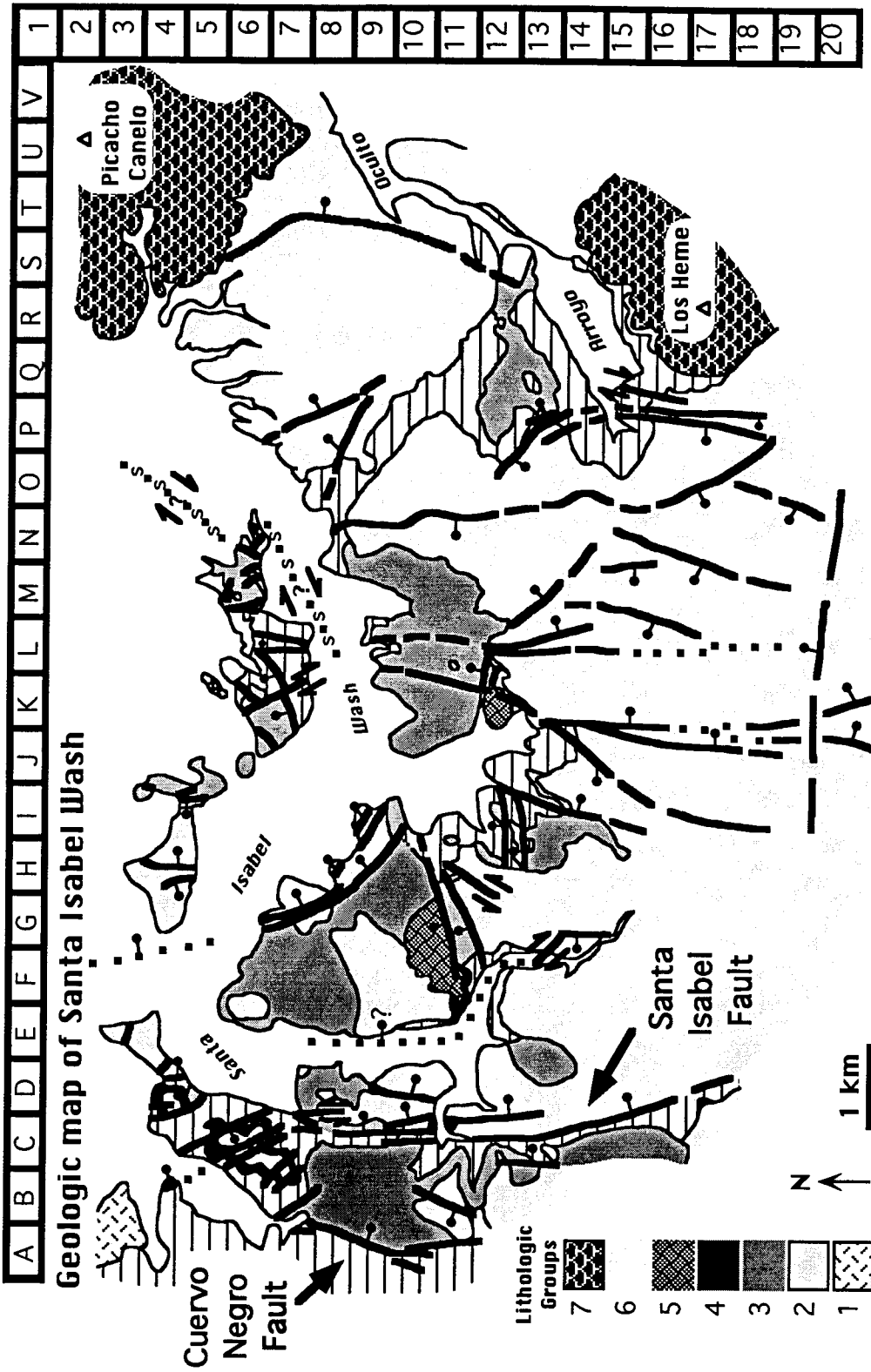




Figure 6.4. Illustration of the relationship between extension direction (assumed to be ENE-WSW) and orientation of extension-related faults given an obliquely oriented zone of weakness. Results are from the oblique rifting model of Withjack and Jamison (1986). The orientation of the “zone of weakness” (which develops into the Matomí accommodation zone) is hypothetical on the basis of an offset in the initial rift margin between the San Pedro Mártir fault (SPMF in lower box) and a sub-parallel fault to the southeast marking the rift edge at that latitude. a) A WNW-ESE-trending zone of weakness predicts normal faults oriented NW-SE. b) An E-W-trending zone of weakness predicts normal faults oriented WNW-ESE and sinistral strike-slip faults oriented NNW-SSE. Both scenarios imply that the NW-SE-trending pre-6 Ma topographic slope in Santa Isabel Wash, interpreted to be the southern boundary of the Matomí accommodation zone, is properly oriented given the late Miocene extension direction.

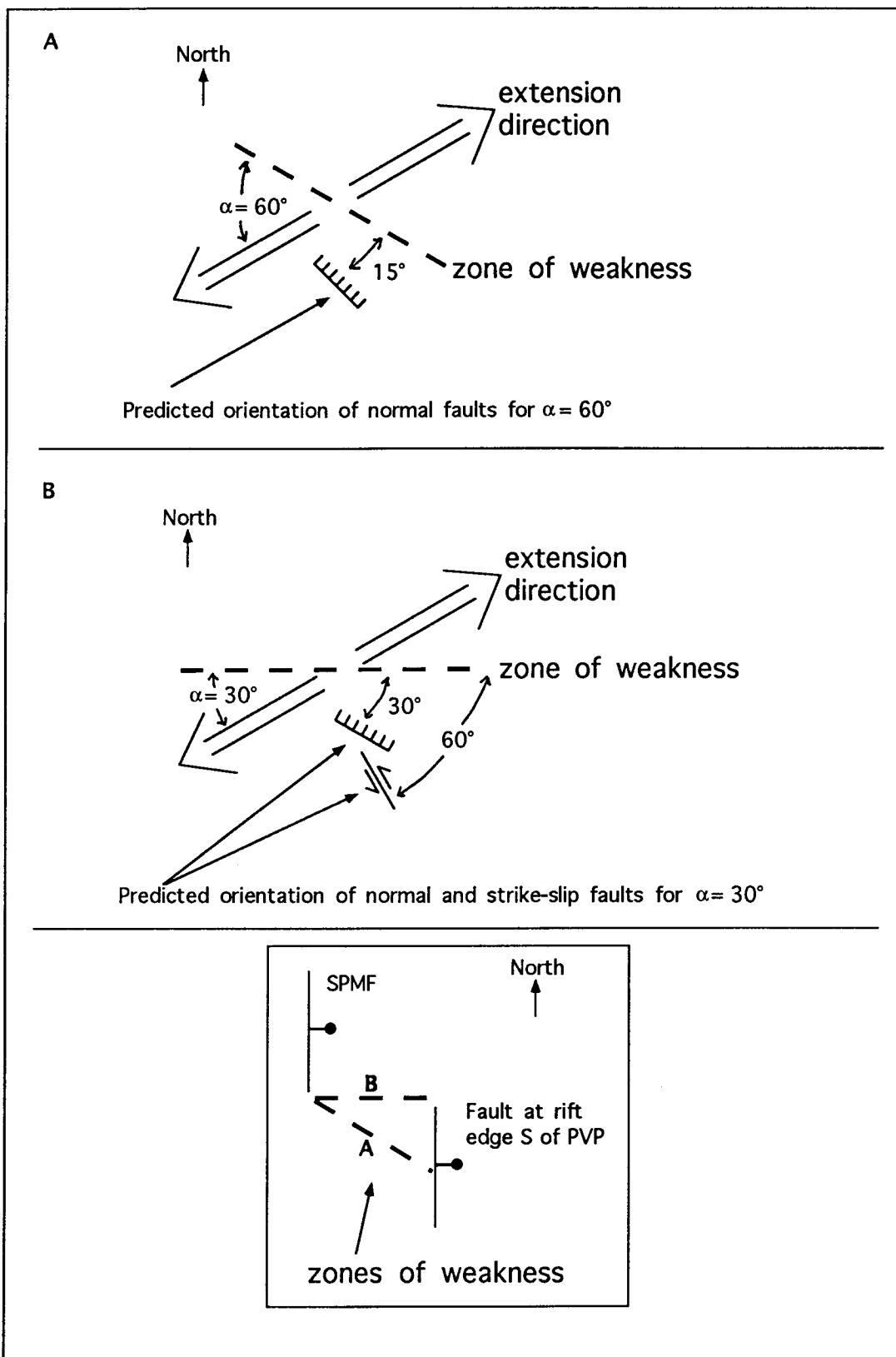


Figure 6.5. One possible scenario for the geometry of the pre-6 Ma Matomí accommodation zone. In this scenario the pre-6 Ma topographic break in Santa Isabel Wash is a continuation of the Matomí accommodation zone which has stepped-over southward from its more northerly position in southern Valle Chico (the Ultima Esperanza fault zone). The step-over creates a basin (“B”) where a large alluvial plain exists today. It is possible that the portion of the Matomí accommodation zone just east of the Ultima Esperanza fault zone has subsequently been offset to the NE along NE-striking sinistral faults such as the one shown here (just north of “B”). Movement along this fault would also enlarge the basin (“B”).

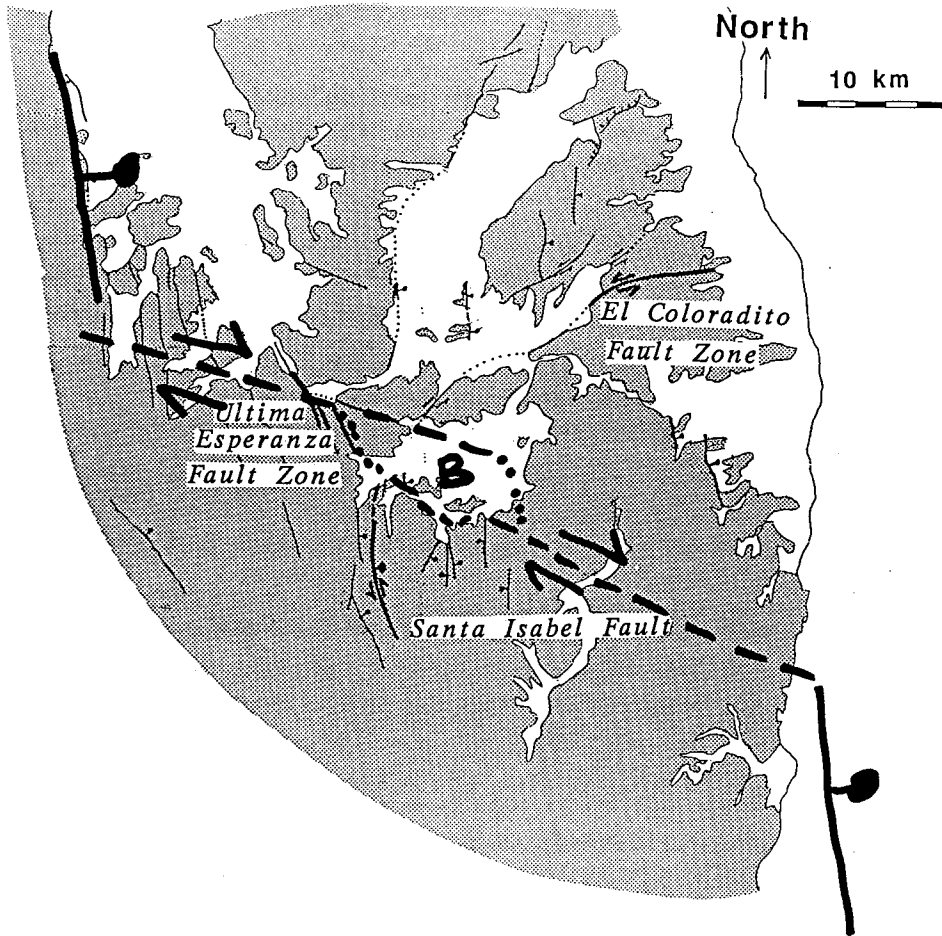
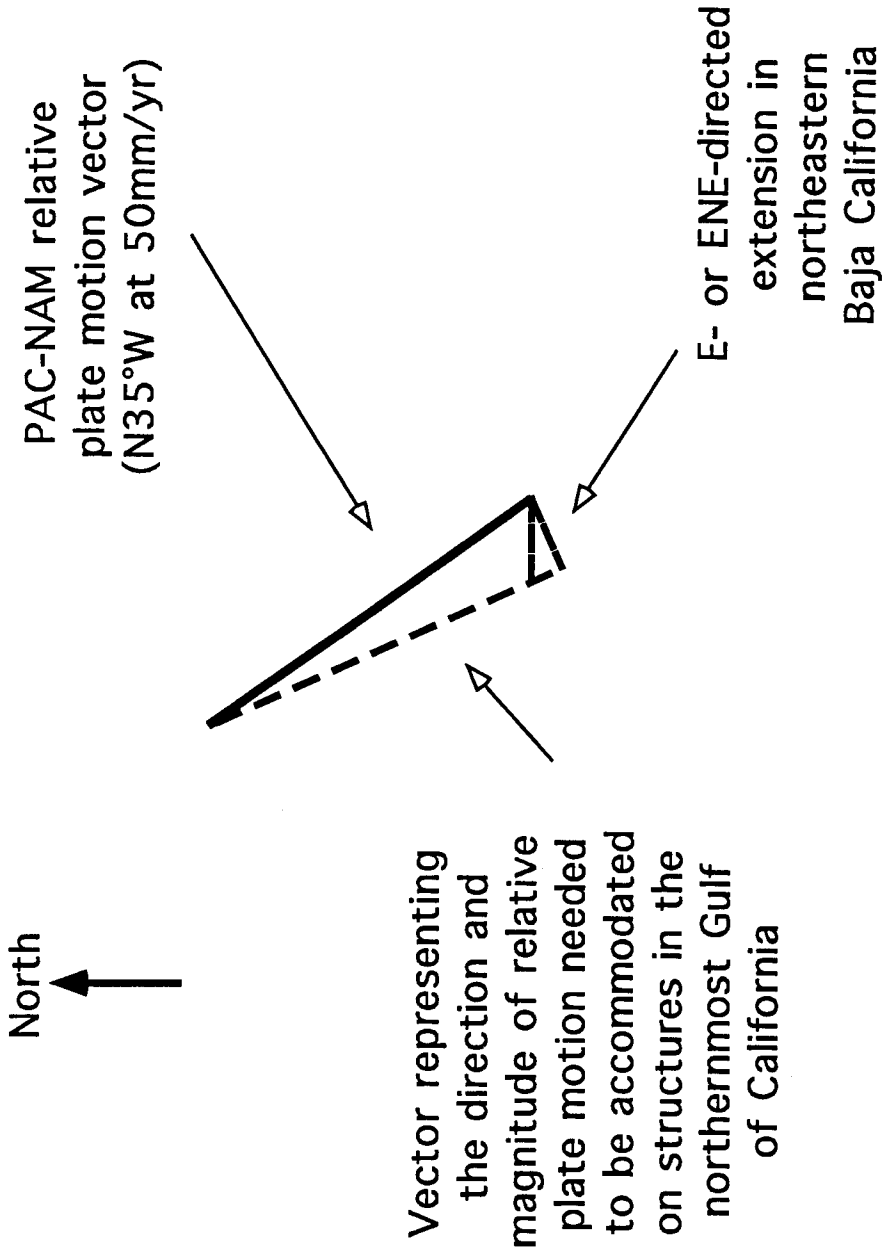


Figure 6.6. (next 2 pages) a) Vector diagram showing present-day PAC-NAM relative plate motion direction (solid line) and two possible vectors (dashed lines) which sum to the plate motion vector. One of these two vectors is chosen on the basis of E- to ENE-directed extension recorded in northeastern Baja California (illustrated here at about 10 mm/yr) while the other is the “remaining” vector required to sum to the plate motion value. b) The “remaining” vector from (a) is shown on the left with some possible fault geometries which could accommodate this motion, including a single dextral strike-slip fault striking parallel to the vector (upper part) and a combination of a N-striking dextral fault and a second dextral strike-slip fault striking more easterly (lower part). The choice of a N-striking fault is made on the basis of bathymetric contours in the northernmost Gulf of California. Oblique motion could also contribute to the accommodation scenario.



Possible structures accommodating  
PAC-NAM plate motion in the  
northernmost Gulf of California

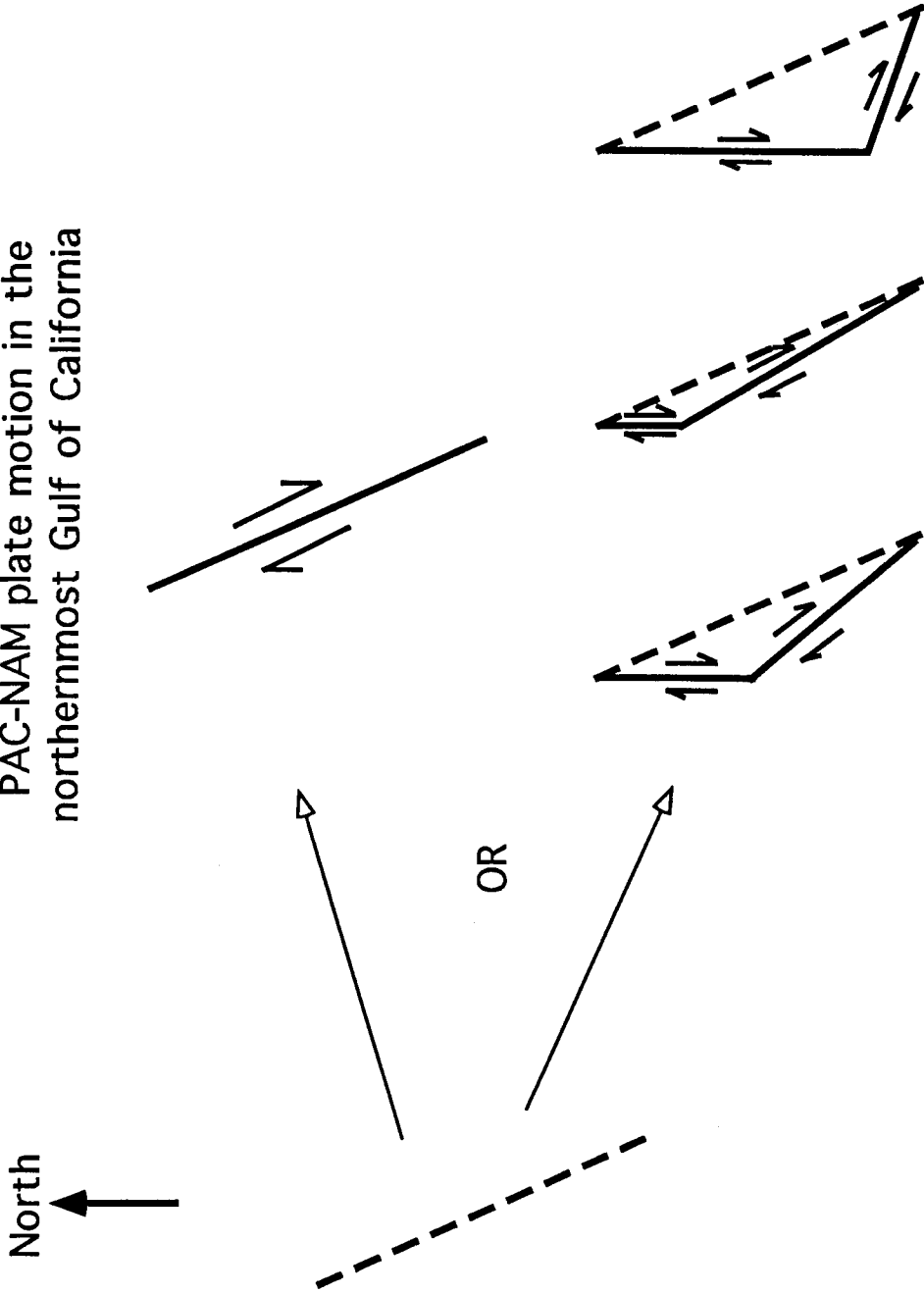


Figure 6.7. Bathymetric contours in the northernmost Gulf of California (reproduced from Dauphin and Ness (1991)). Note the bend in the coastline west of the Gulf of California at latitude 30°N, and a parallel change in the trend of bathymetry from SE-trending near Isla San Luis to N-trending between latitudes 30° and 31°30'N.



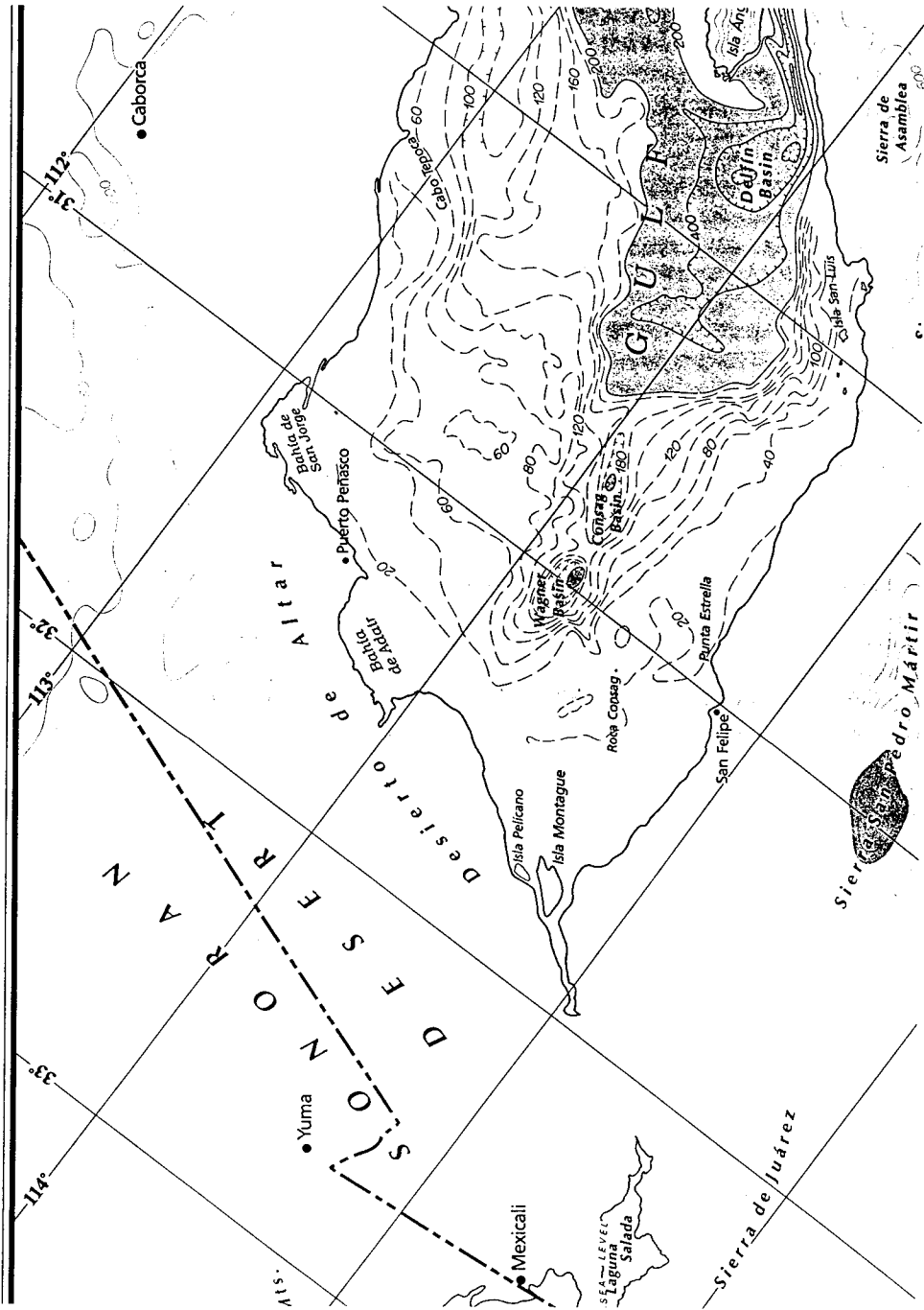


Figure 6.8. Earthquake focal mechanisms for 13 earthquakes recorded in the northern Gulf of California (between 1977 and 1994) with  $M_w$  between 5.0 and 6.0. See text for discussion.

## Focal mechanisms for Mw 5.0-6.0 in the northern Gulf of California

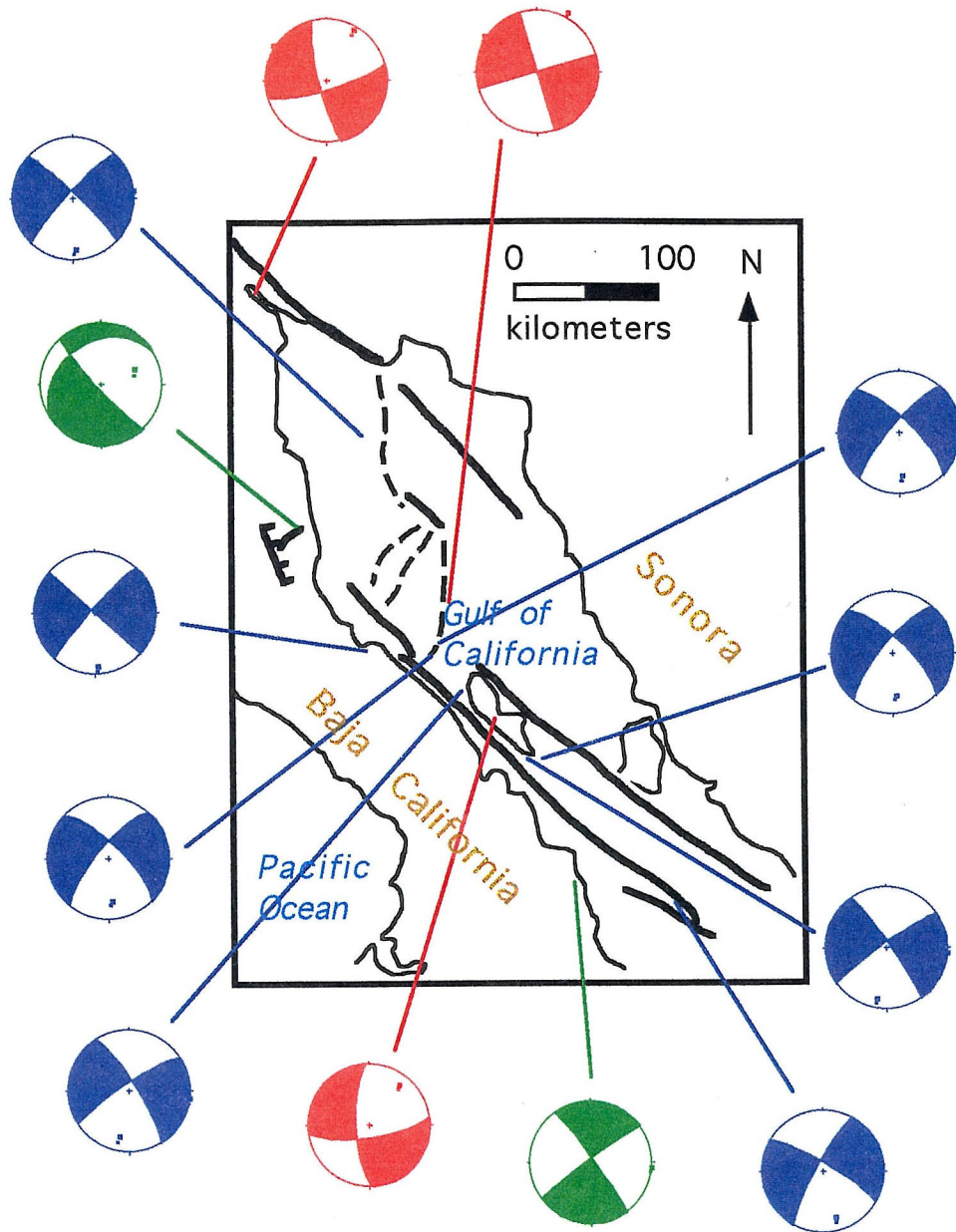
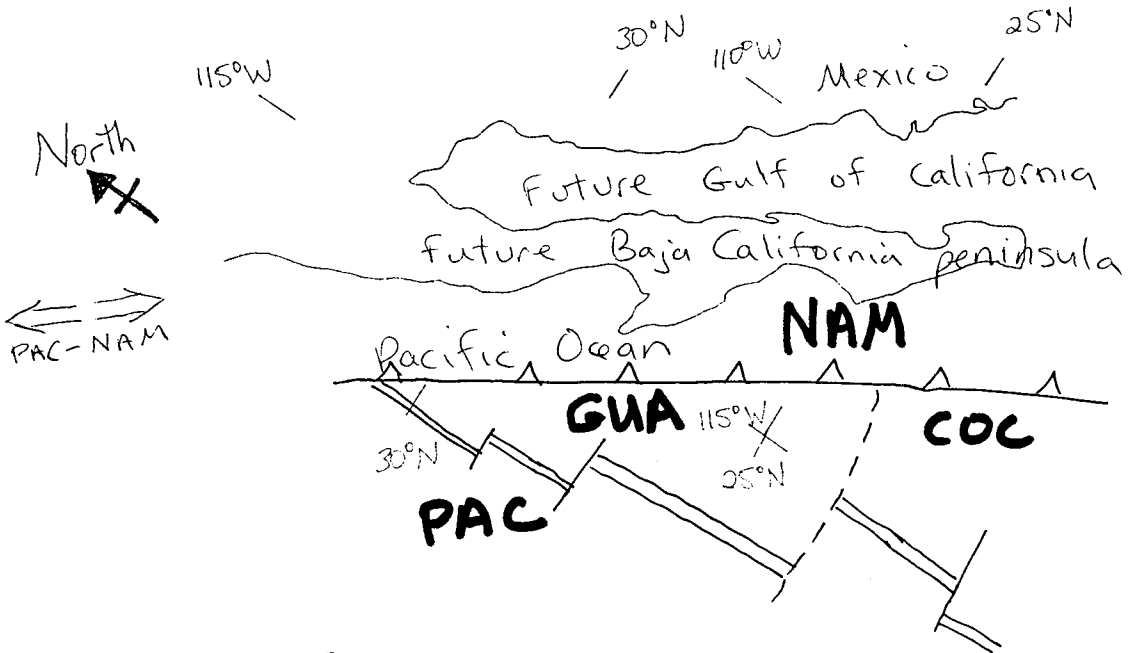
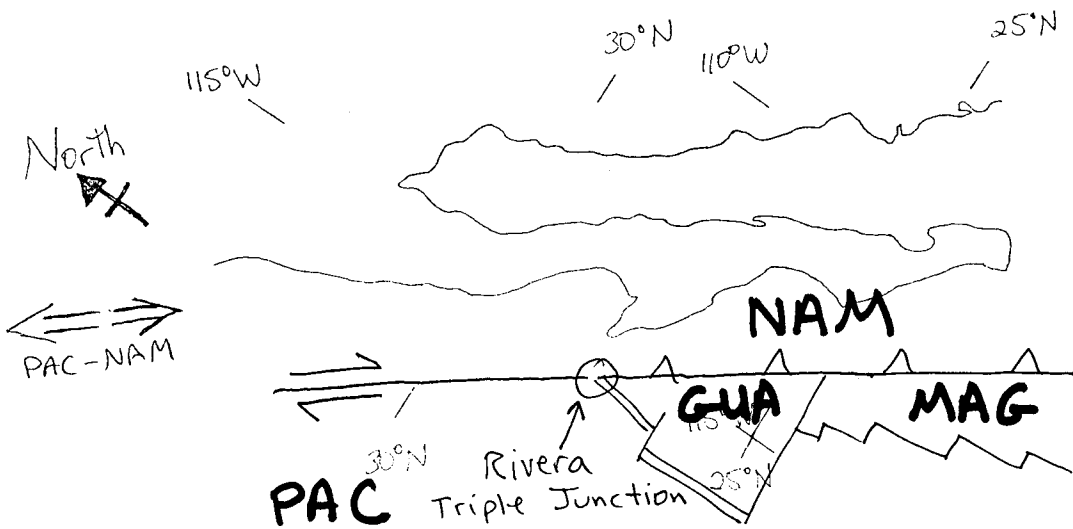


Figure 6.9. (next 3 pages) Six-stage model for the evolution of the Pacific-North American plate boundary along Baja California, Mexico, since the early Miocene. See text for discussion. Abbreviations: Plates: PAC (Pacific plate), GUA (Guadalupe plate), NAM (North American plate), COC (Cocos plate), MAG (Magdalena plate); Faults: SJZ (Sierra Juarez fault), SPM (San Pedro Mártir fault), SB (San Benito fault), TA (Tosco-Abrejos fault), SJ (San Jacinto fault), E (Elsinore fault), SM (San Miguel fault), AB (Agua Blanca fault), SA (San Andreas fault), I (Imperial fault), CP (Cerro Prieto fault); Other features: m (Matomí accommodation zone), T (Isla Tiburón), IA (Isla Angel de la Guarda), WTZ (Wagner Transition Zone), VP (Volcan Prieto).

STAGE I - pre-20 Ma

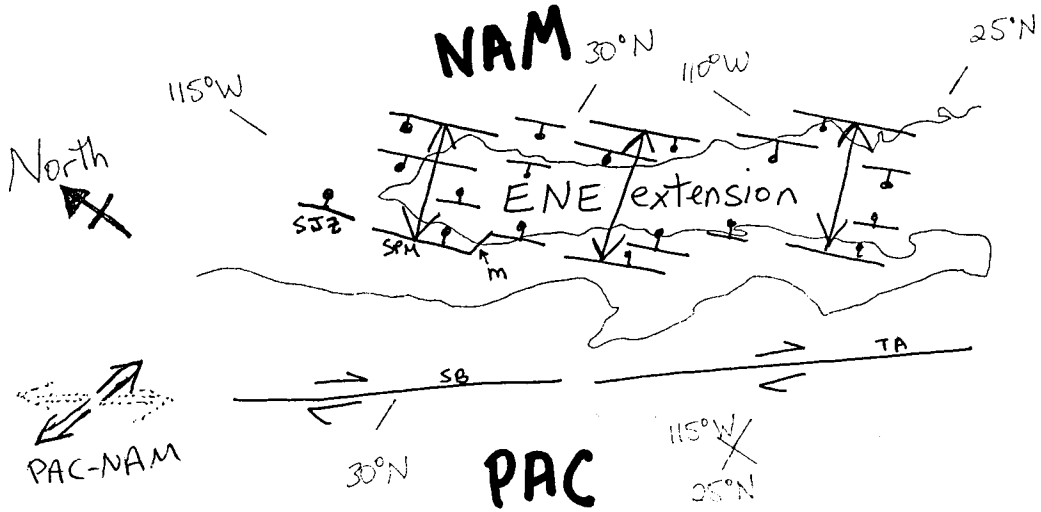


STAGE II - 13 Ma

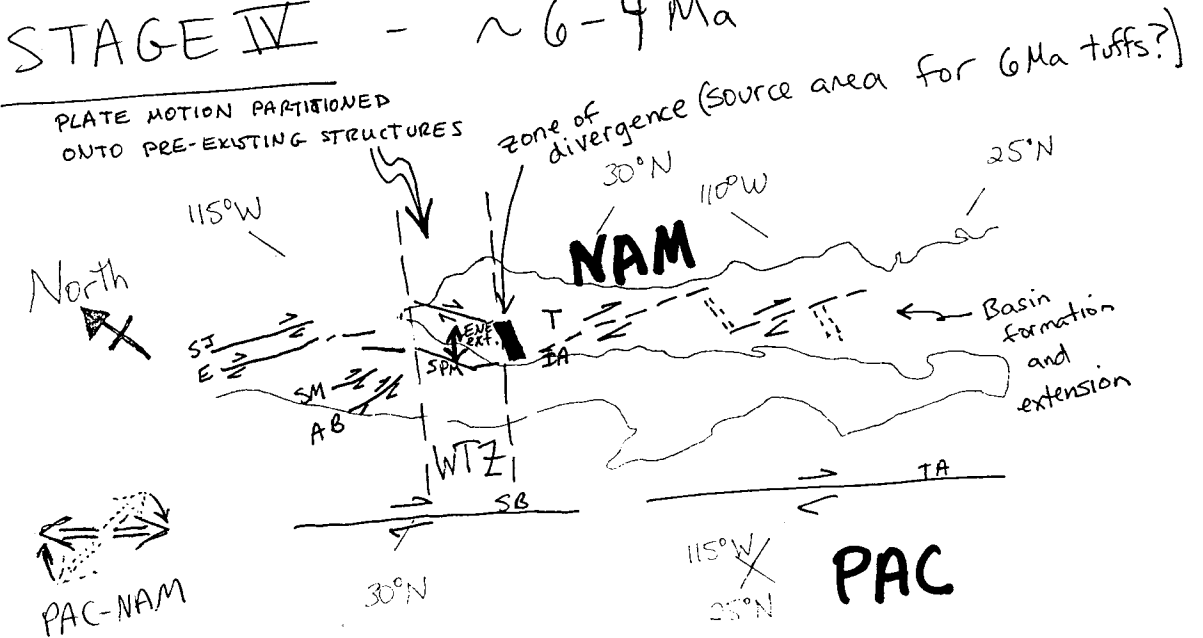


STAGE III - 12-10 Ma

(continued)

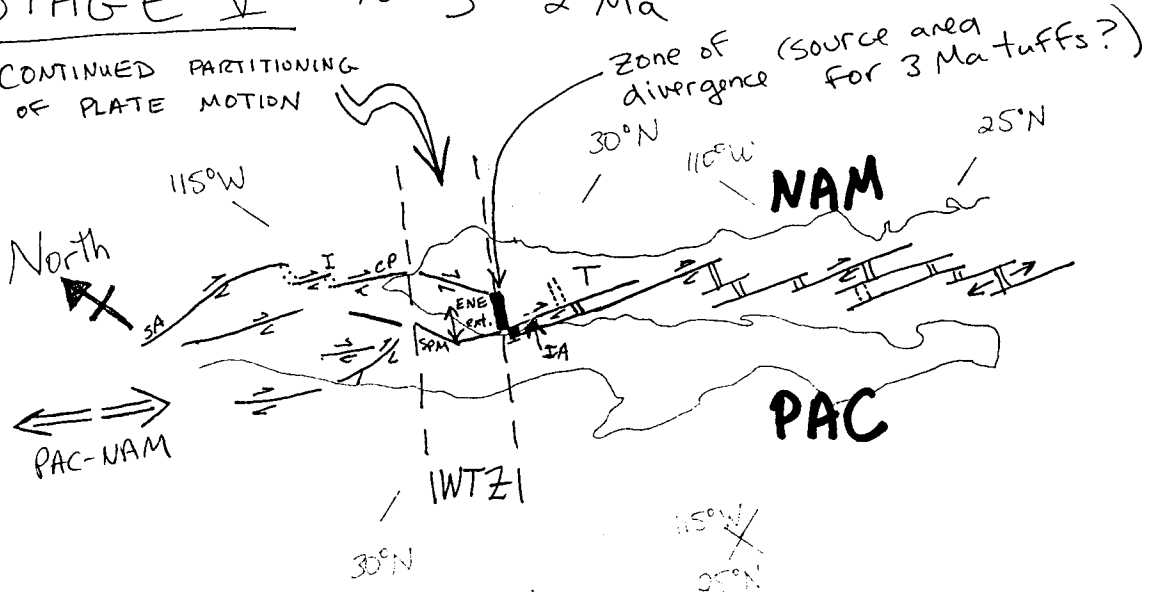


STAGE IV - ~6-4 Ma



# STAGE V ~ 3-2 Ma

CONTINUED PARTITIONING OF PLATE MOTION



# STAGE VI - 2 Ma to present

CONTINUED PARTITIONING OF PLATE MOTION

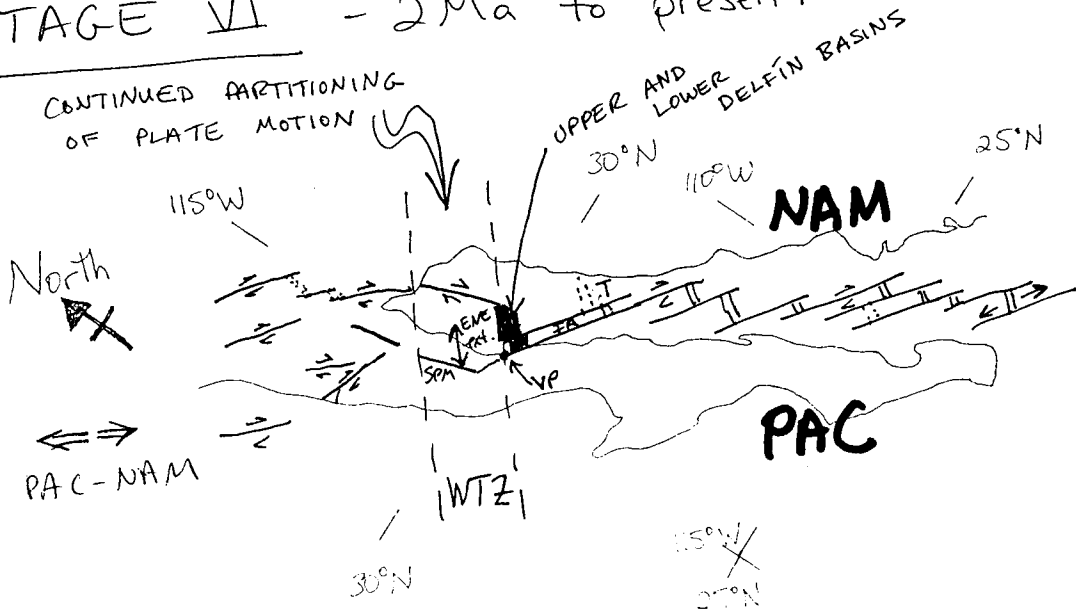
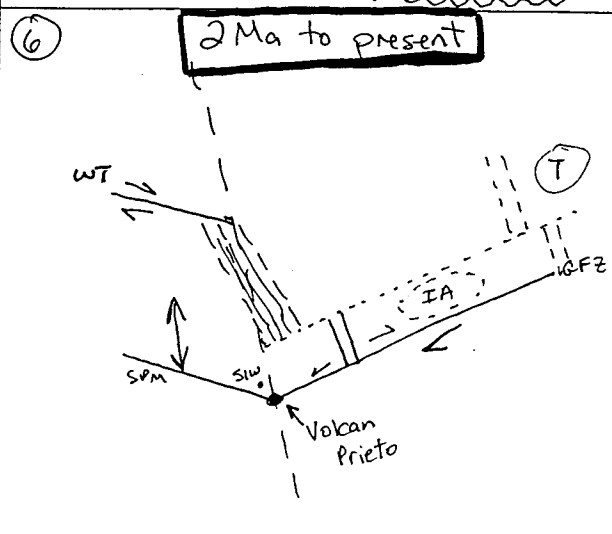
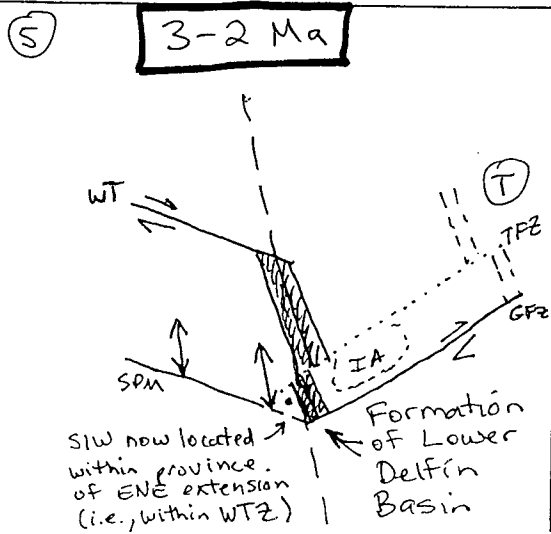
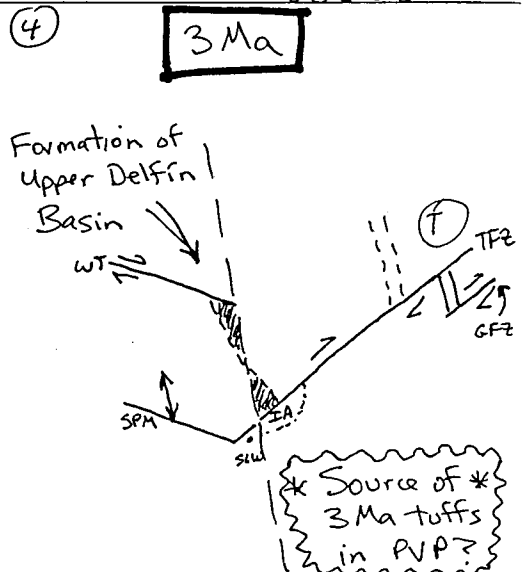
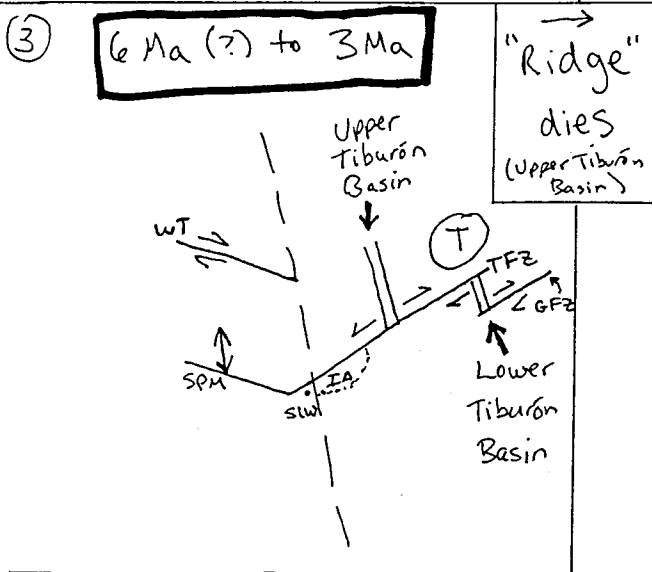
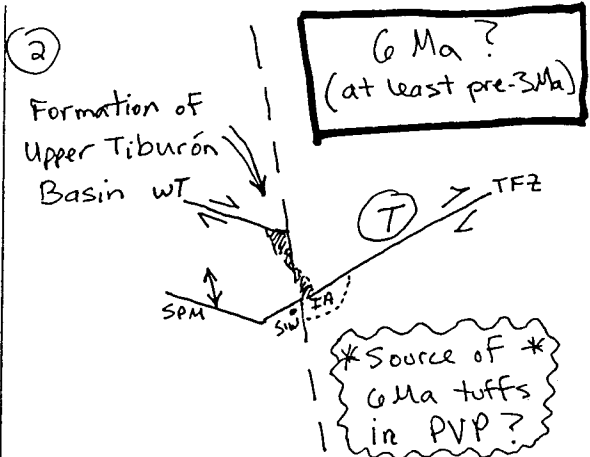
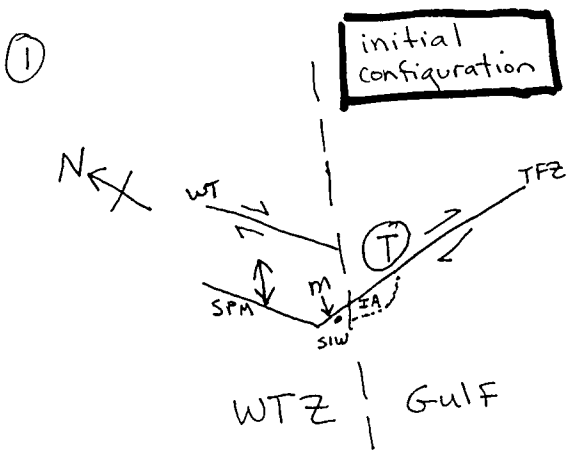


Figure 6.10. Cartoon showing proposed relationship between the WTZ and the history of spreading center and transform formation (after Stock, in press) adjacent to the PVP in the central Gulf of California. All panels are oriented as shown by north arrow in first panel. The dashed line indicates the southeastern boundary of the proposed Wagner Transition Zone (WTZ) and the northernmost portion of the Gulf of California oceanic spreading system. The WTZ is technically confined to the region northeast of the San Pedro Mártir fault and southwest of the (inferred) dextral Wagner transform fault. See text for discussion. Abbreviations: WT (“Wagner Transform” fault), SPM (San Pedro Mártir fault), m (Matomí accommodation zone), SIW (Santa Isabel Wash), T (Isla Tiburón), IA (Isla Angel de la Guarda), TFZ (Tiburón fracture zone), GFZ (Guaymas fracture zone).





Allen, C. R., L. T. Silver, and F. G. Stehli, Agua Blanca fault - a major transverse structure of northern Baja California, Mexico, *GSA Bull.*, 71, 457-482, 1960.

Allègre, C. J., T. Staudacher, and P. Sarda, Rare gas systematics: formation of the atmosphere, evolution and structure of the Earth's mantle, *Earth Planet. Sci. Lett.*, 81, 127-150, 1987.

Angelier, J., B. Colletta, J. Chorowicz, L. Ortlieb, and C. Rangin, Fault tectonics of the Baja California peninsula and the opening of the Sea of Cortez, Mexico, *J. Struct. Geol.*, 3 (4), 347-357, 1981.

Atwater, T., Implications of plate tectonics for the Cenozoic tectonic evolution of western North America, *GSA Bull.*, 81, 3513-3536, 1970.

Atwater, T., Plate tectonic history of the northeast Pacific and western North America, in *The Geology of North America: The Eastern Pacific Ocean and Hawaii*, edited by E. L. Winterer, D. M. Hussong, and R. W. Decker, Geological Society of America, Boulder, Colorado, pp. 21-72, 1989.

Axen, G., Extensional segmentation of the Main Gulf Escarpment, Mexico and United States, *Geology*, 23 (6), 515-518, 1995.

Banks, N. G., and R. P. Hoblitt, Summary of temperature studies of 1980 deposits, USGS Prof. Paper, 1250, 295-313, 1981.

Barnard, F. L., Structural geology of the Sierra de Los Cucapas, northeastern Baja California, Mexico, and Imperial County, California, Ph.D. thesis, University of Colorado, Boulder, 157 pp., 1968.

Barraclough, D. R., Observations of the Earth's magnetic field made in Edinburgh from 1670 to the present day, *Trans. R. Soc. Edinburgh*, 85, 239-252, 1995.

Bennett, R. A., W. Rodi, and R. E. Reilinger, Global Positioning System constraints on fault slip rates in southern California and northern Baja, Mexico, *J. Geophys. Res.*, 101 (B10), 21943-21960, 1996.

Berger, G. W., and D. York, Geothermometry from  $^{40}\text{Ar}/^{39}\text{Ar}$  dating experiments, *Geochim. Cosmochim. Acta*, 45, 795-811, 1981.

Best, M. G., R. T. Shuey, C. F. Caskey, and S. K. Grant, Stratigraphic relations of members of the Needles Range Formation at type localities in southwestern Utah, *GSA Bull.*, 84, 3269-3278, 1973.

Best, M. G., E. H. Christiansen, A. L. Deino, C. S. Grommé, and D. G. Tingey, Correlation and emplacement of a large, zoned, discontinuously exposed ash flow sheet: the  $^{40}\text{Ar}/^{39}\text{Ar}$  chronology, paleomagnetism, and petrology of the Pahrangat Formation, Nevada, *J. Geophys. Res.*, 100 (B12), 24593-24609, 1995.

Blake, S., Viscoplastic models of lava domes, in *Lava flows and domes: emplacement mechanisms and hazard implications*, edited by J. H. Fink, Springer-Verlag, Berlin, 88-126, 1990.

Bohannon, R. G., and T. Parsons, Tectonic implications of post-30 Ma Pacific and North American relative plate motions, *GSA Bull.*, 107 (8), 937-959, 1995.

Bosworth, W., Geometry of propagating continental rifts, *Nature*, 316, 625-627, 1985.

- Bosworth, W., Mesozoic and early Tertiary rift tectonics in East Africa, *Tectonophys.*, 209, 115-137, 1992.
- Bryant, B. A., Geology of the Sierra Santa Rosa basin, Baja California, Mexico, M. S. Thesis, San Diego State University, 75 pp., 1986.
- Buesch, D. C., Incorporation and redistribution of locally derived lithic fragments within a pyroclastic flow, *GSA Bull.*, 104, 1193-1207, 1992.
- Cande, S. C., and D. V. Kent, Revised calibration of the geomagnetic polarity timescale for the Late Cretaceous and Cenozoic, *J. Geophys. Res.*, 100 (B4), 6093-6095, 1995.
- Cas, R. A. F., and J. V. Wright, *Volcanic Successions: Modern and Ancient*, Chapman and Hall, London, 528 pp., 1993.
- Cebula, G. T., M. J. Kunk, H. H. Mehnert, C. W. Naeser, J. D. Obradovich, and J. F. Sutter, The fish canyon tuff, a potential standard for the  $^{40}\text{Ar}/^{39}\text{Ar}$  and fission-track dating methods, in *TERRA Cognita* 6, pp. 139-140, 1986.
- CETENAL, Puertecitos H11B77, Comisión de Estudios del Territorio Nacional, San Antonio, Mexico, 1977.
- Cheilletz, A., A. H. Clark, E. Farrar, G. A. Pauca, M. Pichavant, and H. A. Sandeman, Volcano-stratigraphy and  $^{40}\text{Ar}/^{39}\text{Ar}$  geochronology of the Macusani ignimbrite field: monitor of the Miocene geodynamic evolution of the Andes of southeast Peru, *Tectonophys.*, 205, 307-327, 1992.
- Conrad, J. E., E. H. McKee, J. J. Rytuba, J. T. Nash, and W. C. Utterback, Geochronology of the Sleeper deposit, Humboldt County, Nevada: epithermal gold-silver mineralization following emplacement of a silicic flow-dome complex, *Econ. Geol.*, 88 (2), 317-327, 1993.
- Conway, F. M., J. F. Diehl, and O. Matías, Paleomagnetic constraints on eruption patterns at the Pacaya composite volcano, Guatemala, *Bull. Volcanol.*, 55, 25-32, 1992.
- Conway, F. M., D. A. Ferrill, C. M. Hall, A. P. Morris, J. A. Stamatakos, C. B. Connor, A. N. Halliday, and C. Condit, Timing of basaltic volcanism along the Mesa Butte fault in the San Francisco volcanic field, Arizona, from  $^{40}\text{Ar}/^{39}\text{Ar}$  dates: implications for longevity of cinder cone alignments, *J. Geophys. Res.*, 102 (B1), 815-824, 1997.
- Curry, J. R., and D. G. Moore, Geologic history of the mouth of the Gulf of California, in *Tectonics and sedimentation along the California margin*, edited by J. K. Crouch, and S. B. Bachman, Pacific Section S. E. P. M., Bakersfield, California, pp. 17-36, 1984.
- Dauphin, J. P., and G. E. Ness, Bathymetry of the Gulf and Peninsular Province of the Californias, in *The Gulf and Peninsular Province of the Californias*, edited by J. P. Dauphin, and B. R. T. Simoneit, American Association of Petroleum Geologists Memoir, Tulsa, Oklahoma, pp. 21-23, 1991.
- Dawers, N. H., M. H. Anders, and C. H. Scholz, Growth of normal faults: displacement-length scaling, *Geology*, 21, 1107-1110, 1993.
- DeMets, C., R. G. Gordon, D. F. Argus, and S. Stein, Current plate motions, *Geophys. J. Int.*, 101, 425-478, 1990.
- DeMets, C., R. G. Gordon, D. F. Argus, and S. Stein, Effect of recent revisions to the geomagnetic reversal time scale on estimates of current plate motions, *Geophys. Res. Lett.*, 21 (20), 2191-2194, 1994.

DeMets, C., A reappraisal of seafloor spreading lineations in the Gulf of California: implications for the transfer of Baja California to the Pacific plate and estimates of Pacific-North America motion, *Geophys. Res. Lett.*, 22 (24), 3545-3548, 1995.

Dickinson, W. R., Kinematics of transrotational tectonism in the California Transverse Ranges and its contribution to cumulative slip along the San Andreas transform fault system, *GSA Spec. Paper*, 305, 46 pp., 1996.

Dokka, R. K., and R. H. Merriam, Late Cenozoic extension of northeastern Baja California, Mexico, *GSA Bull.*, 93, 371-378, 1982.

Dorsey, R. J., and B. Burns, Regional stratigraphy, sedimentology, and tectonic significance of Oligocene-Miocene sedimentary and volcanic rocks, northern Baja California, Mexico, *Sed. Geol.*, 88, 231-251, 1994.

Dunai, T. J., and H. Baur, Helium, neon, and argon systematics of the European subcontinental mantle: implications for its geochemical evolution, *Geochim. Cosmochim. Acta*, 59 (13), 2767-2783, 1995.

Durrance, E. M., *Radioactivity in Geology*, Ellis Horwood Limited, Chichester, 441 pp., 1986.

Dymond, J., and L. Hogan, Factors controlling the noble gas abundance patterns of deep-sea basalts, *Earth Planet. Sci. Lett.*, 38, 117-128, 1978.

Ellwood, B. B., Estimates of flow direction for calc-alkaline welded tuffs and paleomagnetic data reliability from anisotropy of magnetic susceptibility measurements: central San Juan Mountains, southwest Colorado, *Earth Planet. Sci. Lett.*, 59, 303-314, 1982.

Faure, G., *Principles of Isotope Geology*, Wiley, New York, 589 pp., 1986.

Fechtig, H., and S. Kalbitzer, The diffusion of argon in potassium-bearing solids, in *Potassium Argon Dating*, edited by O. A. Schaeffer, and Zähringer, J., Springer-Verlag, Berlin, Heidelberg, New York, pp. 68-106, 1966.

Fenby, S. S., and R. G. Gastil, Geologic-tectonic map of the Gulf of California and surrounding areas, in *The Gulf and Peninsular Province of the Californias*, edited by J. P. Dauphin, and B. R. T. Simoneit, American Association of Petroleum Geologists Memoir, Tulsa, Oklahoma, pp. 79-83, 1991.

Féraud, G., P. Lo Bello, C. M. Hall, J.-M. Cantagrel, D. York, and M. Bernat, Direct dating of Plio-Quaternary pumices by  $^{40}\text{Ar}/^{39}\text{Ar}$  step-heating and single-grain laser fusion methods: the example of the Monts-Dore massif (Massif Central, France), *J. Volcanol. Geotherm. Res.*, 40, 39-53, 1990.

Fisher, N. I., T. Lewis, and B. J. J. Embleton, *Statistical analysis of spherical data*, Cambridge University Press, Cambridge, New York, Melbourne, 329 pp., 1993.

Fisher, R. V., and H.-U. Schmincke, *Pyroclastic Rocks*, Springer-Verlag, Berlin, Heidelberg, New York, Tokyo, 472 pp., 1984.

Gastil, R. G., R. P. Phillips, and E. C. Allison, Reconnaissance geology of the state of Baja California (Geologic Map), *Mem. Geol. Soc. Am.*, 140, 1971.

Gastil, R. G., D. V. Lemone, and W. J. Stewart, Permian fusulinids from near San Felipe, Baja California, *AAPG Bull.*, 57 (4), 746-747, 1973.

- Gastil, R. G., R. P. Phillips, and E. C. Allison, Reconnaissance geology of the state of Baja California, *Mem. Geol. Soc. Am.*, 140, 170, 1975.
- Gastil, R. G., and D. Krummenacher, Reconnaissance geology of coastal Sonora between Puerto Lobos and Bahia Kino, *GSA Bull.*, 88, 189-198, 1977.
- Gastil, G., D. Krummenacher, and J. Minch, The record of Cenozoic volcanism around the Gulf of California, *GSA Bull.*, 90, 839-857, 1979.
- Gastil, R. G., Prebatholithic history of peninsular California, in *The Prebatholithic Stratigraphy of Peninsular California: Boulder, Colorado*, edited by R. G. Gastil, and R. H. Miller, *Geologic Society of America Special Paper 279*, pp. 145-156, 1993.
- Geissman, J. W., Paleomagnetism of ash-flow tuffs: microanalytical recognition of TRM components, *J. Geophys. Res.*, 85 (B3), 1487-1499, 1980.
- Geyh, M. A., and H. Schleicher, *Absolute Age Determinations*, Springer-Verlag, Berlin-Heidelberg, 503 pp., 1990.
- Gibbs, A. D., Structural evolution of extensional basin margins, *J. geol. Soc. London*, 141, 609-620, 1984.
- Goff, J. A., E. A. Bergman, and S. C. Solomon, Earthquake source mechanisms and transform fault tectonics in the Gulf of California, *J. Geophys. Res.*, 92 (B10), 10485-10510, 1987.
- Hagstrum, J. T., and P. B. Gans, Paleomagnetism of the Oligocene Kalamazoo Tuff: implications for middle Tertiary extension in east central Nevada, *J. Geophys. Res.*, 94 (B2), 1827-1842, 1989.
- Hamilton, W., Recognition on space photographs of structural elements of Baja California, *USGS Prof. Pap.*, 718, 1-26, 1971.
- Harrison, T. M., and I. McDougall, The thermal significance of potassium feldspar K-Ar ages inferred from  $^{40}\text{Ar}/^{39}\text{Ar}$  age spectrum results, *Geochim. Cosmochim. Acta*, 46, 1811-1820, 1982.
- Hausback, B. P., Cenozoic volcanic and tectonic evolution of Baja California Sur, Mexico, in *Geology of the Baja California Peninsula*, edited by V.A. Frizzell, *Pacific Section S.E.P.M.*, Vol. 39, pp. 219-236, 1984.
- Henry, C. D., Late Cenozoic Basin and Range structure in western Mexico adjacent to the Gulf of California, *GSA Bull.*, 101, 1147-1156, 1989.
- Henry, C. D., and J. J. Aranda-Gomez, The real southern Basin and Range: mid- to late Cenozoic extension in Mexico, *Geology*, 20 (8), 701-704, 1992.
- Hildreth, W., and G. Mahood, Correlation of ash-flow tuffs, *GSA Bull.*, 96, 968-974, 1985.
- Hillhouse, J. W., and R. E. Wells, Magnetic fabric, flow directions, and source area of the lower Miocene Peach Springs tuff in Arizona, California, and Nevada, *J. Geophys. Res.*, 96 (B7), 12443-12460, 1991.
- Hoblitt, R. P., R. L. Reynolds, and E. E. Larson, Suitability of nonwelded pyroclastic-flow deposits for studies of magnetic secular variation: a test based on deposits emplaced at Mount St. Helens, Washington, in 1980, *Geology*, 13, 242-245, 1985.

- Hudson, M. R., D. A. Sawyer, and R. G. Warren, Paleomagnetism and rotation constraints for the middle Miocene southwestern Nevada volcanic field, *Tectonics*, 13 (2), 258-277, 1994.
- Humphreys, E. D., and R. J. Weldon, II, Kinematic constraints on the rifting of Baja California, in *The Gulf and Peninsular Province of the Californias*, edited by J. P. Dauphin, and B. R. T. Simoneit, American Association of Petroleum Geologists Memoir, Tulsa, Oklahoma, pp. 217-229, 1991.
- Jackson, J. A., Active normal faulting and crustal extension, in *Continental Extensional Tectonics*, edited by M. P. Coward, J. F. Dewey, and P. L. Hancock, Blackwell Scientific Publications, Oxford, London, Edinburgh, pp. 3-17, 1987.
- Kaneoka, I., Rare gas isotopes and mass fractionation: an indicator of gas transport into or from a magma, *Earth Planet. Sci. Lett.*, 48, 284-292, 1980.
- Karig, D. E., and W. Jensky, The proto-Gulf of California, *Earth Planet. Sci. Lett.*, 17, 169-174, 1972.
- Kelley, S. P., N. O. Arnaud, and S. P. Turner, High spatial resolution  $^{40}\text{Ar}/^{39}\text{Ar}$  investigations using an ultraviolet laser probe extraction technique, *Geochim. Cosmochim. Acta*, 58 (16), 3519-3525, 1994.
- Kilembe, E. A., and B. R. Rosendahl, Structure and stratigraphy of the Rukwa rift, *Tectonophys.*, 209, 143-158, 1992.
- Kirschvink, J. L., The least-squares line and plane and the analysis of paleomagnetic data, *Geophys. J. R. Astron. Soc.* (62), 699-718, 1980.
- Kraus, D. C., Tectonics, bathymetry, and geomagnetism of the southern continental borderland west of Baja California, Mexico, *GSA Bull.*, 76, 617-650, 1965.
- Krummenacher, D., Isotopic composition of argon in modern surface volcanic rocks, *Earth Planet. Sci. Lett.*, 8, 109-117, 1970.
- Lanphere, M. A., High-resolution  $^{40}\text{Ar}/^{39}\text{Ar}$  chronology of Oligocene volcanic rocks, San Juan Mountains, Colorado, *Geochim. Cosmochim. Acta*, 52, 1425-1434, 1988.
- Larsen, P. H., Relay structures in a Lower Permian basement-involved extension system, East Greenland, *J. Struct. Geol.*, 10 (1), 3-8, 1988.
- Larson, P. A., J. D. Mudie, and R. L. Larson, Magnetic anomalies and fracture-zone trends in the Gulf of California, *GSA Bull.*, 83, 3361-3368, 1972.
- Larson, R. L., H. W. Menard, and S. M. Smith, Gulf of California: a result of ocean-floor spreading and transform faulting, *Science*, 161, 781-783, 1968.
- Lee, J., M. M. Miller, R. Crippen, B. Hacker, and J. Ledesma-Vazquez, Middle Miocene extension in the Gulf Extensional Province, Baja California: Evidence from the southern Sierra Juarez, *GSA Bull.*, 108 (5), 505-525, 1996.
- Legg, M. R., V. Wong O., and F. Suarez V., Geologic structure and tectonics of the inner continental borderland of northern Baja California, in *The Gulf and Peninsular Province of the Californias*, edited by J. P. Dauphin, and B. R. T. Simoneit, American Association of Petroleum Geologists Memoir, Tulsa, Oklahoma, pp. 145-177, 1991.

- Lewis, C. J., Constraints on extension in the Gulf Extensional Province from the Sierra San Fermin, northeastern Baja California, Mexico, Harvard University, Cambridge, Massachusetts, 361 pp., 1994.
- Lewis, C. J., Stratigraphy and geochronology of Miocene and Pliocene volcanic rocks in the Sierra San Fermin and southern Sierra San Felipe, Baja California, Mexico, *Geoffs. Int.*, 35 (1), 3-25, 1996.
- Lewis, C. J., and J. M. Stock, Paleomagnetic evidence of localized vertical-axis rotation during Neogene extension of the Sierra San Fermín, northeastern Baja California, Mexico, *J. Geophys. Res.*, in review, 1997.
- Lewis, C. J., and J. M. Stock, Neogene extension and distributed dextral shear in the Sierra San Fermín, northeastern Baja California, Mexico: late Miocene to Recent transtensional tectonics, *J. Struct. Geol.*, in review, 1997.
- Lipman, P. W., M. A. Dungan, L. L. Brown, and A. Deino, Recurrent eruption and subsidence at the Platoro caldera complex, southeastern San Juan volcanic field, Colorado: new tales from old tuffs, *GSA Bull.*, 108 (8), 1039-1055, 1996.
- Lippolt, H. J., M. Troesch, and J. C. Hess, Excess argon and dating of Quaternary Eifel volcanism, IV: common argon with high and lower-than-atmosphere  $^{40}\text{Ar}/^{39}\text{Ar}$  ratios in phonolitic rocks, East Eifel, F. R. G., *Earth Planet. Sci. Lett.*, 101, 19-33, 1990.
- Lonsdale, P., Geology and tectonic history of the Gulf of California, in *The Geology of North America: The Eastern Pacific Ocean and Hawaii*, edited by E.L. Winterer, D.M. Hussong, and R.W. Decker, Geological Society of America, Boulder, Colorado, pp. 499-521, 1989.
- Lonsdale, P., Structural patterns of the Pacific floor offshore of peninsular California, in *The Gulf and Peninsular Province of the Californias*, edited by J.P. Dauphin, and B.R.T. Simoneit, American Association of Petroleum Geologists Memoir, Tulsa, Oklahoma, pp. 87-125, 1991.
- Lyle, M., and G. E. Ness, The opening of the southern Gulf of California, in *The Gulf and Peninsular Province of the Californias*, edited by J. P. Dauphin, and B. R. T. Simoneit, American Association of Petroleum Geologists Memoir, Tulsa, Oklahoma, pp. 403-423, 1991.
- Mahon, K. I., The new "York" regression: application of an improved statistical method to geochemistry, *Intern. Geol. Review*, 38, 293-303, 1996.
- Mammerickx, J., and K. D. Klitgord, Northern East Pacific Rise: evolution from 25 m.y. B.P. to the present, *J. Geophys. Res.*, 87 (B8), 6751-6759, 1982.
- Martín-Barajas, A., and J. M. Stock, Estratigrafía y petrología de la secuencia volcánica de Puertecitos, noreste de Baja California. Transición de un arco volcánico a rift, in *Contribuciones a la Tectónica del Occidente de México: Monografías de la Union Geofísica Mexicana*, edited by L.A. Delgado-Argote, and A. Martín-Barajas, pp. 66-89, 1993.
- Martín-Barajas, A., J. M. Stock, P. Layer, B. Hausback, P. Renne, and M. López-Martínez, Arc-rift transition volcanism in the Puertecitos Volcanic Province, northeastern Baja California, Mexico, *GSA Bull.*, 107 (4), 407-424, 1995.
- McClay, K. R., and M. J. White, Analogue modelling of orthogonal and oblique rifting, *Mar. Petrol. Geol.*, 12 (2), 137-151, 1995.

- McCloy, C., J. C. Ingle, and J. A. Barron, Neogene stratigraphy, foraminifera, diatoms, and depositional history of Maria Madre Island, Mexico: evidence of early Neogene marine conditions in the southern Gulf of California, *Marine Micropaleo.*, 13, 193-212, 1988.
- McConnell, V. S., C. K. Shearer, J. C. Eichelberger, M. J. Keskinen, P. W. Layer, and J. J. Papike, Rhyolite intrusions in the intracaldera Bishop Tuff, Long Valley Caldera, California, *J. Volcanol. Geotherm. Res.*, 67, 41-60, 1995.
- McDougall, I., and T. M. Harrison, *Geochronology and Thermochronology by the  $^{40}\text{Ar}/^{39}\text{Ar}$  Method*, Oxford University Press, New York, 212 pp., 1988.
- McEldowney, R. C., *Geology of the northern Sierra Pinta, Baja California, Mexico*, M. S. thesis, San Diego State College, San Diego, 79 pp., 1970.
- McElhinny, M. W., *Palaeomagnetism and plate tectonics*, Cambridge University Press, Cambridge, London, New York, Melbourne, 358 pp., 1973.
- McFadden, P. L., and M. W. McElhinny, Classification of the reversal test in palaeomagnetism, *Geophys. J. Int.*, 103, 725-729, 1990.
- McIntosh, W. C., Evolution of paleomagnetism as a correlation criterion for Mogollon-Datil ignimbrites, southwestern New Mexico, *J. Geophys. Res.*, 96 (B8), 13459-13483, 1991.
- Merrihue, C., and G. Turner, Potassium-Argon dating by activation with fast neutrons, *J. Geophys. Res.*, 71 (11), 2852-2857, 1966.
- Metcalfe, R. V., and E. I. Smith, Introduction to special section: magmatism and extension, *J. Geophys. Res.*, 100 (B7), 10249-10253, 1995.
- Minster, J. B., and T. H. Jordan, Present-day plate motions, *J. Geophys. Res.*, 83 (B11), 5331-5354, 1978.
- Moore, D. G., Plate-edge deformation and crustal growth, Gulf of California structural province, *GSA Bull.*, 84, 1883-1906, 1973.
- Nagy, E. A., C. J. Lewis, and J. M. Stock, Change in style of extensional deformation across an accommodation zone based upon paleomagnetic evidence: Gulf Extensional Province, Baja California, Mexico, *Geological Society of America (Abstracts with Programs)*, pp. A189-A190, 1995.
- Neuhaus, J. R., *Volcanic and nonmarine stratigraphy of southwest Isla Tiburon, Gulf of California, Mexico*, M. S. thesis, San Diego State University, San Diego, 170 pp., 1989.
- Neuhaus, J. R., Cassidy, M., Krummenacher, D., and R. G. Gastil, Timing of protogulf extension and transtensional rifting through volcanic/sedimentary stratigraphy of S.W. Isla Tiburon, Gulf of California, Sonora, Mexico, *Geological Society of America (Abstracts with Programs)*, p. 218, 1988.
- O'Reilly, W., *Rock and mineral magnetism*, Blackie & Son, Ltd., Glasgow, London, New York, 220 pp., 1984.
- Onstott, T. C., Application of the Bingham distribution function in paleomagnetic studies, *J. Geophys. Res.*, 85 (B3), 1500-1510, 1980.
- Ozima, M., Ar isotopes and Earth-atmosphere evolution models, *Geochim. Cosmochim. Acta*, 39, 1127-1134, 1975.



Ozima, M., and F. A. Podosek, Noble gas geochemistry, Cambridge University Press, Cambridge, New York, Melbourne, 367 pp., 1983.

Powell, R. E., Balanced palinspastic reconstruction of pre-late Cenozoic paleogeology, southern California: geologic and kinematic constraints on evolution of the San Andreas fault system, in *The San Andreas Fault System: displacement, palinspastic reconstruction, and geologic evolution*, edited by R. E. Powell, R. J. Weldon, II., and J. C. Matti, Geological Society of America, Boulder, Colorado, pp. 1-106, 1993.

Pringle, M. S., M. McWilliams, B. F. Houghton, M. A. Lanphere, and C. J. N. Wilson,  $^{40}\text{Ar}/^{39}\text{Ar}$  dating of Quaternary feldspar: examples from the Taupo Volcanic Zone, New Zealand, *Geology*, 20, 531-534, 1992.

Quidelleur, X., and V. Courtillot, On low-degree spherical harmonic models of paleosecular variation, *Phys. Earth Planet. Inter.*, 95, 55-77, 1996.

Renne, P. R., and A. R. Basu, Rapid eruption of the Siberian Traps flood basalts at the Permo-Triassic boundary, *Science*, 253, 176-179, 1991.

Renne, P. R., M. Ernesto, I. G. Pacca, R. S. Coe, J. M. Glen, M. Prévot, and M. Perrin, The age of Paraná flood volcanism, rifting of Gondwanaland, and the Jurassic-Cretaceous boundary, *Science*, 258, 975-979, 1992.

Revenaugh, J., and C. Reasoner, Cumulative offset of the San Andreas fault in central California: a seismic approach, *Geology*, 25 (2), 123-126, 1997.

Rockwell, T. K., D. L. Schug, and M. E. Hatch, Late Quaternary slip rates along the Agua Blanca fault, Baja California, Mexico, in *Geological Investigations of Baja California*, edited by P.L. Abott, South Coast Geological Society, pp. 53-92, 1993.

Roddick, J. C., High precision intercalibration of  $^{40}\text{Ar}$ - $^{39}\text{Ar}$  standards, *Geochim. Cosmochim. Acta*, 47, 887-898, 1983.

Rose, T. P., R. E. Criss, and G. R. Rossman, Irradiative coloration of quartz and feldspars with application to preparing high-purity mineral separates, *Chem. Geo.*, 114, 185-189, 1994.

Rosenbaum, J. G., Paleomagnetic directional dispersion produced by plastic deformation in a thick Miocene welded tuff, southern Nevada: implications for welding temperatures, *J. Geophys. Res.*, 91 (B12), 12817-12834, 1986.

Rosenbaum, J. G., M. R. Hudson, and R. B. Scott, Paleomagnetic constraints on the geometry and timing of deformation at Yucca Mountain, Nevada, *J. Geophys. Res.*, 96 (B2), 1963-1979, 1991.

Rosenbaum, J. G., Magnetic grain-size variations through an ash flow sheet: influence on magnetic properties and implications for cooling history, *J. Geophys. Res.*, 98 (B7), 11715-11727, 1993.

Rossetter, R. J., *Geology of the San Luis and San Lorenzo Island Groups, Gulf of California*, California State University, San Diego, California, 92 pp., 1973.

Samson, S. D., and E. C. J. Alexander, Calibration of the interlaboratory  $^{40}\text{Ar}/^{39}\text{Ar}$  dating standard, MMhb-1, *Chem. Geol.*, 66, 27-34, 1987.

Sawlan, M. G., Magmatic evolution of the Gulf of California rift, in *The Gulf and Peninsular Provinces of the Californias*, edited by J.P. Dauphin, and B.R.T. Simoneit, American Association of Petroleum Geologists Memoir, Tulsa, Oklahoma., pp. 301-375, 1991.

- Schlinger, C. M., D. R. Veblen, and J. G. Rosenbaum, Magnetism and magnetic mineralogy of ash flow tuffs from Yucca Mountain, Nevada, *J. Geophys. Res.*, 96 (B4), 6035-6052, 1991.
- Scott, D. L., M. A. Etheridge, and B. R. Rosendahl, Oblique-slip deformation in extensional terrains: a case study of the Lakes Tanganyika and Malawi rift zones, *Tectonics*, 11 (5), 998-1009, 1992.
- Silver, L. T., F. G. Stehli, and C. R. Allen, Lower Cretaceous pre-batholithic rocks of northern Baja California, Mexico, *Am. Assoc. Petroleum Geologists Bull.*, 47, 2054-2059, 1963.
- Silver, L. T., C. R. Allen, and F. G. Stehli, Geological and geochronological observations on a portion of the Peninsular Range Batholith of northwestern Baja California, Mexico, *Geol. Soc. America Spec. Paper (abstracts)*, 121, 279-280, 1969.
- Smith, J. T., Cenozoic marine mollusks and paleogeography of the Gulf of California, in *The Gulf and Peninsular Province of the Californias*, edited by J.P. Dauphin, and B.R.T. Simoneit, American Association of Petroleum Geologists Memoir, Tulsa, Oklahoma, pp. 637-666, 1991.
- Smith, R. L., Ash Flows, *GSA Bull.*, 71, 795-842, 1960.
- Sommer, M. A., and J. Garcia, Potassium-argon dates for Pliocene rhyolite sequences east of Puertecitos, Baja California, *GSA Abs. w/ Prog.*, 2, 146, 1970.
- Spell, T. L., and T. M. Harrison,  $^{40}\text{Ar}/^{39}\text{Ar}$  geochronology of post-Valles caldera rhyolites, Jemez volcanic field, New Mexico, *J. Geophys. Res.*, 98 (B5), 8031-8051, 1993.
- Spell, T. L., I. McDougall, and A. P. Doulgeris, Cerro Toledo rhyolite, Jemez Volcanic Field, New Mexico:  $^{40}\text{Ar}/^{39}\text{Ar}$  geochronology of eruptions between two caldera-forming events, *GSA Bull.*, 108 (12), 1549-1566, 1996.
- Spencer, J. E., and W. R. Normark, Tosco-Abreojos fault zone: a Neogene transform plate boundary within the Pacific margin of southern Baja California, Mexico, *Geology*, 7, 554-557, 1979.
- Spencer, J. E., and W. R. Normark, Neogene plate-tectonic evolution of the Baja California Sur continental margin and the southern Gulf of California, Mexico, in *The Geology of North America: The Eastern Pacific Ocean and Hawaii*, edited by E.L. Winterer, D.M. Hussong, and R.W. Decker, Geological Society of America, Boulder, Colorado, pp. 489-497, 1989.
- Stock, J. M., Sequence and geochronology of Miocene rocks adjacent to the Main Gulf Escarpment: southern Valle Chico, Baja California, Mexico, *Geofís. Int.*, 28 (5), 851-896, 1989.
- Stock, J. M., and K. V. Hodges, Pre-Pliocene extension around the Gulf of California and the transfer of Baja California to the Pacific plate, *Tectonics*, 8 (1), 99-115, 1989.
- Stock, J. M., and K. V. Hodges, Miocene to Recent structural development of an extensional accommodation zone, northeastern Baja California, Mexico, *J. Struct. Geol.*, 12 (3), 315-328, 1990.
- Stock, J. M., A. Martín-Barajas, F. Suárez-Vidal, and M. M. Miller, Miocene to Holocene extensional tectonics and volcanic stratigraphy of NE Baja California, Mexico, in *Geologic excursions in southern California and Mexico (GSA Meeting guidebook)*, San Diego State University, edited by M. Walawender, and B. Hanan, pp. 44-67, 1991.

- Stock, J. M., Geologic map of southern Valle Chico and adjacent regions, Baja California, Mexico, GSA Map and Chart Series, MCH076, 1-11, 1993.
- Stock, J. M., and J. Lee, Do microplates in subduction zones leave a geological record? *Tectonics*, 13 (6), 1472-1487, 1994.
- Stock, J. M., A. Martín-Barajas, and M. Tellez-Duarte, Early rift sedimentation and structure along the NE margin of Baja California, edited by P.L. Abbott, and J.D. Cooper, Pacific Section A. A. P. G., GB 73, Field Conference Guide 1996, pp. 337-371, 1996a.
- Stock, J. S., E. A. Nagy, and C. J. Lewis, Definition and correlation of the Tuff of San Felipe, NE Baja California, in *GEOS (Boletín Union Geofísica Mexicana)* 16 (4), pp. 199, 1996b.
- Stock, J. S., C. J. Lewis, and E. A. Nagy, The Tuff of San Felipe: an extensive middle Miocene pyroclastic flow deposit in NE Baja California, Mexico, IAVCEI abstract, pp. 16, 1997.
- Stock, J. M., Relation of the Puertecitos Volcanic Province, Baja California, Mexico, to development of the plate boundary in the Gulf of California, in *GSA Special Paper on Cenozoic Tectonics and Volcanism of Mexico*, edited by H. Delgado-Granados, G. Aguirre-Díaz, and J. M. Stock, Geological Society of America, in press, 1997.
- Tajima, F., and D. M. Tralli, Variation of seismic slip in the Gulf of California and the possible effect on geodetic measurements of Pacific-North American plate motion, *J. Geophys. Res.*, 97 (B4), 4903-4913, 1992.
- Tarling, D. H., *Palaeomagnetism*, Chapman and Hall, London, New York, 379 pp., 1983.
- Tauxe, L., N. Kylstra, and C. Constable, Bootstrap statistics for paleomagnetic data, *J. Geophys. Res.*, 96 (B7), 11723-11740, 1991.
- Thompson, R., and F. Oldfield, *Environmental Magnetism*, Allen & Unwin Ltd., London, 227 pp., 1986.
- Tron, V., and J.-P. Brun, Experiments on oblique rifting in brittle-ductile systems, *Tectonophys.*, 188, 71-84, 1991.
- Turner, G., Argon 40-argon 39 dating: the optimization of irradiation parameters, *Earth Planet. Sci. Letters*, 10, 227-234, 1971a.
- Turner, G., 40Ar-39Ar ages from the Lunar maria, *Earth Planet. Sci. Lett.*, 11, 169-191, 1971b.
- Ultré-Guérard, P., and J. Achache, Core flow instabilities and geomagnetic storms during reversals: the Steens Mountain impulsive field variations revisited, *Earth Planet. Sci. Lett.*, 135, 91-99, 1995.
- Umhoefer, P. J., R. J. Dorsey, and P. Renne, Tectonics of the Pliocene Loreto basin, Baja California Sur, Mexico, and evolution of the Gulf of California, *Geology*, 22, 649-652, 1994.
- Umhoefer, P. J., and K. A. Stone, Description and kinematics of the SE Loreto basin fault array, Baja California, *J. Struct. Geol.*, 18 (5), 595-continues, 1996.
- Vidal, A., and L. Mungúía, Local magnitude and source parameters for earthquakes in the Pensinsular Ranges of Baja California, Mexico, *Bull. Seism. Soc. Am.*, 81 (6), 2254-2267, 1991.

Weldon, R. J., II., K. E. Meisling, and J. Alexander, A speculative history of the San Andreas fault in the central Transverse Ranges, California, in *The San Andreas Fault System: displacement, palinspastic reconstruction, and geologic evolution*, edited by R.E. Powell, R.J. Weldon, II., and J.C. Matti, Geological Society of America, Boulder, Colorado, pp. 161-198, 1993.

Wells, R. E., and J. W. Hillhouse, Paleomagnetism and tectonic rotation of the lower Miocene Peach Springs tuff: Colorado plateau, Arizona to Barstow, California, *GSA Bull.*, 101, 846-863, 1989.

Wendt, I., and C. Carl, The statistical distribution of the mean squared weighted deviation, *Chem. Geo.*, 86, 275-285, 1991.

Williams, H., F. J. Turner, and C. M. Gilbert, *Petrography: an introduction to the study of rocks in thin sections*, W. H. Freeman and Company, New York, 626 pp., 1982.

Withjack, M. O., and W. R. Jamison, Deformation produced by oblique rifting, *Tectonophys.*, 126, 99-124, 1986.

York, D., Least squares fitting of a straight line with correlated errors, *Earth Planet. Sci. Lett.*, 5, 320-324, 1969.

Zanchi, A., The opening of the Gulf of California near Loreto, Baja California, Mexico: from basin and range extension to transtensional tectonics, *J. Struct. Geol.*, 16 (12), 1619-1639, 1994.

Zoback, M. L., R. E. Anderson, and G. A. Thompson, Cainozoic evolution of the state of stress and style of tectonism of the Basin and Range province of the western United States, *Phil. Trans. R. Soc. Lond.*, 300, 407-434, 1981.

Zumbo, V., G. Féraud, P. Vellutini, P. Pigué, and J. Vincent, First  $^{40}\text{Ar}/^{39}\text{Ar}$  dating on Early Pliocene to Plio-Pleistocene magmatic events of the Afar - Republic of Djibouti, *J. Volcanol. Geotherm. Res.*, 65, 281-295, 1995.

APPENDIX A. Results from electron microprobe analyses (atomic proportions)

unit	Na	Mg	Al	Si	K	Ca	Ti	Cr	Mn	Fe	Ba	O
anorthite std	0.008	0.006	6.020	5.980	0.004	2.992	0.003	0.000	0.000	0.000	0.000	24.000
Lake Co. plag.	1.076	0.024	4.898	7.018	0.024	1.974	0.000	0.006	0.000	0.000	0.056	24.000
Nat. B. diop.	0.017	3.920	0.010	7.980	0.005	4.053	0.000	0.005	0.002	0.002	0.029	24.000
Kakanui hnbld	0.822	2.884	2.604	6.199	0.417	1.687	0.572	0.000	0.005	0.005	1.352	24.000
Tmrsw	2.162	0.001	3.634	8.341	0.169	0.664	0.003	0.000	0.002	0.003	0.018	24.000
Tmrsw	2.179	0.000	3.549	8.426	0.189	0.608	0.000	0.002	0.000	0.000	0.021	24.000
Tmrsw	2.162	0.001	3.569	8.405	0.192	0.618	0.001	0.000	0.000	0.000	0.026	24.000
Tmdtomb	1.917	0.000	3.983	8.002	0.079	1.003	0.002	0.000	0.000	0.000	0.014	24.000
Tmdtomb	1.835	0.000	3.993	8.002	0.065	1.035	0.000	0.001	0.000	0.000	0.015	24.000
Tmdtomb	1.756	0.002	4.144	7.835	0.062	1.185	0.000	0.000	0.000	0.000	0.015	24.000
Tmdtomb	1.467	0.003	4.378	7.597	0.069	1.440	0.000	0.001	0.000	0.000	0.028	24.000
Tmdtomb	1.679	0.003	4.171	7.793	0.082	1.245	0.000	0.001	0.000	0.000	0.024	24.000
Tmdtomb	1.544	0.002	4.358	7.606	0.065	1.401	0.004	0.000	0.002	0.000	0.026	24.000
Tmdtomb	1.820	0.001	4.095	7.886	0.086	1.108	0.002	0.000	0.000	0.000	0.013	24.000
Tmdtomb	1.888	0.000	4.013	7.975	0.083	1.029	0.000	0.001	0.000	0.000	0.013	24.000
Tmdtomb	1.697	0.005	4.171	7.797	0.087	1.227	0.001	0.000	0.000	0.001	0.022	24.000
Tmdtomb	1.710	0.000	4.154	7.836	0.091	1.174	0.001	0.003	0.000	0.000	0.014	24.000
Tmdtomb	1.719	0.000	4.204	7.778	0.056	1.232	0.000	0.001	0.000	0.000	0.012	24.000
Tmdtomb	1.638	0.068	4.141	7.829	0.087	1.182	0.000	0.000	0.000	0.000	0.014	24.000
Tmrsw	2.135	0.001	3.664	8.296	0.158	0.730	0.000	0.000	0.000	0.001	0.027	24.000
Tmrsw	2.159	0.000	3.645	8.331	0.175	0.654	0.006	0.000	0.000	0.001	0.024	24.000
Tmrsw	2.131	0.000	3.715	8.247	0.146	0.762	0.001	0.002	0.000	0.000	0.020	24.000
Tmrsw	2.215	0.000	3.587	8.375	0.183	0.638	0.001	0.000	0.000	0.000	0.024	24.000
Tmrsw	2.121	0.000	3.666	8.306	0.156	0.715	0.000	0.001	0.000	0.000	0.024	24.000
Tmrsw	2.200	0.000	3.618	8.362	0.190	0.620	0.000	0.000	0.000	0.001	0.021	24.000
Tmdtomb	0.637	3.010	1.795	6.824	0.228	1.815	0.274	0.015	0.022	1.809	0.000	24.000
Tmdtomb	0.559	3.143	1.518	7.068	0.143	1.824	0.230	0.004	0.019	1.783	0.000	24.000
Tmdtomb	0.025	2.596	0.227	9.100	0.289	0.323	0.004	0.008	0.000	2.362	0.000	24.000
Tmrsw	2.003	0.000	3.115	8.851	0.862	0.166	0.003	0.000	0.000	0.000	0.019	24.000
Tmrsw	1.682	0.000	3.063	8.906	1.249	0.098	0.003	0.001	0.000	0.000	0.018	24.000
Tmrsw	2.070	0.000	3.134	8.830	0.787	0.189	0.000	0.000	0.000	0.000	0.016	24.000
Tmdtomb	1.909	0.000	4.029	7.952	0.074	1.045	0.000	0.000	0.000	0.000	0.016	24.000
Tmdtomb	1.778	0.000	4.154	7.822	0.075	1.170	0.003	0.000	0.000	0.001	0.015	24.000
Tmdtomb	1.758	0.000	4.232	7.756	0.056	1.218	0.000	0.000	0.000	0.000	0.014	24.000
Tmr3	1.907	0.000	3.010	8.960	1.063	0.037	0.000	0.000	0.003	0.002	0.023	24.000
Tmr3	1.886	0.000	3.016	8.959	1.084	0.041	0.000	0.000	0.000	0.000	0.019	24.000
Tmr3	1.972	0.000	3.020	8.962	0.937	0.055	0.000	0.001	0.000	0.000	0.019	24.000
Tmbiol	0.664	3.173	1.974	6.718	0.172	1.876	0.227	0.008	0.020	1.651	0.001	24.000
Tmbiol	0.008	4.468	0.076	7.967	0.003	0.175	0.017	0.002	0.076	3.191	0.000	24.000
Tmbiol	0.008	6.246	0.310	7.821	0.002	0.249	0.021	0.006	0.029	1.311	0.000	24.000
Tmbiol	0.080	3.491	0.589	7.623	0.005	3.402	0.056	0.023	0.023	0.764	0.001	24.000

unit	Na	Mg	Al	Si	K	Ca	Ti	Cr	Mn	Fe	Ba	O	
Tmbiol	0.000	9.856	0.001	0.001	5.970	0.004	0.023	0.000	0.001	0.032	2.144	0.000	24.000
Tmbiol	1.559	0.002	4.405	4.405	7.571	0.057	1.419	0.000	0.001	0.001	0.019	0.000	24.000
Tmbiol	1.805	0.004	4.079	4.079	7.873	0.080	1.142	0.005	0.000	0.001	0.028	0.008	24.000
Tmbiol	0.010	0.820	0.030	0.030	0.007	0.009	0.031	7.278	0.021	0.079	8.414	0.000	24.000
Tmagem	0.010	6.394	0.026	0.026	7.759	0.003	0.242	0.022	0.069	0.024	1.276	0.002	24.000
Tmagem	1.051	0.026	4.843	4.843	7.068	0.026	1.959	0.007	0.000	0.002	0.060	0.000	24.000
Tmagem	0.607	0.015	5.342	5.342	6.582	0.009	2.442	0.003	0.003	0.000	0.048	0.001	24.000
Tmagem	0.084	3.671	0.438	0.438	7.654	0.004	3.300	0.083	0.046	0.018	0.763	0.005	24.000
Tmagem	0.006	6.076	0.306	0.306	7.754	0.004	0.228	0.041	0.028	0.027	1.569	0.004	24.000
Tmagem	0.974	0.022	4.964	4.964	6.941	0.014	2.075	0.007	0.000	0.003	0.065	0.001	24.000
Tmagem	0.098	3.494	0.555	0.555	7.585	0.004	3.156	0.104	0.014	0.021	1.046	0.000	24.000
Tmdtomb	1.899	0.000	3.966	3.966	8.004	0.119	1.019	0.001	0.000	0.000	0.014	0.000	24.000
Tmdtomb	0.132	3.484	1.577	1.577	7.223	0.119	1.633	0.108	0.009	0.036	1.679	0.001	24.000
Tmdtomb	0.119	3.821	1.499	1.499	7.238	0.154	1.599	0.089	0.007	0.039	1.486	0.004	24.000
Tmdtomb	1.914	0.003	3.990	3.990	7.987	0.110	1.004	0.002	0.000	0.000	0.014	0.002	24.000
Tmdtomb	1.712	0.000	4.246	4.246	7.733	0.072	1.254	0.000	0.001	0.000	0.013	0.005	24.000
Tmdtomb	1.548	0.032	3.689	3.689	8.158	0.211	1.028	0.020	0.004	0.001	0.152	0.012	24.000
Tmdtomb	0.179	3.247	1.492	1.492	7.207	0.062	1.832	0.135	0.004	0.043	1.827	0.004	24.000
Tmdtomb	0.015	5.755	0.584	0.584	7.726	0.005	0.220	0.037	0.027	0.027	1.545	0.000	24.000
Tmrec	2.155	0.000	3.587	3.587	3.586	4.414	0.975	2.946	0.367	0.000	0.744	0.000	24.000
Tmrec	2.150	0.000	3.652	3.652	8.303	0.169	0.707	0.004	0.004	0.000	0.030	0.010	24.000
Tmrec	0.017	0.266	0.210	0.210	0.069	0.009	0.014	2.196	0.028	0.248	18.569	0.002	24.000
Tmrec	1.738	0.000	3.066	3.066	8.890	1.118	0.132	0.005	0.000	0.001	0.039	0.012	24.000
Tmrec	2.196	0.000	3.607	3.607	8.358	0.152	0.658	0.002	0.002	0.001	0.028	0.007	24.000
Tmrec	0.052	2.841	1.063	1.063	7.389	0.209	1.758	0.120	0.000	0.075	2.783	0.000	24.000
Tmrec	2.258	0.000	3.508	3.508	8.448	0.205	0.576	0.000	0.000	0.001	0.025	0.009	24.000
Tmrec	1.013	0.000	2.002	2.002	9.950	0.938	0.060	0.012	0.001	0.003	0.026	0.008	24.000
Tmrec	0.013	2.629	1.035	1.035	7.535	0.159	1.720	0.109	0.000	0.071	2.650	0.002	24.000
anorthite std	0.012	0.011	6.035	6.035	5.959	0.006	3.006	0.000	0.001	0.000	0.002	0.000	24.000
Tmrcan	0.081	3.393	0.419	0.419	7.749	0.004	3.470	0.047	0.026	0.018	0.815	0.004	24.000
Tmrcan	0.000	3.303	1.120	1.120	0.030	0.009	2.047	0.002	0.002	0.141	17.704	0.000	24.000
Tmrcan	2.040	0.000	3.614	3.614	8.373	0.276	0.648	0.000	0.000	0.002	0.024	0.003	24.000
Tmrcan	0.010	5.902	0.127	0.127	7.881	0.004	0.211	0.019	0.007	0.045	1.832	0.001	24.000
Tmrcan	0.002	5.884	0.111	0.111	7.912	0.022	0.228	0.027	0.005	0.042	1.793	0.000	24.000
Tmrcan	0.983	0.013	4.955	4.955	6.987	0.022	2.018	0.006	0.002	0.000	0.044	0.000	24.000
Tmrcan	0.920	0.013	5.006	5.006	6.934	0.023	2.065	0.004	0.003	0.000	0.054	0.005	24.000
Tmrcan	0.005	6.215	0.165	0.165	7.915	0.003	0.178	0.013	0.017	0.033	1.441	0.001	24.000
Tmrcan	2.132	0.000	3.583	3.583	8.389	0.259	0.606	0.000	0.003	0.000	0.026	0.016	24.000
Tmrcan	0.013	0.287	0.806	0.806	0.024	0.008	0.004	6.061	0.002	0.106	10.210	0.000	24.000
Tmrcan	0.050	3.530	0.143	0.143	7.908	0.002	3.347	0.034	0.005	0.025	0.966	0.000	24.000
Tmbkc	0.950	0.019	5.019	5.019	6.906	0.018	2.095	0.000	0.000	0.002	0.051	0.009	24.000

unit	Na	Mg	Al	Si	K	Ca	Ti	Cr	Mn	Fe	Ba	O
Tmbkc	0.000	10.575	0.001	5.973	0.004	0.017	0.000	0.000	0.016	1.442	0.000	24.000
Tmbkc	0.001	8.148	0.050	6.198	0.023	0.069	0.004	0.000	0.045	3.247	0.000	24.000
Tmbkc	0.930	0.018	4.983	6.954	0.022	2.067	0.003	0.000	0.000	0.049	0.002	24.000
Tmbkc	0.001	9.300	0.013	6.027	0.009	0.026	0.001	0.003	0.047	2.538	0.003	24.000
Tmbkc	0.103	3.366	0.701	7.524	0.014	3.043	0.063	0.004	0.004	1.267	0.004	24.000
Tmbkc	0.051	3.031	0.283	9.028	0.312	0.249	0.000	0.006	0.001	2.047	0.001	24.000
Tmbkc	0.455	2.682	1.998	7.205	0.038	1.930	0.131	0.012	0.030	1.438	0.006	24.000
Tmbkc	1.216	0.209	2.873	8.814	0.466	0.610	0.071	0.000	0.003	0.249	0.006	24.000
Tmbkc	0.969	0.017	4.975	6.948	0.025	2.054	0.006	0.000	0.003	0.051	0.005	24.000
Tmahem	1.143	0.004	4.847	7.108	0.038	1.854	0.002	0.002	0.002	0.053	0.003	24.000
Tmahem	0.018	6.107	0.210	7.882	0.006	0.199	0.016	0.003	0.029	1.537	0.000	24.000
Tmahem	0.088	3.705	0.378	7.795	0.004	3.394	0.027	0.009	0.012	0.621	0.000	24.000
Tmahem	0.003	6.361	0.313	7.779	0.004	0.166	0.012	0.037	0.027	1.338	0.000	24.000
Tmahem	1.131	0.014	4.795	7.130	0.036	1.873	0.005	0.000	0.002	0.061	0.004	24.000
Tmahem	0.095	3.641	0.414	7.758	0.004	3.471	0.025	0.015	0.016	0.613	0.000	24.000
Tmahem	0.487	0.007	5.499	6.438	0.010	2.573	0.000	0.001	0.000	0.046	0.000	24.000
Tmahem	0.001	6.049	0.296	7.783	0.004	0.176	0.019	0.007	0.034	1.679	0.000	24.000
Tmahem	0.014	5.479	0.277	7.796	0.004	0.195	0.020	0.006	0.046	2.213	0.001	24.000
Tmbnew	0.498	0.025	5.434	6.503	0.011	2.511	0.003	0.000	0.000	0.045	0.000	24.000
Tmbnew	0.027	3.713	0.073	7.934	0.003	0.639	0.030	0.000	0.099	3.493	0.002	24.000
Tmbnew	0.000	0.516	0.048	0.000	0.009	0.001	7.310	0.019	0.066	8.693	0.000	24.000
Tmbnew	1.682	0.005	4.136	7.800	0.103	1.237	0.004	0.001	0.000	0.045	0.008	24.000
Tmbnew	0.090	2.904	0.239	7.825	0.004	3.129	0.047	0.000	0.052	1.759	0.007	24.000
Tmbnew	1.796	0.007	3.969	7.960	0.127	1.098	0.006	0.000	0.000	0.046	0.003	24.000
Tmbnew	0.032	3.807	0.069	7.960	0.005	0.632	0.027	0.001	0.098	3.365	0.000	24.000
Tmbnew	0.018	3.818	0.072	7.982	0.004	0.640	0.027	0.001	0.093	3.311	0.000	24.000
Tmbnew	1.294	0.013	4.577	7.316	0.054	1.694	0.008	0.003	0.000	0.095	0.007	24.000
Tmbkc	0.234	3.414	1.081	7.098	0.032	1.988	0.189	0.004	0.056	2.207	0.000	24.000
Tmbkc	1.722	0.020	3.436	8.491	0.161	0.791	0.008	0.002	0.003	0.078	0.011	24.000
Tmbkc	1.841	0.000	4.113	7.877	0.066	1.037	0.002	0.002	0.015	0.062	0.006	24.000
Tmbkc	0.124	3.646	0.631	7.646	0.008	3.038	0.055	0.079	0.021	0.761	0.000	24.000
Tmbkc	0.440	2.618	2.375	7.135	0.030	1.557	0.177	0.000	0.018	1.385	0.000	24.000
Tmbkc	0.005	10.314	0.002	6.043	0.005	0.021	0.000	0.000	0.023	1.549	0.001	24.000
Tmbkc	1.091	0.909	4.883	7.076	0.037	1.888	0.001	0.000	0.001	0.056	0.003	24.000
Tmbkc	0.001	10.463	0.003	6.049	0.004	0.019	0.000	0.002	0.019	1.390	0.002	24.000
Tmbkc	0.003	10.437	0.001	6.026	0.001	0.019	0.002	0.003	0.017	1.465	0.000	24.000
Tmatoro	1.108	3.366	2.294	6.565	0.051	1.886	0.178	0.005	0.015	1.219	0.000	24.000
Tmatoro	0.922	3.678	1.922	6.822	0.041	1.861	0.170	0.015	0.011	1.079	0.000	24.000
Tmatoro	0.995	3.661	1.876	6.845	0.042	1.896	0.155	0.025	0.009	1.060	0.000	24.000
Tmatoro	1.248	0.006	4.745	7.227	0.035	1.733	0.000	0.000	0.000	0.044	0.003	24.000
Tmatoro	1.412	0.006	4.575	7.398	0.023	1.582	0.002	0.000	0.000	0.032	0.000	24.000

unit	Na	Mg	Al	Si	K	Ca	Ti	Cr	Mn	Fe	Ba	O
Tmatoro	0.000	0.346	0.218	0.104	0.012	0.024	0.206	0.000	0.034	22.643	0.001	24.000
Tmatoro	1.518	0.022	4.446	7.509	0.045	1.454	0.004	0.000	0.003	0.042	0.003	24.000
Tmrslw	2.056	0.000	3.788	8.185	0.137	0.808	0.003	0.000	0.004	0.024	0.009	24.000
Tmrslw	0.092	0.981	0.138	7.923	0.006	3.295	0.031	0.001	0.090	3.468	0.000	24.000
Tmrslw	2.047	0.000	3.755	8.213	0.138	0.809	0.003	0.000	0.000	0.027	0.005	24.000
Tmrslw	1.897	0.000	3.124	8.834	0.926	0.182	0.000	0.002	0.000	0.038	0.011	24.000
Tmrslw	0.092	1.629	0.119	7.920	0.005	3.218	0.034	0.002	0.091	2.922	0.002	24.000
Tmrslw	2.083	0.000	3.273	8.686	0.576	0.332	0.003	0.000	0.000	0.035	0.017	24.000
Tmrslw	0.019	0.176	0.391	0.031	0.008	0.010	1.831	0.009	0.321	19.153	0.000	24.000
Tmrslw	0.096	1.577	0.123	7.932	0.008	3.195	0.026	0.000	0.089	2.988	0.000	24.000
Tmrslw	1.705	0.003	4.255	7.736	0.069	1.240	0.000	0.004	0.000	0.009	0.000	24.000
Tmrslw	2.146	0.000	3.726	8.238	0.147	0.753	0.001	0.000	0.003	0.024	0.008	24.000
Tmrslw	0.022	2.210	0.050	8.485	0.009	0.348	0.007	0.000	0.434	3.933	0.000	24.000
Tmdtomb	0.744	3.075	2.190	6.490	0.115	1.848	0.331	0.001	0.023	1.697	0.002	24.000
Tmdtomb	0.125	3.371	0.929	7.439	0.001	3.309	0.062	0.005	0.022	0.832	0.000	24.000
Tmdtomb	1.166	0.015	4.826	7.107	0.032	1.872	0.001	0.000	0.000	0.058	0.000	24.000
Tmdtomb	0.053	1.202	1.366	8.546	0.065	0.563	0.005	0.008	0.002	3.006	0.006	24.000
Tmdtomb	0.717	3.099	2.075	6.564	0.114	1.847	0.329	0.009	0.023	1.703	0.002	24.000
Tmdtomb	1.340	0.009	4.670	7.266	0.036	1.713	0.001	0.000	0.000	0.049	0.000	24.000
Tmdtomb	0.690	3.112	1.866	6.719	0.106	1.821	0.318	0.000	0.027	1.770	0.000	24.000
Tmdtomb	0.719	3.130	2.006	6.623	0.108	1.835	0.341	0.008	0.022	1.650	0.001	24.000
Tmdtomb	1.498	0.005	4.512	7.442	0.044	1.525	0.002	0.000	0.001	0.036	0.007	24.000
Tmdtomb	0.006	5.411	0.253	7.794	0.001	0.178	0.024	0.000	0.062	2.330	0.000	24.000
Tmdtomb	0.010	5.348	0.242	7.815	0.003	0.181	0.025	0.003	0.063	2.353	0.001	24.000



## Appendix B. Results from electron microprobe analyses (mineral compositions)

Unit	Mineral	Chemical composition
<sup>1</sup> Tmbkc	andesine	Ab <sub>64</sub> An <sub>30</sub> Or <sub>6</sub>
<sup>1</sup> Tmbkc	andesine	Ab <sub>61</sub> An <sub>37</sub> Or <sub>2</sub>
<sup>1</sup> Tmbkc	labradorite	Ab <sub>36</sub> An <sub>63</sub> Or <sub>1</sub>
<sup>1</sup> Tmbkc	amphibole	hornblende
<sup>1</sup> Tmbkc	augite	(Na <sub>0.03</sub> Ca <sub>0.76</sub> Fe <sup>2+</sup> <sub>0.19</sub> Mg <sub>0.92</sub> Fe <sup>3+</sup> <sub>0.00</sub> Ti <sub>0.01</sub> )(Al <sub>0.16</sub> Si <sub>1.92</sub> )O <sub>6</sub>
<sup>1</sup> Tmbkc	subcalic augite	(Na <sub>0.06</sub> Ca <sub>0.49</sub> Fe <sup>2+</sup> <sub>0.35</sub> Mg <sub>0.84</sub> Fe <sup>3+</sup> <sub>0.19</sub> Ti <sub>0.05</sub> )(Al <sub>0.27</sub> Si <sub>1.75</sub> )O <sub>6</sub>
<sup>1</sup> Tmbkc	olivine (Fo <sub>87</sub> Fa <sub>13</sub> )	(Fe <sup>2+</sup> <sub>0.87</sub> Mg <sub>0.13</sub> ) <sub>2</sub> SiO <sub>4</sub>
<sup>1</sup> Tmbkc	olivine (Fo <sub>88</sub> Fa <sub>12</sub> )	(Fe <sup>2+</sup> <sub>0.88</sub> Mg <sub>0.12</sub> ) <sub>2</sub> SiO <sub>4</sub>
<sup>1</sup> Tmbkc	olivine (Fo <sub>88</sub> Fa <sub>12</sub> )	(Fe <sup>2+</sup> <sub>0.88</sub> Mg <sub>0.12</sub> ) <sub>2</sub> SiO <sub>4</sub>
<sup>2</sup> Tmbkc	labradorite	Ab <sub>31</sub> An <sub>68</sub> Or <sub>1</sub>
<sup>2</sup> Tmbkc	labradorite	Ab <sub>31</sub> An <sub>68</sub> Or <sub>1</sub>
<sup>2</sup> Tmbkc	labradorite	Ab <sub>32</sub> An <sub>67</sub> Or <sub>1</sub>
<sup>2</sup> Tmbkc	cummingtonite	(Mg <sub>0.60</sub> Fe <sup>2+</sup> <sub>0.40</sub> ) <sub>7</sub> Si <sub>8</sub> O <sub>22</sub> (OH) <sub>2</sub>
<sup>2</sup> Tmbkc	amphibole	hornblende
<sup>2</sup> Tmbkc	augite	(Na <sub>0.03</sub> Ca <sub>0.76</sub> Fe <sup>2+</sup> <sub>0.24</sub> Mg <sub>0.84</sub> Fe <sup>3+</sup> <sub>0.07</sub> Ti <sub>0.02</sub> )(Al <sub>0.17</sub> Si <sub>1.87</sub> )O <sub>6</sub>
<sup>2</sup> Tmbkc	olivine (Fo <sub>88</sub> Fa <sub>12</sub> )	(Fe <sup>2+</sup> <sub>0.88</sub> Mg <sub>0.12</sub> ) <sub>2</sub> SiO <sub>4</sub>
<sup>2</sup> Tmbkc	olivine (Fo <sub>72</sub> Fa <sub>28</sub> )	(Fe <sup>2+</sup> <sub>0.72</sub> Mg <sub>0.28</sub> ) <sub>2</sub> SiO <sub>4</sub>
<sup>2</sup> Tmbkc	olivine (Fo <sub>79</sub> Fa <sub>21</sub> )	(Fe <sup>2+</sup> <sub>0.79</sub> Mg <sub>0.21</sub> ) <sub>2</sub> SiO <sub>4</sub>
Tmblol	andesine	Ab <sub>51</sub> An <sub>47</sub> Or <sub>2</sub>
Tmblol	andesine	Ab <sub>60</sub> An <sub>38</sub> Or <sub>2</sub>
Tmblol	amphibole	hornblende
Tmblol	ilmenite	(Mn <sub>0.01</sub> Fe <sup>2+</sup> <sub>0.77</sub> Mg <sub>0.10</sub> Fe <sup>3+</sup> <sub>0.25</sub> Ti <sub>0.88</sub> )O <sub>3</sub>
Tmblol	diopside	(Na <sub>0.02</sub> Ca <sub>0.85</sub> Fe <sup>2+</sup> <sub>0.16</sub> Mg <sub>0.87</sub> Fe <sup>3+</sup> <sub>0.03</sub> Ti <sub>0.01</sub> )(Al <sub>0.15</sub> Si <sub>1.91</sub> )O <sub>6</sub>
Tmblol	hypersthene	(Fe <sup>2+</sup> <sub>0.42</sub> Mg <sub>0.58</sub> )SiO <sub>3</sub>
Tmblol	bronzeite	(Fe <sup>2+</sup> <sub>0.17</sub> Mg <sub>0.83</sub> )SiO <sub>3</sub>
Tmblol	olivine (Fo <sub>82</sub> Fa <sub>18</sub> )	(Fe <sup>2+</sup> <sub>0.18</sub> Mg <sub>0.82</sub> ) <sub>2</sub> SiO <sub>4</sub>
<sup>1</sup> Tmdtomb	andesine	Ab <sub>64</sub> An <sub>33</sub> Or <sub>3</sub>
<sup>1</sup> Tmdtomb	andesine	Ab <sub>63</sub> An <sub>35</sub> Or <sub>2</sub>
<sup>1</sup> Tmdtomb	andesine	Ab <sub>59</sub> An <sub>39</sub> Or <sub>2</sub>

<sup>2</sup> Tmdtomb	andesine	Ab <sub>49</sub> An <sub>49</sub> Or <sub>2</sub>
<sup>2</sup> Tmdtomb	andesine	Ab <sub>56</sub> An <sub>41</sub> Or <sub>3</sub>
<sup>2</sup> Tmdtomb	andesine	Ab <sub>51</sub> An <sub>47</sub> Or <sub>2</sub>
<sup>2</sup> Tmdtomb	amphibole	hornblende
<sup>2</sup> Tmdtomb	amphibole	hornblende
<sup>2</sup> Tmdtomb	cummingtonite	(Mg <sub>0.52</sub> Fe <sup>2+</sup> <sub>0.48</sub> ) <sub>7</sub> Si <sub>8</sub> O <sub>22</sub> (OH) <sub>2</sub>
<sup>3</sup> Tmdtomb	andesine	Ab <sub>60</sub> An <sub>37</sub> Or <sub>3</sub>
<sup>3</sup> Tmdtomb	andesine	Ab <sub>63</sub> An <sub>34</sub> Or <sub>3</sub>
<sup>3</sup> Tmdtomb	andesine	Ab <sub>56</sub> An <sub>41</sub> Or <sub>3</sub>
<sup>4</sup> Tmdtomb	andesine	Ab <sub>58</sub> An <sub>39</sub> Or <sub>3</sub>
<sup>4</sup> Tmdtomb	andesine	Ab <sub>57</sub> An <sub>41</sub> Or <sub>2</sub>
<sup>4</sup> Tmdtomb	andesine	Ab <sub>56</sub> An <sub>41</sub> Or <sub>3</sub>
<sup>5</sup> Tmdtomb	andesine	Ab <sub>63</sub> An <sub>35</sub> Or <sub>2</sub>
<sup>5</sup> Tmdtomb	andesine	Ab <sub>59</sub> An <sub>39</sub> Or <sub>2</sub>
<sup>5</sup> Tmdtomb	andesine	Ab <sub>58</sub> An <sub>40</sub> Or <sub>2</sub>
<sup>6</sup> Tmdtomb	andesine	Ab <sub>62</sub> An <sub>34</sub> Or <sub>4</sub>
<sup>6</sup> Tmdtomb	andesine	Ab <sub>63</sub> An <sub>33</sub> Or <sub>4</sub>
<sup>6</sup> Tmdtomb	andesine	Ab <sub>56</sub> An <sub>41</sub> Or <sub>3</sub>
<sup>6</sup> Tmdtomb	andesine	Ab <sub>55</sub> An <sub>37</sub> Or <sub>8</sub>
<sup>6</sup> Tmdtomb	amphibole	hornblende
<sup>6</sup> Tmdtomb	amphibole	hornblende
<sup>6</sup> Tmdtomb	bronzite	(Fe <sup>2+</sup> <sub>0.21</sub> Mg <sub>0.79</sub> )SiO <sub>3</sub>
<sup>7</sup> Tmdtomb	labradorite	Ab <sub>38</sub> An <sub>61</sub> Or <sub>1</sub>
<sup>7</sup> Tmdtomb	labradorite	Ab <sub>43</sub> An <sub>56</sub> Or <sub>1</sub>
<sup>7</sup> Tmdtomb	labradorite	Ab <sub>49</sub> An <sub>50</sub> Or <sub>1</sub>
<sup>7</sup> Tmdtomb	amphibole	hornblende
<sup>7</sup> Tmdtomb	amphibole	hornblende
<sup>7</sup> Tmdtomb	amphibole	hornblende
<sup>7</sup> Tmdtomb	amphibole	hornblende
<sup>7</sup> Tmdtomb	grunerite	(Fe <sup>2+</sup> <sub>0.71</sub> Mg <sub>0.29</sub> ) <sub>7</sub> Si <sub>8</sub> O <sub>22</sub> (OH) <sub>2</sub>
<sup>7</sup> Tmdtomb	augite	(Na <sub>0.03</sub> Ca <sub>0.82</sub> Fe <sup>2+</sup> <sub>0.14</sub> Mg <sub>0.84</sub> Fe <sup>3+</sup> <sub>0.06</sub> Ti <sub>0.02</sub> )(Al <sub>0.23</sub> Si <sub>1.85</sub> )O <sub>6</sub>
<sup>7</sup> Tmdtomb	hypersthene	(Fe <sup>2+</sup> <sub>0.30</sub> Mg <sub>0.70</sub> )SiO <sub>3</sub>
<sup>7</sup> Tmdtomb	hypersthene	(Fe <sup>2+</sup> <sub>0.31</sub> Mg <sub>0.69</sub> )SiO <sub>3</sub>

<i>Tmr<sub>sf</sub></i>	anorthoclase	Ab <sub>56</sub> An <sub>3</sub> Or <sub>41</sub>
<i>Tmr<sub>sf</sub></i>	anorthoclase	Ab <sub>66</sub> An <sub>5</sub> Or <sub>28</sub>
<i>Tmr<sub>sf</sub></i>	anorthoclase	Ab <sub>68</sub> An <sub>6</sub> Or <sub>26</sub>
<i>Tmatoro</i>	labradorite	Ab <sub>41</sub> An <sub>58</sub> Or <sub>1</sub>
<i>Tmatoro</i>	labradorite	Ab <sub>47</sub> An <sub>52</sub> Or <sub>1</sub>
<i>Tmatoro</i>	andesine	Ab <sub>50</sub> An <sub>48</sub> Or <sub>2</sub>
<i>Tmatoro</i>	amphibole	hornblende
<i>Tmatoro</i>	amphibole	hornblende
<i>Tmatoro</i>	amphibole	hornblende
<i>Tmatoro</i>	hematite	(Mg <sub>0.03</sub> Fe <sup>3+</sup> <sub>1.96</sub> Ti <sub>0.02</sub> )O <sub>3</sub>
<sup>1</sup> <i>Tmr<sub>siw</sub></i>	oligoclase	Ab <sub>72</sub> An <sub>22</sub> Or <sub>6</sub>
<sup>1</sup> <i>Tmr<sub>siw</sub></i>	oligoclase	Ab <sub>73</sub> An <sub>20</sub> Or <sub>7</sub>
<sup>1</sup> <i>Tmr<sub>siw</sub></i>	oligoclase	Ab <sub>73</sub> An <sub>21</sub> Or <sub>6</sub>
<sup>2</sup> <i>Tmr<sub>siw</sub></i>	oligoclase	Ab <sub>71</sub> An <sub>24</sub> Or <sub>5</sub>
<sup>2</sup> <i>Tmr<sub>siw</sub></i>	oligoclase	Ab <sub>72</sub> An <sub>22</sub> Or <sub>6</sub>
<sup>2</sup> <i>Tmr<sub>siw</sub></i>	oligoclase	Ab <sub>70</sub> An <sub>25</sub> Or <sub>5</sub>
<sup>3</sup> <i>Tmr<sub>siw</sub></i>	oligoclase	Ab <sub>73</sub> An <sub>21</sub> Or <sub>6</sub>
<sup>3</sup> <i>Tmr<sub>siw</sub></i>	oligoclase	Ab <sub>71</sub> An <sub>24</sub> Or <sub>5</sub>
<sup>3</sup> <i>Tmr<sub>siw</sub></i>	oligoclase	Ab <sub>73</sub> An <sub>21</sub> Or <sub>6</sub>
<sup>4</sup> <i>Tmr<sub>siw</sub></i>	andesine	Ab <sub>68</sub> An <sub>27</sub> Or <sub>5</sub>
<sup>4</sup> <i>Tmr<sub>siw</sub></i>	andesine	Ab <sub>68</sub> An <sub>27</sub> Or <sub>5</sub>
<sup>4</sup> <i>Tmr<sub>siw</sub></i>	anorthoclase	Ab <sub>63</sub> An <sub>6</sub> Or <sub>31</sub>
<sup>4</sup> <i>Tmr<sub>siw</sub></i>	anorthoclase	Ab <sub>70</sub> An <sub>11</sub> Or <sub>19</sub>
<sup>4</sup> <i>Tmr<sub>siw</sub></i>	andesine	Ab <sub>57</sub> An <sub>41</sub> Or <sub>2</sub>
<sup>4</sup> <i>Tmr<sub>siw</sub></i>	oligoclase	Ab <sub>70</sub> An <sub>25</sub> Or <sub>5</sub>
<sup>4</sup> <i>Tmr<sub>siw</sub></i>	ferroaugite	(Na <sub>0.02</sub> Ca <sub>0.83</sub> Fe <sup>2+</sup> <sub>0.87</sub> Mg <sub>0.25</sub> Fe <sup>3+</sup> <sub>0.01</sub> Ti <sub>0.01</sub> )(Al <sub>0.04</sub> Si <sub>1.98</sub> )O <sub>6</sub> ]
<sup>4</sup> <i>Tmr<sub>siw</sub></i>	ferroaugite	(Na <sub>0.02</sub> Ca <sub>0.81</sub> Fe <sup>2+</sup> <sub>0.73</sub> Mg <sub>0.41</sub> Fe <sup>3+</sup> <sub>0.01</sub> Ti <sub>0.01</sub> )(Al <sub>0.03</sub> Si <sub>1.98</sub> )O <sub>6</sub> ]
<sup>4</sup> <i>Tmr<sub>siw</sub></i>	ferroaugite	(Na <sub>0.02</sub> Ca <sub>0.80</sub> Fe <sup>2+</sup> <sub>0.74</sub> Mg <sub>0.40</sub> Fe <sup>3+</sup> <sub>0.01</sub> Ti <sub>0.01</sub> )(Al <sub>0.03</sub> Si <sub>1.99</sub> )O <sub>6</sub> ]
<sup>4</sup> <i>Tmr<sub>siw</sub></i>	clinopyroxene	pigeonite
<sup>4</sup> <i>Tmr<sub>siw</sub></i>	hematite	(Mn <sub>0.03</sub> Fe <sup>2+</sup> <sub>0.12</sub> Mg <sub>0.02</sub> Fe <sup>3+</sup> <sub>1.66</sub> Ti <sub>0.17</sub> )O <sub>3</sub>
<i>Tmb<sub>new</sub></i>	bytownite	Ab <sub>17</sub> An <sub>83</sub>

<i>Tmbnew</i>	andesine	$\text{Ab}_{56}\text{An}_{41}\text{Or}_3$
<i>Tmbnew</i>	andesine	$\text{Ab}_{60}\text{An}_{36}\text{Or}_4$
<i>Tmbnew</i>	labradorite	$\text{Ab}_{42}\text{An}_{56}\text{Or}_2$
<i>Tmbnew</i>	ilmenite	$\text{Mn}_{0.01}\text{Fe}^{2+}_{0.81}\text{Mg}_{0.06}\text{Fe}^{3+}_{0.24}\text{Ti}_{0.88}\text{O}_3$
<i>Tmbnew</i>	clinopyroxene	pigeonite
<i>Tmbnew</i>	clinopyroxene	pigeonite
<i>Tmbnew</i>	clinopyroxene	pigeonite
<i>Tmbnew</i>	augite	$(\text{Na}_{0.02}\text{Ca}_{0.78}\text{Fe}^{2+}_{0.42}\text{Mg}_{0.73}\text{Fe}^{3+}_{0.02}\text{Ti}_{0.01})(\text{Al}_{0.06}\text{Si}_{1.96})\text{O}_6$
<i>Tmr3</i>	anorthoclase	$\text{Ab}_{64}\text{An}_1\text{Or}_{35}$
<i>Tmr3</i>	anorthoclase	$\text{Ab}_{63}\text{An}_1\text{Or}_{36}$
<i>Tmr3</i>	anorthoclase	$\text{Ab}_{66}\text{An}_2\text{Or}_{32}$
<i>Tmrec</i>	oligoclase	$\text{Ab}_{71}\text{An}_{23}\text{Or}_6$
<i>Tmrec</i>	anorthoclase	$\text{Ab}_{58}\text{An}_5\text{Or}_{37}$
<i>Tmrec</i>	oligoclase	$\text{Ab}_{73}\text{An}_{22}\text{Or}_5$
<i>Tmrec</i>	oligoclase	$\text{Ab}_{74}\text{An}_{19}\text{Or}_7$
<i>Tmrec</i>	anorthoclase	$\text{Ab}_{50}\text{An}_3\text{Or}_{47}$
<i>Tmrec</i>	magnetite	$(\text{Fe}^{2+}_{1.27}\text{Mg}_{0.04}\text{Fe}^{3+}_{1.33}\text{Al}_{0.03}\text{Ti}_{0.31})\text{O}_4$
<i>Tmrec</i>	amphibole	hornblende
<i>Tmrec</i>	amphibole	hornblende
<i>Tmagem</i>	labradorite	$\text{Ab}_{35}\text{An}_{64}\text{Or}_1$
<i>Tmagem</i>	bytownite	$\text{Ab}_{20}\text{An}_{80}$
<i>Tmagem</i>	labradorite	$\text{Ab}_{32}\text{An}_{68}$
<i>Tmagem</i>	diopside	$(\text{Na}_{0.02}\text{Ca}_{0.83}\text{Fe}^{2+}_{0.15}\text{Mg}_{0.95}\text{Fe}^{3+}_{0.04}\text{Ti}_{0.02})(\text{Al}_{0.11}\text{Si}_{1.91})\text{O}_6$
<i>Tmagem</i>	augite	$(\text{Na}_{0.02}\text{Ca}_{0.79}\text{Fe}^{2+}_{0.21}\text{Mg}_{0.87}\text{Fe}^{3+}_{0.05}\text{Ti}_{0.03})(\text{Al}_{0.14}\text{Si}_{1.89})\text{O}_6$
<i>Tmagem</i>	bronzeite	$(\text{Fe}^{2+}_{0.17}\text{Mg}_{0.83})\text{SiO}_3$
<i>Tmagem</i>	bronzeite	$(\text{Fe}^{2+}_{0.21}\text{Mg}_{0.79})\text{SiO}_3$
<i>Tmrcan</i>	oligoclase	$\text{Ab}_{69}\text{An}_{22}\text{Or}_9$
<i>Tmrcan</i>	oligoclase	$\text{Ab}_{71}\text{An}_{20}\text{Or}_9$
<i>Tmrcan</i>	magnetite	$(\text{Fe}^{2+}_{1.25}\text{Mg}_{0.04}\text{Fe}^{3+}_{1.26}\text{Al}_{0.16}\text{Ti}_{0.29})\text{O}_4$
<i>Tmrcan</i>	ilmenite	$(\text{Mn}_{0.01}\text{Fe}^{2+}_{0.68}\text{Mg}_{0.03}\text{Fe}^{3+}_{0.55}\text{Ti}_{0.73})\text{O}_3$
<i>Tmrcan</i>	augite	$(\text{Na}_{0.02}\text{Ca}_{0.87}\text{Fe}^{2+}_{0.19}\text{Mg}_{0.85}\text{Fe}^{3+}_{0.01}\text{Ti}_{0.01})(\text{Al}_{0.10}\text{Si}_{1.94})\text{O}_6$
<i>Tmrcan</i>	augite	$(\text{Na}_{0.01}\text{Ca}_{0.84}\text{Fe}^{2+}_{0.24}\text{Mg}_{0.88}\text{Fe}^{3+}_{0.00}\text{Ti}_{0.01})(\text{Al}_{0.04}\text{Si}_{1.98})\text{O}_6$
<i>Tmrcan</i>	bronzeite	$(\text{Fe}^{2+}_{0.19}\text{Mg}_{0.81})\text{SiO}_3$

<sup>x</sup> <i>Tmr</i> can	labradorite	Ab <sub>33</sub> An <sub>67</sub>
<sup>x</sup> <i>Tmr</i> can	labradorite	Ab <sub>31</sub> An <sub>69</sub>
<sup>x</sup> <i>Tmr</i> can	bronzite	(Fe <sup>2+</sup> <sub>0.24</sub> Mg <sub>0.76</sub> )SiO <sub>3</sub>
<sup>x</sup> <i>Tmr</i> can	bronzite	(Fe <sup>2+</sup> <sub>0.23</sub> Mg <sub>0.77</sub> )SiO <sub>3</sub>
<i>Tmahem</i>	labradorite	Ab <sub>38</sub> An <sub>61</sub> Or <sub>1</sub>
<i>Tmahem</i>	labradorite	Ab <sub>37</sub> An <sub>62</sub> Or <sub>1</sub>
<i>Tmahem</i>	bytownite	Ab <sub>16</sub> An <sub>84</sub>
<i>Tmahem</i>	diopside	(Na <sub>0.02</sub> Ca <sub>0.83</sub> Fe <sup>2+</sup> <sub>0.14</sub> Mg <sub>0.93</sub> Fe <sup>3+</sup> <sub>0.02</sub> Ti <sub>0.01</sub> )(Al <sub>0.09</sub> Si <sub>1.95</sub> )O <sub>6</sub>
<i>Tmahem</i>	diopside	(Na <sub>0.02</sub> Ca <sub>0.87</sub> Fe <sup>2+</sup> <sub>0.12</sub> Mg <sub>0.91</sub> Fe <sup>3+</sup> <sub>0.03</sub> Ti <sub>0.01</sub> )(Al <sub>0.10</sub> Si <sub>1.94</sub> )O <sub>6</sub>
<i>Tmahem</i>	bronzite	(Fe <sup>2+</sup> <sub>0.20</sub> Mg <sub>0.80</sub> )SiO <sub>3</sub>
<i>Tmahem</i>	bronzite	(Fe <sup>2+</sup> <sub>0.17</sub> Mg <sub>0.83</sub> )SiO <sub>3</sub>
<i>Tmahem</i>	bronzite	(Fe <sup>2+</sup> <sub>0.22</sub> Mg <sub>0.78</sub> )SiO <sub>3</sub>
<i>Tmahem</i>	bronzite	(Fe <sup>2+</sup> <sub>0.29</sub> Mg <sub>0.71</sub> )SiO <sub>3</sub>

Superscripts before unit names (e.g., <sup>2</sup>*Tmr*<sub>SiW</sub>) indicate different rock samples of same lithologic unit; superscript <sup>x</sup> indicates xenolith within rock sample.

## APPENDIX C

Details of mineral separation techniques for  $^{40}\text{Ar}/^{39}\text{Ar}$  geochronology samples

Hand samples are first crushed by hand using a clean sledge hammer and steel plate on a rock table. After washing with water and acetone, the table is lined with clean brown paper and the sample is also wrapped in clean brown paper to decrease the number of flying chips. The hammer and steel plate are washed with water and acetone between each sample as well as cleaned with an electrical rotating wire-brush. After hand crushing to small pieces (averaging 2 cm in diameter and less), the sample is mechanically crushed to 5 mm size particles and smaller with a table-top rock crusher. The crusher is cleaned carefully between each sample with water and acetone. In some instances samples are pulverized with a larger disk mill to yield a larger fraction of small-size particles. This equipment and the room in which it is located is cleaned between each sample with a vacuum, air hose, water and acetone.

Samples are then sieved in either metal or disposable sieves. Sieve sizes found to be most useful were #30 (0.59 mm) and #60 (0.25 mm), although some #80 (0.177 mm) and #100 (0.149 mm) sieves were also employed. The metal sieves are carefully cleaned between each sample by several rinses in an ultrasonic bath followed by grain removal by hand with forceps under a binocular microscope.

Chosen sieved fractions (usually the #30-#60 fraction) are then repeatedly washed and decanted by hand in clean beakers until the water is fairly clear (5-10 times). The same sample is placed in the ultrasonic bath for 5-10 minutes and decanted in a similar manner until the water is clear (5-10 times). Samples are dried in filter paper-lined funnels placed within Erlenmeyer flasks under a fume hood. Acetone is poured into the sample and allowed to drain three times. Samples finish drying naturally in the air covered with chemical wipes to avoid contamination. In some instances, samples were sieved again to remove fine particles, although this was eventually deemed unnecessary.

Samples are now ready for mineralogical separation. A strong hand magnet cleaned with ethyl alcohol and acetone and wrapped in a chemical wipe is passed through a sample for 10-15 minutes to remove strongly magnetic grains. From this stage onward all

separations are placed in individual glass vials and labeled appropriately. After the removal of hand magnetics, minerals are further separated using a Frantz isodynamic separator. This instrument separates grains based upon variations in magnetic susceptibility. The first pass, typically at around 0.2 amperes (A), yields a magnetic and a non-magnetic fraction. The magnetic fraction is labeled and set aside and the non-magnetic fraction is passed through the Frantz at a higher current, for example 0.4 A. This process is continued in 4 to 6 steps to the maximum current of  $\approx 1.8$  A. At this point the non-magnetic fractions can still be run at maximum current in conjunction with gradual changes in the side/front slope ratio (initially 10/20 to as low as 5/20). The Frantz and several of its removable parts are cleaned with water, acetone, and ethyl alcohol between each sample. The final non-magnetic fractions of each sample, which at this stage ideally consist of at least 1 gram of material, are washed in de-ionized water and placed in the ultra-sonic cleaner for approximately 30 minutes to try to break off any glass from the mineral grains. HF was not used in this study.

Minerals and volcanic glass can be further separated based upon their specific gravities. The principal minerals involved are quartz ( $2.65 \text{ g/cm}^3$ ), alkali feldspar ( $2.55$  to  $2.63 \text{ g/cm}^3$ ), and plagioclase feldspar ( $2.62 \text{ g/cm}^3$  [Ab] to  $2.76 \text{ g/cm}^3$  [An]). Volcanic glass is considerably less dense than any of these minerals. The separation involves the use of heavy liquids. Acetylene tetra bromide (ATB) has a density of  $2.96 \text{ g/cm}^3$  and can be mixed with acetone ( $0.7848 \text{ g/cm}^3$ ) to generate a spectrum of densities in which to sink and float the different minerals. This is performed under a ventilated fume hood with extreme care since ATB is carcinogenic. Separations were generally started with a liquid of the same density as quartz, and the first fractionation removed prior to adding acetone to the liquid to decrease its density. In general, not many crystals sank during the initial step, suggesting that much of the plagioclase in these samples is of an albitic composition. Between 2 and 5 fractionations were made using the heavy liquids for each sample. Fractions are dried using acetone as described above for washed samples.

Following heavy liquid separation, selected separates are placed in an ultrasonic bath in 10% HCl for 10 minutes, washed three times with de-ionized water, and dried with acetone as described above. This removes any carbonate that might be encrusted on the grains.

Samples are finally hand-picked with forceps and the aid of a binocular microscope. A small amount of sample (100-200 mg) is placed in a clean petri dish partially filled with ethyl alcohol. Initially a few individual crystals are placed in clove oil on a glass slide and examined in the petrographic microscope using the Becke line test to insure that feldspars, and not quartz grains, are being selected. After the desired grains are separated they are removed with a clean disposable pipette and dried on weighing paper. The mass of final plagioclase separates ranged from 45 to 150 mg for a given sample and anorthoclase samples ranged from 40 to 50 mg.



APPENDIX D.  $^{40}\text{Ar}/^{39}\text{Ar}$  laser fusion analytical data

Sample	$^{40}\text{Ar}/^{39}\text{Ar}^a$	$^{38}\text{Ar}/^{39}\text{Ar}^a$ ( $\times 10^{-2}$ )	$^{37}\text{Ar}/^{39}\text{Ar}^a$	$^{36}\text{Ar}/^{39}\text{Ar}^a$ ( $\times 10^{-2}$ )	$^{39}\text{Ar}_K$ ( $\times 10^{-15}$ mol)	$^{40}\text{Ar}^*$ (%)	$^{40}\text{Ar}^*/^{39}\text{Ar}_K$	Model Age $\ddagger$ (Ma) ( $\pm 1\sigma$ )
INF-94-53A (Lab Session 1)								
1	13.385	2.771	0.029	1.843	1.71	58.2	7.925	6.0 $\pm$ 0.2
2	16.904	2.867	0.037	2.854	5.89	49.8	8.458	6.4 $\pm$ 0.1
3	15.677	2.418	0.031	2.453	4.70	53.4	8.416	6.3 $\pm$ 0.1
4	17.683	2.376	0.027	3.167	5.74	46.8	8.312	6.3 $\pm$ 0.1
5	35.121	3.690	0.022	9.257	3.63	22.0	7.754	5.8 $\pm$ 0.1
6	10.831	1.864	0.029	0.901	5.05	74.8	8.155	6.1 $\pm$ 0.1
INF-94-53B (Lab Session 1)								
1	19.007	2.321	0.030	3.692	5.45	42.4	8.084	6.1 $\pm$ 0.1
2	24.608	3.301	0.025	5.622	4.32	32.3	7.984	6.1 $\pm$ 0.1
3	12.687	2.295	0.030	1.524	6.35	64.1	8.172	6.2 $\pm$ 0.1
4	27.255	3.275	0.032	6.629	2.58	27.9	7.652	5.8 $\pm$ 0.1
5	38.357	3.437	0.030	10.310	7.92	20.5	7.882	6.0 $\pm$ 0.1
INF-94-53C (Lab Session 1)								
1	11.904	1.832	0.024	1.204	9.05	69.8	8.332	6.2 $\pm$ 0.1
2	19.388	2.765	0.027	3.783	10.00	42.2	8.197	6.1 $\pm$ 0.1
3	17.891	3.362	0.024	3.283	5.28	45.5	8.177	6.1 $\pm$ 0.1
4	19.499	2.633	0.030	3.929	2.74	40.1	7.877	5.8 $\pm$ 0.1
5	11.980	2.386	0.032	1.296	7.07	67.6	8.137	6.0 $\pm$ 0.1
INF-94-53 $\gamma$ (Lab Session 1)								
1	16.912	2.359	0.027	3.020	5.38	47.0	7.974	6.0 $\pm$ 0.1
2	9.880	1.821	0.026	0.545	5.30	83.0	8.257	6.2 $\pm$ 0.1
3	15.333	2.388	0.030	2.436	7.50	52.8	8.121	6.1 $\pm$ 0.1
4	26.885	2.975	0.031	6.390	8.96	29.7	7.990	6.0 $\pm$ 0.1
INF-94-53A (Lab Session 2)								
1	32.504	6.663	0.035	9.964	1.92	9.4	3.049	4.5 $\pm$ 0.7
2	8.779	2.945	0.039	1.539	2.41	48.1	4.219	6.2 $\pm$ 0.4
3	5.840	2.993	0.052	0.506	2.82	74.2	4.334	6.4 $\pm$ 0.4
4	27.622	7.501	0.041	7.989	3.13	14.5	4.003	5.9 $\pm$ 0.5

Sample	$^{40}\text{Ar}/^{39}\text{Ar}^a$	$^{38}\text{Ar}/^{39}\text{Ar}^a$ ( $\times 10^{-2}$ )	$^{37}\text{Ar}/^{39}\text{Ar}^a$	$^{36}\text{Ar}/^{39}\text{Ar}^a$ ( $\times 10^{-2}$ )	$^{39}\text{Ar}_k$ ( $\times 10^{-15}$ mol)	$^{40}\text{Ar}^*$ (%)	$^{40}\text{Ar}^*/^{39}\text{Ar}_k$	Model Age $\dagger$ (Ma) ( $\pm 1\sigma$ )
INF-94-53B (Lab Session 2)								
1	12.846	3.622	0.045	2.975	4.47	31.5	4.044	6.0 $\pm$ 0.3
2	13.755	3.885	0.034	3.379	5.16	27.3	3.760	5.6 $\pm$ 0.3
3	10.141	3.552	0.016	1.943	5.50	43.2	4.386	6.5 $\pm$ 0.3
4	13.349	2.807	0.037	3.098	17.22	31.3	4.183	6.2 $\pm$ 0.2
5	8.477	2.271	0.034	1.406	14.71	50.8	4.310	6.4 $\pm$ 0.2
INF-94-53C (Lab Session 2)								
1	7.803	3.381	0.032	1.138	5.43	56.7	4.428	6.4 $\pm$ 0.2
2	14.001	3.457	0.032	3.313	10.91	30.0	4.200	6.1 $\pm$ 0.2
3	10.520	2.566	0.060	2.078	13.86	41.5	4.370	6.3 $\pm$ 0.2
4	70.068	6.958	0.091	22.835	2.57	3.7	2.583	3.8 $\pm$ 0.7
5	10.914	2.981	0.036	2.238	20.29	39.3	4.290	6.2 $\pm$ 0.1
INF-94-53D (Lab Session 2)								
1	8.888	2.614	0.024	1.540	12.10	48.7	4.325	6.3 $\pm$ 0.2
2	23.537	3.660	0.051	6.611	9.43	17.0	3.992	5.8 $\pm$ 0.2
3	18.362	3.306	0.040	4.837	12.27	22.1	4.057	5.9 $\pm$ 0.2
4	86.286	8.627	0.040	28.677	2.37	1.8	1.534	2.2 $\pm$ 0.9
INF-94-53E (Lab Session 2)								
1	7.433	2.693	0.027	1.059	12.86	57.7	4.292	6.3 $\pm$ 0.1
2	15.738	2.994	0.045	3.937	12.81	26.0	4.094	6.0 $\pm$ 0.2
3	13.016	3.407	0.037	2.966	9.32	32.6	4.241	6.2 $\pm$ 0.2
4	7.161	2.841	0.032	0.961	9.74	60.2	4.309	6.3 $\pm$ 0.2
5	20.411	3.555	0.044	5.541	8.24	19.7	4.027	5.9 $\pm$ 0.2
INF-94-53F (Lab Session 2)								
1	7.450	2.200	0.019	1.022	16.80	59.3	4.417	6.3 $\pm$ 0.1
2	47.080	5.707	0.016	14.792	5.03	7.1	3.356	4.8 $\pm$ 0.4
INF-94-75								
1	12.913	2.138	0.284	1.623	23.10	62.8	8.125	6.1 $\pm$ 0.1
2	14.313	1.843	0.161	1.540	14.80	68.1	9.761	7.3 $\pm$ 0.1
3	14.907	1.722	0.231	1.179	14.80	76.5	11.428	8.6 $\pm$ 0.1

Sample	$^{40}\text{Ar}/^{39}\text{Ar}^a$	$^{38}\text{Ar}/^{39}\text{Ar}^a$	$^{37}\text{Ar}/^{39}\text{Ar}^a$	$^{36}\text{Ar}/^{39}\text{Ar}^a$	$^{39}\text{Ar}_K$ ( $\times 10^{15}$ mol)	$^{40}\text{Ar}^*$ (%)	$^{40}\text{Ar}^*/^{39}\text{Ar}_K$	Model Age $\ddagger$ (Ma) ( $\pm 1\sigma$ )
4	<b>95.274</b>	<b>16.620</b>	<b>0.293</b>	<b>30.880</b>	<b>0.30</b>	<b>4.2</b>	<b>4.036</b>	<b>3.0 <math>\pm</math> 1.8</b>
5	16.771	2.259	0.211	2.925	13.20	48.4	8.132	6.1 $\pm$ 0.1
6	50.670	4.471	0.241	14.720	11.60	14.1	7.164	5.4 $\pm$ 0.2
7	39.737	4.164	0.219	10.060	7.27	25.1	10.004	7.5 $\pm$ 0.1
8	13.870	1.798	0.438	1.779	8.38	62.0	8.636	6.5 $\pm$ 0.1
9	11.660	1.915	0.298	1.074	5.08	72.4	8.497	6.4 $\pm$ 0.1
10	26.282	3.337	0.254	6.168	3.86	30.6	8.063	6.1 $\pm$ 0.1
11	23.745	3.542	0.435	5.431	4.22	32.4	7.718	5.8 $\pm$ 0.1
12	65.443	6.270	0.258	19.860	4.97	10.3	6.768	5.1 $\pm$ 0.2
13	26.552	3.339	0.270	6.339	4.05	29.4	7.827	5.9 $\pm$ 0.1
INF-94-47								
1	16.368	3.928	1.935	2.676	5.96	52.3	8.611	6.5 $\pm$ 0.1
2	14.756	3.715	1.946	2.187	3.98	56.8	8.445	6.4 $\pm$ 0.1
3	19.620	5.580	1.800	3.768	2.61	43.6	8.625	6.5 $\pm$ 0.1
4	<b>129.981</b>	<b>25.200</b>	<b>0.466</b>	<b>44.590</b>	<b>0.12</b>	<b>-1.3</b>	<b>-1.767</b>	<b>-1.3 <math>\pm</math> 3.6</b>
5	14.053	3.636	1.994	1.851	4.23	61.7	8.738	6.6 $\pm$ 0.1
6	13.414	3.497	1.999	1.702	3.27	63.0	8.541	6.5 $\pm$ 0.1
7	<b>49.725</b>	<b>14.620</b>	<b>0.610</b>	<b>14.630</b>	<b>0.37</b>	<b>12.8</b>	<b>6.527</b>	<b>4.9 <math>\pm</math> 1.0</b>
8	11.999	3.149	2.063	1.285	4.03	69.1	8.361	6.3 $\pm$ 0.1
9	13.002	3.435	2.025	1.578	2.86	64.6	8.497	6.4 $\pm$ 0.1
CHO-94-45								
1	16.251	2.072	2.235	2.619	2.59	52.9	8.687	6.5 $\pm$ 0.2
2	14.314	1.896	2.186	1.966	3.75	60.1	8.675	6.5 $\pm$ 0.1
3	13.744	1.796	2.268	1.750	5.12	63.2	8.751	6.6 $\pm$ 0.1
4	18.490	2.230	2.248	3.437	3.58	45.7	8.512	6.4 $\pm$ 0.1
5	<b>124.529</b>	<b>10.250</b>	<b>1.129</b>	<b>41.200</b>	<b>0.25</b>	<b>2.3</b>	<b>2.874</b>	<b>2.2 <math>\pm</math> 1.3</b>
6	14.195	1.881	2.162	1.854	2.95	61.9	8.886	6.7 $\pm$ 0.1
7	20.787	2.222	2.287	4.289	2.48	39.5	8.293	6.2 $\pm$ 0.2
8	14.769	1.969	2.171	2.194	5.63	56.9	8.455	6.4 $\pm$ 0.1
INN-94-33								
1	48.455	4.033	2.271	13.730	4.49	16.6	8.051	6.1 $\pm$ 0.2

Sample	$^{40}\text{Ar}/^{39}\text{Ar}^a$	$^{38}\text{Ar}/^{39}\text{Ar}^a$ ( $\times 10^{-2}$ )	$^{37}\text{Ar}/^{39}\text{Ar}^a$	$^{36}\text{Ar}/^{39}\text{Ar}^a$ ( $\times 10^{-2}$ )	$^{39}\text{Ar}_K$ ( $\times 10^{15}$ mol)	$^{40}\text{Ar}^*$ (%)	$^{40}\text{Ar}^*/^{39}\text{Ar}_K$	Model Age $\ddagger$ (Ma) ( $\pm 1\sigma$ )
2	62.686	5.005	2.362	18.830	4.12	11.5	7.242	$5.5 \pm 0.2$
3	<b>1893.739</b>	<b>124.800</b>	<b>1.612</b>	<b>660.600</b>	<b>0.06</b>	<b>-3.1</b>	<b>-58.246</b>	<b>-44.6 <math>\pm</math> 38.9</b>
4	84.247	6.375	2.196	26.100	2.90	8.6	7.286	$5.5 \pm 0.2$
5	45.429	3.877	2.180	12.750	2.28	17.4	7.928	$6.0 \pm 0.2$
6	79.910	6.242	2.218	24.570	2.94	9.3	7.467	$5.6 \pm 0.3$
7	146.328	10.61	1.987	47.920	0.80	3.3	4.881	$3.7 \pm 0.9$
8	133.443	9.53	2.183	43.170	4.69	4.5	6.039	$4.6 \pm 0.4$
INF-94-68								
1	43.694	3.761	20.655	11.230	1.59	27.6	12.301	$9.3 \pm 0.2$
2	<b>52.647</b>	<b>5.237</b>	<b>14.892</b>	<b>14.900</b>	<b>0.17</b>	<b>17.8</b>	<b>9.887</b>	<b>7.5 <math>\pm</math> 1.5</b>
3	34.267	3.221	21.849	8.440	2.38	32.1	11.215	$8.5 \pm 0.2$
4	<b>44.660</b>	<b>4.067</b>	<b>16.966</b>	<b>11.680</b>	<b>0.29</b>	<b>24.9</b>	<b>11.607</b>	<b>8.8 <math>\pm</math> 1.2</b>
5	33.421	3.271	22.820	7.632	1.40	37.6	12.866	$9.8 \pm 0.4$
6	<b>59.589</b>	<b>6.021</b>	<b>13.097</b>	<b>17.730</b>	<b>0.33</b>	<b>13.5</b>	<b>8.302</b>	<b>6.3 <math>\pm</math> 1.1</b>
7	39.462	3.906	23.926	9.943	0.92	30.0	12.164	$9.2 \pm 0.4$
8	<b>114.844</b>	<b>9.118</b>	<b>11.403</b>	<b>38.910</b>	<b>0.07</b>	<b>0.6</b>	<b>0.759</b>	<b>0.6 <math>\pm</math> 3.6</b>
9	29.662	3.121	22.893	7.132	1.47	34.7	10.557	$8.0 \pm 0.2$
10	<b>71.554</b>	<b>6.994</b>	<b>13.858</b>	<b>22.220</b>	<b>0.26</b>	<b>9.6</b>	<b>7.061</b>	<b>5.4 <math>\pm</math> 1.3</b>
11	31.432	3.208	22.590	6.904	1.24	40.4	13.009	$9.9 \pm 0.3$
12	<b>62.811</b>	<b>5.744</b>	<b>13.210</b>	<b>18.020</b>	<b>0.23</b>	<b>16.4</b>	<b>10.696</b>	<b>8.1 <math>\pm</math> 1.5</b>
13	26.604	2.998	21.670	6.028	0.95	38.9	10.655	$8.1 \pm 0.3$
DIN-94-46								
1	39.912	2.998	7.208	6.874	2.17	50.3	20.255	$15.3 \pm 0.3$
2	38.556	2.742	7.150	6.496	2.18	51.4	20.008	$15.1 \pm 0.2$
3	37.532	2.732	6.903	6.134	3.02	53.0	20.031	$15.2 \pm 0.1$
4	<b>164.824</b>	<b>12.120</b>	<b>6.872</b>	<b>54.280</b>	<b>0.12</b>	<b>3.0</b>	<b>4.991</b>	<b>3.8 <math>\pm</math> 2.8</b>
5	40.067	2.938	6.941	7.176	1.97	48.2	19.489	$14.7 \pm 0.2$
6	64.417	4.410	6.929	15.400	1.86	30.1	19.543	$14.8 \pm 0.3$
7	47.164	3.362	6.803	9.625	1.39	40.6	19.336	$14.6 \pm 0.3$
8	58.309	4.217	6.973	13.270	1.14	33.5	19.732	$14.9 \pm 0.3$
INF-94-52								
1	46.391	6.724	5.935	8.931	2.80	44.0	20.539	$15.5 \pm 0.2$

Sample	$^{40}\text{Ar}/^{39}\text{Ar}^a$	$^{38}\text{Ar}/^{39}\text{Ar}^a$ ( $\times 10^2$ )	$^{37}\text{Ar}/^{39}\text{Ar}^a$	$^{36}\text{Ar}/^{39}\text{Ar}^a$ ( $\times 10^{-2}$ )	$^{39}\text{Ar}_k$ ( $\times 10^{15}$ mol)	$^{40}\text{Ar}^*$ (%)	$^{40}\text{Ar}^*/^{39}\text{Ar}_k$	Model Age $\ddagger$ (Ma) ( $\pm 1\sigma$ )
2	47.604	6.632	5.885	9.477	2.62	42.0	20.131	15.2 $\pm$ 0.1
3	38.272	6.179	5.847	6.165	3.30	53.4	20.584	15.6 $\pm$ 0.1
4	42.106	6.195	6.041	7.492	3.72	48.4	20.516	15.5 $\pm$ 0.1
5	<b>91.008</b>	<b>13.330</b>	<b>1.816</b>	<b>24.390</b>	<b>0.89</b>	<b>20.8</b>	<b>19.075</b>	<b>14.4 <math>\pm</math> 0.6</b>
6	33.205	5.100	6.200	4.392	3.15	62.1	20.791	15.7 $\pm$ 0.1
7	49.169	6.858	5.803	9.966	2.73	40.9	20.244	15.3 $\pm$ 0.2
8	<b>89.103</b>	<b>13.290</b>	<b>1.173</b>	<b>24.120</b>	<b>0.81</b>	<b>20.0</b>	<b>17.929</b>	<b>13.6 <math>\pm</math> 0.6</b>
9	43.148	6.591	5.964	7.781	1.91	47.5	20.695	15.6 $\pm$ 0.2
10	<b>159.065</b>	<b>18.170</b>	<b>1.053</b>	<b>48.330</b>	<b>0.24</b>	<b>10.2</b>	<b>16.334</b>	<b>12.4 <math>\pm</math> 2.0</b>
11	33.185	5.333	6.340	4.446	3.74	61.7	20.622	15.6 $\pm$ 0.1
12	35.968	6.129	5.796	5.655	1.15	54.2	19.779	15.0 $\pm$ 0.2
INN-94-73								
1	80.267	6.360	8.193	20.700	2.18	24.5	19.830	14.9 $\pm$ 0.3
2	83.562	6.020	8.333	21.680	1.76	24.0	20.246	15.2 $\pm$ 0.4
3	66.141	5.589	8.281	15.890	1.25	29.9	19.954	15.0 $\pm$ 0.2
4	62.405	5.026	8.648	14.720	1.48	31.2	19.680	14.8 $\pm$ 0.3
5	74.521	5.901	8.464	18.860	1.71	26.0	19.550	14.7 $\pm$ 0.3
6	<b>1536.629</b>	<b>122.700</b>	<b>3.545</b>	<b>553.900</b>	<b>0.03</b>	<b>-6.4</b>	<b>-99.967</b>	<b>-77.2 <math>\pm</math> 76.9</b>
7	111.795	8.312	8.121	31.720	1.90	16.7	18.803	14.2 $\pm$ 0.5
8	68.382	5.462	8.284	16.510	2.24	29.5	20.355	15.3 $\pm$ 0.2
PHO-94-10								
1	27.069	2.182	6.193	2.347	2.05	75.6	20.696	15.7 $\pm$ 0.1
2	27.995	2.324	6.398	2.559	2.65	74.4	21.016	15.9 $\pm$ 0.1
3	27.696	2.437	6.335	2.420	1.39	75.2	21.124	16.0 $\pm$ 0.2
4	26.932	2.452	6.199	2.395	2.22	75.0	20.417	15.5 $\pm$ 0.1
5	<b>86.003</b>	<b>6.578</b>	<b>4.754</b>	<b>25.380</b>	<b>0.13</b>	<b>12.8</b>	<b>11.414</b>	<b>8.7 <math>\pm</math> 2.7</b>
6	26.102	2.338	6.291	2.080	1.98	77.8	20.528	15.6 $\pm$ 0.1
7	23.864	2.262	6.207	1.225	1.72	86.1	20.808	15.8 $\pm$ 0.2
8	30.978	2.844	6.373	4.706	0.40	55.1	17.639	13.4 $\pm$ 0.6
WIN-94-32								
1	37.478	3.112	7.491	5.936	1.21	54.3	20.619	15.6 $\pm$ 0.3
2	<b>238.600</b>	<b>17.880</b>	<b>4.860</b>	<b>7.879</b>	<b>0.14</b>	<b>2.5</b>	<b>6.163</b>	<b>4.7 <math>\pm</math> 3.0</b>

Sample	$^{40}\text{Ar}/^{39}\text{Ar}^a$	$^{38}\text{Ar}/^{39}\text{Ar}^a$ ( $\times 10^{-2}$ )	$^{37}\text{Ar}/^{39}\text{Ar}^a$	$^{36}\text{Ar}/^{39}\text{Ar}^a$ ( $\times 10^{-2}$ )	$^{39}\text{Ar}_k$ ( $\times 10^{-15}$ mol)	$^{40}\text{Ar}^*$ (%)	$^{40}\text{Ar}^*/^{39}\text{Ar}_k$	Model Age $\ddagger$ (Ma) ( $\pm 1\sigma$ )
3	38.021	3.026	6.719	6.202	2.11	52.9	20.305	15.4 $\pm$ 0.2
4	59.272	4.544	6.427	13.610	1.42	32.8	19.637	14.9 $\pm$ 0.3
5	42.881	3.471	7.155	7.926	1.83	46.5	20.109	15.2 $\pm$ 0.3
6	<b>76.188</b>	<b>6.113</b>	<b>6.320</b>	<b>21.080</b>	<b>0.15</b>	<b>18.2</b>	<b>14.363</b>	<b>10.9 <math>\pm</math> 2.3</b>
7	35.292	2.950	7.125	5.279	1.80	57.0	20.341	15.4 $\pm$ 0.2
8	39.975	3.256	6.631	6.750	0.57	50.6	20.631	15.6 $\pm$ 0.9
CAN-95-12								
1	21.372	3.725	2.786	6.293	0.92	14.0	2.989	4.3 $\pm$ 0.7
2	19.554	2.813	2.643	5.387	1.22	19.6	3.837	5.6 $\pm$ 0.5
3	9.220	4.487	2.463	1.890	1.14	41.4	3.823	5.5 $\pm$ 0.5
4	12.032	2.637	2.258	2.706	1.63	34.9	4.209	6.1 $\pm$ 0.4
5	9.826	3.447	2.226	1.985	1.34	41.9	4.128	6.0 $\pm$ 0.4
6	9.647	2.786	2.329	2.175	1.45	35.1	3.395	4.9 $\pm$ 0.4
SUN-94-30								
1	9.721	2.069	2.212	2.109	3.14	37.5	3.655	5.3 $\pm$ 0.5
2	13.117	2.593	2.329	3.386	3.14	25.0	3.289	4.8 $\pm$ 0.5
3	10.997	2.125	2.292	2.488	4.83	34.7	3.818	5.6 $\pm$ 0.3
4	11.675	2.122	2.254	2.514	3.89	37.8	4.417	6.4 $\pm$ 0.4
5	9.331	2.398	2.285	1.863	3.43	42.8	4.000	5.8 $\pm$ 0.3
6	28.063	3.525	2.286	8.520	6.23	10.9	3.059	4.5 $\pm$ 0.2
7	18.043	2.738	2.289	5.079	5.03	17.8	3.208	4.7 $\pm$ 0.2
8	12.632	2.443	2.365	3.118	4.08	28.4	3.599	5.2 $\pm$ 0.3
9	19.828	3.387	2.354	5.800	2.63	14.4	2.868	4.2 $\pm$ 0.4
10	82.372	6.335	2.891	27.875	1.18	0.3	0.218	0.3 $\pm$ 2.2
11	33.713	2.928	4.166	10.995	0.61	4.6	1.545	2.3 $\pm$ 2.5
12	9.452	1.709	2.941	1.956	1.74	41.2	3.899	5.7 $\pm$ 0.7
13	27.484	3.006	7.379	7.748	1.04	18.8	5.188	7.6 $\pm$ 1.3
14	74.792	6.134	3.288	23.732	0.84	6.6	4.923	7.2 $\pm$ 1.7
15	14.506	3.315	6.049	4.042	0.53	20.9	3.042	4.4 $\pm$ 2.3
16	32.819	3.489	3.980	10.500	0.84	6.4	2.101	3.1 $\pm$ 1.6
LCR-94-110								
1	8.916	1.898	0.441	1.696	2.21	44.0	3.925	5.7 $\pm$ 0.4

Sample	$^{40}\text{Ar}/^{39}\text{Ar}^a$	$^{38}\text{Ar}/^{39}\text{Ar}^a$	$^{37}\text{Ar}/^{39}\text{Ar}^a$	$^{36}\text{Ar}/^{39}\text{Ar}^a$	$^{39}\text{Ar}_K$ ( $\times 10^{15}$ mol)	$^{40}\text{Ar}^*$ (%)	$^{40}\text{Ar}^*/^{39}\text{Ar}_K$	Model Age $\ddagger$ (Ma) ( $\pm 1\sigma$ )
2	23.433	2.859	1.088	6.804	2.41	14.5	3.403	5.0 $\pm$ 0.4
3	8.782	1.743	1.735	1.664	2.10	45.4	3.992	5.8 $\pm$ 0.4
4	19.417	2.562	1.124	5.368	2.76	18.7	3.633	5.3 $\pm$ 0.3
5	30.616	3.104	1.611	9.193	1.84	11.6	3.568	5.2 $\pm$ 0.5
6	10.793	2.019	0.618	2.287	3.91	37.7	4.072	5.9 $\pm$ 0.2
CAN-95-11								
1	14.456	1.865	0.892	4.102	0.47	16.5	2.393	3.5 $\pm$ 2.5
2	13.924	1.437	1.721	3.138	0.57	34.3	4.779	6.9 $\pm$ 1.9
3	23.175	3.972	2.411	8.170	0.26	-3.4	-0.792	-1.1 $\pm$ 4.4
4	5.000	1.323	2.362	0.474	1.67	75.4	3.778	5.5 $\pm$ 0.8
5	5.795	1.431	2.142	0.669	3.07	68.6	3.981	5.8 $\pm$ 0.4
6	5.561	1.648	1.957	0.607	3.03	70.3	3.913	5.7 $\pm$ 0.4
7	5.368	1.307	1.968	0.581	3.21	70.7	3.799	5.5 $\pm$ 0.3
8	6.069	1.131	1.483	0.810	1.38	62.3	3.782	5.5 $\pm$ 0.6
9	6.388	1.363	1.842	0.703	2.40	69.6	4.449	6.4 $\pm$ 0.6
10	5.601	1.174	1.992	0.654	2.00	68.1	3.818	5.5 $\pm$ 0.5
11	6.528	1.434	1.907	0.863	5.98	63.0	4.121	6.0 $\pm$ 0.2
12	6.423	1.905	1.988	0.816	0.99	64.7	4.160	6.0 $\pm$ 0.8
13	7.100	1.922	2.295	1.188	0.99	52.9	3.764	5.4 $\pm$ 0.7
14	5.857	1.440	1.936	0.750	4.94	64.6	3.787	5.5 $\pm$ 0.2
15	5.283	1.621	1.927	0.475	1.77	76.1	4.025	5.8 $\pm$ 0.5
16	9.408	1.968	2.066	2.208	1.89	32.2	3.037	4.4 $\pm$ 0.4
17	6.054	1.458	2.087	0.747	3.05	66.1	4.004	5.8 $\pm$ 0.3
LCS-94-72								
1	10.914	1.510	0.120	0.791	7.37	78.5	8.573	12.5 $\pm$ 0.3
2	10.506	1.383	0.098	0.601	6.71	83.0	8.724	12.7 $\pm$ 0.3
3	10.054	1.378	0.095	0.481	14.84	85.8	8.625	12.6 $\pm$ 0.3
4	9.689	1.295	0.104	0.349	14.87	89.3	8.651	12.6 $\pm$ 0.3

Sample	$^{40}\text{Ar}/^{39}\text{Ar}^a$	$^{38}\text{Ar}/^{39}\text{Ar}^a$	$^{37}\text{Ar}/^{39}\text{Ar}^a$	$^{36}\text{Ar}/^{39}\text{Ar}^a$	$^{39}\text{Ar}_K$ ( $\times 10^{-15}$ mol)	$^{40}\text{Ar}^*$ (%)	$^{40}\text{Ar}^*/^{39}\text{Ar}_K$	Model Age $\dagger$ (Ma) ( $\pm 1\sigma$ )
<b>LCS-94-72<math>\gamma</math></b>								
1	10.818	1.207	0.006	0.697	1.66	80.8	8.743	12.7 $\pm$ 0.8
2	10.683	1.443	0.008	0.657	3.05	81.7	8.728	12.7 $\pm$ 0.5
3	10.641	1.584	0.009	0.778	3.39	78.3	8.328	12.1 $\pm$ 0.5
4	17.900	2.051	0.008	3.232	2.64	46.6	8.334	12.1 $\pm$ 0.6
<b>INF-94-24</b>								
1	17.775	3.171	7.718	2.247	1.62	66.0	11.796	17.2 $\pm$ 0.6
2	18.446	3.842	7.622	2.716	3.19	59.7	11.069	16.1 $\pm$ 0.4
3	26.460	3.659	7.611	5.369	2.42	42.3	11.244	16.4 $\pm$ 0.6
4	25.095	4.322	7.769	5.081	3.10	42.6	10.739	15.7 $\pm$ 0.5
5	26.049	3.974	7.896	5.360	2.21	41.6	10.880	15.9 $\pm$ 0.8
6	23.520	3.094	7.842	4.084	3.32	51.3	12.126	17.7 $\pm$ 0.6
7	15.746	2.586	8.478	2.064	1.70	65.5	10.367	15.1 $\pm$ 0.6
8	16.577	2.908	8.066	1.985	2.12	68.4	11.400	16.6 $\pm$ 0.8
9	26.745	4.371	6.929	5.430	2.80	42.0	11.289	16.5 $\pm$ 0.5
10	22.173	3.834	7.571	3.893	3.87	50.8	11.314	16.5 $\pm$ 0.4
11	23.557	4.322	7.300	4.357	5.54	47.8	11.303	16.5 $\pm$ 0.4
12	24.862	4.361	7.423	4.881	3.16	44.3	11.071	16.1 $\pm$ 0.5
13	24.615	4.311	7.601	4.775	2.65	45.1	11.152	16.3 $\pm$ 0.4
14	21.990	3.846	7.527	3.697	1.60	53.0	11.709	17.1 $\pm$ 0.5
<b>LCR-95-08</b>								
1	13.112	2.793	15.486	1.019	0.83	86.3	11.436	17.0 $\pm$ 0.6
2	22.820	2.789	13.922	4.601	1.48	45.2	10.415	15.5 $\pm$ 0.6
3	14.732	4.327	13.925	1.634	1.19	74.7	11.102	16.5 $\pm$ 0.5
4	13.722	2.213	14.344	1.395	1.27	78.2	10.829	16.1 $\pm$ 0.4
5	14.958	1.920	17.406	2.100	0.27	67.7	10.244	15.3 $\pm$ 1.7
<b>PHO-94-86</b>								
1	26.194	3.209	8.782	6.174	0.88	33.0	8.684	13.0 $\pm$ 1.7
2	27.738	2.563	9.367	5.689	1.92	42.0	11.729	17.5 $\pm$ 0.8



Sample	$^{40}\text{Ar}/^{39}\text{Ar}^a$	$^{38}\text{Ar}/^{39}\text{Ar}^a$	$^{37}\text{Ar}/^{39}\text{Ar}^a$	$^{36}\text{Ar}/^{39}\text{Ar}^a$	$^{39}\text{Ar}_k$ ( $\times 10^{-15}$ mol)	$^{40}\text{Ar}^*$ (%)	$^{40}\text{Ar}^*/^{39}\text{Ar}_k$	Model Age $\ddagger$ (Ma) ( $\pm 1\sigma$ )
3	31.867	2.791	9.367	7.437	1.58	33.3	10.689	15.9 $\pm$ 1.0
4	35.282	3.347	9.352	8.134	1.51	33.9	12.051	18.0 $\pm$ 0.8
5	29.287	3.872	9.593	7.444	1.48	27.5	8.091	12.1 $\pm$ 1.3
6	35.589	3.512	9.312	8.928	2.53	27.9	9.995	14.9 $\pm$ 0.6
PHO-94-86Y								
1	29.250	3.286	9.504	7.103	2.71	30.8	9.059	13.5 $\pm$ 0.5
2	20.685	2.581	9.541	3.808	2.58	49.2	10.242	15.3 $\pm$ 0.6
3	25.636	2.845	9.623	5.738	1.66	36.8	9.492	14.1 $\pm$ 0.8
4	22.781	2.498	9.767	4.681	2.03	42.6	9.776	14.6 $\pm$ 0.7
5	20.518	2.172	9.635	3.824	1.89	48.6	10.036	14.9 $\pm$ 0.7
6	19.087	2.349	9.363	3.145	1.12	55.1	10.591	15.8 $\pm$ 1.1
7	16.664	1.918	9.502	2.337	1.61	63.0	10.567	15.7 $\pm$ 0.9
KC-95-17								
1	139.408	11.327	7.750	44.168	1.11	6.8	9.543	14.1 $\pm$ 2.0
2	175.944	11.597	6.952	56.783	0.87	4.9	8.729	12.9 $\pm$ 2.2
3	288.616	21.342	7.115	97.102	0.91	0.8	2.243	3.3 $\pm$ 3.4
4	506.448	34.396	8.196	173.360	0.49	-1.0	-5.220	-7.7 $\pm$ 8.4
5	160.211	11.073	7.968	52.757	0.98	3.1	4.961	7.3 $\pm$ 2.6
6	286.209	19.893	7.394	95.260	0.60	1.8	5.316	7.8 $\pm$ 7.4
7	82.590	6.914	8.168	25.446	0.62	9.7	8.078	11.9 $\pm$ 2.2
8	173.809	13.171	7.534	57.376	1.83	2.8	4.873	7.2 $\pm$ 1.7
9	139.019	10.423	7.865	44.964	1.37	4.9	6.797	10.0 $\pm$ 2.0
10	418.780	29.630	8.065	142.316	0.79	-0.3	-1.142	-1.7 $\pm$ 5.9
11	90.733	6.971	8.116	27.741	1.17	10.3	9.440	13.9 $\pm$ 1.3
12	203.177	14.606	8.315	66.580	1.10	3.5	7.122	10.5 $\pm$ 2.9
13	101.476	9.573	7.044	31.545	1.34	8.7	8.850	13.0 $\pm$ 1.4

Sample	$^{40}\text{Ar}/^{39}\text{Ar}^a$	$^{38}\text{Ar}/^{39}\text{Ar}^a$	$^{37}\text{Ar}/^{39}\text{Ar}^a$	$^{36}\text{Ar}/^{39}\text{Ar}^a$	$^{39}\text{Ar}_k$ ( $\times 10^{-15}$ mol)	$^{40}\text{Ar}^*$ (%)	$^{40}\text{Ar}^*/^{39}\text{Ar}_k$	Model Age $\ddagger$ (Ma) ( $\pm 1\sigma$ )
KC-95-19								
1	49.719	8.843	7.401	13.718	1.34	19.6	9.806	14.3 $\pm$ 1.5
2	104.113	15.460	4.267	34.953	0.32	1.1	1.156	1.7 $\pm$ 5.9
3	37.674	7.881	7.130	10.041	1.40	22.7	8.597	12.5 $\pm$ 1.4
4	74.947	11.118	6.024	22.801	0.43	10.7	8.068	11.8 $\pm$ 4.9
5	34.440	8.687	6.424	8.758	0.54	26.3	9.098	13.2 $\pm$ 3.4
6	35.604	11.519	4.667	9.431	0.45	22.7	8.118	11.8 $\pm$ 4.0
7	36.146	13.117	4.359	9.902	0.49	20.0	7.238	10.5 $\pm$ 3.9
8	31.156	6.425	8.260	6.566	0.47	39.8	12.465	18.1 $\pm$ 3.4
9	39.615	8.818	6.767	10.266	0.40	24.7	9.846	14.3 $\pm$ 3.7
10	45.859	11.083	4.645	11.436	0.30	27.1	12.459	18.1 $\pm$ 4.9
11	32.034	7.083	8.463	7.515	0.37	32.7	10.546	15.3 $\pm$ 4.2
12	15.272	2.296	9.652	1.426	1.19	77.4	11.888	17.3 $\pm$ 1.2
13	41.102	5.630	9.654	11.104	0.42	22.0	9.101	13.3 $\pm$ 3.6
14	28.685	9.522	7.597	6.029	0.27	40.0	11.518	16.8 $\pm$ 5.7
15	23.941	6.785	6.513	2.481	0.12	71.5	17.186	24.9 $\pm$ 13.9

<sup>a</sup> Ratio corrected for non-atmospheric backgrounds, atmospheric line blanks, mass discrimination, abundance sensitivity, and radioactive decay but not for atmospheric argon or interfering nuclear reactions

$\ddagger$  Assumes atmospheric trapped argon ( $^{40}\text{Ar}/^{36}\text{Ar} = 295.5$ )

## APPENDIX E

## Collection techniques for paleomagnetic samples

A brass orienting sleeve with attached frontal plate is slid around each drilled core while it is still attached at the back to the rock, and the strike and dip of the plate is measured with a Brunton compass (magnetic declination conventionally set to  $0^\circ$ ) and recorded. If the sun is shining on the core plate then an orientation with a sun compass is taken as well. This can help identify local magnetic anomalies which might affect the Brunton compass reading. (Fortunately, good agreement was generally found between sun compass measurements and directions recorded with the Brunton compass.) With the orienting sleeve still in place, the top of the core is marked on the outside face with a marking pen or scraped with a small piece of aluminum. The core is broken from the rock and is marked along its length starting at the mark on the top side. Sample numbers and arrows indicating the direction out of the rock are drawn on all samples as well.

If a core is inadvertently broken prior to the orientation step, the core is removed and the orientation of the hole measured. In these cases the brass orienting sleeve is somewhat loose in the hole, and the position of it is subject to slightly greater uncertainty than when positioned for unbroken cores. There is also a risk of measurement error associated with broken cores if the core cannot be precisely reoriented in the hole in order to be properly marked. Fortunately the irregular nature of the broken base of a core usually yields only one possible fit between the broken core and the rock. A core was not collected if the broken base was smooth or had broken further into additional pieces at this contact. All broken samples included in this study (total of 23) were noted as "broken" in case misorientation occurred, although the results of this study suggest that none of the broken samples were misoriented.

Hand samples drilled in the lab with the drill press were oriented using lines of known trend and plunge drawn on the rocks in the field. After drilling several cores in each sample, the samples were positioned using modeling clay into the same orientation in the lab as they had been in the field. Orientation measurements for each core were made and recorded.